THE UNIVERSITY *of* EDINBURGH

This thesis has been submitted in fulfilment of the requirements for a postgraduate degree (e.g. PhD, MPhil, DClinPsychol) at the University of Edinburgh. Please note the following terms and conditions of use:

This work is protected by copyright and other intellectual property rights, which are retained by the thesis author, unless otherwise stated.
A copy can be downloaded for personal non-commercial research or study, without prior permission or charge.
This thesis cannot be reproduced or quoted extensively from without first obtaining permission in writing from the author.
The content must not be changed in any way or sold commercially in any format or medium without the formal permission of the author.
When referring to this work, full bibliographic details including the author, title, awarding institution and date of the thesis must be given.

Photovoltaics as High-Speed Optical Wireless Communication Receiver

Sovan Das

THE UNIVERSITY *of* EDINBURGH

A thesis submitted for the degree of Doctor of Philosophy
The University of Edinburgh
2021

Declaration

I hereby declare that the research recorded in this thesis and the thesis itself was composed and originated entirely by myself in the Institute of Digital Communications (IDCOM) of the School of the Engineering at the University of Edinburgh.

The exceptions to the above are,

1. The optical simulations for the laser transmitter design used in the FSO links mentioned in Chapter 6 were carried out by Dr John Fakidis during his time as a Post-doctoral Research Associate at the LiFi Research & Development Centre as part of IDCOM at the University of Edinburgh.
2. The MATLAB codes used for the measurement results in 6.2.1.3 are based on the codes developed originally by Dr Stefan Videv and Dr Dobroslav Tsonev in IDCOM at the University of Edinburgh. The OFDM and PAM modifications were added by Dr Rui Bian and Dr Mohamed Islim Sufyan at the LiFi Research & Development Centre as part of IDCOM at the University of Edinburgh.

I declare that the concepts presented in this thesis have not been used for the purposes of obtaining another degree or professional qualification.

Sovan Das

Abstract

With an ever-growing network of billions of interconnected smart devices in the era of the Internet of Things, high-speed communication has inspired research into the use of low energy and high-speed free-space optical (FSO) communication systems. In FSO communication, light-emitting diodes (LEDs) and lasers are used for wireless data transmission in indoor and outdoor environments and photodiodes are used as data receivers. But these receivers have two main disadvantages – they require an external power source to operate, and their small active area makes alignment challenging. A promising solution to these problems is the use of solar panels as data receivers. As photovoltaic (PV) panels have a larger active area compared to that of conventional photodiodes, they relax the strict alignment requirements and can also simultaneously harvest energy from sunlight.

The current work investigates the use of Si-based off-the-shelf PV panels as FSO receivers to build an energy-neutral and high-speed FSO system. As solar panels were never built as optical data communication receivers, they have a very small communication bandwidth compared to photodiodes. In this work, a theoretical model of the solar panel is provided and, using analogue equalization, the usable communication bandwidth of a solar panel is extended. PV panels were primarily designed to harvest energy from sunlight. Using the analytical model, simultaneous energy harvesting, and data communication performances are evaluated. Moreover, the trade-off between the energy harvesting and data communication capability of the solar panel is shown. Furthermore, the use of different spectrally efficient modulation techniques such as direct current optical orthogonal frequency division multiplexing (DCO-OFDM) and discrete multitone pulse-amplitude modulation (DMT-PAM) are compared when used with a solar panel as an

optical receiver. It has been found that each modulation scheme is usable under different applications.

Using the simulated results from the analytical model an FSO prototype was designed and developed, demonstrating the use of solar panels as the receivers. A receiver circuit to interface the solar panel with the FSO system was designed and developed to demonstrate the data communication and energy harvesting performance. Data rates as high as 75 Mb/s is demonstrated using DCO-OFDM and offline processing using an off-the-shelf Si-based solar panel. The PV panel-based FSO system was used to provide internet access to two residential properties on a remote island in the northern part of Scotland. The performance of the prototype was carefully studied under various weather conditions. Furthermore, the maximum user throughput achieved by the prototype is 28.3 Mb/s with the simultaneous energy harvesting capability of up to 4.5 W. Lastly, the design of a custom-built solar panel is proposed which doubles the data rates shown in this work and can be implemented alongside a small-scale to large-scale solar energy harvesting infrastructure.

Lay Summary

Wireless data access has become a necessity in today's digital data-driven world, which plays a significant role in all aspects of modern societies, including healthcare, commerce, politics, and education. The demand for easily accessible high-speed internet has been growing exponentially. This growth inspired research into using solar panels as optical wireless communication receivers. The solar panels could simultaneously harvest energy from the sunlight and receive optical data. This proposed solution offers multiple advantages over existing systems. Mainly, the proposed system can harvest energy and is self-sustainable. Therefore, it can be deployed easily in the most challenging geographical locations to provide data connectivity and power.

Current literature focuses primarily on the research and development of electronic circuits and techniques which allow the solar panels to be used as high-speed optical data receivers, while harvesting power from sunlight. Moreover, different popularly used optical modulation techniques are also reviewed when used with the solar panel as a receiver. It was found that the highest data rates could be achieved using direct current optical orthogonal frequency division multiplexing (DCO-OFDM). The theoretical maximum data rate that could be achieved using an off the shelf 5 W silicon solar panel was estimated to be 75 Mb/s.

A free-space optical communication prototype was designed and developed using a solar panel as a receiver. The prototype demonstrated a maximum user available data rate of 28.3 Mb/s while simultaneously harvesting a peak power of 4.5 W. The data rate and energy harvesting capability of the system was enhanced further by proposing a new design of the solar panel.

Acknowledgements

My deepest gratitude goes to my family for their love and support: this thesis would have been impossible without them. I am indebted to my parents, Shyam Sundar Das and Suranjita Das for shaping me into who I am today. I am grateful to my late grandfather Goura Gobinda Das who always encouraged my curiosity and strengthened my mathematics and science basics since childhood.

I would like to extend my gratitude to Prof. Harald Haas for giving me this opportunity to pursue a PhD under him and for the invaluable guidance he has given me throughout my research. His enthusiasm for research and his encouragement helped me to push my limits. Furthermore, I would like to thank Dr Stefan Videv, Dr Enrique Poves, Mr Adrian Sparks, Dr John Fakidis, Mr Damian Parol and Mr Pedro Gomez who helped and guided me through the building of the prototypes required for my research. Working with them helped me enhance my engineering skills which has played a major role in my research and further career development. Also, they have been an integral part of my entire academic experience and made it enjoyable. My sincerest gratitude also extends to Ms Hannah Brown who helped me with the linguistic corrections in my thesis and several research papers.

Last but not least, I would like to thank my friends for tirelessly supporting me throughout my studies. Thank you, Ankit, Sap and Abhijeet Sirji for making my stay in Edinburgh very memorable. Thank you, Abhinash, Agyanta, Arko, Lovely Lady, Manish, Hobo, Aman, Varun, Classique and Ilhaam who have always kept me motivated when things went sideways and encouraged me to bring out the best in myself.

Contents

List of Figures

List of Tables

Acronyms and Abbreviations

AC	Alternating Current
ADC	Analogue-to-Digital Converter
ADSL	Asymmetric Digital Subscribers' Line
AFE	Analogue Front End
APD	Avalanche Photodiode
AR	Anti-Reflective
ARM	Advanced RISC Machine
ASIC	Application Specific Integrated Circuit
AWG	Arbitrary Waveform Generator
BER	Bit Error Rate
BMS	Battery Management System
BPSK	Binary Phase Shift Keying
CdTe	Cadmium Telluride
CPU	Central Processing Unit
CPV	Concentrated Photovoltaic
DAC	Digital-to-Analogue Converter
DC	Direct Current
DCO-OFDM	Direct Current Optical Orthogonal Frequency Division Multiplexing
DD	Direct Detection
DFT	Discrete Fourier Transform
DSP	Digital Signal Processing
EM	Electromagnetic

EQE	External Quantum Efficiency
FCC	Federal Communications Commission
FEC	Forward Error Correction
FFT	Fast Fourier Transform
FIR	Finite Impulse Response
FM	Frequency Modulation
FPGA	Field-Programmable Gate Array
FSO	Free Space Optical
FWHM	Full Width Half Maximum
GaAs	Gallium-Arsenide
GaInP	Gallium Indium Phosphide
HD	High Definition
IC	Integrated Circuit
IFFT	Inverse Fast Fourier Transform
IM	Intensity Modulation
IP	Internet Protocol
IQE	Internal Quantum Efficiency
IR	Infrared
ISI	Inter-symbol Interference
ISP	Internet Service Provider
Laser	Light Amplification by Stimulated Emission & Radiation
LED	Light Emitting Diode
LiFi	Light Fidelity
Li-ion	Lithium Ion

LiPo	Lithium Polymer
LPF	Low Pass Filter
MAC	Medium Access Control
MCM	Multi-carrier Modulation
MOSFET	Metal Oxide Semiconductor Field Effect Transistor
MPE	Maximum Permissible Exposure
MPPT	Maximum Power Point Tracking
NHZ	Non ocular Hazard
OFDM	Orthogonal Frequency Division Multiplexing
OOK	On-Off Keying
OWC	Optical Wireless Communication
PAM	Pulse Amplitude Modulation
PAM-DMT	Pulse Amplitude Modulation Discrete Multitone
PCB	Printed Circuit Board
PD	Photodiode
PHY	Physical
PIN	Positive-Intrinsic-Negative
PN	Positive-Negative
PoE	Power-over-Ethernet
PPM	Pulse Position Modulation
PV	Photovoltaic
PWM	Pulse Width Modulation
QAM	Quadrature Amplitude Modulation
RF	Radio Frequency

RG	Radio Guide
RISC	Reduced Instruction Set Computer
Si	Silicon
SNR	Signal-to-Noise Ratio
SoC	System on Chip
SoM	System on Module
SPICE	Simulation Program with Integrated Circuit Emphasis
TCP	Transfer Control Protocol
TRL	Technology Readiness Level
USB	Universal Serial Bus
VCSEL	Vertical Cavity Surface Emitting Laser
VLC	Visible Light Communication
WDM	Wavelength Division Multiplexing
WiFi	Wireless Fidelity
WLAN	Wireless Local Area Network
WMC	Wideband Multicore Circulator
WOPT	Wireless Optical Power Transfer

Nomenclature

B	Bandwidth
c	Velocity of light in vacuum
C	Capacitance
C_d	Diffusion capacitance
C_j	Junction capacitance
E	Electric field across the depletion region
f	Frequency
h	Plank's constant
I	Current
I_0	Diode saturation current
I_D	Diode current
I_d	Dark current
I_{DC}	Direct current
I_{ph}	Photo generated current
I_s	Alternating current
I_{sc}	Solar panel short-circuit current
K	Boltzmann constant
L	Inductance
M	Constellation size
P	Incident optical power
P_{MP}	Maximum power harvested by the solar panel
P_o	Power harvested by the solar panel

P_s	Time-varying optical signal
q	Charge of an electron
R	Resistance
R_d	Diode resistance
R_L	Load Resistance
R_s	Series resistance
R_{sh}	Shunt resistance
T	Temperature
t	Time
V	Voltage
V_D	Diode voltage
V_{oc}	Solar panel open-circuit voltage
W_n	Width of n-doped region
W_p	Width of p-doped region
x_n	Thickness of the depletion region in the n-doped region
x_p	Thickness of the depletion region in the p-doped region
Z_{amp}	Trans-impedance gain of an amplifier
z^{-1}	Unit delay in Z transformation notation
α	Absorption coefficient
η	Quantum efficiency
λ	Wavelength
μ_e	Electron mobility factor
μ_h	Hole mobility factor
Σ	Sum of multiple terms

σ_D^2	Dark current noise spectral density
σ_{sh}^2	Shot noise spectral density
σ_{th}^2	Thermal noise spectral density
τ_e	Time taken by an electron to travel through the depletion region
τ_h	Time taken by a hole to travel through the depletion region
τ_n	Minority charge carrier lifetime
φ	Spectral responsivity
$\langle i_{th}^2 \rangle$	Thermal noise power
$\langle i_{sh}^2 \rangle$	Shot noise power
$\langle i_D^2 \rangle$	Dark current noise power
$\langle i_{amp}^2 \rangle$	Input noise power
$\langle I_s^2(t) \rangle$	Photogenerated signal power
$\langle v_{amp}^2 \rangle$	Output noise power of an amplifier

Chapter 1 Introduction

In recent years, the commercial, industrial, and scientific communities have shown an increase in interest towards wireless communication technologies. However, the present radio frequency (RF) based wireless network infrastructure is not able to fully satisfy these traffic demands. Therefore, the wireless communication community has started adopting the use of millimetre wave (mmWave) radiation of the electromagnetic (EM) spectrum. This part of the spectrum is undergoing significant research, development, and nascent adoption in commercial mobile internet. In the telecommunication industry, this is the fifth generation (5G) technology [1] standard for broadband cellular networks. The 5G mobile network is envisioned to exploit the enormous amount of spectrum in the millimetre wave bands to greatly increase communication capacity. The potential applications of mmWave communications in the 5G network includes the small cell access, the cellular access, and the wireless backhaul. Although, the rapidly growing technologies such as self-driving vehicular technology [2], virtual reality and artificial intelligence powered IoT devices [3] is increasing the demand for the communication bandwidth. Therefore, soon there will be a sixth-generation standard for wireless communication technologies supporting cellular data networks.

In the sixth generation, the data rates will be expected to be significantly faster than their predecessor. Hence, the research, development and adoption will move to the optical spectrum of EM radiations. Free Space Optical communication (FSO) and its variant of the visible light communication (VLC) are promising new approaches towards mitigating the looming radio frequency (RF) spectrum crisis in the upcoming generations of wireless

communication technologies [4]. The optical spectrum is 2600 times larger than the entire 300 GHz radio frequency (RF) spectrum, including the mmWave [5]. It has been shown that terabit per second (Tb/s) wireless access network could be built using the optical spectrum [5]. Moreover, mmWave and optical spectrum behave similarly while interacting with solid surfaces [6]. Whereas optical wavelengths, especially in infrared region, have lower attenuation compared to mmWave when propagating through free space or air [6]. Hence, to future-proof wireless communication optical wireless communication should be the way forward.

Simultaneously, mankind is shifting from fossil fuel to other renewable sources of energy, such as solar power, to reduce the carbon footprint left by the human race. An energy-neutral optical wireless communication (OWC) system is the need of the hour. A system that can simultaneously harvest energy from a renewable source and enable high-speed wireless communication can solve a lot of problems at present. This work presents a potential candidate for the energy neutral OWC system, which uses solar panels as wireless optical data receivers and simultaneously harvests energy from the sunlight.

1.1 Motivation

In this era of the Internet of Things (IoT) [7], high-speed wireless communication faces many challenges. One of these is the rapidly growing digital divide between urban and rural areas. In many rural parts of the world, the internet-based transformation of healthcare education and commerce is slowed by poor network infrastructure. This, coupled with an ever-rising demand for network capacity in urban areas, effective solutions to improve rural connectivity is urgently needed. Furthermore, the inadequate electrification in remote areas makes the installation of wireless base stations in rural areas challenging. Laying optical fibre cables for broadband internet

connectivity can be a solution to the problem but not economically feasible. Installing and maintaining fibre optic cables from the data centres to remote locations with challenging terrains can be challenging and expensive. Therefore, using off-the-shelf solar panels as wireless optical data receivers to provide connectivity to these remote locations can be an ideal solution.

The solar panels are capable of harvesting energy from sunlight, making the FSO link self-sustainable. Also, the surplus harvested energy from the sunlight can be used for other domestic or commercial use, enabling 100% electrification in remote locations. Furthermore, solar cell technology is rapidly developing. The efficiency of solar cell is continuously increasing by the efforts of many researchers. Also, due to the green technology issue, solar cells have been widely used in many devices such as smartwatches and other portable consumer electronic devices, to gather optical energy from the environment (usually from the Sun). Currently, solar cells are commonly used to obtain optical energy. However, if the solar cells can also receive a wireless optical signal, those portable consumer electronic devices can use the solar cells for communication and simultaneous energy harvesting, making them eco-friendly.

1.2 Contributions

For the first time, in this thesis an 80 m outdoor FSO prototype with an off-the-shelf 5 W silicon (Si) solar panel as a data receiver is developed and deployed as shown in Figure 1-1. The data is transmitted by varying the intensity of optical power output of a laser and received using an off-the-shelf 5 W Si-based solar panel. The solar panel is capable of harvesting power from sunlight while simultaneously receiving optical data. This FSO system was used to provide connectivity in remote locations. The solar panel is used to harvest energy from the sunlight and simultaneously receive optical data signal. The developed system is classified to be class 1M as per the British

laser safety standards [8]. The class 1M classification is considered to be eye-safe unless and until an optical aid, such as a binocular or telescope, is used to observe the output beam directly in front of the transmitter enclosure opening within a non-ocular hazard distance.

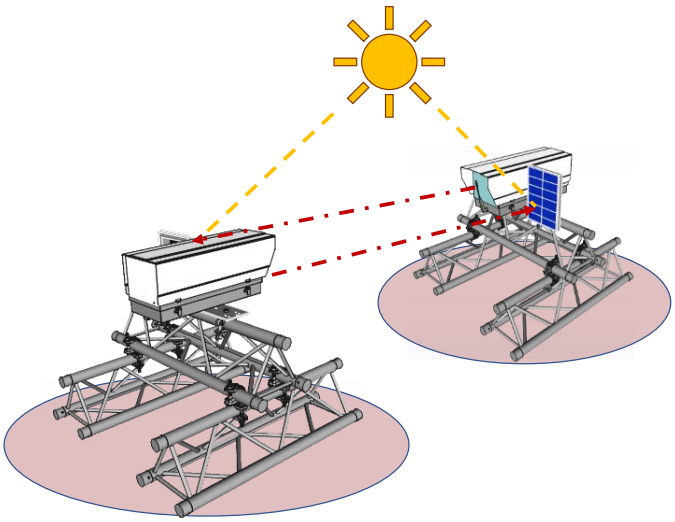

Figure 1-1: Solar panel as an FSO receiver

As part of the system development, a receiver circuit is designed and developed to enhance the inherent low communication bandwidth of a solar panel. The different methods of interfacing the solar panel with the receiver circuit are investigated.

Furthermore, to enable real-time communication, field-programmable gate array (FPGA) and application-specific integrated circuit (ASIC) based digital signal processing (DSP) platforms are used. These platforms provided the physical (PHY) layer and medium access control (MAC) layer which is based on the IEEE 802.3 ethernet standards and IEEE 802.11 wireless local area network (WLAN) standards. This enables the system to be easily interfaced with the existing networking infrastructure and provide wireless connectivity while being energy neutral.

The system was further tested in the laboratory with offline digital signal processing on MATLAB using two different spectrally efficient modulation techniques *i.e.,* orthogonal frequency division multiplexing (OFDM) [9] and pulse amplitude modulation with discrete multitone (PAM-DMT) [9]. The application of OFDM and PAM are compared, and the benefits are shown for different use cases of the system. The highest ever data rate was achieved using off-the-shelf large Si-based solar panels with the OFDM modulation technique. Furthermore, using an analytical model, the electrical characteristics of a solar panel as an optical data receiver is studied in depth. This analytical study is further verified experimentally by developing an end-to-end prototype in the laboratory. The effects of varying sunlight on the data communication performance of the solar panel are studied thoroughly. It is shown that there is a trade-off between energy harvesting capability and data communication performance when an off-the-shelf solar panel is used. To overcome this trade-off, a custom solar panel design is proposed which is built out of off-the-shelf PV modules. This design doubles the overall communication performance of the system and enhances the energy harvesting capabilities. The maximum raw throughput achievable, over two wavelengths, with this receiver was estimated to be over 100 Mb/s with a simultaneous power harvesting functionality of up to 9.1 W.

1.3 Thesis layout

The rest of the thesis is organised as follows. Chapter 2 introduces the previous work on using solar panels as data receivers. This chapter also includes the introduction to the fundamental concepts used in building a high-speed FSO link. Chapter 3 describes the analytical model of the solar panel used to study the electrical characteristics which are relevant for data communication and energy harvesting performance. In Chapter 4, an experimental setup is developed to verify the estimations obtained from the analytical model in Chapter 3. Using the knowledge from Chapters 2-4, in

Chapter 5 a receiver circuit is designed to enhance the communication bandwidth of the solar panel using analogue equalisation. Also, the different methods of interfacing the solar panel with the receiver circuit are mentioned and compared extensively. In chapter 6, the FSO prototype design, architecture and integration are shown. This FSO prototype is deployed at two locations and the results obtained from these deployments are presented and discussed in this chapter as well. The limitations found in the prototype developed in Chapter 6 are solved in Chapter 7 by building a custom solar panel. The design process and the simulated results obtained for this custom solar panel are presented in Chapter 7. In Chapter 8, the key findings of this thesis are provided with concluding remarks. Finally, the limitations of using solar panels as an FSO receiver are discussed along with possible future work.

1.4 Summary

Solar panels have the capability of harvesting energy and simultaneously receiving an optical data signal which is expected to solve the rural digital divide. The FSO system, with an off-the-shelf Si-based solar panel as a data receiver, has been studied in detail and a deep understanding of the underlying issues has been obtained. Despite the in-depth research efforts in the field, a lot of the questions remain unanswered. The current work provides a further understanding of analogue electronics techniques which are used to enhance the usable communication bandwidth of a solar panel. This chapter presents the motivation behind this problem statement, the major contributions of this thesis and provides an outline of the subsequently presented work.

Chapter 2 Background

The photovoltaic (PV) effect was first observed by French physicist Alexandre Emond Becquerel in 1839 while he was experimenting with metal electrodes and electrolytes [10]. While experimenting, he discovered that conductance increases with illumination. In 1904, Wilhelm Hallwachs made a semiconductor-junction solar cell with copper and copper oxide. The first silicon solar cells were used to power the Telstar communication satellite launched in 1962 and were developed further for use in terrestrial installations. Modern manufacturing techniques have made low-cost silicon solar cells readily available. This has prompted an investigation into their application in areas other than direct sunlight to electrical energy conversion. Solar cells can harvest electrical energy from electromagnetic radiation generated by lasers and light-emitting diodes (LEDs) as well as sunlight. This prompted the investigations into using solar cells for wireless optical power transfer (WOPT) and as optical receivers in OWC systems.

2.1 Introduction

Since their invention, solar panels have already undergone three generations of development to optimize their power efficiency. The first generation consists of solar panels made of monocrystalline or polycrystalline silicon (Si) which is still the most commonly used type in conventional applications. Monocrystalline panels have a higher power output, better temperature stability and last longer than polycrystalline panels [11]. These solar panels are also low-cost, easily available and, are commonly deployed for large-scale solar energy harvesting. The second generation of solar panels consists of different types of thin-film solar cells and are mainly integrated into building's solar windowpanes, solar car windshields, smartwatches, *etc.* The

increment in optical-to-electrical energy conversion efficiency is minimal compared to that of first-generation solar panels. Among the many benefits achieved in second-generation solar panels was their availability in different form factors. The third-generation solar panels are based on solar cells that use organic and inorganic materials to harvest energy. Third-generation solar panels refer to a variety of thin-film technologies which are mostly still in research and development. Some inorganic semi-conductor compounds commonly used are cadmium telluride (CdTe), gallium arsenide (GaAs), and gallium indium phosphide (GaInP). They harvest energy in the same way as conventional solar panels but have a smaller active area. An additional optical element, such as a Fresnel lens, is required to concentrate the optical energy onto the small active area. Therefore, they are also commonly referred to as concentrated photovoltaic (CPV) cells. These solar cells have recorded efficiencies as high as 47.1% under illumination density that corresponds to the equivalent of 143 suns concentration [12]. There are solar cells that use hybrid organic-inorganic substances, such as the perovskite solar cell. Perovskite solar cells have a perovskite structured compound of tin or lead halide-based material as the light-harvesting layer [13]. The main advantage of perovskite solar cells over Si-based cells is that they are cheaper to manufacture [13]. All the above-mentioned generations of solar cell technologies are capable of simultaneous energy harvesting and data communication, as the fundamental principle of optical-to-electrical conversion of these cells is based on the same photovoltaic effect discovered two centuries ago.

2.2 Free space optical communication systems

A free-space optical (FSO) communication system is an optical communication technology that uses the visible or infrared part of the EM spectrum propagating in free space to wirelessly transmit data for telecommunications and computer networks [14]. Here “Free space” can refer

to air, outer space, vacuum, or media with similar properties. This is contrary to using solids such as optical fibre cable or an optical transmission line, but analogous to wireless RF communication. An advantage of using FSO is that there is no license required from the Federal Communications Commission (FCC) to install the FSO system [15]. Apart from that, the cost of installation is primarily low because there is no extra cost of digging the street to lay fibre. In terms of communication security, FSO uses a narrow beam which makes detection, interpretation and jamming very difficult which is opposite in the case of RF communication. Moreover, FSO hardware is also portable and quickly deployable [16]. Therefore, FSO communication is the most practical alternative to RF and optical fibre communication to solve the bottleneck broadband connectivity problem. Both point-to-point, point-to-multipoint, multipoint-to-point and multipoint-to-multipoint FSO communications are possible, depending on different established optical link scenarios [16].

In FSO systems, the characteristics of the channel or the media determine the transmission and reception of optical signals for designing reliable and efficient communication systems. In Figure 2-1, the block diagram of an FSO communication system is shown. The digital data fed by the user to the system is first encoded into symbols, in a form that is suitable for transmission over the free space, by the microprocessor. Then the Field Programmable Gate Arrays (FPGAs) or Application Specific Integrated Circuit (ASIC) modulates the encoded data to generate a digital baseband signal. The digital signal is then converted to analogue signal by the digital-to-analogue converter (DAC). The generated analogue baseband signal is then converted to optical signal by the transmitter block for transmission. On the receiver end, the same process happens in the reverse order. The analogue-to-digital converter (ADC) converts the analogue signals to digital baseband signal, which can be then demodulated by the FPGA/ASIC. Then the processor decodes the data from the received symbols for the user. The transmitter and

receiver constitute the analogue front ends (AFEs) of the FSO system, while the processor, FPGA/ASIC, ADC, and DAC constitute the Digital signal processing (DSP) platform.

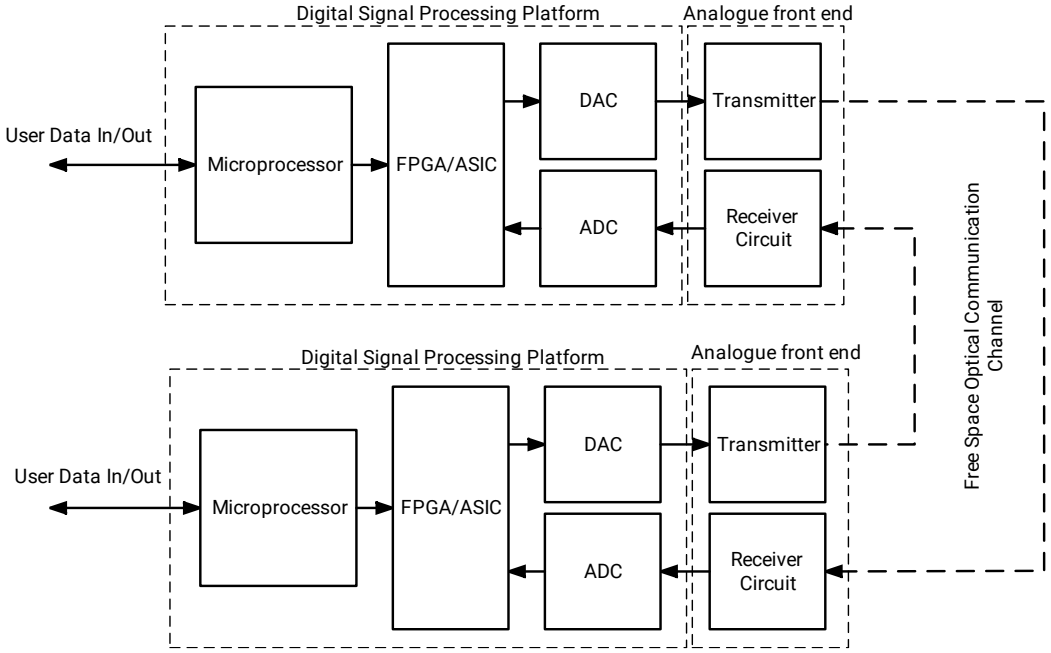

Figure 2-1: Block diagram of an FSO communication system

In this thesis, the idea of using an off-the-shelf Si-based solar panel as an FSO receiver has been introduced. Traditional FSO systems use Photodiodes (PDs) as receivers. PDs have a small area and can be very difficult to align when used for long-distance communication. They require additional optical elements to focus the optical signal on to the active area. With added optical elements, complex alignment systems are required. Using solar panels, these complexities can be avoided. Furthermore, the optical energy harvested by a solar panel can be used to offset the energy consumed by the rest of the components of the communication system. Also, the large active area of the solar panel eases the system alignment. Using a solar panel as an FSO inherits all the advantages of using an FSO system *i.e.*, ease of deployment, security, cost of installation. As a matter of fact, using solar panels as receivers simplifies the overall system by eliminating the need for complex alignment

systems and the need for external power source. As there is no external power source required, it makes deploying the system easily in remote locations.

2.3 OWC systems using photovoltaics as receivers

The concept to use a Si-based solar cell as a data detector was demonstrated for the first time in 1976 [17]. However, the concept of simultaneous wireless information and power transfer in the optical spectrum was studied in this decade in [18] and [19] using white LEDs and first-generation Si-based solar cells. The data rate of 3 kb/s achieved with on-off keying in [20] is considered insufficient for high-speed data communication. A significant data speed of 7 Mb/s and harvested power of 2.1 mW are reported in [19] by using a polycrystalline Si PV panel and OFDM. Going forward from these initial demonstrations, a 12 Mb/s wireless data link with a distance of 1 m was created in [18] using a white LED and the same solar panel receiver with that in [19]. The third-generation solar cells are designed and developed considering the dual usage of energy harvesting and communication. The third-generation PV technologies used for data detection include organic [21] and GaAs PV cells [22]. Those devices offer lower capacitances than Si-made solar panels due to their reduced sizes and their electrical bandwidth is much higher, *i.e.,* of the MHz order. In [21], a data rate of 34.2 Mb/s is reported for a 1 m OWC link using an organic solar cell. The highest data rate reported using organic PV cells is 363 Mb/s, using 4-by-4 multiple-input multiple-output (MIMO), with a simultaneous harvested power of 10.9 mW in [23]. Using a GaAs PV cell as a data detector a data rate of 522 Mb/s has been achieved in [22] at a 2 m link distance. In [22] it was found that using a single variable resistor as load, simultaneous energy harvesting, and communication was not possible. Hence, a follow-up study was carried out in [24] with an AC-DC coupled receiver circuit which achieved a record data rate of 1 Gb/s under short circuit conditions. However, the additional advantage of high efficiency and data rate increases system complexity adding several disadvantages.

Such as, requiring a cooling system to avoid damaging the PV cells from highly concentrated solar irradiation. Additional optical elements are required to concentrate the sunlight and optical signal onto the small active area of the PV cell. Furthermore, complex systems are needed to align the optical elements and track the optical signal [25] and sun.

In the above-mentioned solar panel based OWC systems, only the concept of using the different generations of solar panels has been explored. The pathway to enhancing the communication bandwidth of existing solar cell technology is missing. The simultaneous energy harvesting performance and data communication performance of a solar panel has not been studied.

In the last five decades the application of photovoltaic (PV) panels in a wide variety of scenarios such as space technology, military applications, domestic usage, and self-powered pocket devices has been driving the research and development of PV technology. Therefore, in this work, a first-generation solar panel as a high-speed optical data detector is considered for studying the simultaneous energy harvesting and data communication capability, as it mitigates the issues faced by the third-generation PV cell technologies, discussed previously. Furthermore, a receiver circuit design is proposed to maximise the communication bandwidth of a solar panel while simultaneously harvesting power from sunlight. Such that this knowledge can be used to upgrade the existing solar energy harvesting systems, which are mostly based on first-generation solar panels due to the ease of availability of Si and the low manufacturing cost of Si wafers. Furthermore, this study can be extended to later generations of solar panels to enhance their energy harvesting and data communication capabilities as they are developed with the same underlying photovoltaic effect principles.

2.4 Analogue front-end elements

2.4.1 Transmitter

FSO systems generally use semiconductor based optical sources, namely LEDs and lasers, in the visible or infrared (IR) part of the optical spectrum [26]. The encoded data is transmitted as a variation in the intensity of the light emitted by the source. The LED is envisioned to serve the dual purpose of illumination and communication in indoor environments. Although, for long-distance optical communication using LEDs becomes challenging as the radiation is spatially and temporally non-coherent. On the contrary, the radiation from lasers is coherent and can have a significantly higher coherence length than LEDs. Coherence length can be defined as the space over which the phase of a wave of beam can be predicted [27]. If the centre of the range of wavelengths emitted by an optical source is λ and the range of wavelengths emitted is $\Delta\lambda$, then the coherence length of the optical source equals $\lambda^2/2\Delta\lambda$ [28]. Additionally, lasers are more efficient than LEDs.

Lasers are commonly used in long-distance wireless optical communication systems because coherent light can be transmitted over much greater distances than incoherent light. With the appropriate optical setup, coherent laser light can be transmitted in the order of kilometres in free space. LEDs on the other hand, tend to distribute their power over a larger area, but without being spatially coherent and disperse easily over a short distance. In telecommunication, there are two laser structures that are commonly used: edge-emitting lasers and vertical-cavity surface-emitting lasers (VCSEL). In an edge-emitting laser, the light propagates in a direction along the wafer surface of the semiconductor chip and is reflected or coupled out at a cleaved edge [29]. In VCSEL, the laser beam is emitted perpendicular to the top surface, in contrast to conventional edge-emitting semiconductor lasers which emit from surfaces formed by cleaving the individual chip out of a wafer [30]. VCSELs are

used in various laser products, including computer mice, fibre optic communications, laser printers, face recognition, and smart glasses. Two important aspects of VCSEL are the low beam divergence compared to that of edge-emitting lasers and the symmetric beam profile. This makes it easy to collimate the output beam with a simple optical element. Also, VCSELs have 3-dB communication bandwidth as large as 20 GHz [30]. These advantages make VCSEL an ideal choice as the optical signal source for long-distance transmission. The selection of wavelength is important in order to reduce the scattering coefficient and atmospheric attenuation. The infrared spectrum produces less effect in scattering coefficient and attenuation [31].

2.4.2 Receiver

On the receiver side, typically photodiodes (PD) are used due to their high bandwidth and linear response [32]. The most common types of PD used in FSO technology are positive-intrinsic-negative (PIN) PDs and avalanche photodiodes (APDs). The bandwidth of a PD is enhanced by increasing the width of the depletion region. This is achieved in PIN photodiodes with the insertion of the intrinsic region. The construction of an APD is similar to that of a PIN PD, but the reverse voltage applied across an APD is very large which causes impact ionization [33]. This increases the number of carriers and increases the sensitivity of an APD compared to that of a PIN PD. This increased sensitivity helps to detect optical signals with very low power. APDs are highly susceptible to noise if the background irradiance is high [34]. These devices require additional power to generate high voltage. Therefore, solar cells can be a good energy-neutral alternative to photodiodes (PDs) as they can convert variations in the intensity of the light to electrical signals without the application of reverse bias voltage. Furthermore, solar panels are by default manufactured with multiple solar cells connected in series and parallel configuration. This results in the communication receiver having a large active area and increases the energy harvesting capability. The amount of light that

is collected by a PD is proportional to its active area. Therefore, the larger the area of the device is, the more light it can collect, and the higher is its tolerance to misalignment. At the same time, the larger the area, the slower is the switching speed of the device and the worse the communication bandwidth is.

2.5 Modulation techniques

In an FSO system, the maximum usable communication bandwidth limitation is generally set by the analogue front ends *i.e.,* the transmitter and receiver. By using the appropriate modulation techniques, the utilisation of the communication bandwidth can be maximised to achieve very high data rates. In FSO, intensity modulation and direct detection (IM/DD) is used, *i.e.,* the intensity of the optical source is modulated with the desired signal to be transmitted, the change in the intensity is detected by a receiver and the signal is demodulated. Furthermore, multicarrier modulation techniques use the frequency spectrum efficiently to transmit data [9]. The two most widely used, spectrally efficient, modulation schemes with IM/DD are direct current optical orthogonal frequency division multiplexing (DCO-OFDM) [35] and pulse amplitude modulation with discrete multitone (PAM-DMT) [36].

2.5.1 Orthogonal frequency division multiplexing

OFDM [37] belongs to a broader class of multicarrier modulation (MCM) in which data is carried over many lower rate subcarriers. The structure of a generic implementation of an OFDM system is shown in Figure 2-2. In Figure 2-2, C_N is the information symbol to be transmitted and C'_N is the information symbol received. Typically, the digital data is encoded using quadrature amplitude modulation (QAM) on multiple carrier frequencies that are orthogonal to each other [38].

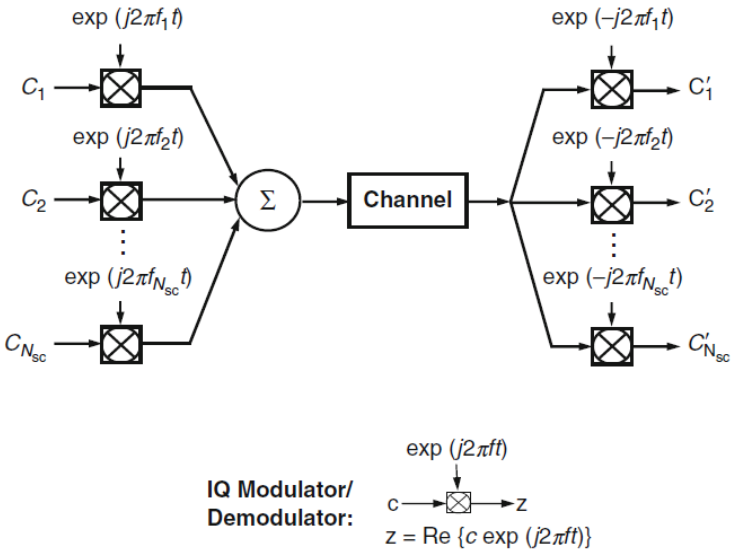

Figure 2-2: Conceptual diagram for a generic OFDM system [38]

In OFDM systems, cyclic prefix is used to primarily act as a guard band between successive symbols to overcome inter-symbol interference (ISI). Use of cyclic prefix is a key element of enabling the OFDM signal to operate reliably. In conventional wireless and wired communication, OFDM is used because of its robustness against inter-symbol interference (ISI) caused by a dispersive channel [38]. The use of OFDM can be commonly seen in mobile communications. For optical communication, OFDM has an advantage over on-off-keying (OOK) and pulse position modulation (PPM) because of its spectral and power efficiency [36]. In conventional OFDM, the generated signal is bipolar and complex. Bipolar and complex signals cannot be used in optical communication as the intensity of light cannot be negative and phase modulation and detection in incoherent systems are not possible [36]. Therefore, real signals in OFDM are generated using Hermitian symmetry. This is achieved by mapping $N/2$ complex symbols to subcarriers 0 to $N/2-1$ and then assigning the respective complex conjugate value to the respective subcarrier with a negative index, where N is the total number of subcarriers. The discrete Fourier transform (DFT) of this symbol set results in a real-valued time-domain signal. This is normally performed after symbol mapping. When

this signal is superimposed over the DC bias of the light source it becomes unipolar and is termed as DC-Optical OFDM. In DCO-OFDM after the channel estimation, if the channel response is not flat then additional power could be added to the attenuated sub-carriers. The spectral efficiency of an OFDM, when all the subcarriers are loaded with the same constellation of size *M,* is defined as shown in equation (1) [38]. N_{cp} is the length of the cyclic prefix.

$$\eta_{\mathrm{DCO}} = \frac{\log_2(M)(N-2)}{2(N-N_{\mathrm{cp}})} \tag{1}$$

In practical systems, pre-distortion or pre-emphasis is useful due to the low pass filter response introduced by the transmitter, receiver, and channel. This process is known as adaptive power loading [39]. Similarly, based on the SNR of each subcarrier, the appropriate modulation scheme is selected; this is known as adaptive bit-loading [40]. The spectral efficiency of an OFDM system with adaptive bit-loading is:

$$\eta'_{\mathrm{DCO}} = \frac{\sum_{k=0}^{\frac{N}{2}-1}(1-\delta[M_{\mathrm{k}}])\log_2(M_{\mathrm{k}})}{(N+N_{\mathrm{cp}})} \tag{2}$$

Where the factor $\log_2(M_{\mathrm{k}})$ indicates the number of bits that are encoded in the M-QAM constellation at subcarrier k; and $\delta[\cdot]$ denotes the Kronecker delta function.

2.5.2 Pulse amplitude modulation

PAM is a signal modulation technique where the data is encoded onto the amplitude of a series of pulses [9]. It can be visualised as a switch that closes every T_{s} seconds for τ seconds and remains open otherwise. The PAM signal is thus multiplication of the continuous-time signal s(t) by a periodic signal h(t) consisting of pulses of width τ, amplitude $1/\tau$ and period T_{s}. This whole process of generating PAM signal is depicted in Figure 2-3.

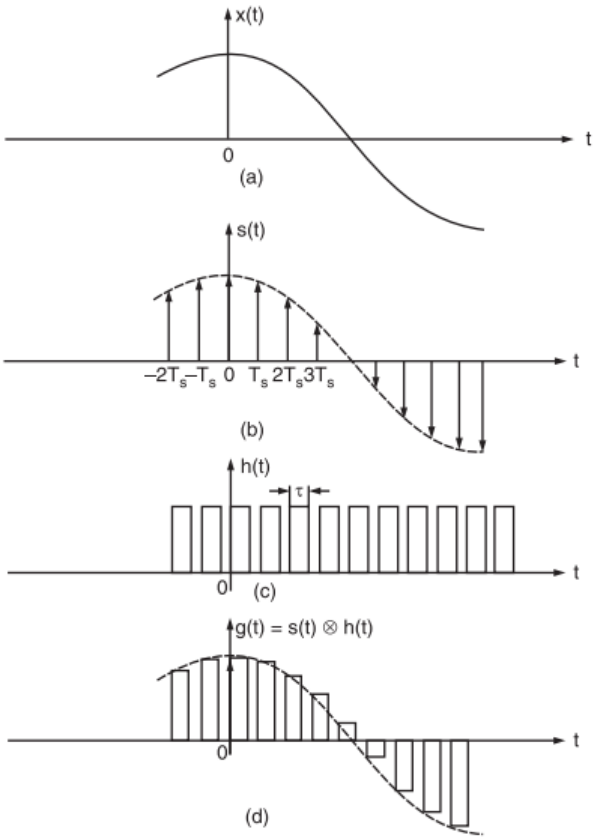

Figure 2-3: Generating a PAM signal [9]

PAM is used in many systems, including Ethernet communication and digital television transmission. In optical systems, the channel can be accurately estimated since there is no fading, and the channel varies slowly. Thus, pulse shapes are not distorted as easily as in RF communication. The generated digital PAM samples have real bipolar values. To avoid signal clipping, the analogue time-domain PAM signal needs to be scaled and biased to fit the dynamic range of the laser transmitter. Hence, this makes it an ideal choice for optical communication and the implementation is straightforward. Also, to use the bandwidth efficiently, multiple subcarriers are used, similar to that in OFDM, and this type of PAM is referred to as Pulse Amplitude Modulated Discrete Multitone (PAM-DMT) [36]. The spectral efficiency of PAM-DMT with adaptive bit loading can be calculated using (1) [9], where *M*

denotes the *M*-PAM modulation order. When all subcarriers are loaded with the same constellation of size *M*, (1) reduces to:

$$\eta_{\mathrm{PAM}} = \frac{\log_2(M)(N-2)}{2(N+N_{\mathrm{cp}})} \tag{3}$$

It can be seen that OFDM has better spectral efficiency as $\eta_{\mathrm{DCO}} > \eta_{\mathrm{PAM}}$ for the same number of subcarriers and constellation size.

2.6 Digital Signal Processing Platform

The digital signal processing (DSP) platform is a system built around state-of-the-art Field Programmable Gate Arrays (FPGAs) and Application Specific Integrated Circuit (ASIC). The platform allows almost any logical or signal processing function to be configured within the hardware simply by reprogramming the processor integrated circuits (ICs). In an FSO system, the DSP platform carries out all the logical and signal processing functions to encode and decode the digital data onto and from the analogue waveforms. In this work, two DSP platforms have been used to demonstrate an FSO system with the solar panel as a receiver. The first one is a highly re-configurable ARM9, and FPGA based System on Module (SoM) *i.e.,* MityDSP-L138F [41]. Due to its highly configurable design, the Transfer Control Protocol and Internet Protocol (TCP/IP) network stack can be implemented on this platform along with the physical (PHY) layer and medium access control (MAC) layer. This platform design is based on IEEE 802.3 ethernet standard [42]. The MAC and higher network layers were based on the IEEE 802.3 ethernet standard, but the lower PHY layer was modified. In the PHY layer, OFDM and PAM could be used for modulation. The supported baseband bandwidth for this platform is 2.5 MHz and 5 MHz. The second one is an ASIC from pureLiFi which has been designed and manufactured for DSP application in LiFi systems [43]. The ASIC is based on the IEEE 802.11 wireless local area network (WLAN) standard [44]. The ASIC provides only the functionality of the

PHY layer and lower MAC layer, a host processor is needed to implement the remaining layers of the TCP/IP network stack. In this platform, the supported baseband bandwidth could be varied depending on the clock divider inputs. The lowest supported bandwidth is 1 MHz and the highest being 32 MHz.

2.7 Summary

In this chapter, the prior experiments and demonstrations of using Si-based and other solar cells technology as data receivers are discussed in detail. Furthermore, the building blocks of an FSO system is described. The different types of AFEs used with FSO systems are introduced. Additionally, two spectrally efficient MCM schemes, DCO-OFDM and PAM-DMT are discussed, which are used in this work at a later stage. Moreover, two types of DSP platforms are discussed and introduced which are used later to build a fully functional FSO system.

Chapter 3 Analytical model of a solar panel as an FSO receiver

Solar panels were never designed to function as OWC receivers. Until now, PV solar systems were used in various configurations to harvest energy from the sun. Hence, there have been several analytical models proposed for the energy harvesting functionality of the solar panel, as the commercial demand for solar panels has been driven by the energy harvesting capability of the panels. Therefore, the communication bandwidth of a solar panel was never considered during its design and manufacturing process. In order to use a solar panel as a data receiver, the electrical characteristics of the solar cells must be studied in detail. This investigation will show the limitations and capabilities of the solar panel as an OWC receiver.

3.1 Introduction

In this chapter, two electrical circuit equivalent models of a solar cell are discussed and used to estimate the data communication parameters. Photovoltaic energy conversion in solar cells consists of two essential steps. First, the absorption of light generates an electron-hole pair. The electron and hole pair is then separated by the structure of the device; electrons to the negative terminal and holes to the positive terminal, thus generating electrical power. An ideal solar cell can be represented by a current source connected in parallel with a rectifying diode. This equivalent circuit model is commonly referred to as the single diode model [45]. Using this single diode model of a solar cell the communication parameters have been studied. Furthermore, a double diode model [45] has been considered to estimate the simultaneous energy harvesting and communication parameters. Also, the effects of

simultaneous energy harvesting on the data communication performance are investigated.

3.2 Communication model

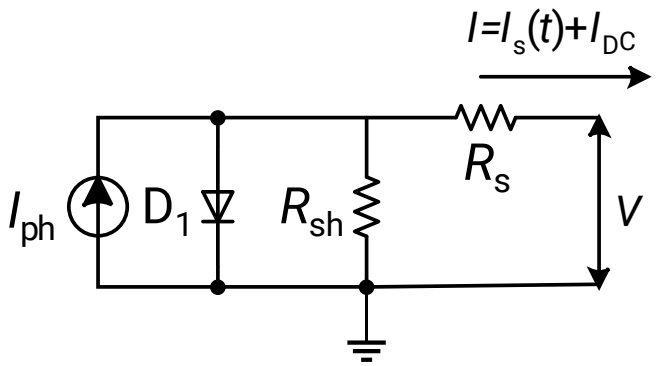

Figure 3-1: Circuit model of a solar panel as a data receiver

The single diode model has been considered as shown in Figure 3-1 to study the modes of operation, optical sensitivity, speed of response, linearity, temperature stability and noise performance which determines the communication performance of a solar cell. This model has been selected as it is simple, provides accurate simulation results for high solar insolation and reveals deficiencies when subjected to temperature variations. The series resistance, R_s, in the model represents the resistance offered to the current flow due to Ohmic contact and resistance due to impurity concentrations along with junction depth. The leakage current across the junction is modelled by the shunt resistance R_{sh} connected parallel to the diode. The diode D_1 represents the semiconductor PN junction of the solar cell and I_{ph} represents the current generated due to optical power incident on the solar panel.

3.2.1 Optical sensitivity

The solar panel can be modelled as a PN diode structure as shown in Figure 3-2, where W_p and W_n are the widths of p-doped and n-doped regions respectively, V is the voltage generated, I is the current flowing through the

load resistance R_L. An important specification of a solar cell that needs to be considered is quantum efficiency. The quantum efficiency of a solar panel η quantifies the capability of converting optical energy in different wavelengths to electrical energy, *i.e.,* sensitivity to the incident light. It can be calculated using [46]:

$$\eta = (1 - \varphi)\left[1 - e^{-\alpha(x_n + x_p)}\right] \tag{4}$$

where φ is the responsivity, α is the absorption coefficient and $x_n + x_p$ denotes the thickness of the depletion zone as shown in Figure 3-2. The responsivity of a solar cell can be defined as a ratio of generated photocurrent to the incident optical power at a given wavelength, as shown in equation (5).

$$\varphi(\lambda) = \frac{I}{P} \tag{5}$$

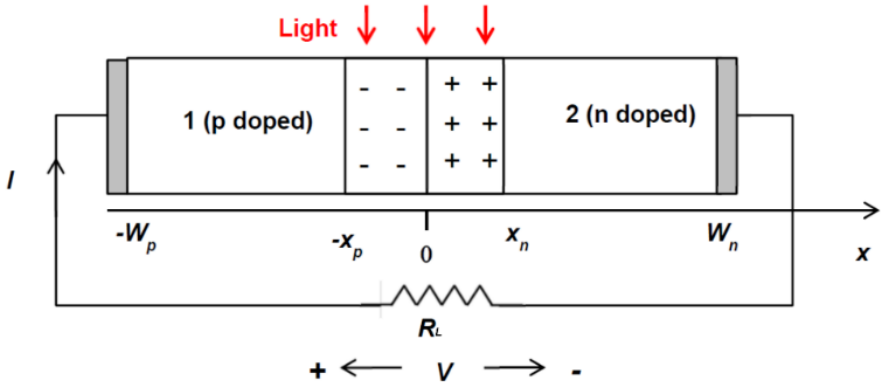

Figure 3-2: PN junction of a solar cell

3.2.2 Speed of response

The bandwidth of a solar cell is critical, which affects the maximum data rate of the communication system. The bandwidth of a solar cell is dependent on intrinsic bandwidth and extrinsic bandwidth. The intrinsic bandwidth is determined by the doping level which determines the transit times of the charge carriers through the depletion region. When light is incident on the depletion region, an exciton (*i.e.*, an electron-hole pair) is generated,

resulting in a potential difference across the terminals. As the electric field is directly proportional to the potential difference for a given distance, assuming the doping level across the substrate is homogenous, the electric field through the semiconductor will be homogenous. The time taken by these charge carriers to traverse through the depletion region will determine the intrinsic bandwidth of this semiconductor device. Let the time taken by an electron be τ_e and for a hole be τ_h. The velocity at which these charges will be moving will be given by $\mu_e E$ and $\mu_h E$, where μ is the mobility factor and E is the electric field across the semiconductor. Hence, the time can be simply expressed by the distance divided by velocity:

$$\tau_h = \frac{x_n + x_p}{\mu_h E} \tag{6}$$

and

$$\tau_e = \frac{x_n + x_p}{\mu_e E} \tag{7}$$

From (6) and (7), it can be observed that the thinner the depletion region, the lower the electric field will be which will increase the transit time. This transit time of the charge carriers is inversely proportional to the bandwidth of the solar cell.

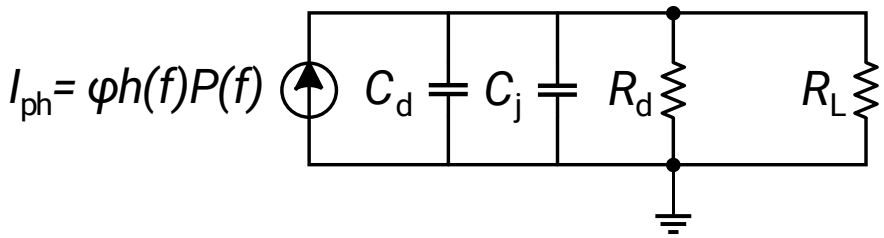

Figure 3-3: Equivalent circuit model of a diode with current source

As can be seen from (5)—(7), the optical to electrical conversion efficiency and the speed of the response is dependent on the doping level. The higher the doping level, the higher is the conversion efficiency, however, the solar cell will

have a lower bandwidth as the doping level is high to maximise the optical to electrical conversion. Therefore, during the manufacturing of a solar cell, there will always be a trade-off between the energy harvesting capability and bandwidth.

The second factor which determines the bandwidth of a solar panel is the extrinsic bandwidth. The extrinsic bandwidth is dependent on the parasitic and junction capacitance between the interconnection of each solar cell in a PV module. In a semiconductor device, the capacitance associated with the charge variation in the depletion layer is called the junction capacitance. The capacitance associated with the excess carriers in the quasi-neutral region is called diffusion capacitance.

The solar cell can be represented as a current source with the equivalent electrical circuit of a diode [46] as shown in Figure 3-3. In the Figure 3-3, *h(f)* is the parameter that is dependent on the intrinsic bandwidth and is further defined in equation (8), φ is the responsivity of the solar panel, and *P(f)* is the time-varying optical signal as a function of frequency which is expressed as *f* [46]. The responsivity of the panel depends on the wavelength of the incident light and the material used. In the case of Si, the responsivity peaks at the wavelength window between 900 and 1000 nm.

$$\mathrm{h}(f)=-\left(\frac{1/2}{1+\mathrm{j}2\pi f_{\tau\mathrm{e}}}+\frac{1/2}{1+\mathrm{j}2\pi f_{\tau\mathrm{h}}}\right) \tag{8}$$

$$\mathrm{I}(f)=\varphi\mathrm{h}(f)\mathrm{P}(f)\frac{R_{\mathrm{d}}}{R_{\mathrm{d}}+R_{\mathrm{L}}+\mathrm{j}2\pi f\left(C_{\mathrm{j}}+C_{\mathrm{d}}\right)R_{\mathrm{d}}R_{\mathrm{L}}} \tag{9}$$

Where $f_{\tau\mathrm{e}} = 1/\tau_{\mathrm{e}}$, $f_{\tau\mathrm{h}} = 1/\tau_{\mathrm{h}}$, R_{L} is the external load resistance, R_{d} the diode resistance, C_{d} and C_{j} the diffusion and junction capacitance of the solar cell. It can be observed that if the solar cells are connected in series, the effective

diffusion capacitance reduces. The junction capacitance will completely depend on how each solar cell is connected.

3.2.3 Linearity

The linearity of the solar panel can be verified by considering its two different modes of operation, commonly referred to as the PV mode and the short-circuit mode. In the PV mode, the load resistance R_L is very low compared to the effective cell shunt resistance R_{sh}.

For an open circuit, *I=0,* hence the generated photocurrent I_{ph} can be expressed as:

$$I_{ph}=I_D+I_{sh} \tag{10}$$

As the solar cell has been modelled as a PN diode we can use the diode equation:

$$I_D=I_o\left(e^{\frac{qV_D}{KT}}-1\right) \tag{11}$$

where I_D is the current through the diode, I_o is the saturation current, q is the charge of an electron, V_D is the voltage across the diode, K is the Boltzmann's constant and T is temperature. For a constant temperature $\gamma=(q/KT)$ can be considered as a constant.

Substituting equation (11) in equation (10) and solving for V_D we have:

$$V_D=\frac{1}{\gamma}\ln\left(\frac{I_{ph}-I_{sh}}{I_o}+1\right) \tag{12}$$

Assuming $I_L >> I_{sh}$ and $I_L >> I_o$,

$$V_D = \frac{1}{\gamma} \ln\left(\frac{I_{ph}}{I_o}\right) \tag{13}$$

Using the small-signal approach, it can be assumed that:

$$\frac{V_s}{I_{Ls}} \sim \frac{dV_D}{dI_{ph}} = \frac{1}{\gamma I_{ph}} \tag{14}$$

where V_S is the output voltage signal of the detector and I_{Ls} is the portion of I_{ph} related to the incident optical signal. Here it is seen that the signal voltage gain is inversely related to the total radiant energy incident to the detector, which is composed of both the carrier and background illumination. In many applications, the detector will operate under conditions of widely varying signal strength and background illumination, which would make this mode of operation undesirable.

If we consider the short-circuit mode, in which $R_S + R_L$ is very small, as compared to the diode effective shunt resistance, then:

$$I_{ph} = I \tag{15}$$

and the small-signal gain is given by:

$$\frac{dI_s}{dI_{ph}} = 1 \tag{16}$$

Equation (16) indicates a perfectly linear response with no dependence on the signal strength and background illumination, which is highly desirable.

3.2.4 Modes of operation

A solar cell can operate in two modes, photoconductive (reverse-bias) or photovoltaic mode (zero bias). In photoconductive mode, when light falls on the PN junction, an electron and hole pair is generated. These move toward

opposite directions due to applied bias voltage. Applying a reverse bias increases the width of the depletion junction. The increase in the width of the depletion junction translates to an increased responsivity with a decrease in junction capacitance. As seen previously in section 3.2.1 and 3.2.2, decreased junction capacitance enhances the communication bandwidth. In the photovoltaic mode, the solar cell is zero biased. The flow of current out of the device is restricted and a voltage builds up.

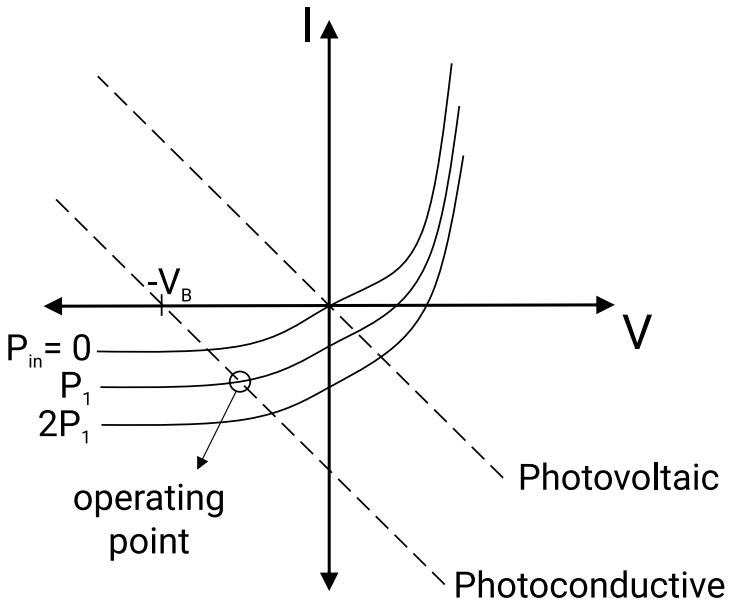

Figure 3-4: Modes of operation of a solar cell

Figure 3-4 depicts the I-V curve of a solar cell for different modes of operation. The I-V curve represents the operation of a solar cell summarising the relationship between the current and voltage at different conditions of irradiance at a constant temperature. The light has the effect of shifting the I-V curve down. It can be seen that the internal resistance decreases in the photoconductive mode and increases in the photovoltaic mode. Furthermore, from the figure it can be inferred that in photoconductive mode the solar cell dissipates power rather than generating power from the incident optical power.

3.2.5 Temperature stability

Temperature affects the characteristics of Si cells in two ways. Firstly, the diode saturation current depends strongly on temperature. Secondly, the photogenerated current varies because the spectral response of the cell shifts towards the infrared region as the temperature is increased. This impact is reflected through the voltage temperature coefficient, which is expressed as the output voltage decrease for every 1 K increase in temperature from 298 K.

Differentiating equation (12) with respect to temperature T we get,

$$\frac{dV_D}{dT} = \frac{1}{\gamma}\left(\frac{1}{I_{ph}}\frac{dI_{ph}}{dT} - \frac{1}{I_o}\frac{dI_o}{dT}\right) + \frac{V_D}{T} \tag{17}$$

Since $I_{ph} >> I_o$

$$\frac{dV_D}{dT} = \frac{V_D}{T} - \frac{1}{\gamma I_o}\frac{dI_o}{dT} \tag{18}$$

For Si, at T=298 K, γ=(q/KT) [17]

$$\frac{1}{\gamma I_o}\frac{dI_o}{dT} = 0.08 \text{ /K} \tag{19}$$

Typically, for Si V_D = 0.7 V. Hence, the voltage temperature coefficient obtained is -0.078 V/K per solar cell. The voltage

3.2.6 Noise analysis

Solar panels convert an incident optical power P_s into an electric current I using the photovoltaic effect. In the photovoltaic effect, $P_s \propto I$ which implies $I=\varphi P_s$ where φ is a constant at a given wavelength and is defined as the responsivity of the material the solar cell is made of. The relation $I=\varphi P_s$ is valid only if I is interpreted as the average current generated. However, this is not the case for an ideal optical receiver. The four noise mechanisms (thermal

noise, shot noise, dark current noise, and input noise) must be considered to understand the effects of simultaneous energy harvesting and communication performance.

Thermal noise [47], also known as Johnson noise, is generated by the random motion of the charge carriers inside the load on the solar panel at a given temperature equilibrium. Thermal noise increases with temperature and zero thermal noise can only be achieved at an absolute zero temperature. Thermal noise is independent of the voltage across the load and the frequency of the signal. Therefore, it can be referred to as white noise. Hence, the spectral density of the thermal noise follows a Gaussian distribution and can be characterized by its constant power spectral density given in (20), where R_L is the load resistance, K is the Boltzmann's constant, and T is the absolute temperature. The unit of σ_{th}^2 is W/Hz. For the solar panel as a receiver with communication bandwidth B, the mean-square noise current representing the total thermal noise power can be expressed as $\langle i_{th}^2 \rangle$ and is defined in (21).

$$\sigma_{th}^2 = \frac{4KT}{|R_L|} \tag{20}$$

$$\langle i_{th}^2 \rangle = \sigma_{th}^2 B \tag{21}$$

Shot noise [48], also known as quantum noise, is generated from the quantum nature of photodetection. For example, assume P optical power is received at λ wavelength by the solar panel. Hence, P can be expressed as $P = Nhc/\lambda$ where h is Planck's constant, c is the speed of light in a vacuum and N is the number of photons. The N photons hit the solar panel in an unsynchronized, random way. Therefore, the generated photocurrent will fluctuate as a result of the random nature of the photon arrival. Thus, the shot noise will be directly proportional to the photocurrent generated. Shot noise is also white, therefore a Gaussian distribution can be used to define the shot noise statistics. The shot noise power spectral density σ_{sh}^2 can be expressed

as in (22), where I is the photocurrent and q is the electron charge. As $I=RP_s$, σ_{sh}^2 can alternatively be defined by the responsivity and total optical power received as shown in (22). The mean-square noise current $\langle i_{sh}^2 \rangle$ for the interested bandwidth is shown in (23).

$$\sigma_{sh}^2=2qI=2q\varphi P_s \tag{22}$$

$$\langle i_{sh}^2 \rangle=\sigma_{sh}^2 B \tag{23}$$

Dark current noise [49] is the constant current that exists when no light is incident on the solar panel. The dark current noise can also be treated as white noise with Gaussian distribution because the statistical nature of the charge carrier generation process is similar to that discussed for the shot noise. For I_D from (29), the noise power spectral density σ_D^2 is defined in (24). The dark current noise power $\langle i_D^2 \rangle$ for the selected bandwidth B can be expressed as shown in (25).

$$\sigma_D^2=2qI_D \tag{24}$$

$$\langle i_D^2 \rangle=\sigma_D^2 B \tag{25}$$

The optical signal is converted into current by a solar panel, but for further processing in the communication chain, the time-varying photocurrent signal needs to be converted to electrical voltage. An electrical transimpedance amplifier is used to amplify the photocurrent signal and convert it to voltage. Noise generated by the first stage of the amplifier must also be considered in the receiver Signal-to-Noise Ratio (SNR) analysis because the amplifier noise power is comparable to the electrical signal power fed to the amplifier. The transimpedance gain $Z_{amp} = v_{out}/i_{ac}$, where i_{ac} is the input signal current and v_{out} is the output signal voltage from the amplifier. The output voltage error v_{amp} is the output voltage from the amplifier when the

input signal current is zero. This parameter is generally provided by the manufacturer of the operational amplifier in the datasheet. Henceforth, the output noise power from the amplifier is defined as $\langle v_{amp}^2 \rangle$ and the input noise power $\langle i_{amp}^2 \rangle$ can be calculated using (26).

$$\langle i_{amp}^2 \rangle = \frac{\langle v_{amp}^2 \rangle}{Z_{amp}^2} \tag{26}$$

Under real-world conditions, many communication devices are transmitting and receiving signals simultaneously and every wire connecting an optical receiver to the subsequent stages can be considered as an antenna. These radio frequency (RF) signals can be picked up unintentionally by the wires and terminals which creates interference with the signal of interest. This problem is solved by creating a Faraday cage [50] around the exposed terminals and wires. Therefore, for noise estimation purposes, the interference and noise due to RF can be approximated as zero.

3.3 Energy harvesting and simultaneous communication model

A double diode model [51] has been considered to understand the effects of simultaneous energy harvesting on the data communication performance of a solar cell. Generally, a single diode model is used to represent a solar cell as used previously in [19] and [20]. The single diode model structure is identical to the structure shown in Figure 3-1. For simultaneous energy harvesting and communication, the single diode model is not considered because the single diode equation assumes a constant value for the ideality factor *n* as studied previously in [19] and [20]. The ideality factor is a function of the voltage across the device [52]. At high voltages, when the recombination at the junction in the device is dominated by the surfaces and the bulk regions, the ideality factor is close to one, which is represented by the diode D_1.

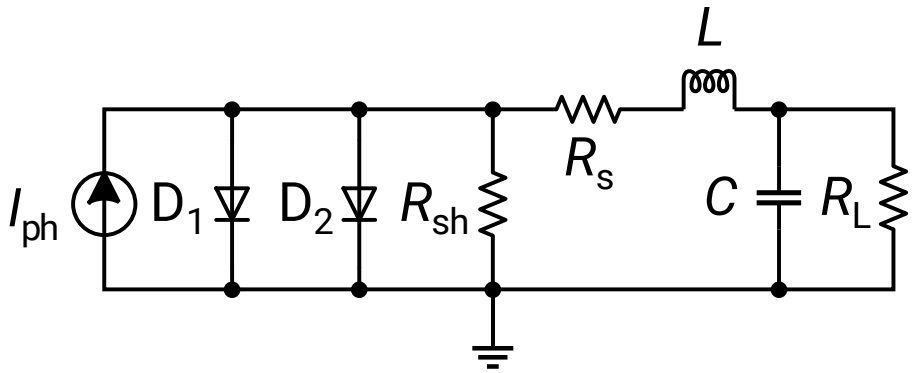

Figure 3-5: Double diode model of a solar cell for energy harvesting

However, at lower voltages, recombination in the junction dominates and the ideality factor approaches two. As in this study, the communication performance will be evaluated under the varying condition of solar irradiation and the voltage across the PN-junction will vary drastically. Therefore, the ideality factor needs to be considered for accurate modelling and estimation. The recombination current in the space charge region is modelled by adding a second diode, which is depicted as D_2 in Figure 3-5. The ideality factor for the second diode is set typically to two [52]. The ideality factor is multiplied with the temperature in the exponential term, in the diode equation, for the second diode. Therefore, the total current generated by the solar cell is represented as I and defined by using Schottky's diode equation as shown in (27), where I_{o1} is the diode saturation current for D_1 and I_{o2} is the diode saturation current for D_2. and I is the sum of alternating current (AC) generated due to the received optical signal and the direct current (DC) generated due to the solar irradiation.

Therefore $I=I_s(t)+I_{DC}$, where $I_s(t)$ is the AC signal component and I_{DC} is the DC signal component.

$$I=I_{ph}-I_{o1}\left[e^{\frac{q(V+IR_{sh})}{KT}}-1\right]-I_{o2}\left[e^{\frac{q(V+IR_{sh})}{2KT}}-1\right]-\frac{V+IR_s}{R_{sh}} \quad (27)$$

In (27) the -1 terms with exponentials can be ignored for the approximation which makes the analysis easy. This is because the exponential terms give values typically much larger than 1 [52]. Therefore, (27) can be further simplified to (28).

$$I=I_{ph}-I_{o1}\left[e^{\frac{q(V+IR_{sh})}{KT}}\right]-I_{o2}\left[e^{\frac{q(V+IR_{sh})}{2KT}}\right]-\frac{V+IR_s}{R_{sh}} \quad (28)$$

As I_{ph} in (28) represents the generated photocurrent, but when there is no photocurrent generation $I_{ph}=0$ and the solar panel will act as a passive load. Therefore, the dark current for the panel can be denoted as I_d, shown in (29) [52].

$$I_d=I_{o1}\left[e^{\frac{q(V-IR_{sh})}{KT}}\right]+I_{o2}\left[e^{\frac{q(V-IR_{sh})}{2KT}}\right]+\frac{V-IR_s}{R_{sh}} \quad (29)$$

Hence, using equations (24) and (25) the total current generated by the solar panel under different illumination conditions can be modelled.

3.3.1 Effects of sunlight on the solar panel

Using the equations (6)-(9) and (28)-(32) and the equivalent circuit models discussed previously, the frequency response of the panel was simulated using TINA-TI [53], which is a simulation program with integrated circuit emphasis (SPICE). The simulation was carried out with the circuit structure as shown in Figure 3-5. In the simulation, the temperature was kept constant at 298 K. The diffusion capacitance, series, and shunt resistances were defined by the equations as shown in (30)-(32). In equation (30) C_d is the diffusion capacitance [54], K is the Boltzmann's constant, I_D is the current through the diode, τ_n is the minority carrier lifetime, which is defined in detail in section 3.2.2 and T is the temperature. The diffusion capacitance for D_1 and D_2 is estimated separately for each diode using this equation. Furthermore, the

series resistance is defined in equation (31) [55] where P_o is the power harvested for the incident optical power, P_{MP} is the maximum power that can be harvested by the panel, V_{oc} is the open-circuit voltage across the panel and I_{sc} is the short-circuit current. The open-circuit voltage and short-circuit current of the solar panel can be found in the datasheet of the solar panel [56]. Similarly, the shunt resistance R_{sh} is defined in equation (32).

$$C_d = \frac{K\tau_n I_D}{T} \tag{30}$$

$$R_s = \left(\frac{P_o}{P_{MP}} + 1\right)\frac{V_{oc}}{I_{sc}} \tag{31}$$

$$R_{sh} = \left(\frac{P_{MP}}{P_o + P_{MP}}\right)\frac{V_{oc}}{I_{sc}} \tag{32}$$

The simulated frequency response of the solar cell model was plotted for various solar irradiation as shown in Figure 3-6. In Figure 3-6, the frequency of the solar cell model varies for different solar irradiation. This variation in frequency response occurs due to the variation in the intrinsic bandwidth of the solar cell. As seen previously in section 3.2.2, the electric field E is dependent on the number of photogenerated charge carriers and this affects the transit time of the electron and hole through the depletion region as seen in equations (6) and (7).

Furthermore, the received signal power variation is plotted against the varying solar irradiation as shown in Figure 3-7. This is simulated in TINA-TI with a constant signal frequency of 1 MHz, as that is the crossover point in Figure 3-6. It can be seen that the received signal power reduces with the increase in the solar irradiation up to 100 W/m^2 and then stays constant, as expected from the frequency versus solar irradiation plot.

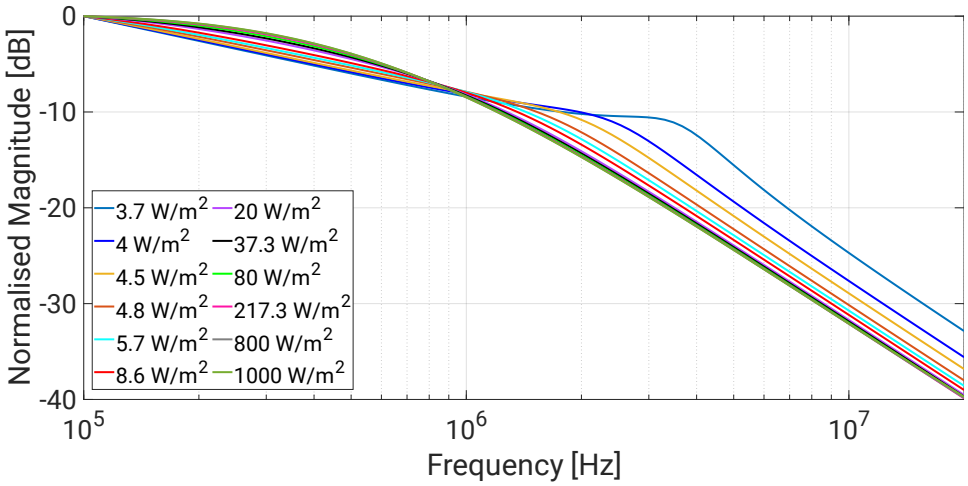

Figure 3-6: Variation in the frequency response of a solar panel due to variation in sunlight

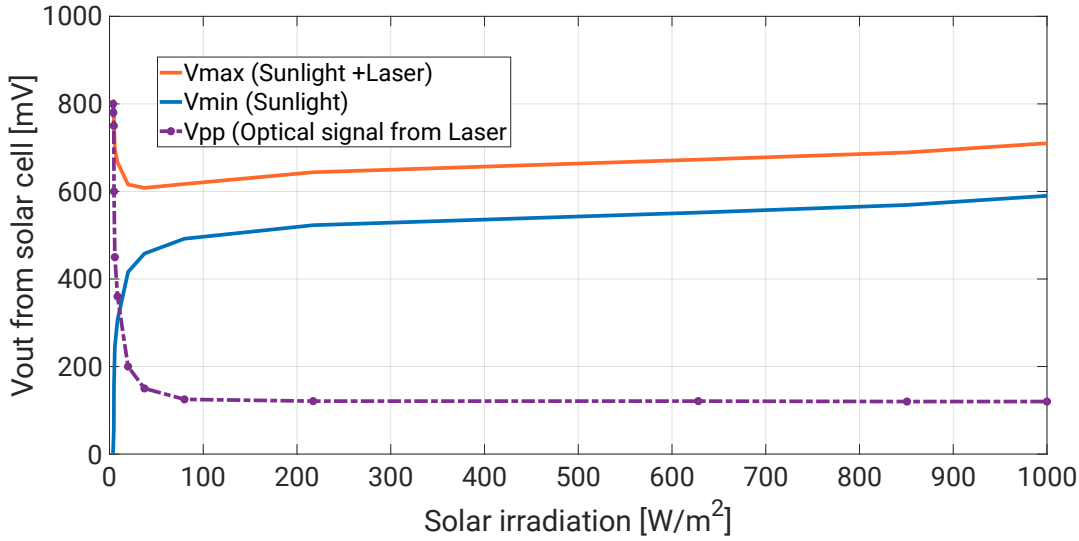

Figure 3-7: Variation in received signal power due to variation in sunlight

The next important parameter, which determines the performance of the solar panel as a communication receiver, is SNR. The magnitude of the SNR of the frequency subcarriers determines the modulation order that could be used over the selected communication bandwidth for a given bit error rate. The SNR for the received signal was calculated using the simulation results and equation (33) obtained from TI-TINA in MATLAB for the solar panel model. In equation (33), $\langle I_s^2(t)\rangle$ is the incident optical signal power. The SNR for the received signal was plotted for different values of emulated solar irradiance

incident on the panel in Figure 3-8. The SNR estimated in Figure 3-8 depicts the degradation introduced by the solar panel during the optical to electrical signal conversion.

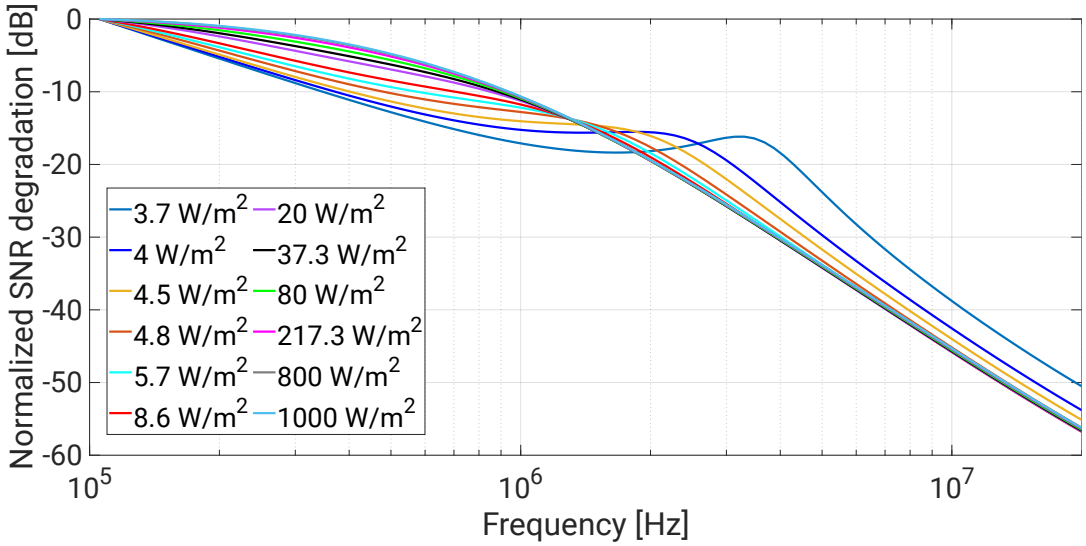

Figure 3-8: Variation in SNR due to variation in sunlight

$$\text{SNR}=\frac{\langle I_s^2(t)\rangle}{\langle i_{th}^2\rangle+\langle i_{sh}^2\rangle+\langle i_D^2\rangle+\langle i_{amp}^2\rangle} \tag{33}$$

In Figure 3-8, the SNR increases at lower frequencies with the increase in emulated solar irradiance on the solar panel. The increase in SNR at the lower frequencies can be explained by the reduction of the diode resistances of D_1 and D_2 due to an increase in the photogenerated current. At higher frequencies, the depreciation in SNR with an increase in optical intensity can be explained by the increase in shot noise and thermal noise. As seen in equations (22) and (23), the shot noise increases with the increase in the total optical incident power P. In the case of thermal noise, the solar spectrum consists of both long and short IR radiation. This IR can generate heat in most of the materials as the molecules resonate with the IR wavelength. Therefore, an increase in temperature T in equation (20) results in an increase in the

thermal noise. On the contrary, the dark current noise and the amplifier input noise are constant for the varying optical intensity as they are independent of the optical power incident and the temperature of the solar panel. Therefore, the estimations in this section show that there will be a decrement in communication performance when the solar panel is simultaneously harvesting solar energy.

3.4 Summary

Solar panels were never designed as wireless optical communication receivers; therefore, the intrinsic bandwidth is very small, and it alters with the variation in sunlight. However, a Si-based solar panel inherently has a similar responsivity, linearity, and temperature stability with respect to that of a conventional OWC Si-based high speed photoreceiver as they are constructed from the same material *i.e.,* Si, and use similar dopants. Furthermore, a double diode model of a solar cell has been used for the first time in this thesis to estimate the simultaneous energy harvesting and data communication performance. It is shown that variations in the incident solar power on the panel encumbers the frequency response. Moreover, the SNR of the received signal deteriorates with the increase in solar irradiation, therefore the communication performance of a solar panel will certainly deteriorate at its peak energy harvesting capabilities compared to the communication performance under dark conditions. This effect can be explained using the effect of the voltage across the panel on the depletion region. The higher the voltage across the panel, the thinner depletion region is, which reduces the overall sensitivity and speed of response of the solar panel.

Chapter 4 Experimental analysis of a solar panel as an FSO receiver

A solar panel also referred to as a Photovoltaic (PV) module, comprises of photovoltaic sub-modules which are made up of PV elements, commonly known as solar cells. These cells or elements are connected in a desired configuration *i.e.,* series or parallel, to obtain high voltage or high current. When using a solar panel as an OWC receiver it is important to understand that the different sizes of the panel will have different data communication performances. Similarly, the communication performance of a solar panel will depend on its mode of operation, *i.e.,* photovoltaic or photodiode mode. Furthermore, the choice of the transmitter wavelength and the optical signal beam shape can affect the bandwidth of a solar panel. In this chapter, the solar panels are tested under different conditions to see how it affects the communication bandwidth.

4.1 Introduction

As discussed in the previous chapter, the communication bandwidth of a Si-based solar panel is influenced by several factors such as the doping level of the semiconductor, temperature coefficient and responsivity of silicon. However, these factors are intrinsic to the solar panel and cannot be mitigated easily to optimise the bandwidth of a solar panel. Nevertheless, there are extrinsic factors that can be controlled to maximise the frequency response of a solar panel. The choice of the optical signal transmitter can play a significant role in the data communication performance of a solar panel. Also, the beam shape of the optical signal can play a significant role in the communication bandwidth. Additionally, the electric field across the terminals of a solar panel can be modified externally to affect the bandwidth. Likewise, the active area

of the solar panel plays a significant role in using a solar panel as an OWC receiver.

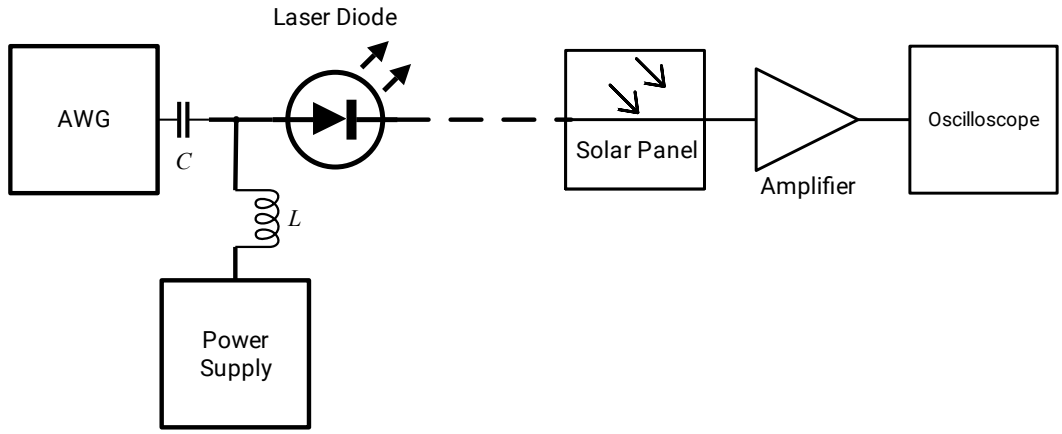

Figure 4-1: Experimental setup

To investigate the effects on the solar panel under different conditions, an experimental setup was built as shown in Figure 4-1. A 650 nm laser diode with a maximum optical output power of 130 mW was used as the optical signal source. The signal from an arbitrary waveform generator (AWG) and the laser bias current was fed to the laser through a Bias-Tee. In order to meet the laser safety standards and illuminate the panel uniformly, an engineered optical diffuser with an output angle of 20° full angle beamwidth in a circular shape was used. An engineered optical diffuser scatters the incident beam in a controlled fashion *i.e.,* it provides non-Gaussian intensity distribution in various patterns such as a square, circle and line. The output beam divergence angle is also constant, irrespective of the distance between the optical source and the diffuser. The signal output from the solar panel was in the order of a few mV peak-to-peak, therefore an amplifier stage with 10 dB of gain was used as shown in the setup. The frequency response of a 5 W solar panel was measured using the experimental setup. Furthermore, using the analytical models discussed in the previous chapter, the frequency response of a 5 W solar panel was simulated and compared as shown in Figure 4-2. The measured frequency response aligns with the simulated frequency response.

This validates the accuracy of the experimental measurements and the analytical model. Henceforth, using this setup as a baseline reference further experiments were carried out to investigate the various effects on the communication bandwidth of a solar panel due to the different extrinsic factors.

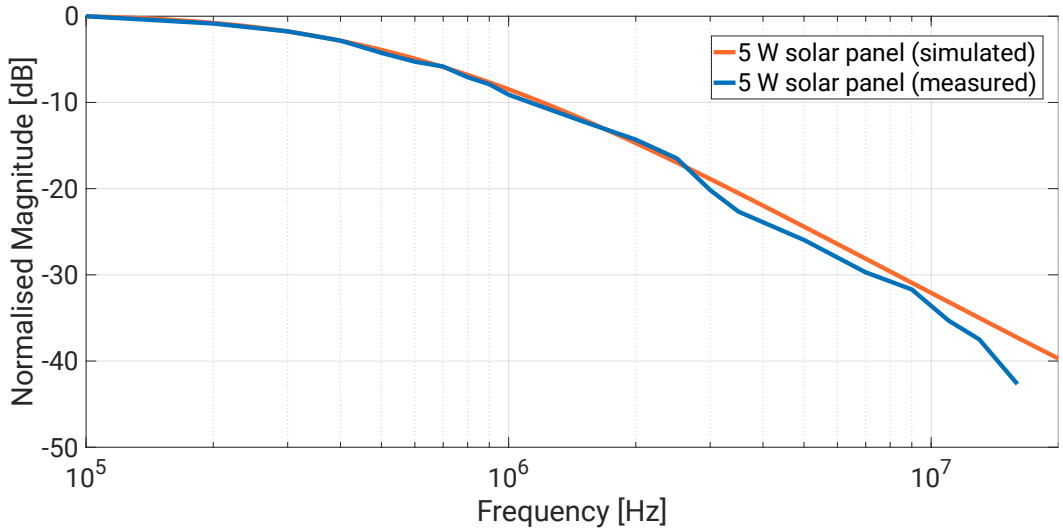

Figure 4-2: Frequency response of a solar panel

4.2 Effects due to different wavelength

Normally in FSO systems, any wavelength in the optical spectrum can be used. However, because of the atmospheric conditions and the laser safety regulations, longer wavelengths are the preferred option. FSO links in the troposphere are mainly influenced by weather conditions. Rain does not influence optical transmissions drastically, because the size of a raindrop is a few millimetres, which is much larger than the operating optical wavelength, thus causing minimal scattering of the laser beam [57]. The optical attenuation faced by such long-wavelength lasers during a clear day is 3 dB/km [57]. However, FSO links are affected radically by heavy fog because the fog droplets have comparable size, as the used wavelengths, causes much scattering of the laser beam. The attenuation under such heavy fog conditions

is 30 dB/km [57]. On the other hand, the electric current signal generated by a solar cell due to the incident optical signal depends on its quantum efficiency.

The quantum efficiency of a solar cell is defined as the ratio of the number of electrons in the external circuit produced by an incident photon of a given wavelength. Thus, one can define the external and internal quantum as EQE*(λ)* and IQE*(λ)* respectively. They differ in the treatment of photons reflected from the cell: all photons impinging on the cell surface are taken into account in the value of EQE*(λ)* but only photons that are not reflected are considered in the value of IQE*(λ)*. The EQE*(λ)* can be defined in terms of spectral response. The spectral response is defined as the ratio of the photocurrent generated by a solar cell under monochromatic illumination of a given wavelength to the value of the spectral irradiance at the same wavelength. It is denoted by *φ*. The relationship between EQE*(λ)* and *φ* is formulated:

$$EQE(\lambda)=\frac{hc}{q\lambda}\varphi \tag{34}$$

where *h* is Plank's constant, *c* is the speed of light, *q* is the charge of an electron, and *λ* is the wavelength. Therefore, from equation (34) it can be concluded that the external quantum efficiency is directly proportional to the spectral response. The spectral response of Si solar cells peaks between 850 nm and 950 nm [58], and the precise values are influenced by the cell manufacturing process, especially the Anti-Reflective (AR) coating. When the cells are embedded in the panel, the top layer refractive index changes from 1 (air) to a value in the range of 1.4-1.5, which is typical for common encapsulant materials. This optical coupling to the AR coating changes the spectral response of the encapsulated cell by changing the reflective properties of the cell surface. Therefore, an experiment was conducted with three wavelengths of laser device with the same output optical power in a dark room. There have been experiments conducted with Si-based photodiodes with different

wavelengths [59], but there have been no experiments showing the effect of different wavelengths on the communication bandwidth of a solar panel.

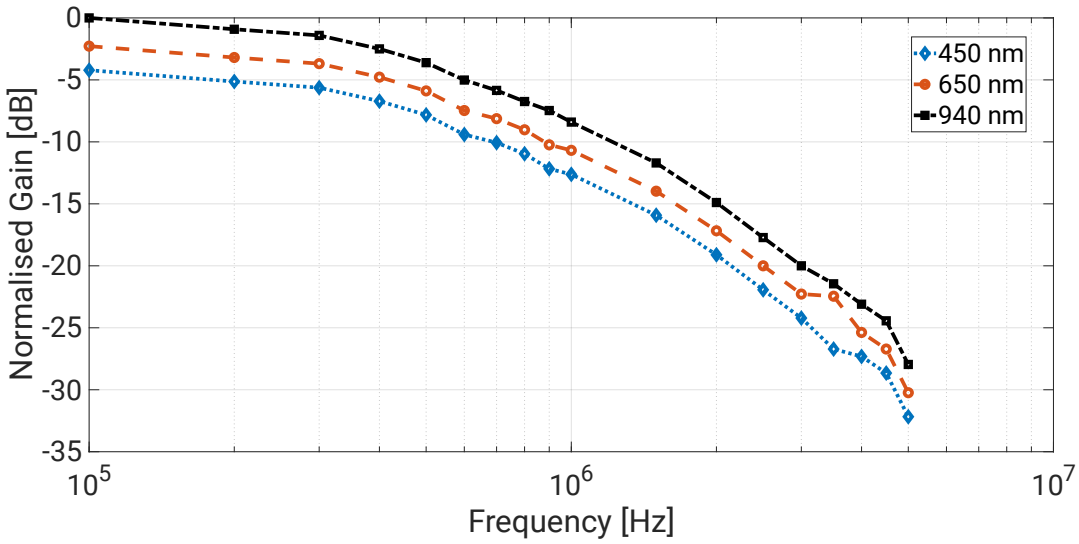

Figure 4-3: Frequency Response of solar panel with different wavelength

The frequency response of the solar panel was measured with 450 nm, 650 nm, and 940 nm laser devices and the normalised response was plotted as shown in Figure 4-3. These three wavelengths were chosen as the spectral response of a Si-based optical detector is limited within 350 nm to 1100 nm [60].

In Figure 4-3, it can be seen that the frequency responses remain similar, but the signal gain varies. This variation in signal gain will affect the SNR of the received signal. The gain is the highest at 940 nm amongst the three chosen wavelengths, therefore the choice of the optical signal transmitter should be a 940 nm laser device. Furthermore, the 940 nm wavelength has three times higher maximum permissible exposure (MPE) than the visible spectrum of light in terms of laser safety [8]. Moreover, this wavelength is part of the near-infrared spectrum, hence it has a lower scattering coefficient [31] compared to that of the visible spectrum of light.

4.3 Effects due to different signal beam patterns

The solar panel as an FSO receiver is envisioned to be used as a long-distance wireless communication link. The optical signal beam launched from the transmitter is affected by various factors before arriving at the receiver. The physics and transmission properties of the beam penetrating the atmosphere are similar in the visible and near-IR spectrum. Therefore, visibility can be used to characterise particles that absorb or scatter light for near-IR radiations as well. Under clear atmosphere conditions, the atmospheric loss associated with visibility is mitigated by the choice of wavelength as discussed in the previous sub-section. However, there is another adverse effect that the signal beam faces, known as scintillation or fading [57].

Scintillation is the rapid fluctuation in the amplitude and phase of the signal as observed from a receiver. Tropospheric scintillation is caused by small-scale inhomogeneities of the refractive index appearing in the path of the propagating wave. The atmosphere refractive index in the troposphere decreases gradually with altitude. However, this is true for calm and clear sky conditions, but the troposphere is very prone to dynamics. The presence of thermal gradients and pressure differences cause motions in the atmosphere, which leads to the mixing of the different layers. However, this mixing is slow and uneven. Typically, strong turbulence in vertical winds results in inhomogeneous mixtures of constituents. The wet components of the air, like the water vapour, are not uniformly distributed over the atmospheric regions. This uneven mixing and irregular distribution of wet components of the air cause random smaller and larger regions of variations in the refractive index, both spatially and temporally. These regions of different random densities, and hence different refractive indices, move with the wind and intersect the line of sight from the transmitter to the receiver. Furthermore, due to the strong wind, the transmitter and receiver are prone to mechanical vibrations leading to

misalignment. The scintillation effect and misalignment due to mechanical vibrations can be mitigated by the receiver aperture averaging.

In receiver aperture averaging a direct detection receiver collects the irradiance flux over a large area. The large active area of the solar panel alleviates this issue. However, due to the atmospheric turbulence and misalignment, all the cells of the solar panel may not be illuminated uniformly. Furthermore, this raises the question if the size of the optical beam should be comparable to the size of the active area of the solar panel. There has been no experimental study on the effect of varying optical signal beam pattern on the communication bandwidth of a solar panel.

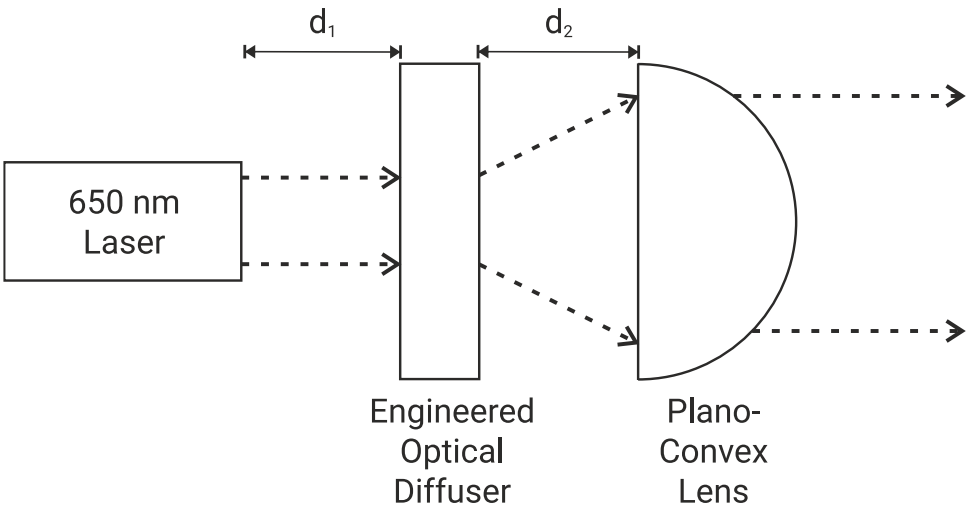

Figure 4-4: Optical setup for the transmitter

Therefore, to investigate further the effects of different beam patterns on a solar panel, an experiment was carried out. A 650 nm laser device was chosen as the transmitter so that the beam shape could be visualised, also it has been verified in the sub-section 4.2 that the different wavelengths do not affect the frequency response of the solar panel, rather it affects the gain of the signal. To control the beam size, a plano-convex lens with the engineered optical diffuser is used as shown in Figure 4-4. By changing the distance between the diffuser and the lens *i.e.*, d_2, the divergence of the beam changes.

Hence, this results in the variation of beam size incident on the solar panel. The frequency response of the solar panel for three cases was measured. The first case, where the signal beam is highly concentrated on a few cells of the solar panel, as shown in Figure 4-5 (a). Secondly, Figure 4-5 (b) shows the signal beam is partially illuminating the panel and the optical power is not uniformly distributed over the active area of the solar panel. In the third case, the whole panel is uniformly illuminated by the signal beam. In all cases, the total optical power transmitted from the laser was kept constant at 130 mW.

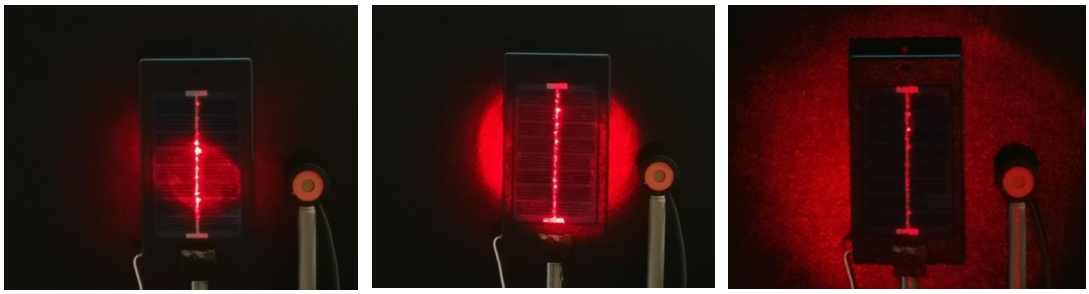

(a) (b) (c)

Figure 4-5: Optical signal illumination on a solar panel (a) highly concentrated (b) partially illuminated (c) uniformly illuminated

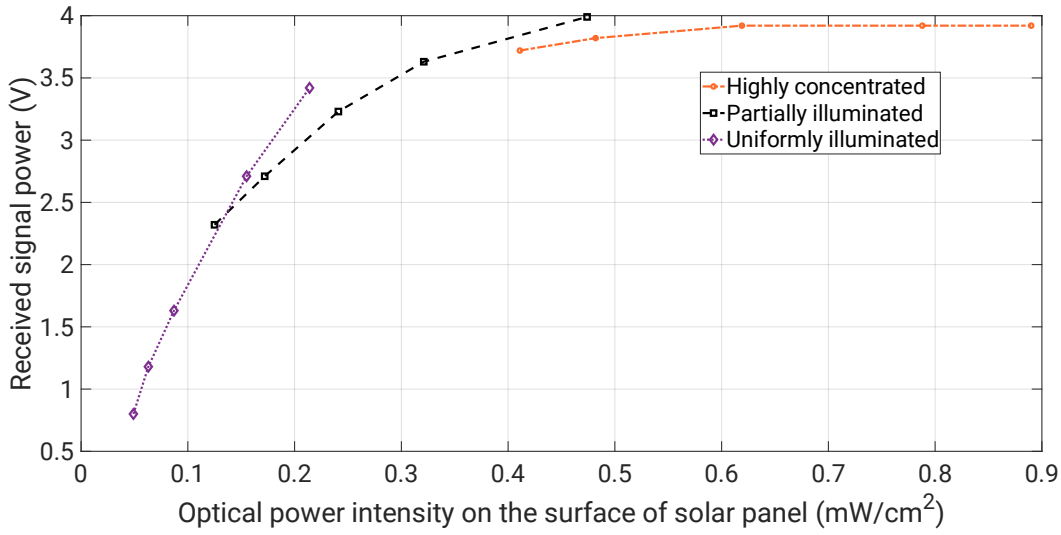

Figure 4-6: Variation in received signal power due to varying optical signal intensity

The measured frequency response of the solar panel for the three cases is shown in Figure 4-7. Furthermore, the optical power intensity and the received electrical signal power for each case is shown in Figure 4-6. From Figure 4-6 and Figure 4-7, it can be concluded that when the whole solar panel is uniformly illuminated by the signal beam, the frequency response has a lower roll-off rate compared to the other two cases even though the received signal power is lower than the other two cases. Whereas, in the case when only a few cells are illuminated by the highly concentrated signal beam, the frequency response rolls off quickly. The solar cells which are not illuminated by the signal beam act as a capacitive load on the cells which are illuminated by the optical signal. This results in a degradation in the communication bandwidth of the overall solar panel. Therefore, to achieve an optimal communication performance, all the cells of the solar panel need to be uniformly illuminated by the optical signal beam. Hence, the transmitter optics needs to be designed in such a way that the signal covers the whole panel to achieve the best communication performance. This will also ensure that the system will be insusceptible to fading or scintillation. Moreover, in the case (c), the optical power intensity is lower than the other two cases which is beneficial to meet eye safety regulations according to [8].

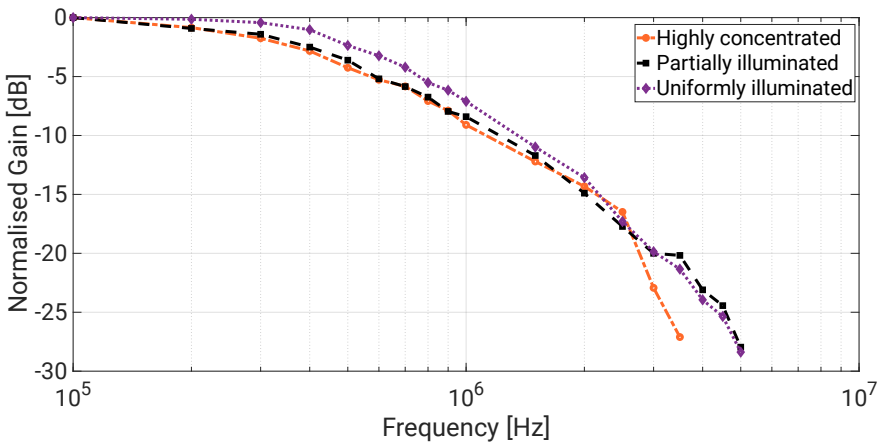

Figure 4-7: Frequency response of solar panel with different optical signal illumination

4.4 Effects due to different size of solar panels

Commercially, solar panels are manufactured in various shapes and sizes, depending upon the application and the energy harvesting capability. With the increase in energy harvesting capability, the number of solar cells per panel and the active area of each solar cell increases. The increase in the active area plays a major advantage in using a solar panel as an FSO receiver as it significantly eases the challenges faced during the alignment and helps to mitigate the effects due to the atmospheric turbulence. With reference to section 3.2.2, it is evident that the communication bandwidth of a solar panel is dependent on the junction capacitance and diffusion capacitance. The junction capacitance depends on the configuration of the interconnections of the solar cells. Therefore, the increase in the number of solar cells interconnects will increase the junction capacitance, resulting in a decrease in the bandwidth of the solar panel. Study has been carried out on the variation of communication bandwidth due to different array size of photodiodes and different active area [61]. Although, there have been no published data on the effect of different sizes of solar panel on its communication bandwidth.

Table 4-1: Variation in -3 dB bandwidth due to different sizes of solar panels

Maximum Power Harvested (under 1 kW/m^2 of solar irradiance) (in W)	**Active Area (in cm^2)**	**-3 dB Bandwidth (in kHz)**
1	57.85	450
5	667.08	270
10	1111.6	150
30	3531	110

An experiment was conducted to verify that an increase in the active area of the solar panel will result in a decrease in the bandwidth of the solar panel. A 1 W, 5 W, 10 W, and a 30 W solar panel were chosen for the

experiment. The experiment was conducted in a dark room to ensure that there was no external lighting source to affect the bandwidth of the solar panels. The distance between the optical signal source and the solar panel under test were kept constant for all four cases. Then, the frequency response of each solar panel was measured using the same setup as shown in Figure 4-1.

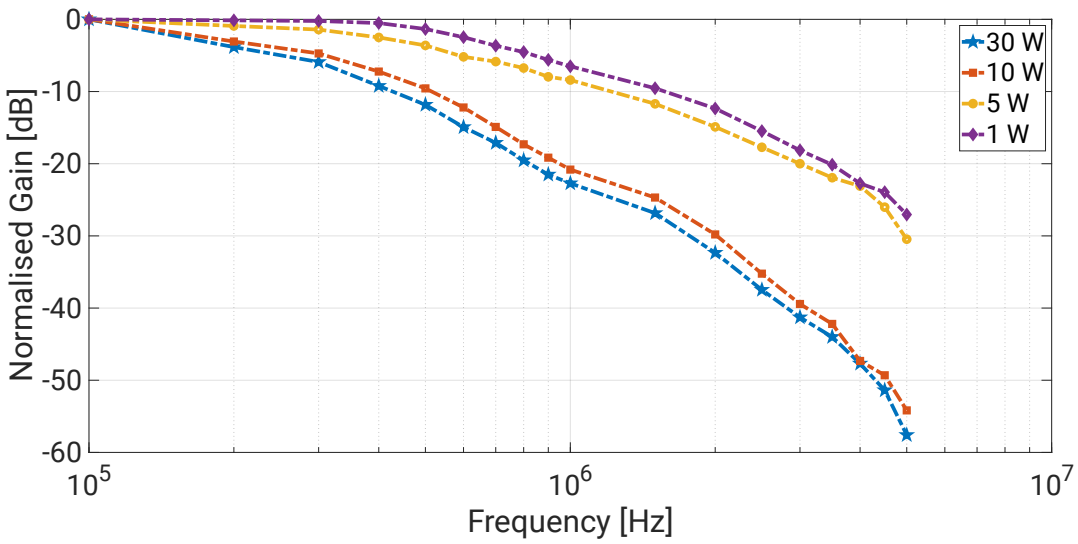

Figure 4-8: Frequency response for different sizes of solar panel

Table 4-1 shows the different wattages of solar panels with their corresponding active area and the measured -3 dB bandwidth. The measured frequency responses of the four solar panels have been shown in Figure 4-8. From the measurements, it is evident that an increase in the active area of the solar panel reduces the communication bandwidth. On the contrary, an increase in the active area increases the energy harvesting capability, mitigates the atmospheric turbulence issues, and eases the transmitter and receiver alignment.

4.5 Effects under the reverse-bias condition

Until now the solar panel was investigated under the forward bias condition, which also can be referred to as the photovoltaic mode. In the

photovoltaic mode, when the photons strike the silicon, they either travel through the material by transmission, if its energy is lower than the bandgap energy of the silicon semiconductor or get absorbed by the silicon, if its energy is higher than the bandgap energy. With high enough energy, an electron-hole pair is produced. The electron and hole are separated by the depletion region of the p-n junction and a current is generated through a connected circuit. This occurs because the positive carriers prefer the p-type material and the negative carriers prefer the n-type material, thereby increasing the conductivity of the material. When no light or photons are incident on the solar cell, a balance exists between drift and diffusion. In this case, there is no net current flow as the number of electrons and holes are equal between the two regions. The solar cell is in fact a photodiode that readily conducts a large amount of current in one direction and hardly any in the other. With solar cells, there is a need to apply a reverse bias to increase the effectiveness of an internal electric field in the junction, thus causing an imbalance of drift and diffusion across the depletion region. For the solar cell, the holes tend to stay preferentially in the p-region and the electrons in the n-region, with reverse biasing this tendency is enhanced. When a stream of photons is absorbed into the silicon and localised within the transition region, then electron-hole pairs are formed. These photons generated charge carriers prefer the n/p type material, respectively. This creates an additional reverse current through the junction that should result in better conditions for the purpose of communication.

An experimental setup was built to reverse bias a 5 W solar panel as shown in Figure 4-9. The solar panel under test was connected to a DC power supply and the reverse bias voltage was gradually increased until the received signal peak-to-peak voltage was maximised. The reverse bias voltage was measured to be -7.22 V. The experiment conducted here was first time demonstrated in [62]. In [62], the authors have self-reverse-biased the solar cell

to enhance the communication bandwidth. Also, they have demonstrated that self-reverse biasing the solar panel enhances the energy harvesting performance of the solar panel as well. In this sub-section, the experiment is conducted to quantify the increment in communication performance with solar panel being reverse biased compared to its operation under photovoltaic mode.

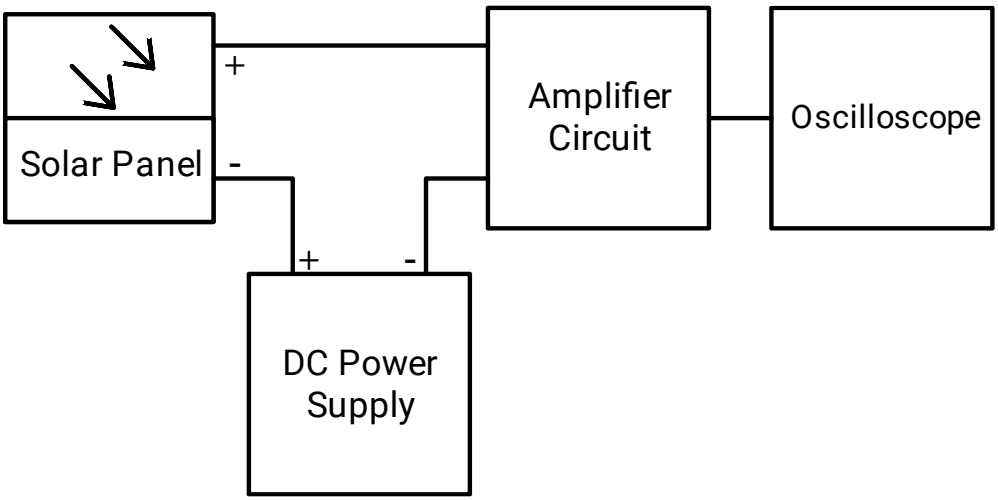

Figure 4-9: Reverse biasing a solar panel

The frequency response of the solar panel was measured under the reverse bias condition and was compared with the frequency response of the solar panel when operated in the photovoltaic mode, as shown in Figure 4-10. From the plot, it can be seen that the -10 dB bandwidth of the solar panel has been increased by 500 kHz which was previously 1.5 MHz. Furthermore, to verify the signal quality, a sinusoidal wave of 1 MHz was transmitted from the transmitter with the solar panel as receiver under the reverse bias condition. On the oscilloscope, the signal was captured in the time domain and the FFT of the captured signal was also calculated and captured.

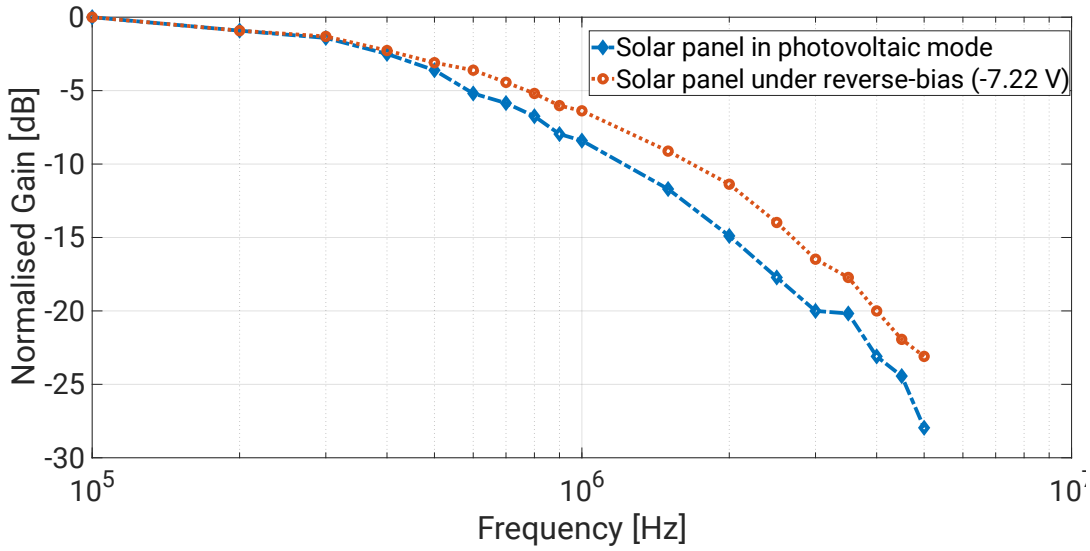

Figure 4-10: Frequency response of solar under the reverse-bias condition

The same experiment was repeated with the solar panel under photovoltaic mode. The signal captures are shown in Figure 4-11.

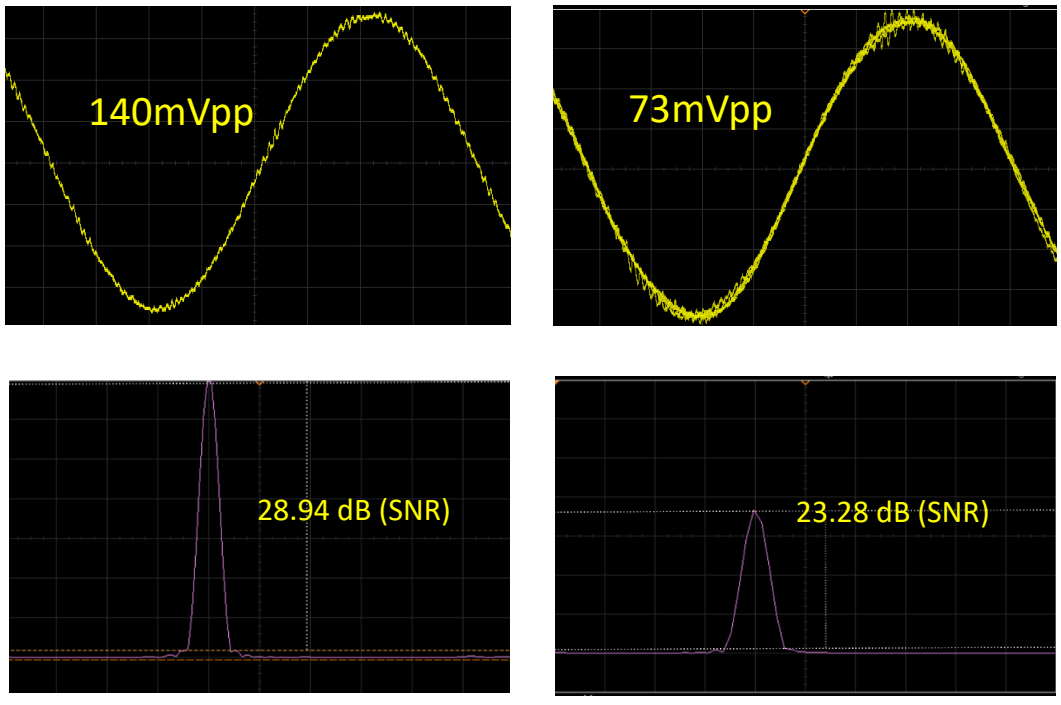

(a) *(b)*

Figure 4-11: Captures from oscilloscope (a) reverse-biased (7.22V) (b) unbiased

From the signal capture, it can be inferred that the received signal under the reverse bias condition has approximately four times more power than the signal received under the photovoltaic mode. This additional power translates into approximately 6 dB gain in SNR as shown in the FFT captures in Figure 4-11. Although in the case of reverse biased panel, the received signal power has 3 dB additional power over the unbiased panel, the increment in SNR shows that there is a reduction of 3 dB in the noise power. This also aligns with the frequency response measurement. Therefore, upon reverse biasing, the solar panel enhances the communication capability of the solar panel as an optical receiver.

4.6 Summary

Using a solar panel as an FSO receiver inherits several advantages, such as the ability to use any transmitter wavelength between 400-1100 nm, the large active area palliates fading or scintillation effects, self-powering the FSO system, and the adeptness to use the panel in photovoltaic or photodiode mode. On the contrary, the advantage of having a large active area is traded-off with the communication bandwidth of the solar panel. Furthermore, from the experiments, it was also found that the beam shape of the optical signal incident on the solar panel affects the communication bandwidth of the solar panel. Therefore, it can be summarised that to maximize the communication performance of a solar panel, the following design considerations must be included in the FSO system: the transmitter wavelength should be between 800-1000 nm, the transmitted optical signal beam should cover the whole active area of the panel uniformly, and the smallest size panel available should be considered. However, the choice of the receiver will completely depend on the energy harvesting requirement and the link distance. Moreover, depending on the application and the link reliability conditions, the solar panel can be designed to operate in an adaptive mode between photovoltaic and photodiode modes.

This page has been left blank intentionally.

Chapter 5 Designing and developing a receiver circuit

A solar panel is envisaged to be used as an FSO receiver, to simultaneously harvest power from sunlight and receive wireless optical data. Therefore, a receiver circuit is required to separate the harvested power and the communication signal components of the photocurrent generated by the panel. Furthermore, the received communication signal needs to be conditioned appropriately before feeding it to the DSP. This sub-system is analogous to the receiver circuits used in conventional RF and FSO systems. In such systems, the receiver circuit uses electronic filters to separate the desired frequency band of the signal from the received signal. Moreover, using an electronic amplifier, the power of the signal is increased for further processing. In this chapter, the design methods and functionality of the receiver circuit are described.

5.1 Introduction

As discussed previously in Chapters 3 and 4, solar cells have a complex relationship with their operating environment, communication performance and the maximum power they can harvest. For any given set of operational conditions, solar cells have a single operating point where the values of the current and voltage of the cell result in maximum power output. These values correspond to a particular load resistance, which is equal to the voltage divided by current, as specified by Ohm's law. Similarly, for a given solar panel, the communication performance is dependent on the ambient light, mode of operation, wavelength of the transmitter, and beam shape of the optical signal incident on the panel. To use the solar panel as a high-speed optical receiver under such varying conditions a specialised receiver circuit is required. The

receiver circuit should be able to do the following: separate the harvested energy from the sunlight and the received communication signal, ensure maximum AC and DC power transfer, store the harvested power, filter out the unwanted frequency components from the received signal, and increase the power of the signal.

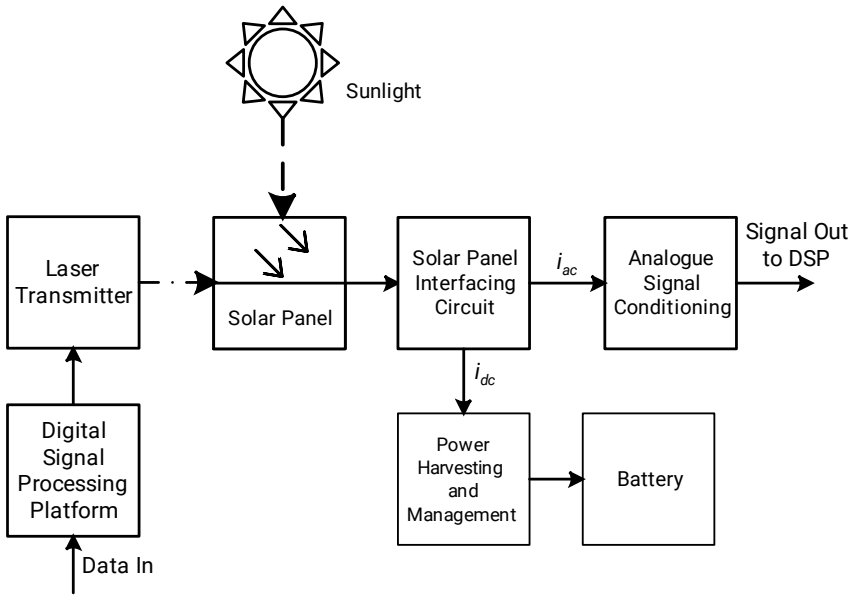

Figure 5-1: Receiver circuit functional block diagram

The functional block diagram of the envisioned receiver circuit is shown in Figure 5-1. In the figure, the solar panel interfacing circuit separates the AC and DC component of the photogenerated current. This circuit also ensures the mode of operation of the solar panel *i.e.,* photodiode or photovoltaic mode. The analogue signal conditioning circuit performs all the essential unwanted signal filtering and increases the desired signal's power before the signal is fed to the DSP. This block of the circuit also performs analogue equalization on the signal, which helps to extend the usable -3 dB communication bandwidth of the solar panel. The power harvesting and management circuit ensure the maximum power is harvested from the solar panel and the harvested power is stored in a battery for further use.

5.2 Designing the equalizer circuit

Solar panels inherently have a very low communication bandwidth compared to conventional photodiodes. Therefore, an equalization technique could be used to extend the usable communication bandwidth of the solar panel. Equalization is the reversal of distortion incurred by the signal through the channel. The equalization could be analogue or digital.

In the previous chapters, the frequency response of the solar panel under all possible operating conditions has been studied in detail. Normally, the frequency response of a 5 W Si-based solar panel has the shape of a low-pass filter (LPF), rolling off at 40 dB/decade. This quick roll off makes digital equalization and pre-distortion challenging as the higher frequency subcarriers have very low signal power, which results in poor SNR.

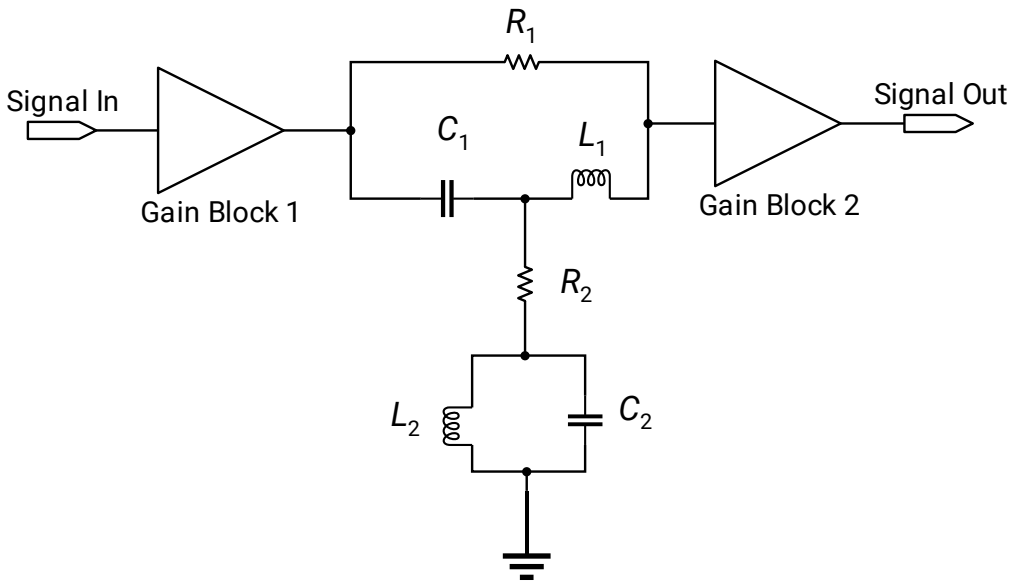

Figure 5-2: Equalizer circuit structure

This is because the quantization noise of the digital-to-analogue and analogue-to-digital converters (DAC and ADC) is dominant over the low signal power. If the signal power is increased, the lower frequency subcarriers are clipped due to the limited dynamic range of the DAC and ADC. Therefore, equalization is

the preferred approach. A passive filter within two amplifier stages has been designed, as shown in Figure 5-2, to perform the analogue equalization. The frequency response of such a structure has a 40 dB/decade gain and hence this will perform the reverse distortion of the signal, *i.e.,* equalization. To perform the equalization, a second-order filter was designed based on a modified version of a notch filter and a bandpass filter. The modified notch filter provides the reverse distortion to compensate for the 40dB/octave roll-off and the bandpass filter is used to attenuate the undesired low and high frequencies. The resulting filter structure can be mathematically expressed as shown in equation (49), in Appendix A. The values of R_1, C_1, L_1, R_2, L_2, and C_2 determines the filter's stability and peak gain at the desired frequency. This is simulated in TINA-TI and the values of the passive components for different equalization bandwidths are provided in Table 5-1. The equalizer was designed such that it could be used with different DSP platforms with different communication bandwidth. Furthermore, the derivation of the transfer function of the filter is provided in Appendix A.

Table 5-1: Values of the Passives for different bandwidths of the equalizer

Bandwidth (MHz)	**Values of the Passive electronic devices**					
	R_1	C_1	L_1	R_2	C_2	L_2
2.5	1.5 kΩ	470 pF	4.7 uH	51	470 pF	4.7 uH
5	1.5 kΩ	750 pF	680 nH	0	750 pF	680 nH
12	5.1 kΩ	220 pF	150 nH	51	680 pF	150 nH
16	5.1 kΩ	100 pF	100 nH	10	470 pF	100 nH
18	7 kΩ	100 pF	220 nH	0	470 pF	100 nH

Table 5-1 shows the equalization bandwidth only up to 18 MHz as equalization is not possible over infinite bandwidth. During the process of equalization, the gain of the signal is traded-off for additional bandwidth.

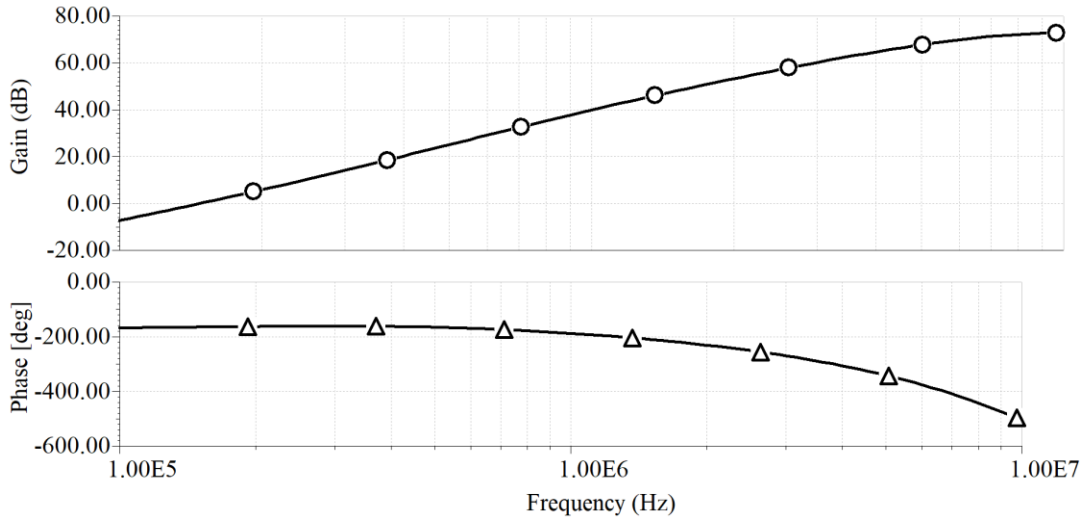

Figure 5-3: Equalizer response

Therefore, it was found that for this 5 W solar panel, the equalization beyond 18 MHz was not possible as the SNR of the signal deteriorates massively at the higher frequencies and the additionally gained frequency sub-carriers were unusable. Furthermore, the choice of communication bandwidth is dependent on the DSP platform. The five values of the communication bandwidth depicted here are supported by the DSP platforms, as described in section 2.6.

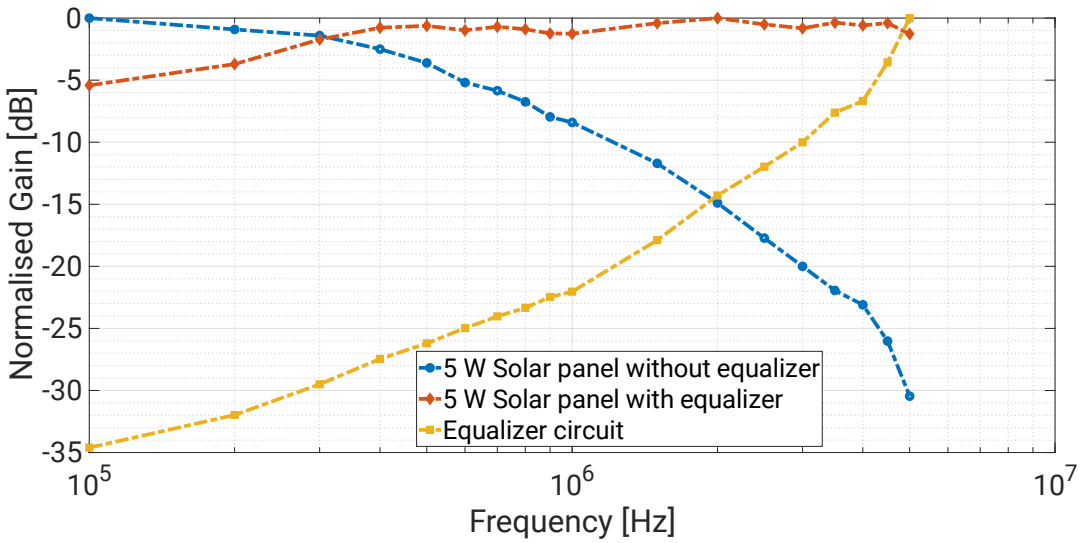

Figure 5-4: Equalizer response with the frequency response of the solar panel

The overall AC transfer characteristics of the equalizer circuit for the overall response of -3dB, 5 MHz communication bandwidth is shown in Figure 5-3. Furthermore, the functioning of the equalizer circuit is shown in Figure 5-4. It can be seen that the overall response of the solar panel with the equaliser circuit is flattened. The figure shown here is for -3 dB, 5 MHz bandwidth of the equalizer circuit. Similarly, the equalisation is done for 2.5 MHz, 12 MHz, 16 MHz, and 18 MHz of communication bandwidth.

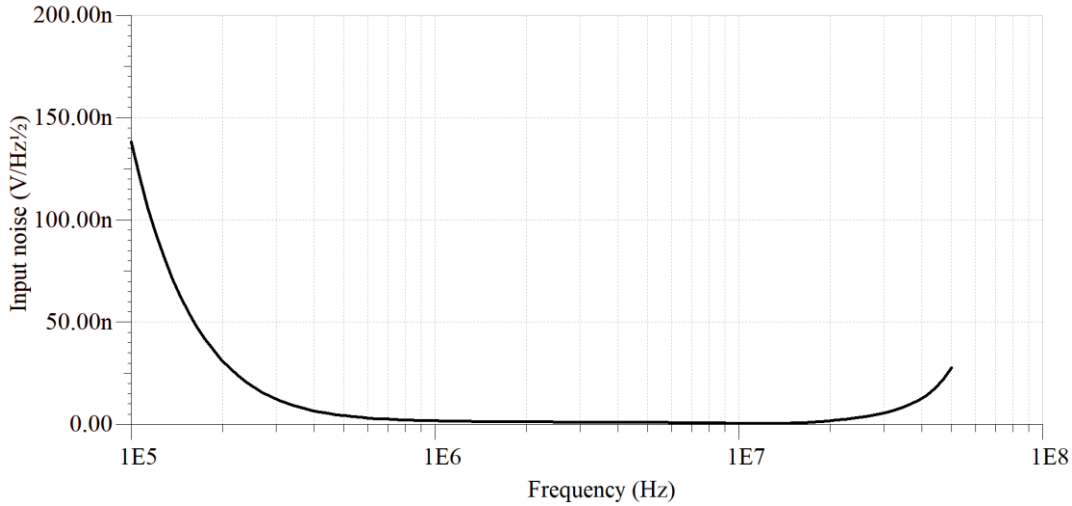

Figure 5-5: Input noise performance of the equalizer circuit

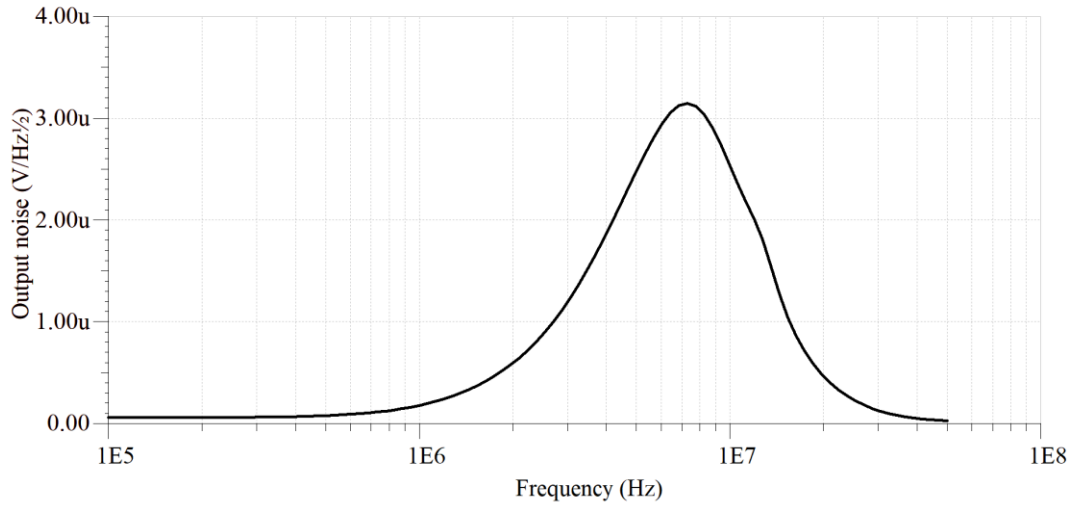

Figure 5-6: Output noise performance of the equalizer circuit

These communication bandwidths were chosen based on the supported baseband bandwidth supported by the DSP platforms mentioned in section 2.6. The overall noise performance of the circuit was simulated in TI-TINA and the plots are shown in Figure 5-5, Figure 5-6, Figure 5-7, and Figure 5-8. In the circuit design, the input noise degrades with an increase in frequency and has been minimised by the choice of amplifiers.

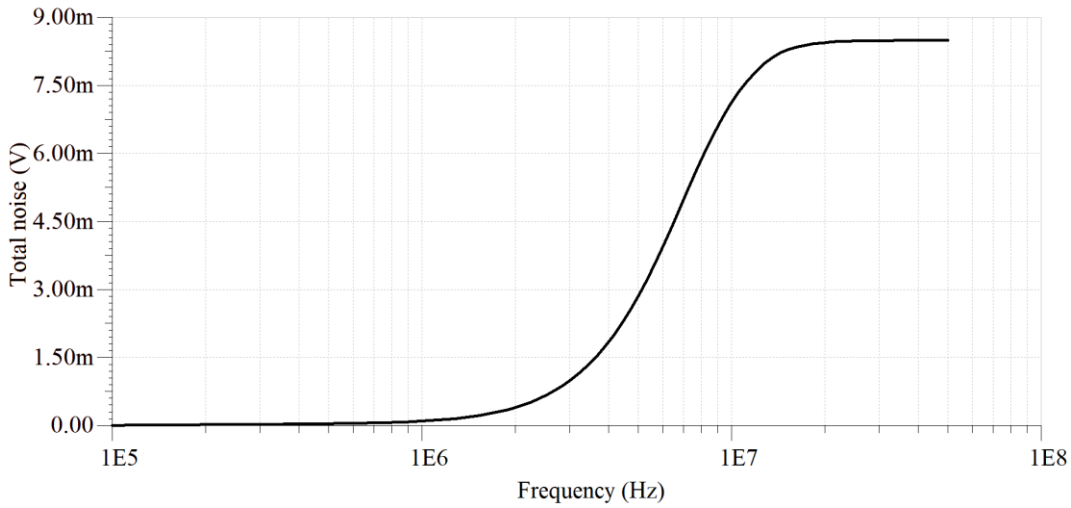

Figure 5-7: Total noise introduced by equalizer circuit

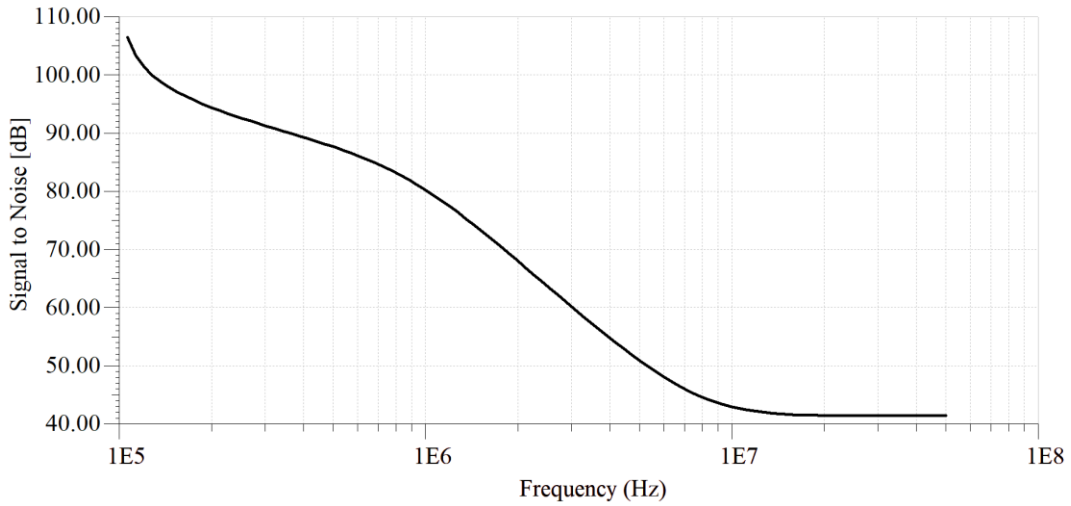

Figure 5-8: SNR performance of the equalizer circuit

The detailed schematic of the circuit is provided in Appendix B. The output noise shape follows the shape of the equalizer response which in turn explains the shape of total noise added by the circuit to the received signal. Therefore, the SNR of the overall circuit decreases with the increase in frequency and the minimum SNR achieved is 40 dB, which is still higher than the estimated optical signal SNR as discussed in Chapter 3. Hence, the SNR of the received signal will always be limited by the performance of the solar panel as an optical data receiver.

5.3 Different methods of interfacing with solar panel

Normally, the conventional photoreceivers are AC coupled with the rest of the stages of the receiver circuit in an FSO system, as the DC signals are of no interest. The DC signals make designing the amplifier and filter stages challenging, as they can easily saturate the operational amplifiers. When using the solar panel, the AC and DC signals must be extracted with maximum power transfer efficiency. In the past, in [18]- [21], a bias-tee structure has been used to separate the AC and DC components of the signal. In the bias-tee, an inductor was used to block the AC component and extract the DC, and a capacitor was used to block the DC component and extract the AC. On both the branches, the signal was drawn as a voltage signal across a resistor as shown in Figure 5-9. In the DC branch, a potentiometer was used as the optimal value of this resistance would vary for different lighting conditions as the internal resistance of the solar panel varies, which was studied in Chapter 3. Furthermore, as shown in [18] the values of the resistor, inductor and capacitor have an impact on the communication performance of the solar panel. The effects of the DC and AC load resistances, P_1 and R_4, as shown in Figure 5-9, were investigated using the analytical model of the solar panel as discussed in Chapter 3. For different values of AC load resistance, the circuit was simulated in TINA-SPICE and the frequency response for three different resistor values was plotted as shown in Figure 5-10. In the figure, the highest -

3 dB bandwidth is obtained with the lowest resistance 7.3 Ω which is 300 kHz. On the other hand, the gain is also the lowest.

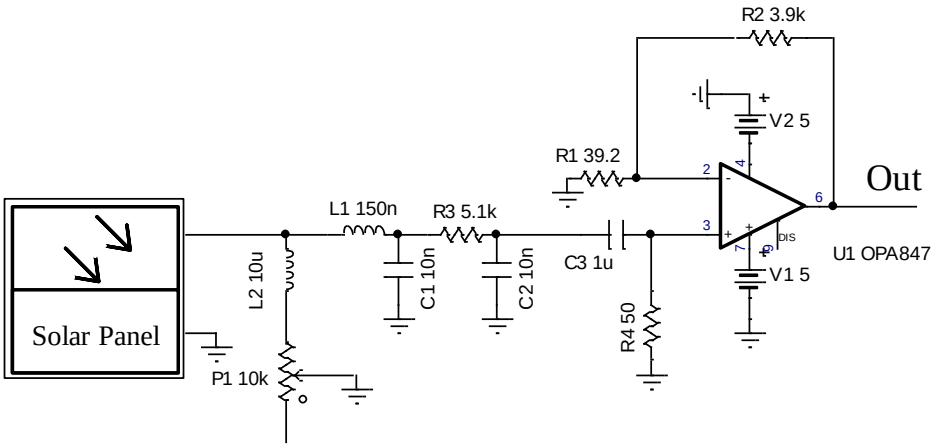

Figure 5-9: PV interfacing circuit with bias-tee

Therefore, the 50 Ω resistance was chosen as the measured gain and bandwidth are optimised at this point. The normalised gain with the 50 Ω resistance is -8 dB and -3dB bandwidth is 280 kHz. Furthermore, keeping the AC load resistance constant, the DC load resistance was varied. The variation in the frequency response for three different DC load resistor values is shown in Figure 5-11.

The frequency response of the interfacing circuit with 6.8 kΩ has the least -3 dB bandwidth, although the energy harvested is highest as the voltage across the resistor will be the highest and the power dissipated by the resistor will be the least. On the contrary, with 7.3 Ω resistance, the frequency response roll-off rate is lower compared to the other resistor values, but at this resistor value, the energy harvesting performance will be adversely affected. Therefore, 781 Ω was chosen as the optimal DC load resistor value as the gain and bandwidth are optimised at this value. This simulation was carried out with the assumption that there was 100 W/m^2 of sunlight irradiation incident

on the panel. Upon varying the sunlight irradiance, the optimal resistor values were changed.

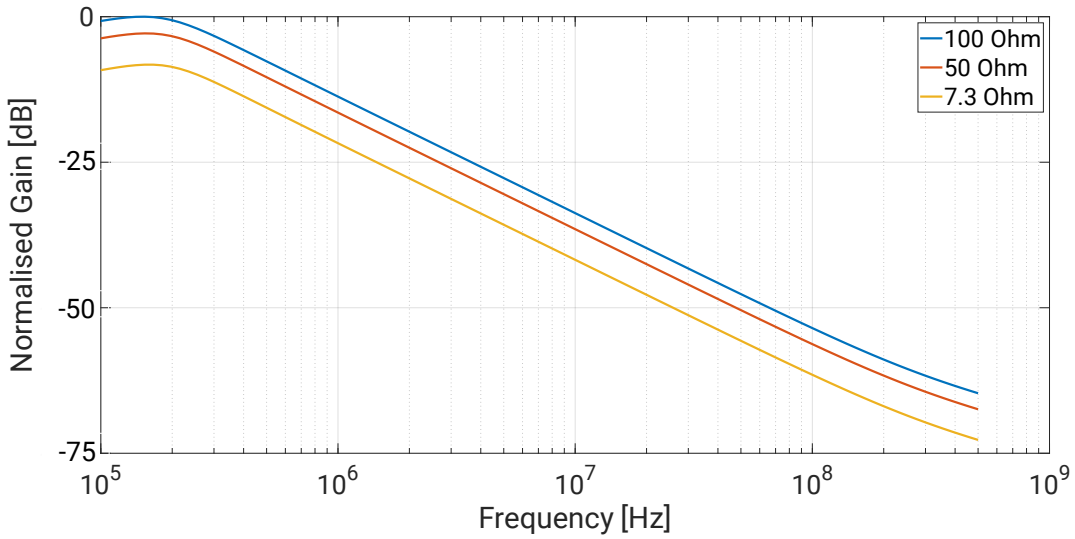

Figure 5-10: Variation in the frequency response due to the varying AC load resistor

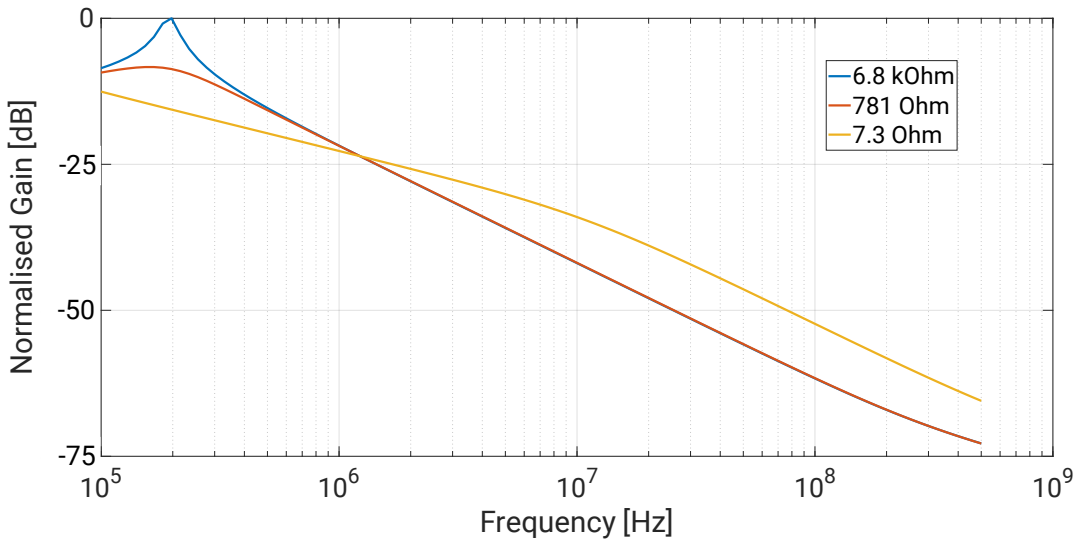

Figure 5-11: Variation in the frequency response due to the varying DC load resistor

The other disadvantage with this circuit design is that there is no control on the voltage across the PV panel for different lighting conditions, which will result in a change in the electric field across the diffusion region, resulting in the frequency response of the solar panel being affected, as seen previously

in section 3.3.1. Therefore, another solar panel interfacing circuit design was proposed as shown in Figure 5-12.

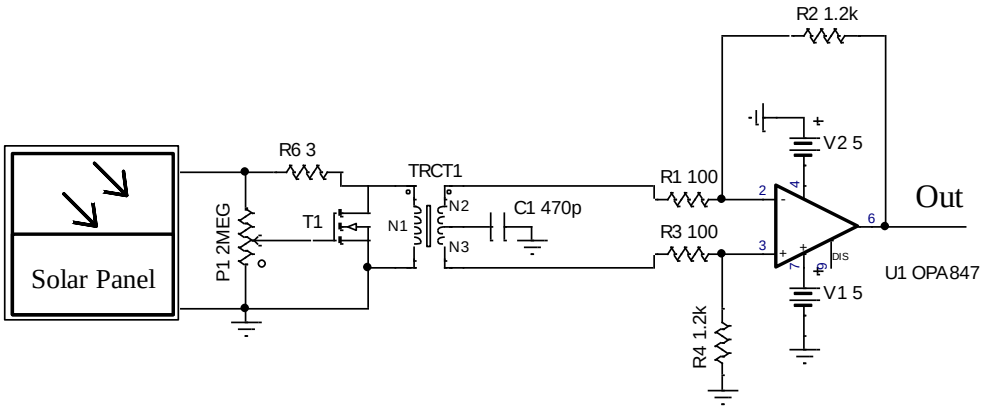

Figure 5-12: PV interfacing circuit with MOSFET

In this design, a Power-over-Ethernet (PoE) transformer has been used to AC couple the panel with the rest of the receiver circuit. A PoE transformer was chosen because these transformers are specifically designed for separating DC and AC signals in the IEEE 802.3 standard for ethernet [42]. These transformers are capable of handling DC as high as 300 mA and the coupling frequency lies in the region of 0.1-100 MHz.

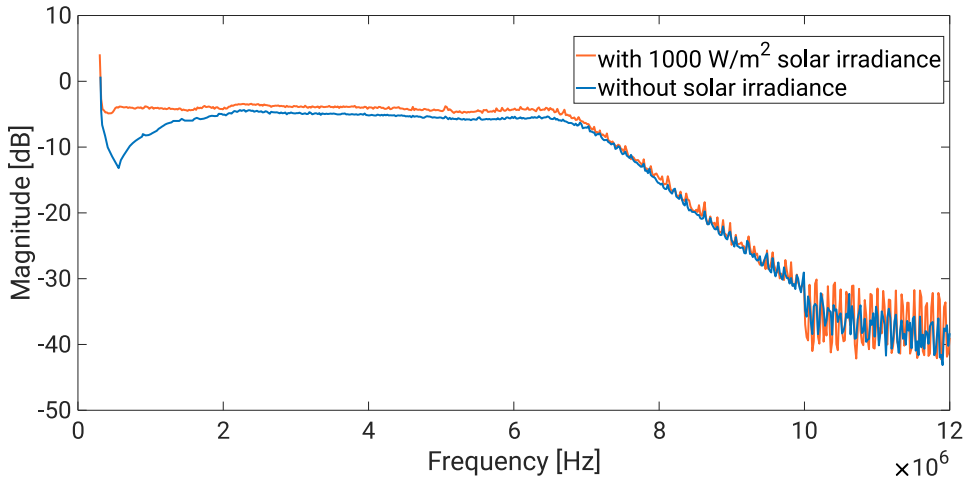

Figure 5-13: Variation in frequency response with MOSFET interfacing circuit

Furthermore, a Metal-oxide-semiconductor Field-effect transistor (MOSFET) has been used to hold the voltage across the panel constant.

In a MOSFET, the voltage at the gate terminal controls the flow of current between the source and drain terminal. In this circuit, the gate voltage is set by a voltage divider, which is built using a potentiometer. The end terminals of the potentiometer were connected to the panel. Using the potentiometer, the gate voltage was set such that the minimum voltage is fixed across the panel, *i.e.,* around 1-1.5 V. The panel voltage cannot be set below the minimum source-drain voltage of the transistor, which sets the transistor in saturation mode of operation. When the voltage generated across the panel varies, the gate voltage also varies, which results in a change in the electrical conductivity across the drain and source terminal of the transistor. This way the current through the transistor would vary, but the voltage across the solar panel remains constant. This circuit was designed and manufactured for testing. Using the transmitter setup as mentioned in Chapter 4 and a spectrum analyser, the channel response was captured for conditions both with no illumination and 1000 W/m^2 solar irradiance, as shown in Figure 5-13. In the figure, it can be seen that, at the lower end of the baseband frequency spectrum, the response varies by -7 dB for different illumination conditions. This variation could be attributed to a variation in the operating regions of the transistor. When there is no solar irradiance, the voltage across the panel is below the threshold voltage of the gate of the transistor, which results in different frequency response. To eliminate this issue, the solar panel interfacing circuit was modified. In this circuit, the solar panel was directly connected to the PoE transformer with a 3Ω resistor in series, as shown in Figure 5-14. As the DC load across the panel was very low, the panel voltage was also very low. The short-circuit current for the selected solar panel is 300 mA, therefore the maximum voltage that can be measured across the panel is 0.9 V. Hence, the variation in frequency response due to different illumination

conditions will be minimal as the maximum variation in panel voltage will be 0-0.9 V.

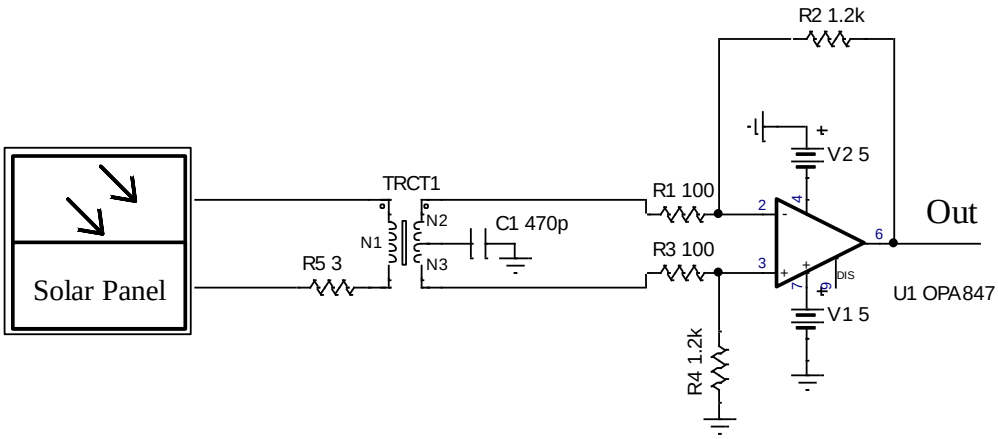

Figure 5-14: PV interfacing circuit with PoE transformer

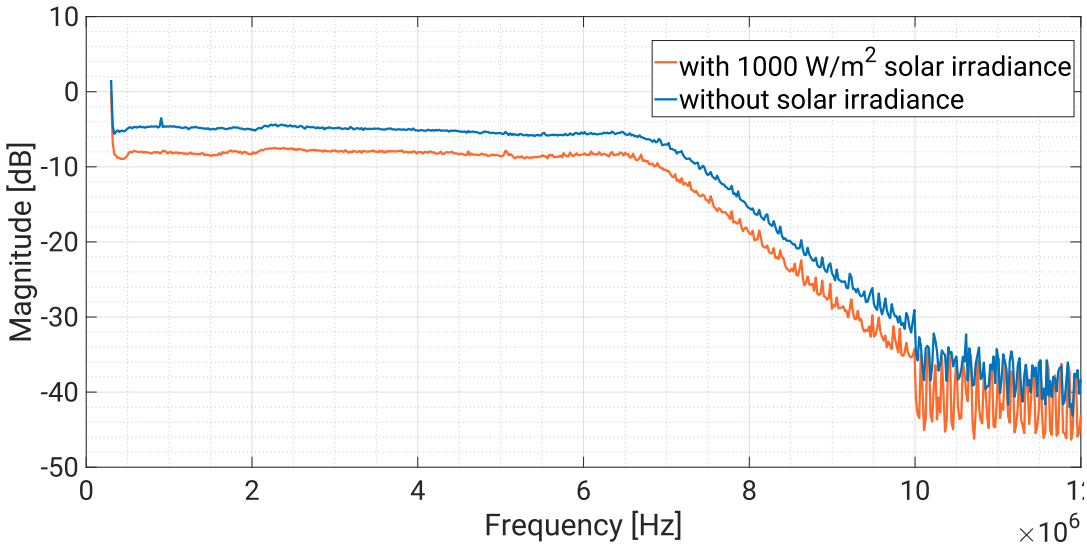

Figure 5-15: Variation in the frequency response of solar panel with PoE transformer

Furthermore, the overall channel response under no solar irradiance and 1000 W/m^2 is measured and shown in Figure 5-15. From the figure, it can be concluded that there is no variation in the shape of the frequency response. Although, the gain under 1000 W/m^2 solar irradiance is 4 dB less than the gain under no illumination conditions. This circuit enables the use of a solar panel

as a high-speed optical communication receiver under various illumination conditions without trading off the communication bandwidth.

5.4 Energy harvesting and storage

Solar energy harvesting by no means a new idea. An elementary solar energy harvesting consists of a solar panel, DC-DC converter, rechargeable battery, a battery charge protection circuit called a battery management system (BMS) and a DC-DC converter control unit [63]. Typically, there are two methods used for DC-DC converter control methods: Pulse Width Modulation (PWM) and Maximum Power Point Tracking (MPPT). MPPT has been proven to be the best, as it operates at the maximum power point of the panel [64] [65]. A solar panel has a unique point on the *I-V* curve, at which the entire photovoltaic system operates with maximum efficiency and produces its maximum output power; this is the point defined as the maximum power point. Figure 5-16 shows a block diagram of an MPPT controlled charger circuit. The incident solar irradiance is harvested using the solar panel and converted into electrical energy. The DC-DC converter steps down and regulates the magnitude of the voltage generated by the solar panel and supplies it to the rechargeable battery. The MPPT controller tracks the voltage and current from the solar panel and adjusts the duty cycle for the DC-DC converter. Finally, the BMS controls the charge and discharge rate to avoid over-heating and over-charging of the battery. As the FSO system with a solar panel as the optical receiver is envisioned to be an energy-neutral system, therefore, the choice of battery is important to enable the operation of the system at night, when there is no solar energy harvesting. Two types of batteries are widely used with PV standalone systems: Lead-Acid batteries and Lithium-ion (Li-ion) batteries. Li-ion batteries have many advantages for PV energy harvesting systems in comparison to lead-acid batteries [66].

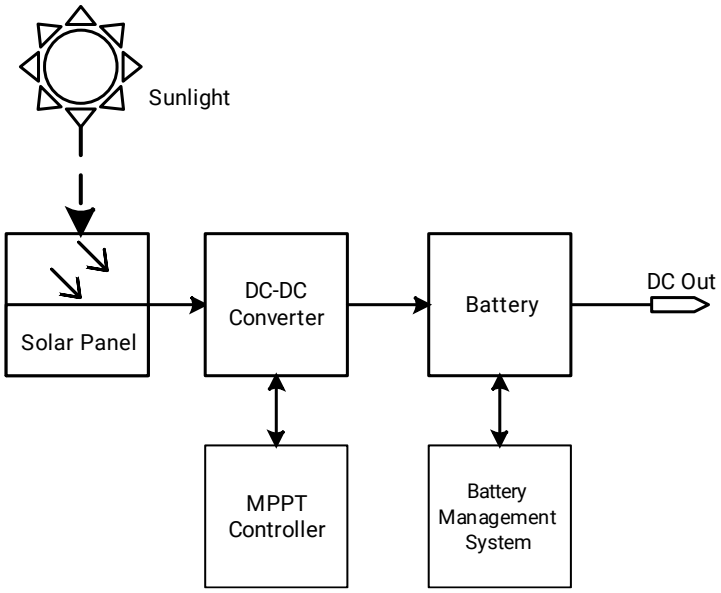

Figure 5-16: Block diagram of a PV energy harvesting system

Li-ion batteries have high energy capacity, low maintenance and a higher life cycle than a lead-acid battery. A comparison between the specifications of the lead-acid battery and Li-ion battery is shown in Table 5-2.

Table 5-2: Battery specifications [66]

Characteristics	Lead-acid	Lithium-ion
Energy Density (Wh/L)	54-95	250-360
Specific energy (Wh/kg)	30-40	110-175
Depth of discharge	50%	80%
Temperature range of charge	-40˚C-27˚C	-20˚C-55˚C
Efficiency	75%	97%
Replacement timeframe (year)	1.5-2	5-7

Therefore, a 38 Wh (7.4 V/5.2 A) Li-ion battery will be used to store the harvested energy. Based on the battery type, a battery management circuit is needed to charge and discharge the battery. Hence, an integrated battery charger BQ24650 [64] from Texas Instruments Inc. was chosen. This device has the capability of MPPT by ±0.6% input voltage regulation, the maximum

power point can be set and can charge the battery with ±0.5% charge voltage and ±3% charge current regulation. The charge controller supports charging Li-ion/Polymer, $LiFePO_4$ and lead-acid batteries [64]. It uses a constant voltage algorithm which is the simplest MPPT method, which is also desirable for the communication circuitry. The device can be set to a charging voltage threshold, at which the voltage is held constant with only the charging current varying depending upon the power generated. Depending on the battery chosen, the charging current and voltage can be set.

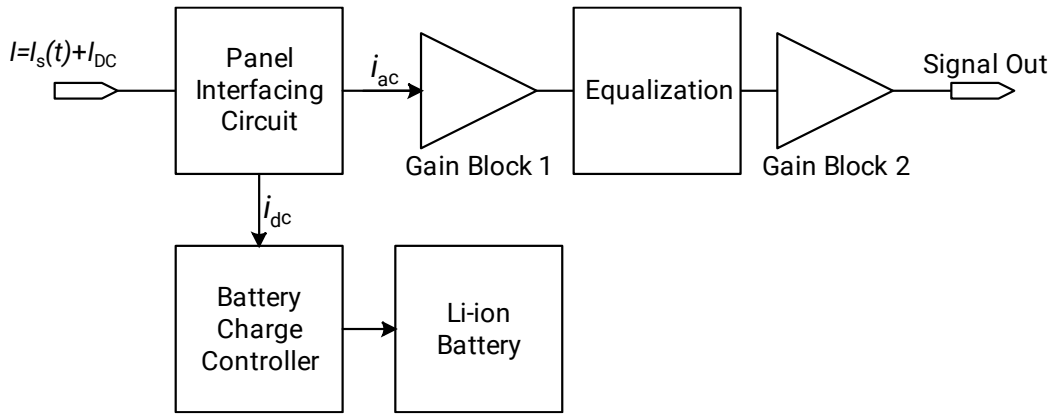

Figure 5-17: Receiver circuit with battery charge controller

The battery charger circuit was designed based on the reference design shown in [64]. The input voltage from the PV panel was set to 8.22 V at the maximum charging current of 2 A, which is the nominal charging voltage and maximum charging current respectively, of the selected Li-ion battery. The battery charging circuit was then integrated with the rest of the receiver circuit as shown in Figure 5-17. The PV panel interfacing circuit of the receiver had to be modified to accommodate the battery charging circuit. An additional bias-tee was introduced in between the PoE transformer and the solar panel to separate the DC and AC signals, as shown in Figure 5-18. In the circuit, the battery charger circuit is connected across R_5. The battery charger circuit holds the panel voltage constant at 8.22 V. When the photogenerated voltage is below the threshold input voltage, the charging circuit is switched off.

Furthermore, when the battery is fully charged, the charging circuit is switched off to avoid overcharging the battery. The overall frequency of the receiver circuit was measured, and it was found that there is no variation in performance compared to the plot shown in Figure 5-15. Therefore, the whole receiver was designed and developed with all the blocks integrated on a single printed circuit board (PCB). Further details on the schematic design and implementation of the receiver are depicted in Appendix B.

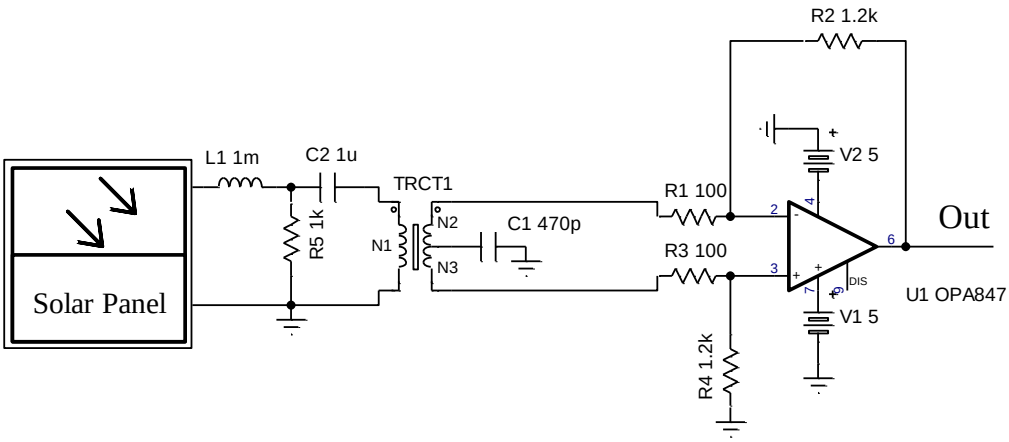

Figure 5-18: Modified PV panel interfacing circuit

To test the operation of the energy harvesting capability of the system, a sunlight simulator was developed. The sunlight simulator consisted of a 1.8 kW halogen lamp, with a parabolic reflector. The colour temperature of the halogen lamp is 3200 K and the colour temperature of the daylight on the surface of the earth is around 5700-6000 K [67]. Therefore, an appropriate colour filter [68] was used in front of the halogen lamp to produce a light spectrum equivalent to the spectrum of sunlight. A dimmer with the lamp was used to control the light output from the halogen lamp. The sunlight simulator was placed at a distance of 1 m from the PV panel and the maximum intensity measured on the surface of the PV panel, using a lux meter, which was around 57,785 lux. Using the solar irradiance to lux illuminance conversion factor of

0.079 W/lux [69], it was estimated that 456.5 W/m^2 was incident on the panel. Hence, the total optical power captured by the PV panel with an active area of 667 cm^2 is 30.45 W. Then, the power generated by the PV panel and the power delivered to the battery is measured, which is shown in Table 5-3.

Table 5-3: Power generated from the solar panel & power delivered to the battery

Incident light on the PV panel (W)	Power generated (W)	Power delivered (W)
30.45	4.11	3.81

From the table, it can be seen 92.7 % of the electrical power generated by the solar panel was delivered to the battery, using MPPT. The efficiency of the 5 W polycrystalline solar panel under test, is calculated to be 13.5 % and the efficiency of the overall system is 12.5 %.

5.5 Summary

A receiver circuit for the solar panel was designed to extend its communication bandwidth, enable simultaneous energy harvesting and interface it with the DSP platform. Using analogue equalization, the -3 dB communication bandwidth of the solar panel was extended up to 18 MHz. The design for 2.5 MHz, 5 MHz, 12 MHz, 16 MHz and 18 MHz equalizer circuit is provided with the transfer function of the equalizer circuit network. Moreover, the different methods of interfacing the receiver circuit with the solar panel are proposed and compared with their respective advantages and disadvantages. Furthermore, the efficiency of the energy harvesting, and storage system was measured to be 92.7%. The harvested energy is stored in a 38 Wh Li-ion battery. The power consumed by the receiver circuit board is 1 W. Therefore, the whole receiver system can function without requiring any external power input. The proposed receiver design was developed, tested and verified with the theoretical studies. Finally, the overall receiver circuit schematic layout and implementation are provided in Appendix B.

Chapter 6 Demonstration of FSO links using solar panels as receivers

The digital divide is the gap between people in society who have full access to digital technologies, such as the internet and computers, and those who do not. Access to the internet has revamped economies, education, and healthcare around the globe. However, there are still sections of society that do not have reliable access to the internet or have access at all. To bridge this gap, an FSO system with an off-the-shelf Si solar panel was designed and deployed to provide the last mile connectivity to residents on a remote Scottish Island. Meanwhile, the system also had potential applications in military deployment. The demand for bandwidth on the battlefield has increased significantly over the past 20 years. Fibre-optic cable technology is more than capable of meeting this bandwidth demand. However, in most tactical situations, it is not feasible to run cables from one node to another. Moreover, the use of RF links is not desirable in such situations as there is always a possibility of eavesdropping and RF signal jamming. The requirement for such scenarios is a quick deployment, point-to-point link, energy neutral, robust against challenging weather conditions and highly secured. All these characteristics were considered in the design process of the PV receiver FSO system.

6.1 Introduction

The concept of using a Si-based solar panel as an OWC receiver is almost five decades old. All the previously developed experiments and prototypes have been deployed and tested in an indoor laboratory environment only. In this chapter, the design of a state-of-the-art FSO system deployed with an off-the-shelf Si solar panel as the receiver under outdoor conditions is discussed.

The prototype was developed in multiple iterations. In the first iteration, the maximum communication distance was achieved as the research was mainly focused on optical design and implementation. In subsequent iterations, the electronics and the DSP platform of the prototype were enhanced to achieve higher data rates. The system design used in each iteration of the prototypes and the results obtained from each prototype is discussed in this chapter. Furthermore, issues are raised regarding RF interference from FM radio stations and the solutions to these issues are discussed in this chapter.

6.2 Demonstration I

The prototype was developed as a solution for backhaul communication over a short-range distance to distribute internet connectivity to two residential properties from a lighthouse, on a remote island as depicted in Figure 6-1. The system was used as a replacement for a fibre optic or copper cable installation as it had the advantage of rapid and cost-effective deployment.

Figure 6-1: Deployment concept [70]

Furthermore, the deployment aimed to upgrade the internet accessibility of the residents over the existing asymmetric digital subscribers' line (ADSL) broadband connection, which had several disadvantages. The existing ADSL broadband connection had very low download speeds and extremely poor upload speeds. ADSL broadband connection uses two copper wires, which are used for telephone lines, to transmit and receive data using PAM-DMT. The maximum achievable speed on an ADSL line is 10 Mbps, out of which 9 Mbps is generally allocated for downlink and 1 Mbps for uplink by the internet service provider (ISP), as the system is half-duplexed over the two copper wires [71]. Moreover, the data rate decreases with the increase in cable length. Therefore, the farther away the property is from the telephone exchange, the slower the internet connection is. This was the only medium of communication available on the island to provide an internet connection to the residents. Due to the poor internet connection, the residents were not able to get the full user experience of modern age internet services such as high-definition (HD) video streaming services, video calls, online gaming *etc.*

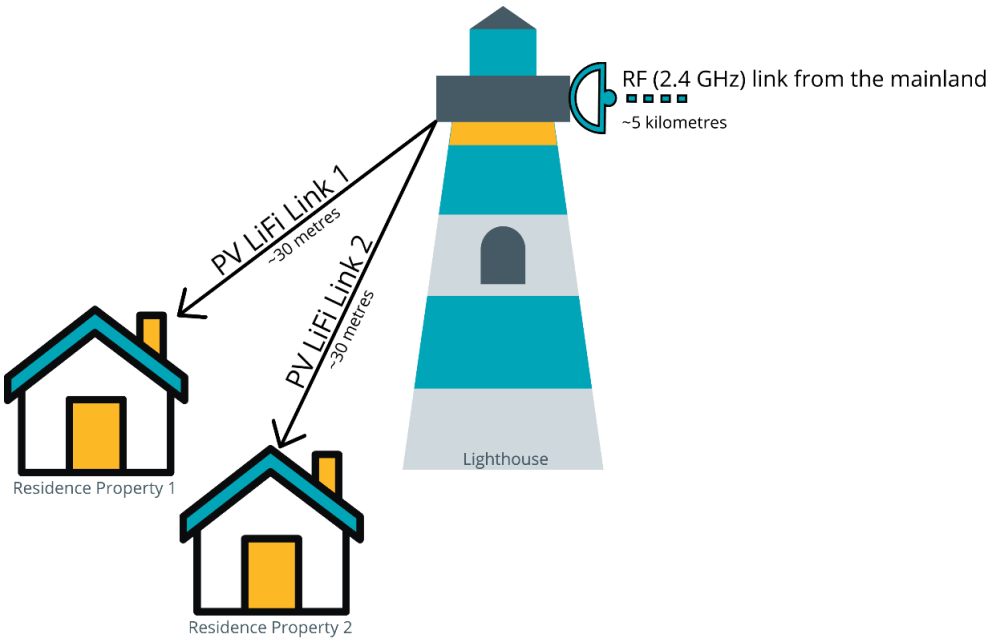

Figure 6-2: Deployment architecture

As a pilot project, the PV FSO prototype was meant to enable the residents to access all the high-speed internet services by aggregating both the FSO link connection and the ADSL broadband connection. The architecture of the system installation is shown in Figure 6-2. The focus of this project was to demonstrate the usage of solar panel as FSO receivers. Therefore, the development was mainly focused on the communication performance.

A high-speed internet connection was provided using an RF link from the mainland to the lighthouse on the remote island. The connection was then distributed to each resident's property using the PV FSO link, as shown in Figure 6-2. The PV FSO internet link was aggregated with the existing ADSL broadband link using a load balancing router installed at the resident's property. The internet connection was made accessible to the residents through Wi-Fi or ethernet connection. The detailed network architecture, design and configuration of the deployment is shown in detail in Appendix B.

6.2.1 System design

This section describes the flow of information from the transmitter to the receiver as well as the energy harvesting and storage capability of the system. Figure 6-3 depicts the working of the transmitter on one end and the receiver unit on the other end. The whole system is designed to be a fully functional bidirectional link with full networking capability. The data flow path through the system shown in Figure 6-3. The data is first fed to the processor to generate the packet with the information to be transmitted as the payload. Then this whole packet is passed on to the FPGA where this is converted to a time-based digital samples using the suitable modulation technique. The DAC then converts the time-based samples to an analogue waveform. Then the signal is modulated onto the output optical intensity of the laser, which is transmitted over the air. Then the solar panel receives the optically modulated data and converts it into electrical signal. The receiver circuit performs

analogue signal processing and equalization as described previously in chapter 5. The data is then fed to the ADC which converts the analogue waveform back to digital samples. The FPGA then demodulates the digital samples to retrieve the information in bits. The processor then reconstructs the packet which is passed on to the end-user device.

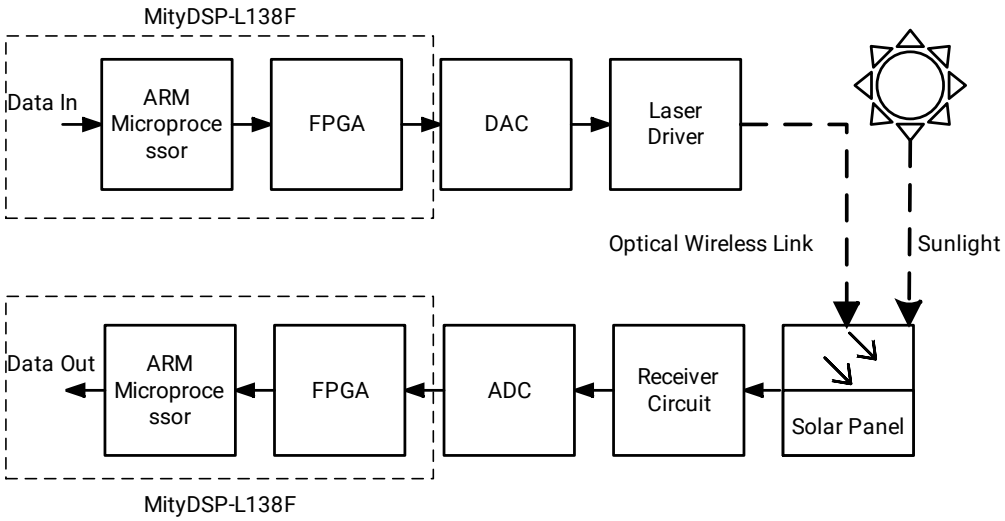

Figure 6-3: Version 1 prototype system architecture

6.2.1.1 Transmitter

A voltage-controlled current-driven laser driver circuit was designed. An off-the-shelf 2x2 VCSEL array [72] was used as the optical source. A temperature sensor and digitally controlled attenuator were added to the design in order to control the signal input to the laser to maximise the link performance, as mentioned previously. The control circuit varies the voltage at the gate of the MOSFET to control the bias current of the laser. The signal power is varied by the digitally controlled attenuator, which can provide attenuation from 0 dB to 31.5 dB.

The frequency response of the laser driver was measured using a 1 GHz PIN PD optical receiver. From Figure 6-4, it can be inferred that the –3 dB bandwidth of the driver is 100 MHz, which is much higher than the bandwidth

of the receiver. One of the most important limitations in the design of an FSO communication system is eye safety [73]. The majority of FSO transmitters operate at a wavelength of 1550 nm due to their high maximum permissible exposure (MPE), which is 100 mW/cm^2 [8]. However, the laser wavelength in this research is selected to be 940 nm because of the peak responsivity of Si cells in the region between 940 nm and 1000 nm. The MPE of 940 nm lasers is 3.1 mW/cm^2 and the laser system is certified to be classified as Class 1M. Another requirement in the optical domain is the transmission of a divergent laser beam that can overfill the solar panel. This is not only to project a uniform beam covering the entire solar panel but also to tackle any misalignment due to unfavourable weather conditions such as strong winds.

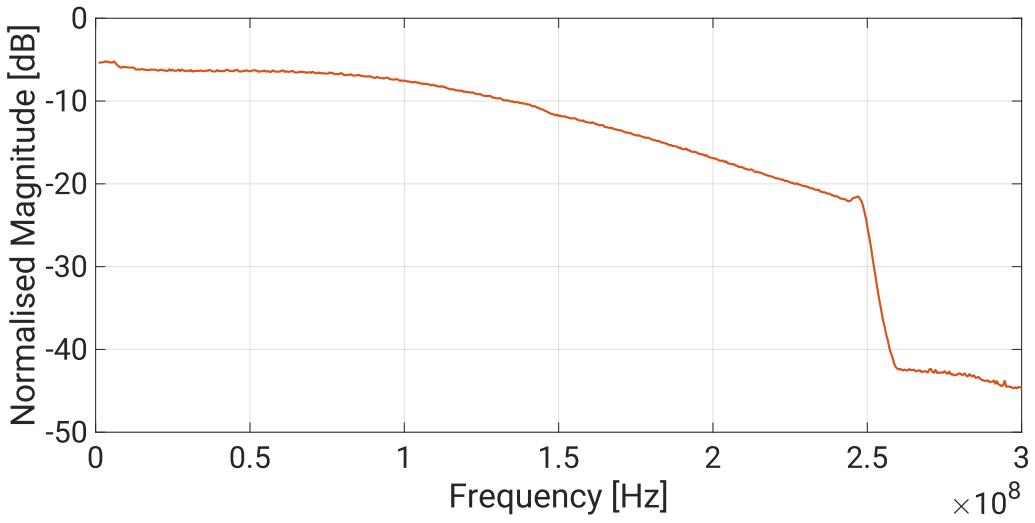

Figure 6-4: Frequency response of the laser driver

The optical design software Zemax was used for ray tracing and a calculation of the power budget of the link. A 2x2 vertical-cavity surface-emitting laser (VCSEL) array [72] is used with a diffuser on top of the package. The maximum DC optical power of the laser is 0.5 W. The VCSEL generates a rectangular beam pattern with four hot spots as shown in Figure 6-5. The laser beam has a wide horizontal and vertical divergence of 65° and 78°, respectively. In order to increase the directivity of the diffused laser beam and

overfill the solar panel at a link distance of 30 m (designated for the installation in Orkney), an off-axis parabolic mirror Edmund Optics 35-533 [74] with a diameter of 76.2 mm is used.

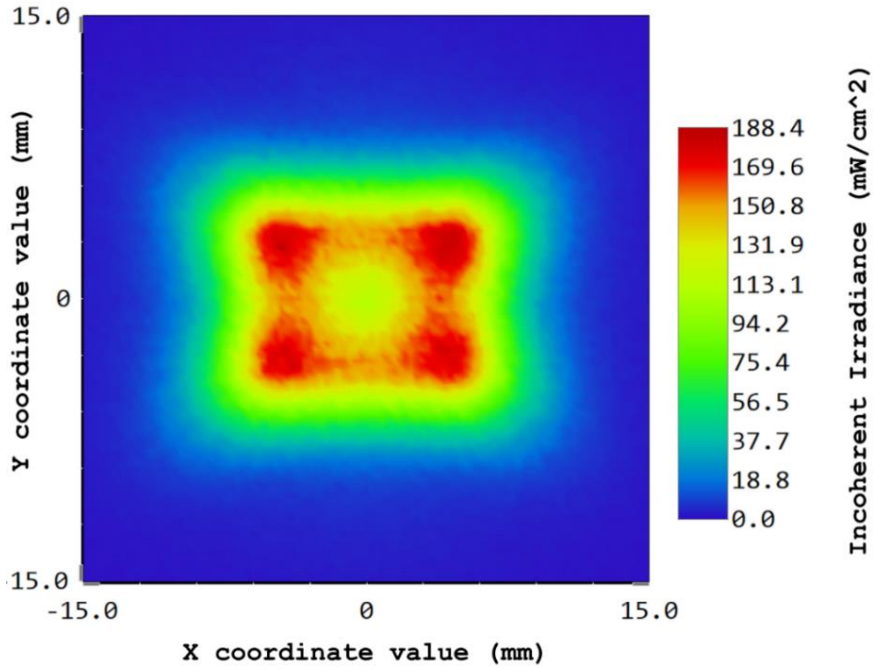

Figure 6-5: Incoherent irradiance of the VCSEL array on a square detector at 1 cm

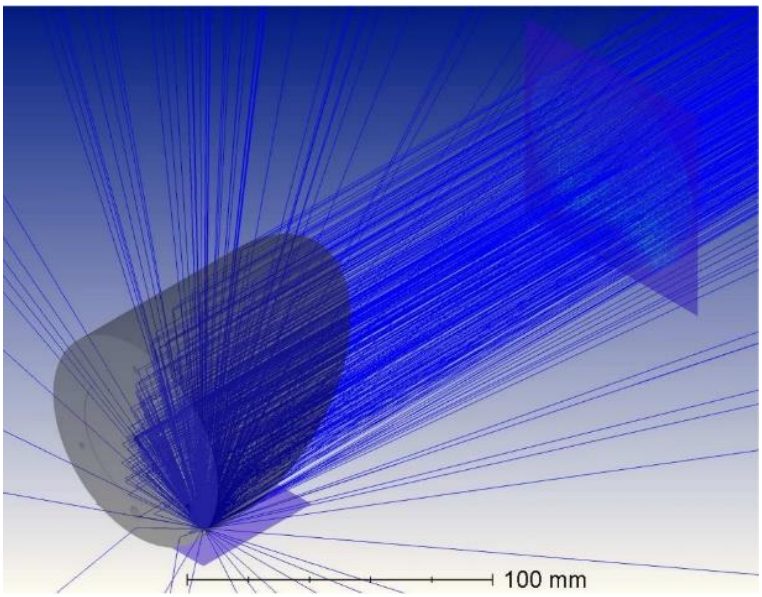

Figure 6-6: Optical setup at the transmitter

To ensure that no user can open the enclosure of the prototype and be exposed to any radiation above the MPE limit, the enclosure is locked with bolts as recommended by the laser safety agency. The transmitter's optical setup and the illumination pattern of the laser beam at the enclosure aperture are given in Figure 6-6. It was observed that only two of the four initial hotspots are transmitted in free space. This is because the rays of the bottom two hotspots of the rectangular VCSEL pattern travel a shorter distance than those of the top two hotspots towards the mirror; thus, they are getting reflected with higher power from the mirror. In practice, to make sure that the laser source was placed at the focal point of the off-axis parabolic mirror; a pitch, yaw, x, y, and z translation stage [75] is used as shown in Figure 6-7. The optical source is attached to the printed circuit board (PCB) of the laser driver and the PCB is mounted on the translation stage. Thus, the beam shape and size can be controlled by modifying any of the five degrees of freedom of the translation stage. In order to ensure that the beam covers the entire area of the solar panel at the 30m link distance, the beam shape and size were optimized at a 20 m distance.

Figure 6-9 gives the simulated irradiance distribution of the beam, and the beam observed at a 20 m distance through a camera with an infrared bandpass filter. As the beam is not uniform, it is analysed along the vertical x and y axes and not along a single axis in Zemax. The system was then classified by Lasermet, which is a laser safety solution provider company, as class 1 M and the non-ocular hazard (NHZ) distance was estimated to be 56 m. The NHZ distance is defined as the minimum distance within which the beam is not eye-safe if observed with an optical aid being in the line of sight of the optical transmission. Furthermore, it was inferred from the testing that the maximum optical output of laser could be increased to 1.5 W still being classified as class 1M, although the NHZ distance needs to re-estimated.

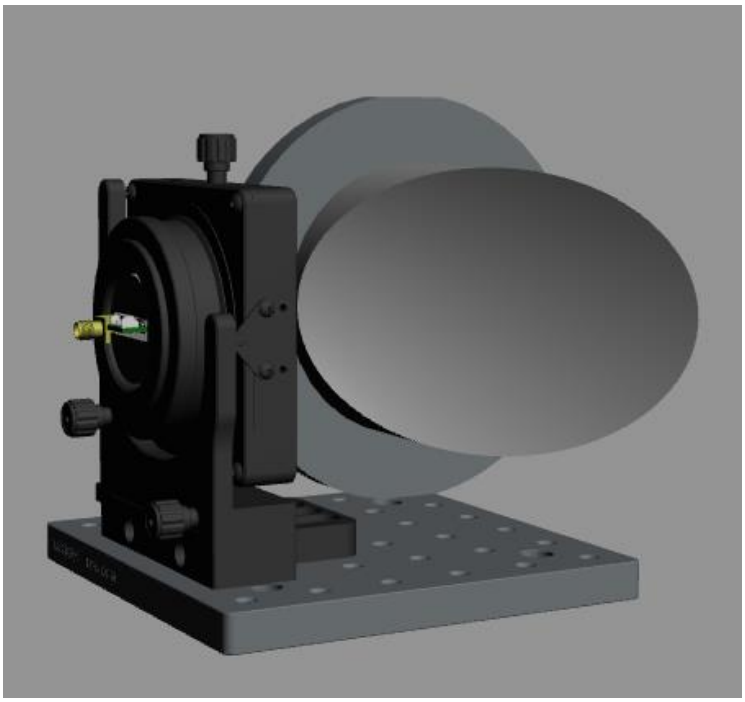

Figure 6-7: Optomechanical setup

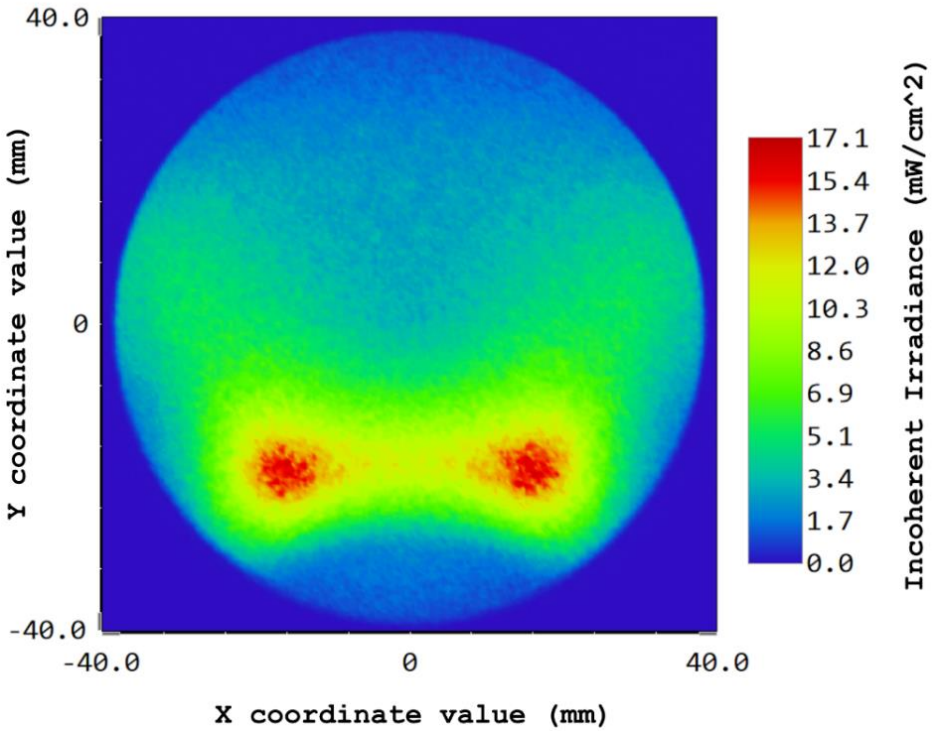

Figure 6-8: Laser beam at the enclosure's aperture

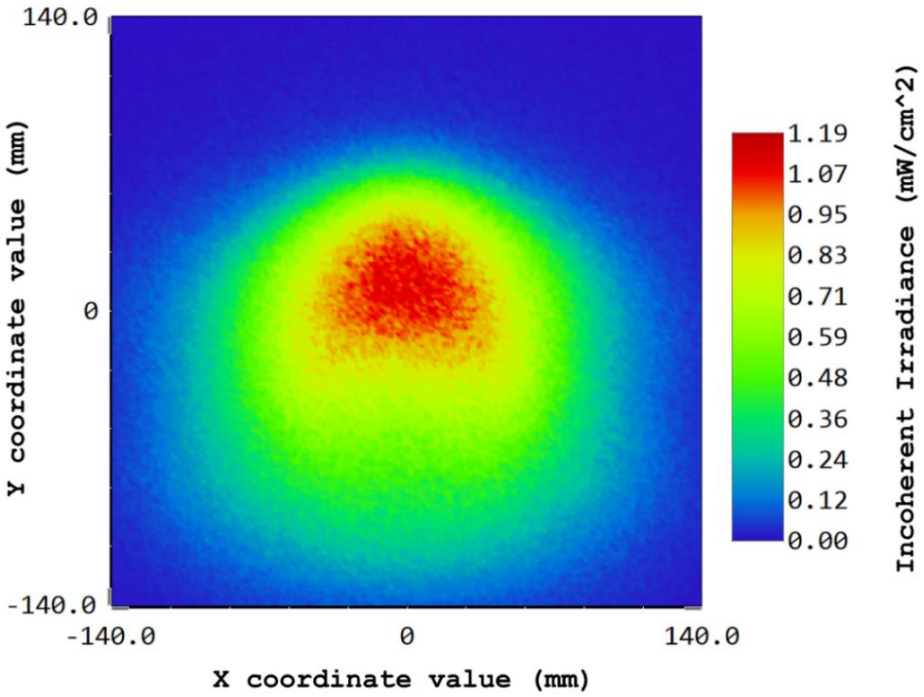

(a)

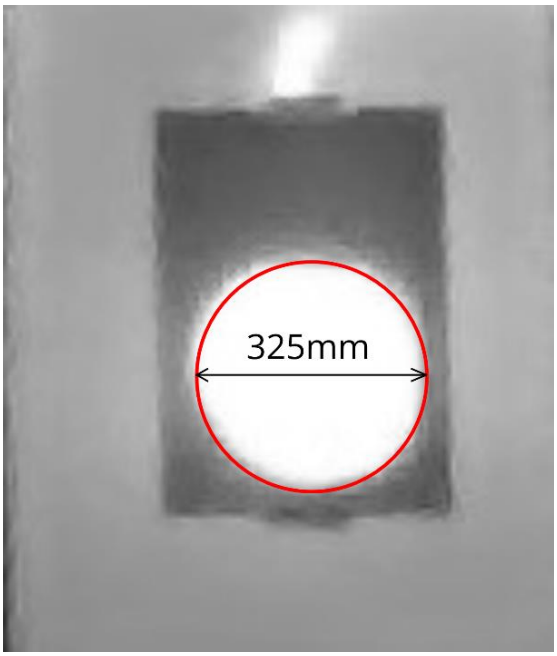

(b)

Figure 6-9: Beam profile at 20 m (a) simulated using Zemax (b) captured using an infrared camera

6.2.1.2 Receiver

The receiver circuit discussed in Chapter 5 was used in the prototype with the 2.5 MHz and 5 MHz variants, as the maximum supported bandwidth of the DSP platform is 5 MHz. The detailed schematics of the receiver design of these variants are provided in Appendix B. Furthermore, during the testing, it was found that the strips on the solar panel which connect the solar cells act as RF antennae. This hampered the communication performance as the RF signal picked up by the strips interfered with the optical signal. This problem was solved by creating a faraday cage [50] around the solar panel using a mesh made of stainless-steel wire, which was then connected to the circuit ground of the system.

6.2.1.3 Modulation techniques

In section 2.2, it was shown that with on-off keying the maximum data rate was 3 kb/s. Most of the systems researched and developed previously, as mentioned in chapter 2, used OFDM or PAM demonstrating data rates in the order of Mb/s, as they are the most spectrally efficient. The maximum data rate achieved with an off-the-shelf 5 W Si-based solar panel was 11.34 Mb/s [18] which was using OFDM. The maximum data rate achieved with PAM was 17.05 Mb/s, although the size of solar panel was smaller than a 5 W panel and the solar panel was used in reverse-biased mode [62]. Therefore, OFDM or PAM should be the preferred modulation techniques instead of on-off keying. Furthermore, the two mentioned modulation techniques have been widely researched to be used in optical wireless communication [14].

In this section, an experiment was conducted to investigate the performance of OFDM and PAM modulation techniques when used with a solar panel as an optical receiver for an FSO system. The modulation techniques were implemented in MATLAB [76]. The experimental setup is shown in Figure 6-10.

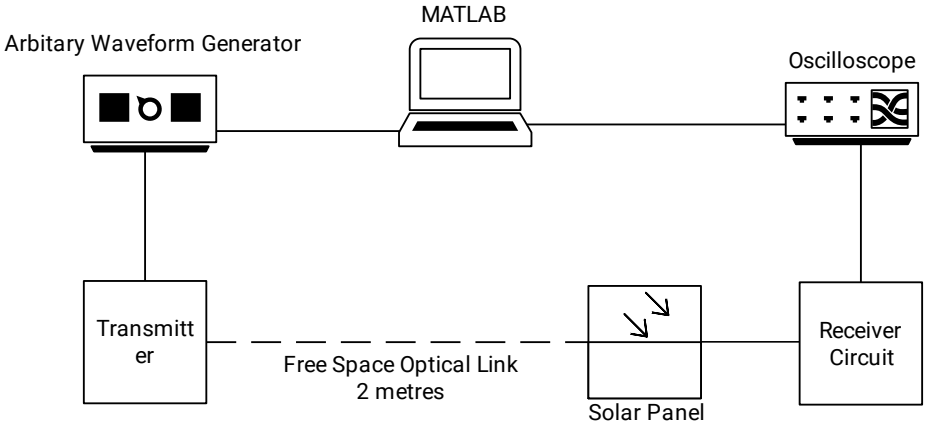

Figure 6-10: Communication test setup

The detailed design and description of the transmitter are given in section 6.2.1.1 and the design and description of the receiver circuit are provided in Chapter 5.

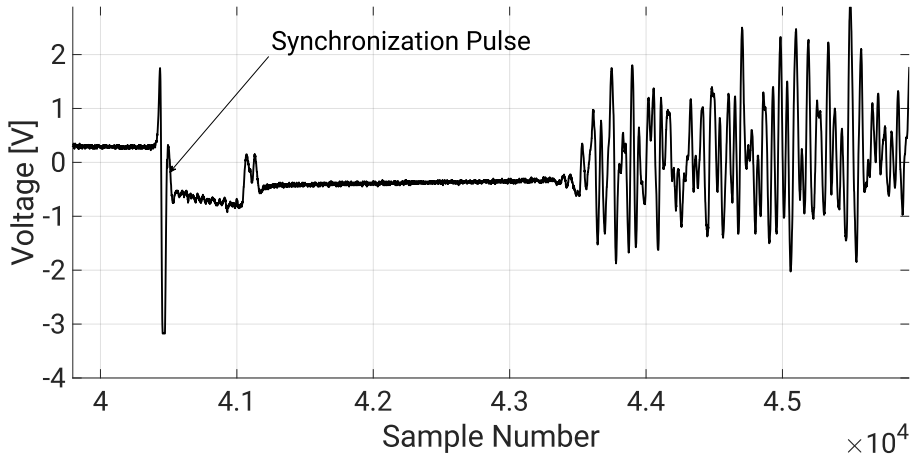

Figure 6-11: Acquired OFDM packet with synchronisation pulse

The OFDM and PAM packets are generated on a computer and then fed to an arbitrary waveform generator (AWG) over Ethernet. The signal is then fed to the transmitter circuit over a coaxial cable, type RG-18. The transmitter and receiver circuits are powered using benchtop power supplies. Ferrite cores are used on the power supply cables to ensure external powerline and RF noise is not added to the transmitter and receiver circuits. Powerline noise can affect

the SNR of the transmitted or received signals significantly. The signal output of the receiver circuit is connected to an oscilloscope using an RG-18 coaxial cable. The signal on the oscilloscope is then captured and transferred to the computer over USB for processing. For data rate and BER measurement with OFDM, the signal is generated with 250 MSa/s and 5 Sa/symbol. Hence, the resulting symbol rate is 50 MBd and the bandwidth of the signal is 25 MHz. This generated signal was passed through the analogue frontends and captured on the oscilloscope. A synchronization pulse as shown in Figure 6-11 is used to trigger the oscilloscope.

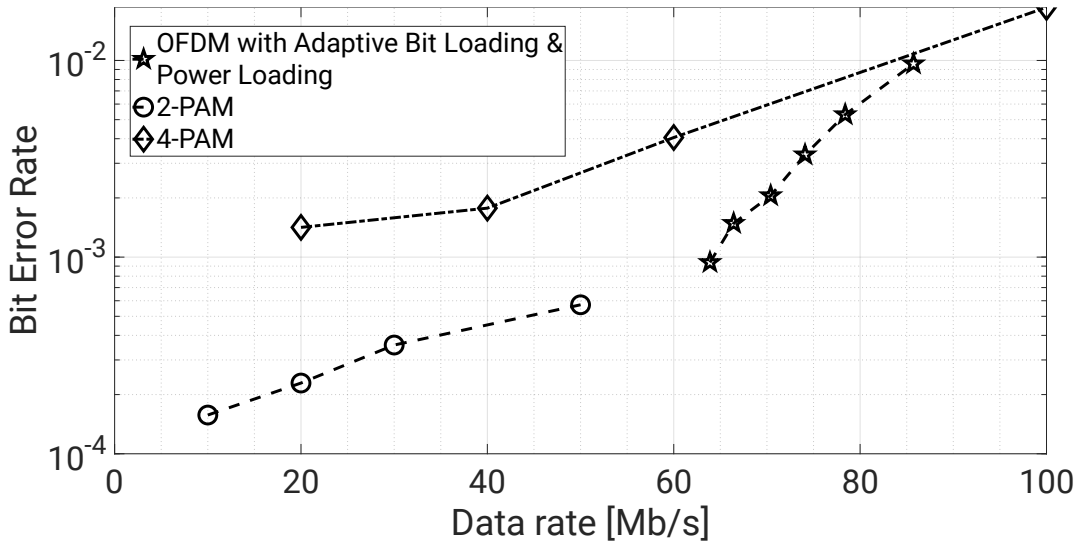

Figure 6-12: Comparison of data rate & BER for OFDM and PAM

The captured signal was then processed in MATLAB and the experiment was repeated for different targeted BERs. The data rate is estimated and plotted against the respective BER. Similarly, the experiment was repeated for PAM-DMT with 5 MHz, 10 MHz, 15 MHz and 25 MHz signal bandwidths for different modulation orders. The highest modulation order achieved is 4-PAM. 8-PAM or higher-order modulation could not be used due to the lack of sufficient SNR for the selected bandwidths. The measured data rate and BER for all the cases are tabulated in Table 6-1. Also, the data measurements are plotted in Figure 6-12 for comparison. Upon successful

completion of the experiment, the highest data rate achieved within the forward-error correction (FEC) limit is 74.03 Mb/s with a BER of 3.3×10^{-3}. The highest data rate that is achieved in the experiment is 100 Mb/s with 4-PAM, but the BER is 1.9×10^{-2}, which is over the FEC limit of 3.8×10^{-3} [77] and the erroneous data may not be recoverable. The additional results obtained from the experiment are the overall channel response and the estimated SNR as depicted in Figure 6-13 and Figure 6-14 respectively.

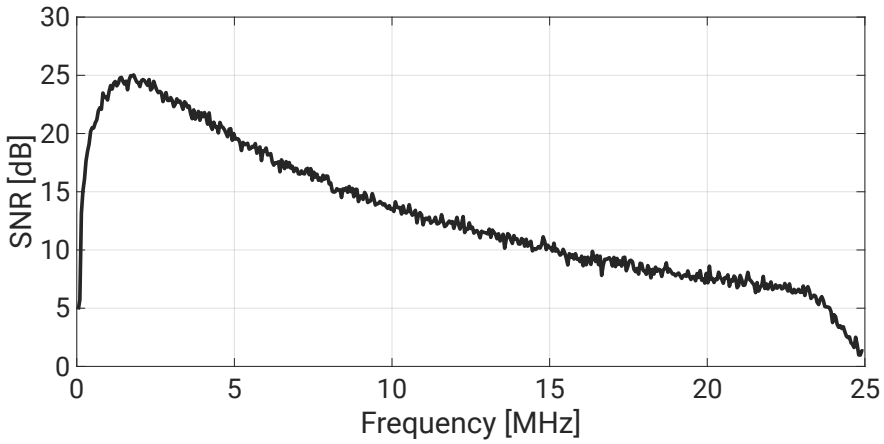

Figure 6-13: SNR estimation

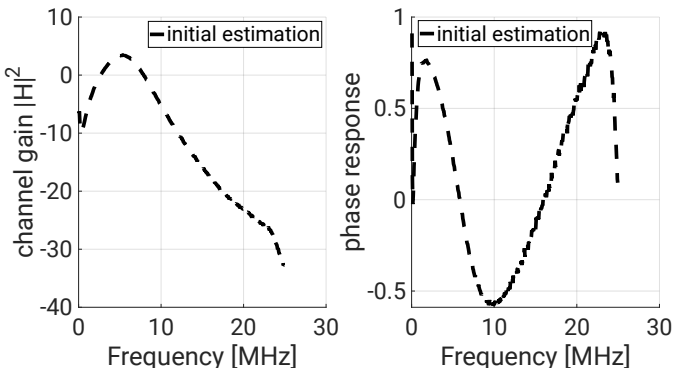

Figure 6-14: Channel response

Figure 6-15 and Figure 6-16 show that the adaptive bit and power loading has used the bandwidth efficiently. The subcarriers with an SNR below 10 dB are modulated with binary phase-shift keying (BPSK) while the subcarriers with

SNR higher than 10 dB are modulated using constellations from 4-QAM to 256-QAM based on the SNR thresholds for the respective modulation orders.

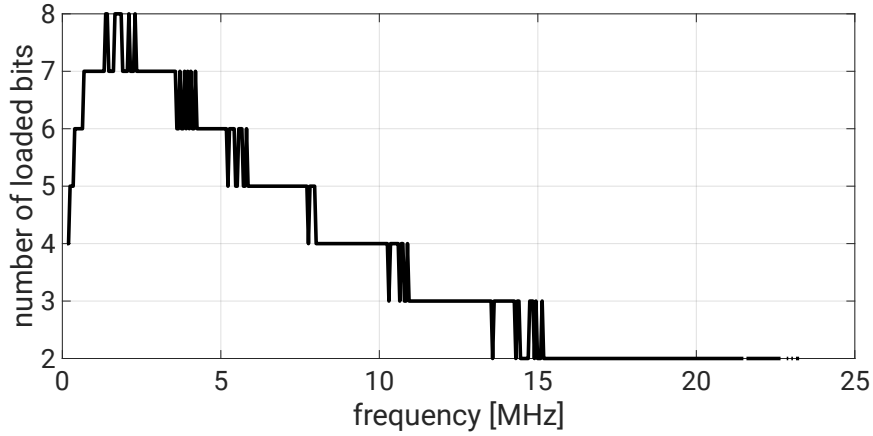

Figure 6-15: Bit loading

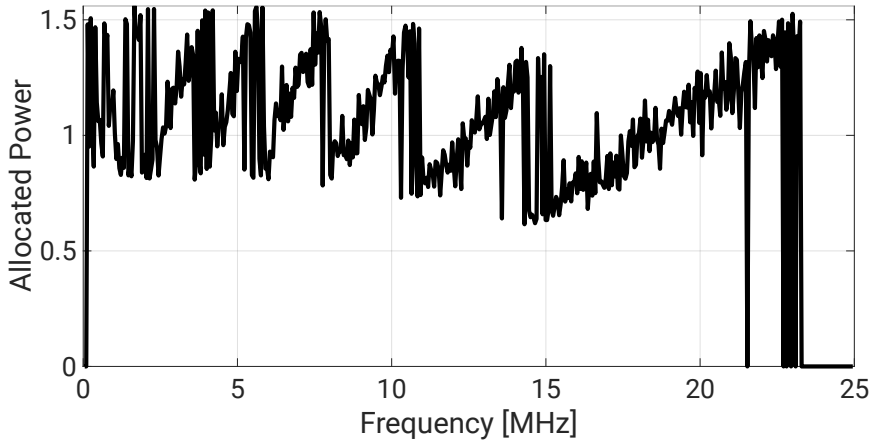

Figure 6-16: Power loading

Figure 6-17 shows the received signal's constellation diagrams for 256-QAM and 128-QAM. From the received signal's constellation diagrams, it can be qualitatively inferred that most of the signal bits were decoded. Further investigating Figure 6-13 and Figure 6-16, it can be seen that the high-frequency subcarriers between 15 MHz – 22 MHz have a gradual increment in power which is comparable to the roll-off in channel gain. The intermittent peaks in power allocation could be attributed to compensation for signal

harmonics. These harmonics could be generated by non-linearities in the signal chain amplifiers.

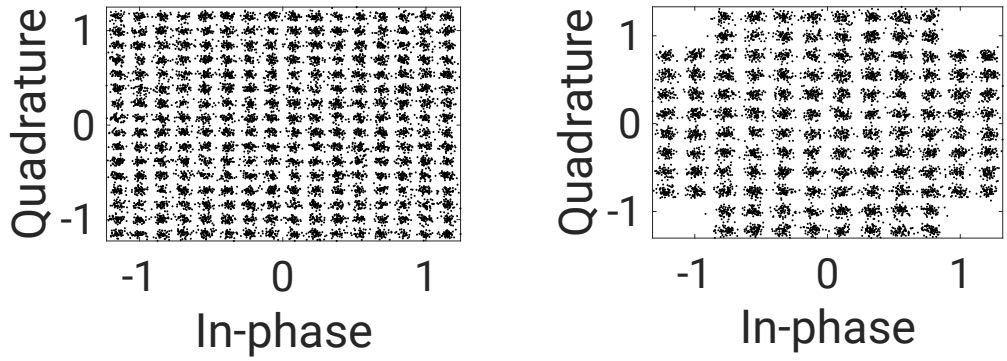

(a) *(b)*

Figure 6-17: Constellation diagrams (a) 256-QAM (b) 128-QAM

For PAM-DMT upon investigating Figure 6-13 and Table 6-1 it is noticeable that the BER is comparatively lower than OFDM. The performance of 2-PAM is highly robust over the whole bandwidth of 25 MHz achieving 50 Mb/s with a BER of 5.7×10^{-4} which is 6.6 times below the FEC limit [77]. On the other hand, for 4-PAM the maximum usable bandwidth is 15 MHz as the BER of 4×10^{-3} is on the limits of FEC [77]. From this, it can be concluded that PAM-DMT is favourable over QAM-OFDM when the system design is desired to be uncomplicated and link reliability takes priority over a high data rate.

Table 6-1: Data rate and BER measurements for PAM

Bandwidth (MHz)	Modulation Order			
	2-PAM		4-PAM	
	Data rate (Mb/s)	BER	Data rate (Mb/s)	BER
5	10	1.5×10^{-4}	20	1.4×10^{-3}
10	20	2.2×10^{-4}	40	1.8×10^{-3}
15	30	3.5×10^{-4}	60	4×10^{-3}
25	50	5.7×10^{-4}	100	1.9×10^{-2}

From Figure 6-12 it is clear that OFDM achieves significantly higher data rates than PAM-DMT. The lowest data rate achieved with QAM-OFDM is 63.89 Mb/s with a BER of 9.39×10^{-4} while the highest usable data rate with PAM-DMT is 60 Mb/s with a BER of 4×10^{-3}. This difference in data rate can be attributed to the added benefit of adaptive bit and power loading in OFDM. The pre-distortion introduced by adaptive power loading and the efficient use of subcarriers with high SNR enhances the data rate achieved. In PAM-DMT, the modulation depth is fixed for the whole bandwidth, even if the subcarriers between 500 kHz – 5 MHz have an SNR above 20 dB. As the PAM levels are not adaptively loaded. Thus, the maximum modulation depth that could be used is 4-PAM which is dictated by the subcarriers beyond 10 MHz that have SNR below 13 dB.

Hence, it can be concluded that to achieve high data rates with a BER that is lower than the FEC limit using a solar panel receiver, OFDM with adaptive bit and power loading is desirable, at the cost of system complexity. However, the use of PAM-DMT can be helpful in cases where link reliability and simple system design are the major requirements and high data rates are not so important.

6.2.1.4 Digital Signal Processing Platform

MityDSP-L138F was used as the DSP platform for the prototype. The firmware built for this platform was developed by pureLiFi. As the firmware was for a product that was designed to be used indoors, the firmware needed modification to adapt it for the point-to-point and outdoor link use case. In the firmware, DCO-OFDM was used for modulating the digital information and the QAM modulation order switching was dependent on the number of received packets decoded and dropped. Therefore, it was necessary to set the optimum threshold values for the number of successfully received packets to switch to the higher modulation level and the number of received packets dropped to

switch to the lower modulation level, to stabilize the link performance. By Brute-force, it was determined that for every 5 continuous successfully decoded received packets the modulation level had to switch to the higher modulation order. Similarly, for every 3 continuous received packets dropped, the modulation level had to be switched to the lower order. The link was stabilised using these threshold values. The DSP platform was capable of maximum 64-QAM at ¾ code-rate, and the lowest modulation level was BPSK over the maximum supported baseband bandwidth of 5 MHz. The maximum achievable data rate of the platform is 13 Mb/s over the cable.

6.2.1.5 Signal gain control algorithm

The channel varies continuously due to changes in ambient light, weather, wind and visibility, the laser driver circuit needs to precondition this analogue waveform. Hence, the control unit becomes crucial in order to maintain the link throughout varying weather conditions including cloud cover, rain and fog.

In long distance backhaul links, FSO systems use RF control channels or vice-versa to optimise the communication channel. The transmitter and receiver need to set appropriate gain settings with regards to the varying atmospheric conditions [78]. Although, the system described in this thesis, instead of using a separate channel for link optimisation, a link optimisation algorithm has been developed which maintains the link performance during its operation. The implementation of this link optimisation algorithm avoids the use of additional control channels and reducing the system complexity at the hardware level. The optimisation of the link is based on the feedback of the channel conditions, which is determined by the number of received packets dropped and ping time interval. When these two factors go above a given threshold, the optimum signal power search algorithm is triggered which is shown in Figure 6-18. In the Figure 6-18, variables RX_packets and TX_packets denote the number of packets received and transmitted respectively. Variables

deltaRX and deltaTX store the difference between the packets received and transmit before and after altering the signal power. The variable ping_state is a Boolean which depicts the availability of a bidirectional link. The signal power is varied in a cyclic order of low-high-low on both the transmitters at each end. There is a random back-off time between the transmitted signal power variation. This random back-off time is denoted as variable wait_time in the flow diagram. The transmitted signal is varied in steps of 0.5 dB from 0 dB to -31.5 dB. The transmitted signal power is stored as the variable counter. The random back-off time avoids the probability of varying the transmitted signal power on both ends simultaneously.

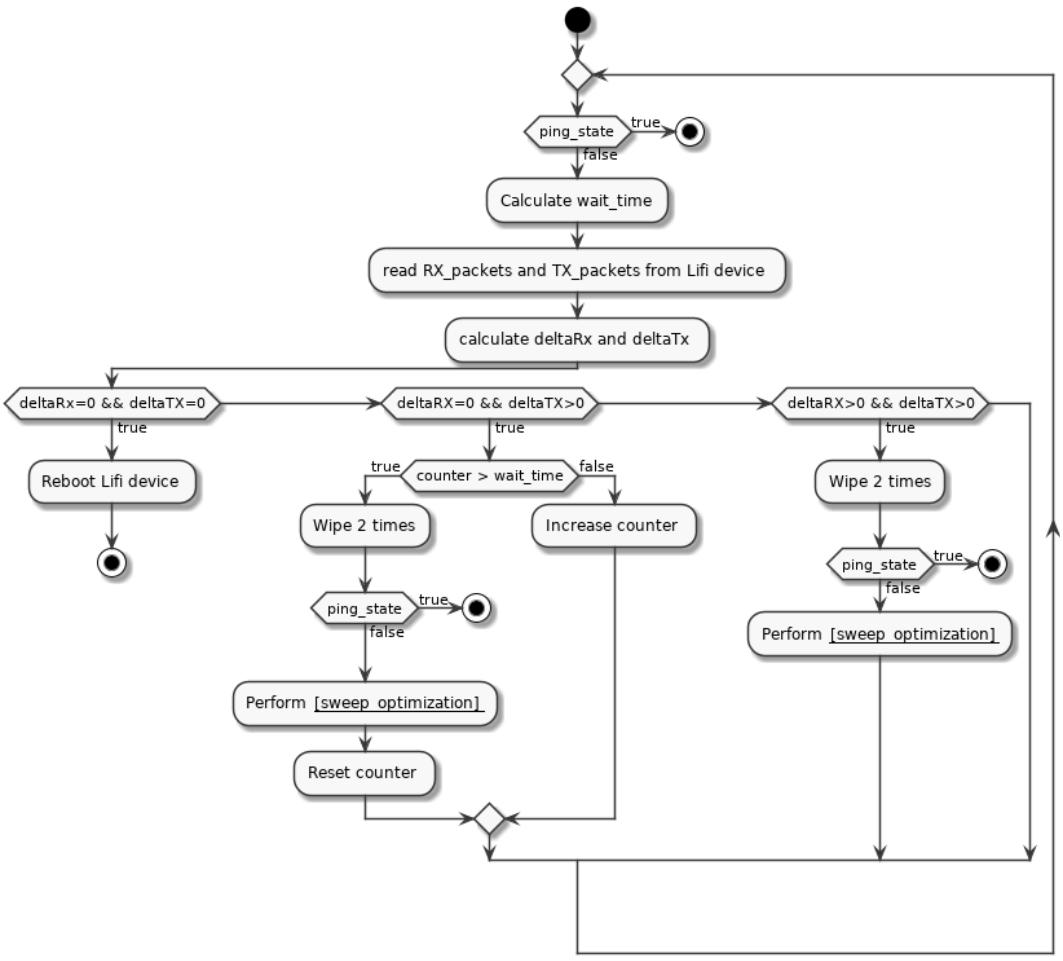

Figure 6-18: Link optimisation algorithm

Meanwhile, on both communication nodes, the received packets dropped, and the ping time interval is monitored. The final goal of the algorithm is to maximise the deltaRX and deltaTX while the ping_state is true, on both the transceivers.

Furthermore, due to the variation in temperature, the output optical power of the laser varies. Under cold weather conditions, the optical output power of the laser increases which may violate the maximum laser radiation recommended for eye safety. To control the optical output power of the laser, a temperature sensor was added to the design of the laser driver circuit. A temperature monitor and laser current bias control loop were added into the control software as shown in Figure 6-19. In the figure, variable T stores the temperature of the laser, and the variable Param-T is 25˚C. The optical output power of the laser is measured at 25˚C, under controlled laboratory conditions. This measurement is used as reference to set the laser bias current such that the system can track the laser's output optical current at different temperature. The software loop monitors the temperature and sets the corresponding bias current for the laser for the set optical output power.

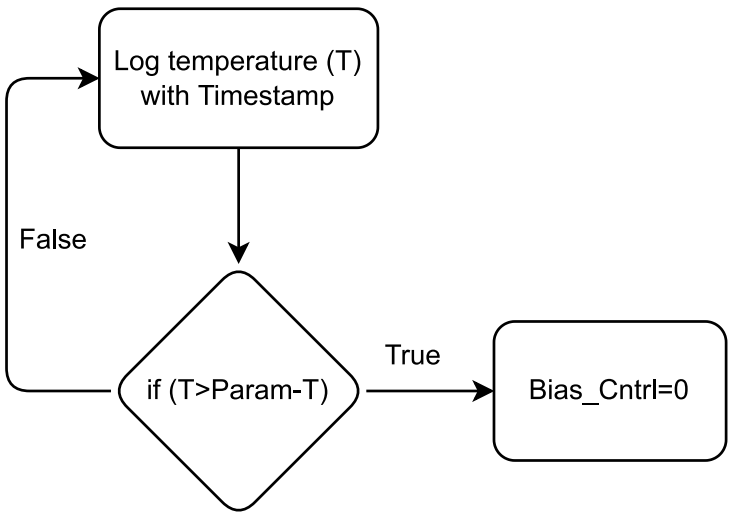

Figure 6-19: Temperature & laser bias control loop

6.2.2 Results and discussion

The developed FSO system was first deployed on the premises of the University of Edinburgh to test the communication performance under different daylight and weather conditions. The maximum distance achieved with this system was 80 metres with a maximum data rate of 6.5 Mbps. Although for the given application, the link distance was 30 m, the link was left unattended for two weeks to gather data for further investigation. Figure 6-20 shows the variation of the data rate of the link against varying wind speeds, visibility, daylight and weather conditions on a day.

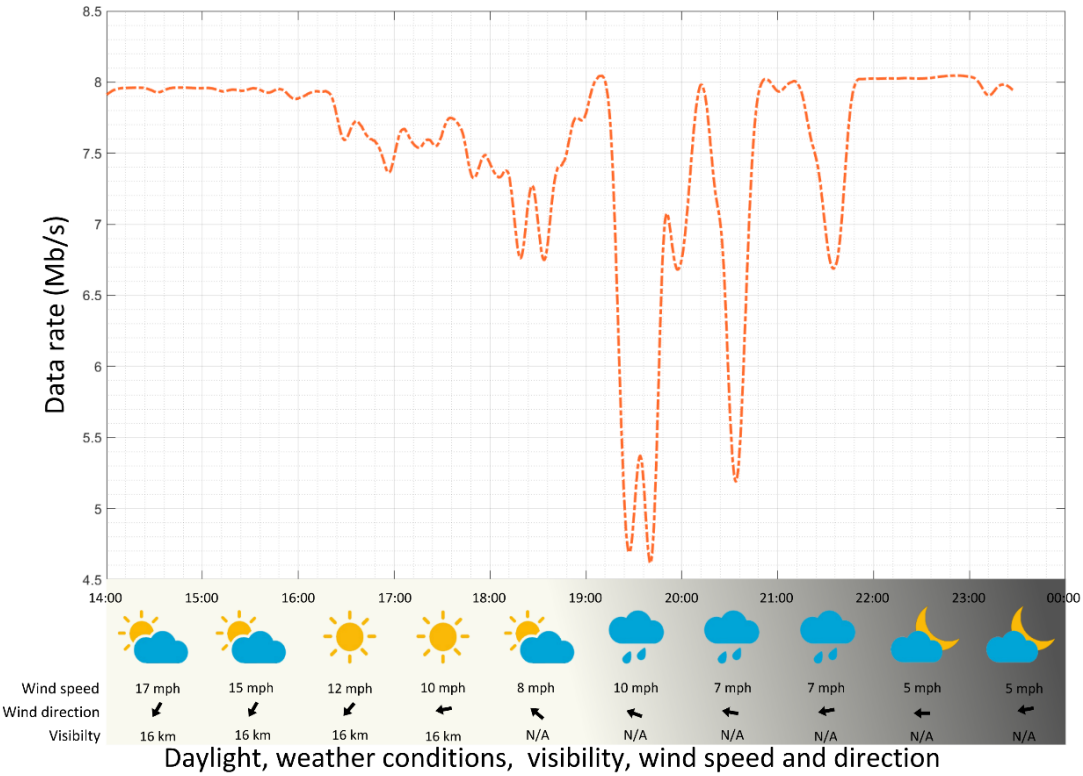

Figure 6-20: Data rate measurements plot against the daylight and varying weather conditions

The weather data were collected from [79] for 7th May 2019 in Edinburgh. The throughput measurement was done using iPerf [80] and the traffic was forced to TCP/IP to emulate real-world bandwidth usage. The data rate peaks at 8

Mbps at night-time with cloudy conditions. But during the sunnier parts of the day, the data rate dropped to 6.5 Mbps. This can be attributed to the additional thermal noise and shot noise generated in the solar panel when the sunlight hits the panel directly. In this scenario, the generation of exciton would be at its peak which increases the thermal and shot noise. The added noise induces a fall in the signal-to-noise ratio leading to a noticeable drop in the data rate. This aligns with the investigations performed previously in Chapters 3 and 4.

The next noticeable drop is during periods of rain, where the data rate dropped to the lowest level of 4.5 Mbps. This fall in data rate can be attributed to the bad channel condition due to the presence of rain droplets that attenuate the signal power received [57]. After the testing phase, the system was deployed in Graemsay, one of the Orkney Islands in northern Scotland. Figure 6-21 shows the installation of the units on the properties. A comparison between the installed optical link and the existing broadband connection shows that the upload speed increased by 8 times and the download speed increased by 20% (see Figure 6-25).

(a) *(b)*

Figure 6-21: Installation at the location (a) residence property (b) lighthouse to the residence property

The two links were aggregated and provided to the residents, thereby doubling the user download experience and enabling them to use higher bandwidth-demanding services such as streaming multiple high-definition

videos, high-definition video calls, etc. Furthermore, the installed link on one of the properties was monitored for four weeks to evaluate the system performance. The bandwidth usage and peak uplink-downlink speeds were measured along with the corresponding variation in transmitted signal power every 2 hours in a day. The CDF plots of accumulated data points are shown in Figure 6-22 and Figure 6-23.

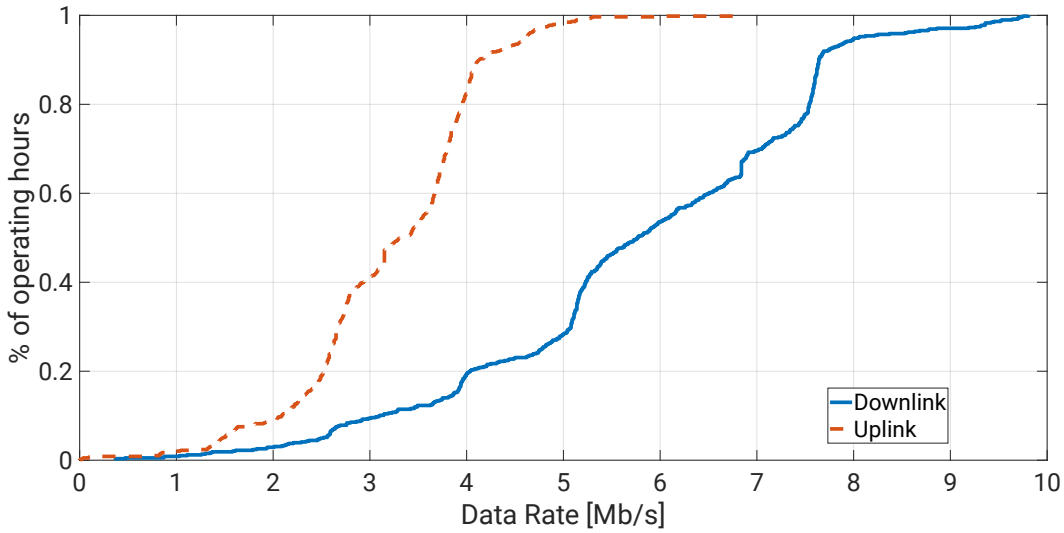

Figure 6-22: CDF of data rate variation

The peak download data rate measured is 10 Mb/s and 90 % of the operating hours the download data rate was around 8 Mb/s, while the upload speed being 5 Mb/s. From the CDF plot of TX signal power attenuation, it can be concluded that the control algorithm is successfully controlling the signal power to maintain the link and optimise the data rate. During most of the operating hours, the TX signal power was attenuated between 15 t0 20 dB. The system was certified to be eye-safe (Class 1M) for the maximum operating optical signal power output *i.e.*, at 0dB. Hence, this shows that the operating the distance of the system could be increased. Furthermore, the system can still operate under fog or rain conditions. Moreover, the temperature of the CPU and laser driver was also logged over the same duration, as shown in Figure 6-24. Furthermore, it can be seen that the communication performance

is independent of the temperature, which confirms the successful operation of the temperature and laser bias current control loop. The temperature of the laser was maintained around 33˚C and the temperature of the CPU was maintained around 40˚C.

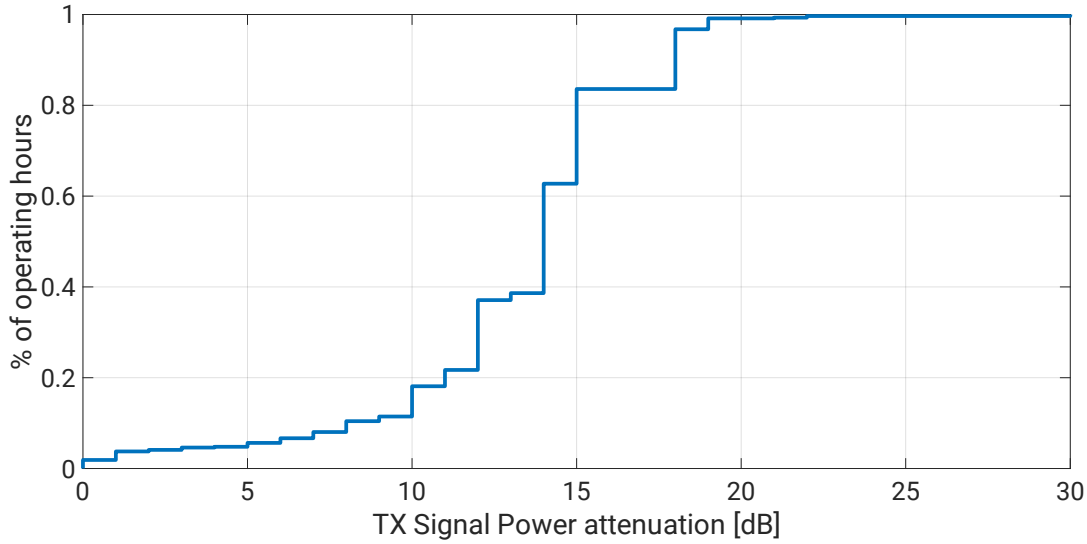

Figure 6-23: CDF of TX signal power variation

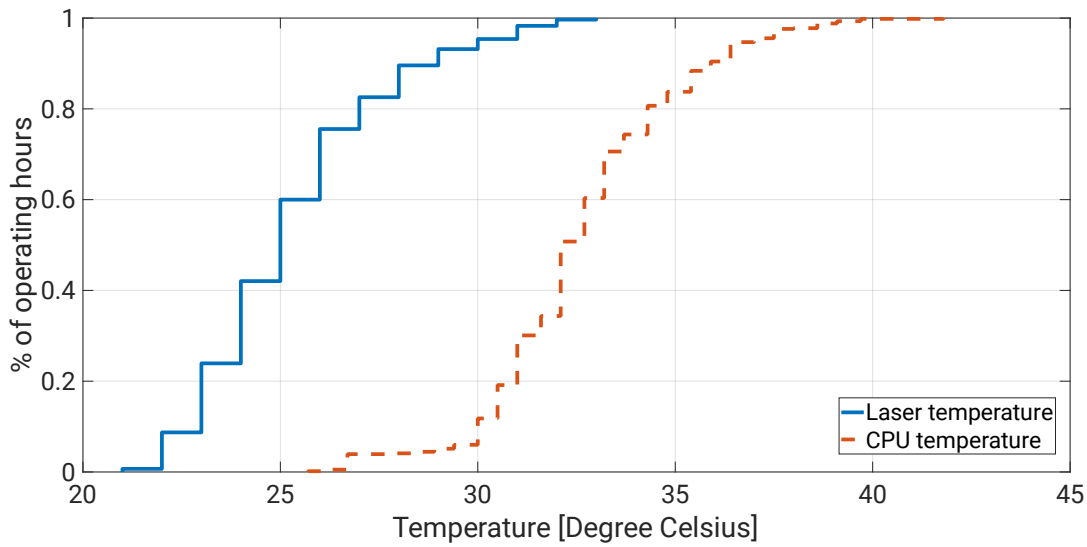

Figure 6-24: CDF of CPU & laser driver temperature variation

The data obtained shows no dropouts in the installed link and 90% of the time the data throughput was in excess of the existing landline-based

broadband connection. Figure 6-25 shows a snapshot of internet speed tests comparing the speeds through the optical link and the landline broadband.

(a)

(b)

Figure 6-25: Internet speed test measurements (a) through the optical link (b) through landline broadband

6.3 Demonstration II

The second demonstration was developed based on a military application. The system was envisaged to have a higher data rate and energy harvesting capability. It was designed for quick deployment, to be able to establish a node-to-node communication link, to be self-sufficient in terms of energy requirements and highly secured. Most of the objectives were already achieved in the first demonstration, such as an FSO link is inherently more secure than an RF link, as the likelihood for eavesdropping and signal jamming is not possible without being in the line of sight of the optical link. Furthermore,

the system was already designed mechanically in such a way that it was rapid deployment ready. Therefore, the main objective of this demonstration was to enhance the data rate throughput and demonstrate the simultaneous energy harvesting and communication capability.

6.3.1 System design

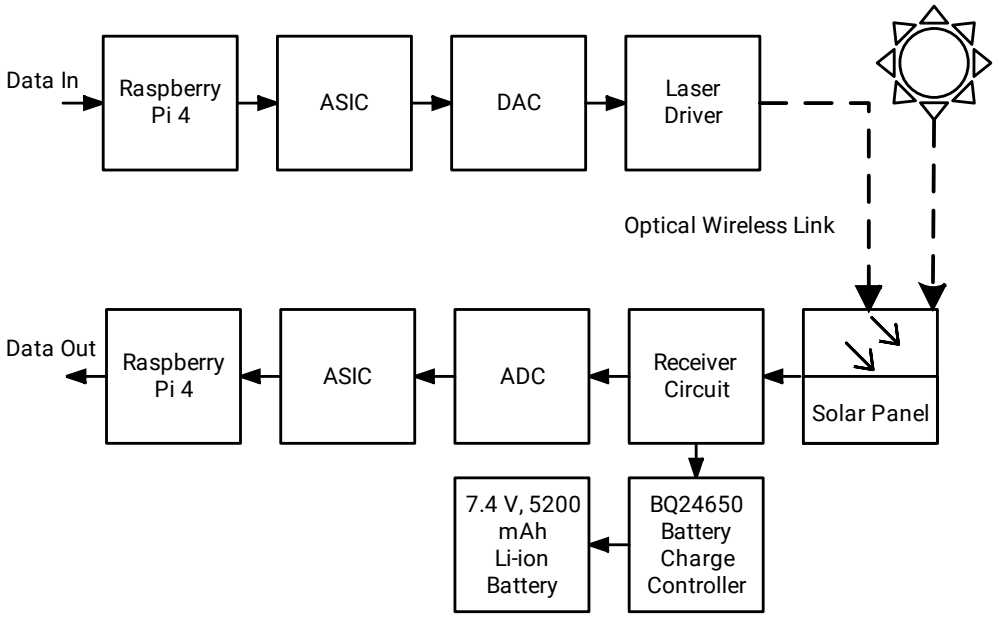

Figure 6-26: Version 2 prototype system architecture

This section explains the overall system architecture of the developed prototype, which is illustrated in Figure 6-26. In the previous prototype, the data rate throughput was limited by the supported baseband bandwidth of the DSP platform. Therefore, in this system, the DSP platform was upgraded to an ASIC based platform [43]. This ASIC was specifically designed by pureLiFi for the implementation of a DSP platform in LiFi systems, as previously mentioned in section 2.5. As the lower MAC layer and PHY layer functions were performed by the ASIC, the rest of the networking stack was implemented on the RaspberryPi 4 [81]. RaspberryPi 4 is a system on chip (SoC) that is based on an ARM8 processor. All the control algorithms and higher-level networking stack were implemented on this SoC. The ASIC supported a maximum

baseband bandwidth of 32 MHz; therefore the 18 MHz bandwidth variant of the receiver circuit along with the battery charge controller circuit and the Li-ion battery described in section 5.4, was chosen for this prototype. The schematics of the 18 MHz variants of the receiver circuit are provided in Appendix B. The rest of the transmitter design was carried forward from the previous version of the prototype as described in section 6.2.1.

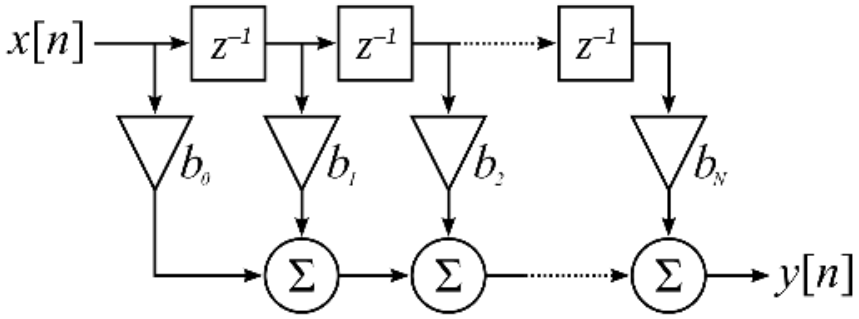

Figure 6-27: Direct form discrete-time FIR filter structure

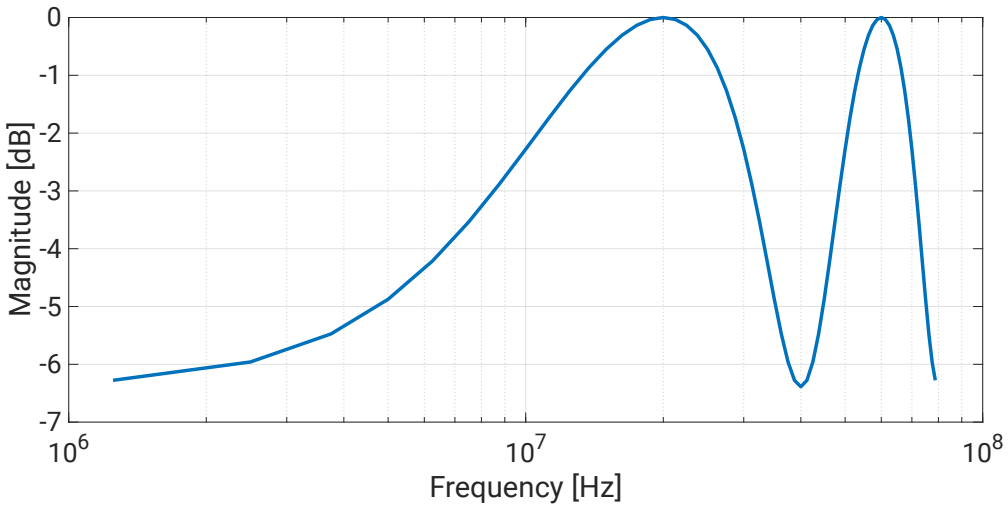

Figure 6-28: Magnitude response of the FIR filter

As shown earlier in section 6.2.1.3, adding pre-distortion helps to achieve a better performance in data communication. A direct form discrete-time Finite Impulse Response (FIR) filter was implemented to improve the

signal gain at the higher frequencies. The structure of a direct form discrete-time FIR filter is shown in Figure 6-27. The firmware for the ASIC could support only a 16-tap filter. Therefore, using MATLAB, the coefficients of a 16-degree polynomial were calculated, such that the slope of the resulting filter is 6 dB/decade [82]. The FIR filter consists of 16 taps with the following tap coefficients: [-5 0 0 0 -44 0 0 0 255 0 0 0 -44 0 0 0]. Furthermore, the magnitude response of the filter is shown in Figure 6-28. The magnitude response is plotted for a sampling frequency of 80 MSa/s, as this is the sampling frequency used in the DSP platform.

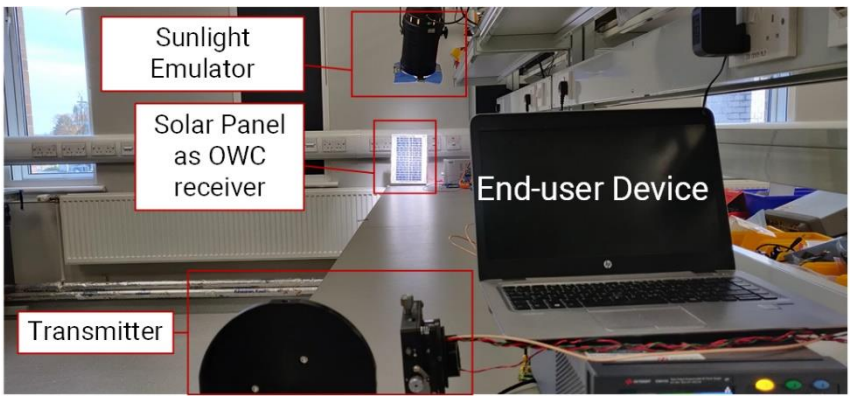

Figure 6-29: Lab test setup

Before deploying the system outdoors, the system performance was evaluated in the lab with a link distance of 4 m. The sunlight emulator developed in Chapter 5 was used to simulate the variation in sunlight and test the communication performance of the system while harvesting energy from the sunlight emulator. The lab setup for the system performance evaluation is shown in Figure 6-29.

6.3.2 Results and discussions

The second version of the prototype, after testing was deployed on the roof of the James Maxwell Clerk's Building, at the King's Building campus of the University of Edinburgh for further outdoor testing and system evaluation.

The evaluation was done with a link distance of 30 m, as shown in Figure 6-30. The main objective of this prototype development was to enhance data throughput and enable simultaneous energy harvesting and storage. Hence, Figure 6-31 shows the variation in the maximum TCP/IP throughput of the system against the variation in solar irradiation. The highest data rate achieved between the two end-user devices is 28.3 Mb/s while harvesting no power. Alternatively, the peak power harvested with a 5 W solar panel during a bright sunny day *i.e.,* with 1000 W/m^2 of solar irradiance is 4.5 W with a data rate of 6.34 Mb/s between the two end-user devices.

(a) *(b)*

Figure 6-30: Installation at the JCMB, King's Building, University of Edinburgh

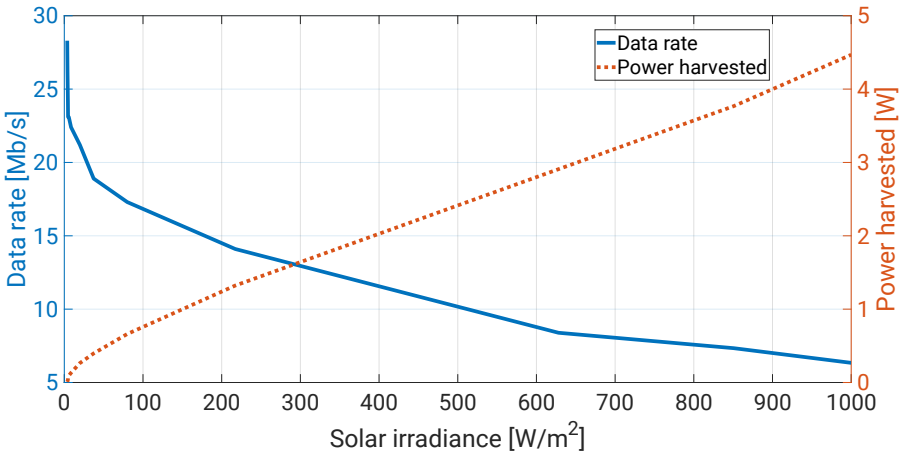

Figure 6-31: Variation in data rate with simultaneous energy harvesting

These results align with the results obtained in section 3.3. The decrement in data rate with the increase in solar irradiance follows the same trend as the frequency response and SNR plot shown in Figure 3-6 and Figure

3-8, in Chapter 3. From this plot, it can be deduced that there is a trade-off between communication and solar energy harvesting when a solar panel is used simultaneously for both. At 240 W/m^2 solar irradiance, there is an intersection of the data rate achieved and energy harvested. At this point, the achieved data rate is 13.7 Mb/s, and 1.6 W of power is harvested. Furthermore, it was measured that the peak power delivered to the 38 Wh Li-ion battery is 4.14 W, which aligns with the experimental measurements carried out in section 5.4.

6.4 Power consumption of the system

The PV-based FSO system is envisioned to be self-powered as it is capable of harvesting power from the sunlight and store in a Li-ion battery. Therefore, the power consumption of each sub-system needs to be considered carefully and optimised. The current prototype was designed with the intention to demonstrate the concept and enable further research and development. Therefore, the system consists of lot of test and logging features which makes the system power inefficient.

Table 6-2, depicts the peak power consumption of each sub-system in the prototype. The receiver circuit comprises of the solar panel interfacing circuit, analogue signal processing and equalization. In future, the power consumption could be optimised by using ultra low power amplifiers to design the circuit. The transmitter circuit consists mainly of the laser driver circuit. Out of the 3.75 W consumed by the transmitter circuit, the laser alone consumes 3.7 W. The only way to improve the efficiency of this sub-system is by reducing optical signal transmission losses, so that the optical power output of the laser could be reduced. The maximum power consumption depends on the clock rate and bandwidth usage. Therefore, without changing the part, the power consumption cannot be reduced at this stage. In the CPU, the power consumption could be drastically optimised by reducing the data

logging and measurement intervals. These features were implemented to gather study for further research.

Table 6-2: PV-based FSO system power consumption

Sr. No.	Sub-system	Power consumption
1.	Receiver Circuit	1.1 W
2.	Transmitter Circuit	3.75 W
3.	ASIC	2.75 W
4.	CPU	5 W
5.	Heater	2.5 W
6.	Cooling Fan	2 W
7.	Alignment Laser	0.5 W
Total peak power consumption		17.6 W

Heater, cooling fan and alignment laser are the accessories used in the prototype to enable its operation outdoors under extreme weather conditions. The alignment laser is a 50 mW optical power output 535 nm laser. This laser is used during the installation to align the prototypes. These lasers are not required during the normal operation of the FSO system. The total peak power consumption of the prototype adds up to 17.6 W. Out of which 12.6 W is consumed by the core functional system of the prototype. Currently, the system is capable of harvesting a maximum power of 4.5 W. Hence, in the future generations of the system with improved energy harvesting capability and more power efficient sub-systems the PV-based FSO system could be self-powered.

6.5 Summary

A state-of-the-art FSO system with a solar panel as a receiver was successfully demonstrated in this chapter. It was seen that the maximum data rate achieved with an off the shelf Si-based solar panel, under laboratory conditions, prior to this work was 15.03 Mb/s. In this chapter, it is shown that the maximum data rate that can be achieved under laboratory conditions is 74 Mb/s. Furthermore, it can be concluded that to utilize a solar panel as a receiver in an FSO system, OFDM should be the choice of modulation technique to achieve the highest possible data rates. However, where link reliability and system complexity are prioritised over data rate, PAM should be considered for such applications. Additionally, the design methodology of a fully functional FSO system using a PV as the receiver is provided. The maximum link demonstrated by the prototype was 80 m, with a user throughput of 7.5 Mb/s. Furthermore, the maximum user throughput achieved was 28 Mb/s with a link distance of 30 m, with the capability of harvesting a maximum power of 4.5 W and storing 4.14 W. The prototypes were IEEE 802.3 and IEEE 802.11 standard compliant which allowed interfacing with the end-user devices easily. The system performances were evaluated under real-world conditions and one of the prototype iterations was used to solve the issue of the digital divide between urban and rural places. Moreover, the prototypes exhibited a technology readiness level (TRL) of 6, which means the system adequacy has been validated in the relevant environment. A link optimisation algorithm was developed and implemented which could maintain the link performance throughout the prototype operation under varying weather and atmospheric conditions. With the help of this algorithm, the requirement of an additional control channel was avoided. Moreover, it was shown that the FSO system consumes 17.6 W and can harvest a maximum of 4.5 W. Therefore, the net power consumption of the system is 13.1 W.

Chapter 7 Building a high-speed solar panel data receiver

The application of PV panels in a wide variety of scenarios such as space technology, military applications, domestic usage, and self-powered pocket devices has been driving the research and development of PV technology. The research trend has primarily focused on lowering the manufacturing cost of solar cells, increasing efficiency and performance, and improving the reliability of PV technologies, in order to support the widespread deployment of electricity produced directly from sunlight. There has been very limited research on the building of customised solar panel from off-the-shelf solar cells to enhance the optical communication performance of a solar panel.

7.1 Introduction

The active area of the Si-based off-the-shelf PV panel plays a major role in both the communication bandwidth and the energy harvesting capability. The smaller the active area is, the larger the communication bandwidth is. On the contrary, the larger the active area is, the higher the energy harvesting capability is. In this chapter, the design of building a customised solar panel built from off-the-shelf PV sub-modules will enhance the overall system performance in terms of data throughput and power harvesting. The concept of wavelength division multiplexing (WDM) [83] is five decades old. This technique has consistently been used to enhance the data throughput of optical communication systems. The proposed design is based on WDM and the design has been tailored to maximise the energy harvesting function of a PV panel. Furthermore, a transmitter design has been proposed to complement the new receiver architecture. The transmitter design is again based on the concept of WDM, which is used in fibre optic communication.

7.2 Design of the custom-built PV receiver

As discussed in previous chapters, a solar panel constitutes of several PV sub-modules which are in turn built out of individual Si-based solar cells. The solar cells and PV sub-modules are interconnected using metal strips. These PV sub-modules can be separated and used individually for power harvesting and optical communication. A solar panel mainly comprises of solar cells, a back plate, frame and an optical window made out of glass. In this case, the interconnect of the PV sub-modules and the optical window are modified to enhance the communication performance of the solar panel.

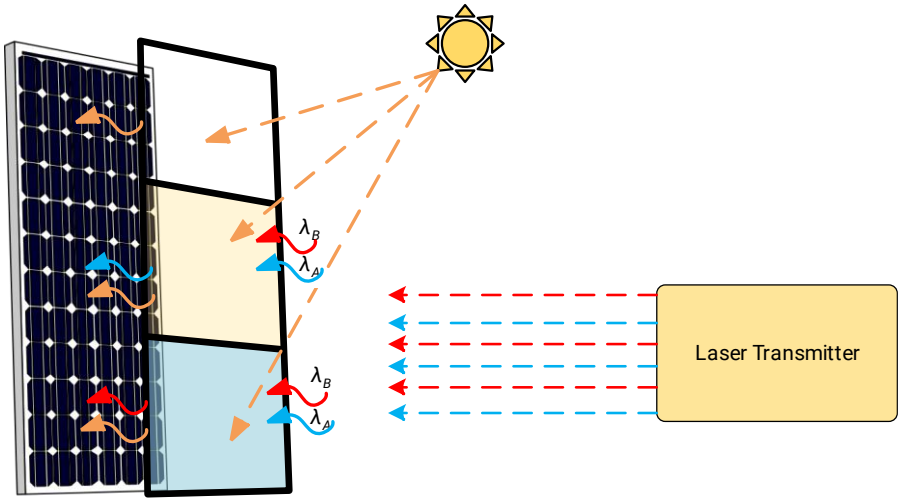

Figure 7-1: Construction of a custom solar panel [84]

Here, three 5 W PV sub-modules are used to construct a single solar panel and the optical window is modified as shown in Figure 7-1. One of the 5 W sub-modules is covered by an optical notch filter with a band blocking response at λ_A. The second sub-module is covered by another notch filter with a band blocking response at λ_B. The third sub-module is covered with plain glass. The PV sub-module, which is covered by a λ_A notch filter, can receive optical wavelengths from the entire spectrum, with the exception of λ_A. Similarly, the sub-module covered with λ_B cannot receive any optical power at

λ_B wavelength. The third PV sub-module can receive optical power from the entire optical spectrum just as a conventional solar panel normally does. In this way, the solar panel has been enabled for WDM at λ_A and λ_B, without significantly compromising the energy harvesting capability of the two sub-modules which are covered by the notch filter. The two PV sub-modules can harvest energy from the entire solar spectrum except at the wavelengths centred around λ_A or λ_B. The third PV sub-module is used for the sole purpose of energy harvesting and will not contribute to the data communication function. This way the solar panel-based receiver design is scalable in terms of energy harvesting and communication performance. The communication performance of the system could be increased by increasing the number of wavelengths used in the system. Similarly, the more the number of solar panel sub-modules, the higher the total power harvested by the system.

An optical notch filter is designed to block a pre-selected wavelength region or bandwidth while transmitting all other wavelengths within the design range of the filer. There are different methods to design and manufacture optical notch filters, however, the two most common methods widely used in the optics industry are the dielectric stack method and the Rugate method [85]. In the dielectric stack method, simple filters are stacked using a series of thin discrete layers of dielectric materials, of alternating refractive indices. This method is very economical but suffers from the presence of harmonic structures, which can severely limit the transmission band. In the Rugate method, the notch filter is constructed using a single thin layer of film in which the refractive index varies continuously with the position in a direction perpendicular to the substrate plane. This design eliminates the issue of harmonic structures caused by the dielectric stack method. Therefore, the filters manufactured using the Rugate method yield a high transmission range free from harmonics. Furthermore, the process allows the filters to have deep blocking bands as well as a high degree of reflectivity at wavelengths within

the notch [85] [86]. Furthermore, these optical coatings can be done on Indium Tin Oxide (ITO) coated glass [85]. ITO is a good conductor of electricity and typically used for RFI shielding in electronics with displays [85]. As discussed previously, the metal strips connecting the solar cells act as an antenna and can receive Amplitude Modulated (AM) radio signals. Using the metal frame and the ITO optical window a Faraday cage can be constructed to block the RF signals. These custom-designed filters with an ITO coating can be manufactured to the dimension of the PV sub-module's active area.

As the optical data signals have been separated optically, now each sub-module needs to be interconnected through an electronic circuit such that the AC signal generated by the individual sub-modules can be processed separately. The interconnection of the sub-modules is shown in Figure 7-2.

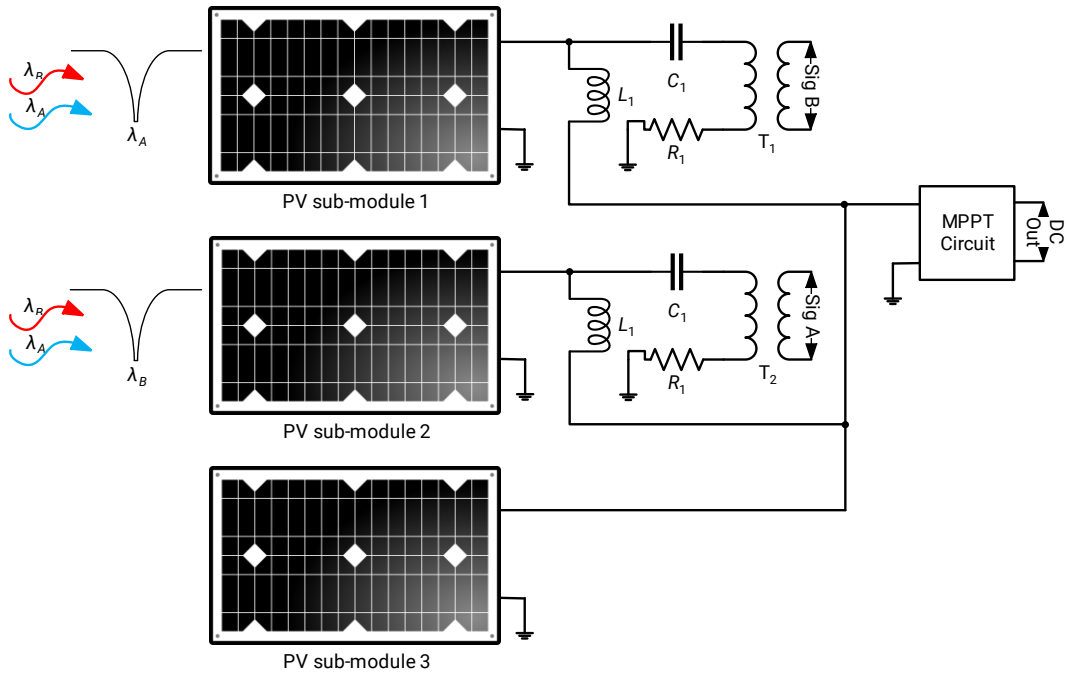

Figure 7-2: Design of a high-speed solar panel-based optical receiver

The PV sub-module 1 receives λ_B and sub-module 2 receives λ_A. The rest of the electronics and DSP stages remain the same, as developed in the previous chapter for data communication. As sub-module 3 is not used for

communication, therefore only its DC branch is connected to the MPPT circuit. The MPPT circuit used here is the same as discussed in Chapter 5. Due to the optical coatings, each sub-module would receive different solar spectral irradiance, which would affect the energy harvesting performance.

The energy harvesting and data communication performance of the custom PV panel was estimated using some experimental data and simulations in MATLAB. The λ_A was chosen to 785 nm and λ_B was chosen to be 980 nm. These wavelengths were chosen for the following reasons:

a. These are typical values of wavelengths available for off-the-shelf lasers.
b. The responsivity of Si-based solar cells peaks between around 800-1000 nm, as discussed in Chapters 3 & 4.
c. The eye safety limitation of NIR wavelengths is relaxed compared to the visible wavelengths of the optical spectrum [8].
d. These are the typical values of optical notch filters available readily in the market [87].

The optical transmission of 785 nm and 980 nm were obtained from an optical component manufacturer and supplier [87]. The AM 1.5 Global solar spectrum data was obtained from the National Renewable Energy Laboratory [88]. The AM 1.5 G is the standard solar spectra defined by the American Society for Testing and Materials. This solar spectra data is predominantly used for commercial terrestrial PV applications. The optical transmission and the AM 1.5 G solar spectral irradiance are shown in Figure 7-3. Using the optical transmission data of the notch filters, the solar spectral irradiance received by each PV sub-module was estimated and shown in Figure 7-4. Furthermore, the typical spectral response of a Si-based polycrystalline solar cell is also shown in Figure 7-4 [13]. The responsivity of the solar cell determines the part of the solar spectra responsible for the photo-current generation.

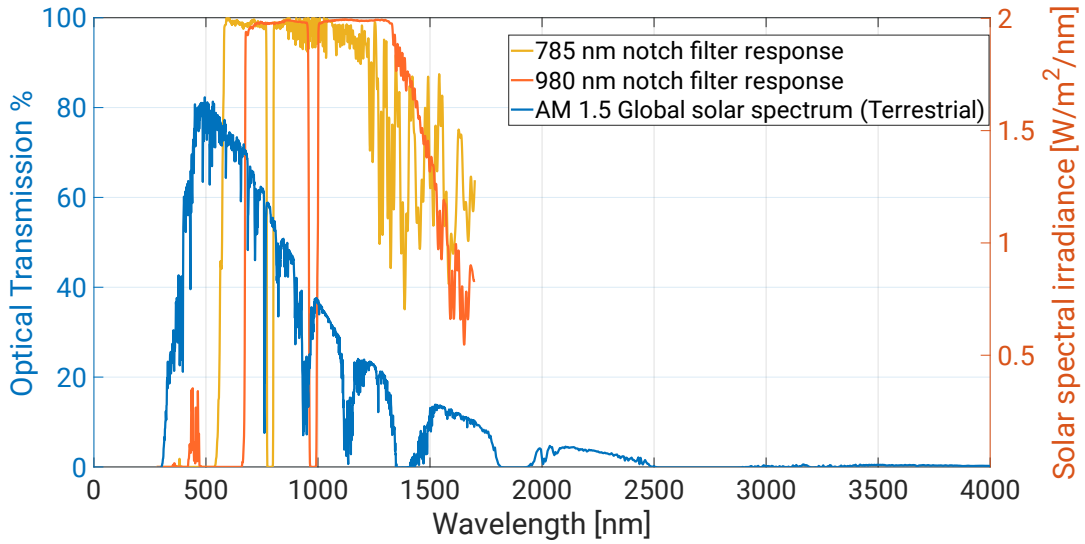

Figure 7-3: Notch filter response and terrestrial solar spectrum

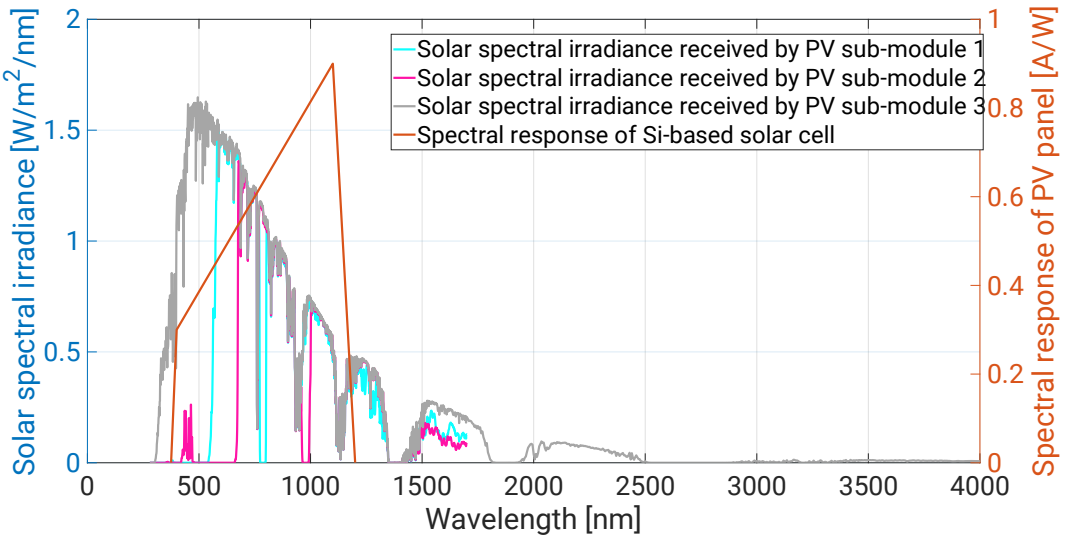

Figure 7-4: Solar irradiance received by the PV panel and spectral response of Si-PV cell

The area under the curves of the solar spectral irradiance is the maximum optical power that will be received by each PV sub-module. The maximum solar power that can be captured by each PV sub-module was calculated and shown in Table 7-1. The maximum solar power received by PV sub-module 1 and PV sub-module 2 are limited by the currently available designs of notch filters.

Table 7-1: Total solar power received by each PV sub-module

	Solar power incident (in W)
PV sub-module 1	581.74
PV sub-module 2	451.98
PV sub-module 3	1000

A simulation was carried out based on the data obtained from the experiment conducted in section 6.3. The data rates were estimated for the varying solar irradiance for the proposed design of the solar panel. The data rate variation was estimated according to the DC current generated by the solar panel. The relation between the solar irradiance emulated by the sun simulator and the photo-generated current is shown in Figure 7-5. Using this plot and the spectral response of a typical Si-solar cell, the power harvested by each PV sub-module was estimated. Furthermore, in the experiment, the optical transmitter used 940 nm, therefore for 785 nm and 980 nm, the optical power was adjusted according to the responsivity of the solar cell.

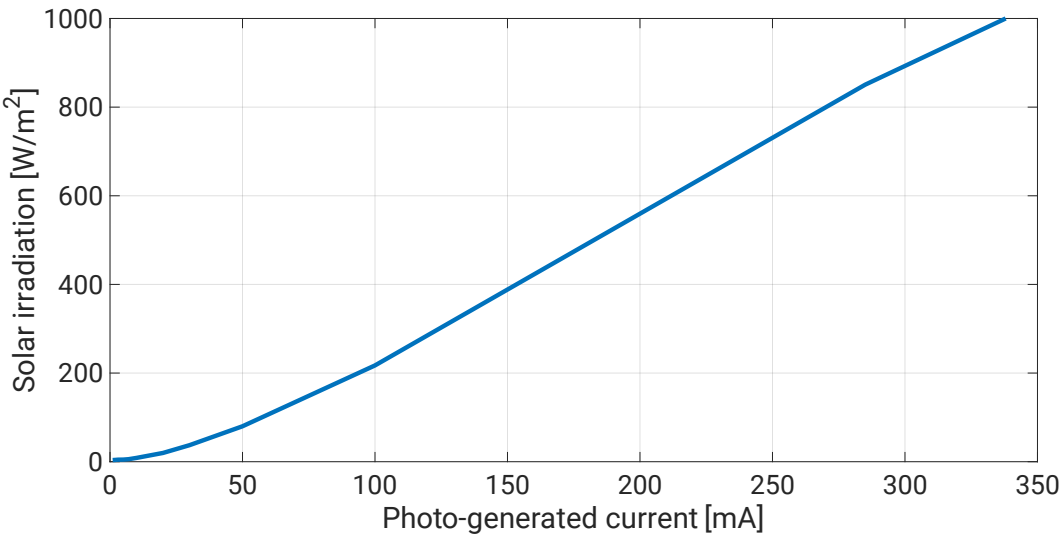

Figure 7-5: Relation between photo-generated current and solar irradiance

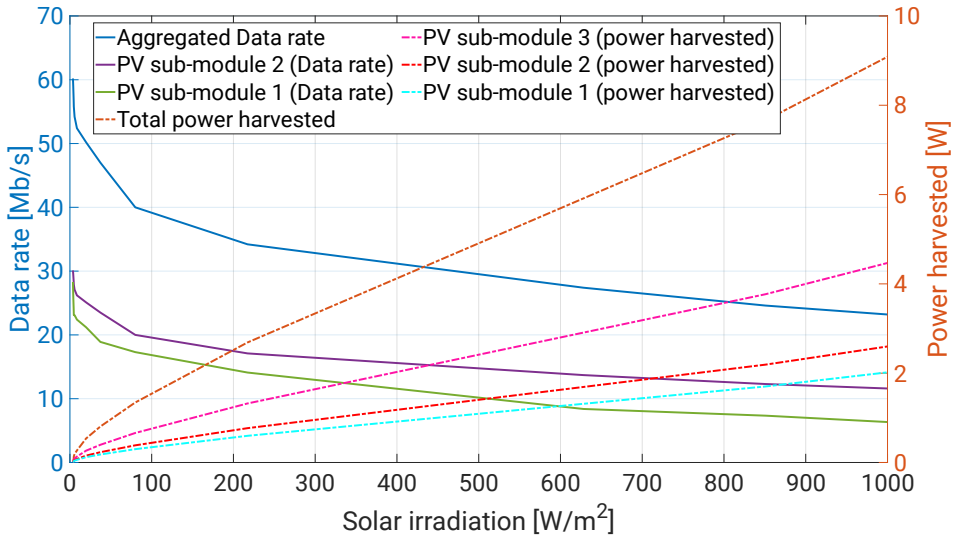

Figure 7-6: Aggregated data rate for two links and total power harvested by the custom PV panel

It was shown in section 4.2 that there is no variation in the communication bandwidth of the panel due to a change in wavelength. Hence, a similar performance could be expected with different wavelengths. The individual and aggregated data rate of the 980 nm and 785 nm links were plotted against the varying solar irradiance as shown in Figure 7-6. The simultaneous energy harvesting performance of the system is also depicted in Figure 7-6. Also, it can be seen that the communication performance for the PV sub-module 2 is slightly better than the sub-module 1 because the solar power incident on the sub-module is lower than the sub-module 1. The peak user throughput achieved by PV sub-module 1 and 2 are 29 Mb/s and 31 Mb/s respectively. The peak power harvested by PV sub-module 1, 2 and 3 are 2.7 W, 2.1 W and 4.5 W respectively. As discussed previously in chapter 3, the higher solar power incident affects the frequency response and SNR of the sub-module. From the figure, it can be concluded that with the new design of the PV panel the maximum data rate and the maximum power harvesting has been doubled, compared to the previously developed PV based FSO system, discussed in Chapter 6. Also, the user data rate was estimated based on an IEEE 802.11 based DSP platform. In IEEE 802.11 systems, the MAC layer

overheads are estimated to be 45 % of the total packet length [89]. Therefore, the raw throughput of the proposed system is 1.818 times the data rate shown in Figure 7-6. In order to achieve this increment in the performance, the total active area of the receiver has been increased to three times the PV receiver used in the FSO prototypes. Moreover, the way the PV sub-module 3 has been connected, more solar panels or sub-modules could be connected in the same manner to increase the energy harvesting capability without affecting the data communication performance. The only limitation of adding more panels would be the electrical power input handling capacity of the MPPT circuit, which is a maximum of 280 W [64].

7.3 Proposed modifications in the transmitter

The estimations given in the previous section were based on the choice of wavelengths available for an off-the-shelf laser. Those wavelengths were chosen so that a single transmitter optics could be used for optical signal transmission over long distances. The easiest method to achieve WDM over a single optics is by mixing the two wavelengths using a wideband multimode circulator (WMC) fibre as shown in Figure 7-7. The optical circulators function in the same way as an RF circulator. The technical specification of an off-the-shelf WMC is provided in [90]. Furthermore, the use of WMC opens up the possibility to use butterfly packaged lasers, which are inherently designed for high bandwidth [91] and high optical power output as they are meant to be used in long-distance and ultra-high-speed fibre optic communication.

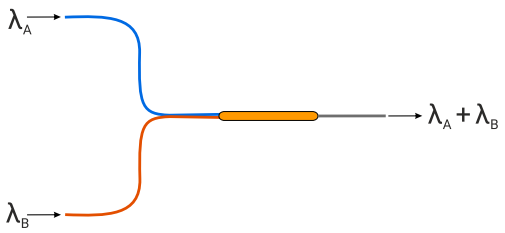

Figure 7-7: Wideband multimode circulators for wavelength division multiplexing

The second advantage of using a fibre-coupled laser source is that the beam profile from the aperture of a laser could be a flat top or Gaussian distribution [92] [93]. The main advantages of a Gaussian beam distribution are the following:

a) Gaussian beams have a Gaussian intensity profile at any location along the beam axis; only the beam radius varies.
b) A Gaussian beam remains Gaussian also after passing simple kinds of optical elements such as lenses with optical aberration [94].

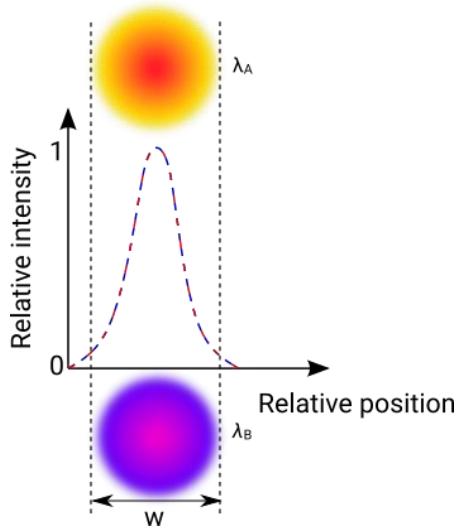

Figure 7-8: Gaussian beam

Additionally, having a uniformly distributed and large beam profile is desired for eye safety regulations [8] and optimum for data communication performance as described previously in section 4.2. Also, the optical output from a multimode (MM) fibre is circular [92]. When a circular beam is focused, the spot size is larger than the spot size of a focused elliptical beam [95]. Larger spot sizes have lower irradiances. Hence, relaxing the eye-safety requirements. Therefore, higher total optical power could be transmitted.

Gaussian circular irradiance profiles are symmetric around the centre of the beam and decrease as the distance from the centre of the beam

perpendicular to the direction of propagation increases [95], as shown in Figure 7-8. However, this irradiance profile does not stay constant as the beam propagates through space [94]. Hence, the waist of the Gaussian beam is dependent on the distance from source. The waist of a Gaussian beam is defined as the location where the irradiance is $1/e^2$ (13.5 %) of it's maximum value. In Figure 7-8, the waist of the Gaussian beam is depicted by *w*. Due to diffraction, a Gaussian beam will converge and diverge from an area called beam waist (w_0) [95], which is where the beam diameter reaches minimum value. The beam converges and diverges equally on both sides of the beam waist the divergence angle θ. The beam waist and divergence angle are both measured from the axis. The relationship between beam waist and divergence can be seen in (35).

$$w_o = \frac{\lambda}{\pi\theta} \tag{35}$$

The divergence half-angle of a MM fibre can be calculated from the numerical aperture (NA) using the relationship (36), where n is the refractive index of the medium. The MM fibre circulator proposed here has a NA of 0.22 [90]. Therefore, the divergence half-angle is calculated to be 0.2218 rad.

$$\mathrm{NA} = n \sin\theta \tag{36}$$

Using (35), for 980 nm and 785 nm, the beam waist radius is estimated to be 1.42 µm and 1.14 µm.

To further increase the directivity of the beam the on-axis parabolic (OnAP) mirror Edmund Optics 32-065-522 [96] with a diameter of 108 mm is selected for collimating the optical beam from the aperture of the MM fibre. The MM fibre aperture needs to be placed at the focus of the OAP mirror. The effective focal length of the mirror is 444.5 mm [74]. From the beam divergence angle the beam radius at 444.5 mm is estimated to be 97.6 mm.

As the mirror is 108 mm, the beam will almost fill the aperture of the mirror. Using Zemax, the beam profile at 1 km from the source was simulated as shown in Figure 7-9. In the beam profile, it can be seen that there is obscuration at the centre of the beam due to the MM fibre connector being placed in the optical path, as this is an on axis parabolic mirror.

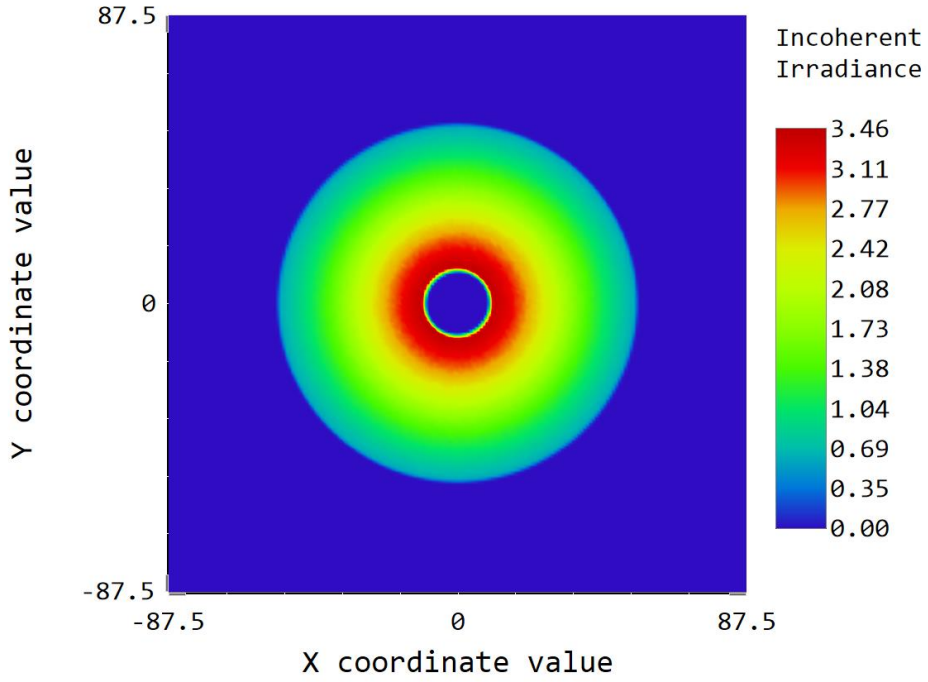

Figure 7-9: Beam profile at 1 km simulated using Zemax

In the simulation, 200 mW was transmitted, and 143.1 mW was received. The peak irradiance was estimated to be 3.46 mW/cm^2. This is calculated for a single wavelength. For both 980 nm and 785 nm the power will be doubled. Therefore, the total peak irradiance will be 6.92 mW/cm^2, which is more than 3.2 mW/cm^2 [8]. Hence, the proposed system fails to be classified as class 1 but can be classified as class 1M as the total power is less than 500 mW and the source is an extended optical source with an aperture greater than 100 mm [8]. Therefore, the system is eye safe unless until the beam is directly observed through optical aids such as telescopes, binoculars, *etc.*

7.4 Summary

A novel design for a custom-built solar panel has been proposed in this chapter. The design exploits the advantages of WDM to enhance data communication performance and energy harvesting capability. Using previously generated experimental data sets and simulations, it was estimated that, with the proposed PV receiver design, a maximum raw throughput of 109.1 Mb/s could be achieved. The maximum power harvested with this design was estimated to be 9.1 W, additionally with the option to expand the energy harvesting capability by attaching more PV panels or sub-modules to the MPPT circuit up to 280 W of input power from the solar panels. This improvement in power harvesting capability of the system bridges the gap in self-powering the whole system, as the peak power consumption of the system was calculated to be 17.6 W. Previously, with a 5 W Si-based solar panel the maximum data rate achieved was 74 Mb/s while harvesting zero power. With the new design the same 74 Mb/s can be achieved while harvesting 2.1 W of solar power. Moreover, a potential design roadway has been proposed for the transmitter which would complement the custom-built PV panel. The main advantage of this optical transmitter is that multiple wavelengths can be transmitted using single collimation optics up to a distance of 1 km. The maximum number of wavelengths that can be used with this setup will be limited by the eye safety restrictions. Furthermore, the optical setup is more efficient in optical power transmission over long distances compared to the previously used optical setup by 20%.

This page has been left blank intentionally.

Chapter 8 Conclusions, limitations and future work

In this thesis, the main objective was to explore the use of Si-based off-the-shelf solar panels as high-speed FSO receivers. However, the research focused on using solar panels as optical data receivers. Therefore, the latest generation of solar cells was not considered in the study. The investigation was primarily focused on enabling the use of cheap and readily available PV panels as optical data receivers with simultaneous solar energy harvesting using analogue electronics. Using an analytical model of a solar cell and experimenting with the solar cell under various scenarios, the optimum configurations are shown in this work to achieve the maximum possible data throughput. Furthermore, the trade-off between the data communication performance and energy harvesting capability of a panel was studied in detail. With the help of the results obtained from the analytical model and experiments, a prototype was developed and demonstrated to solve a real-life problem in our society. The application was not limited to only a backhaul link for remote residential properties, the potential of the application of the technology was also demonstrated in military communication. During these demonstrations, several engineering challenges were faced. Thus, the design of a custom-built solar panel is provided which mitigates these issues and enhances the overall communication and energy harvesting capability of the system. The research outcomes in this study can be extended to recent generations of solar cells to achieve comparatively higher data throughputs and better solar power harvested numbers. As the solutions proposed in this work address the issues faced with any optical receiver when operated under the photovoltaic mode, *i.e.*, forward-biased mode.

8.1 Conclusions

Chapter 2 in this thesis, describes the prior state-of-the-art demonstrations of Si-based and other solar cell technologies as FSO communication receiver. Additionally, the relevant background information that the rest of this thesis is based on is provided in this chapter. The main objective is to lay the foundation for free space optical communication systems and their technical details.

In the third chapter, an analytical model of the solar panel is discussed. Using this model, the characteristics of a solar panel, when used as an optical data receiver, are estimated. The model helped to study the following characteristics of the PV panel: optical sensitivity, speed of response, linearity, modes of operation, temperature stability, and noise performance. Moreover, a double diode model was used, for the first time, to estimate the trade-off between solar energy harvesting and data communication performance. It is shown that the estimations using a double model are more accurate and closer to the practical results. The analytical study also highlights the basic issue of every optical receiver when used under the forward biased condition *i.e.*, the relation between the diffusion capacitance and the voltage across the device. In addition to this, it was also found that the noise performance of the receiver deteriorates when subjected to high solar irradiance for energy harvesting. Ultimately, these factors explain the trade-off between peak power harvesting and peak data throughput numbers.

The theoretical study carried out in Chapter 3 was verified experimentally in Chapter 4 by subjecting the solar panel under varying conditions. Furthermore, the operation of a solar panel was studied and compared under photovoltaic and photodiode mode. Furthermore, it is shown that if a higher data rate is prioritised over energy harvesting, then the solar panel could

operate under the reverse-bias condition to improve the responsivity and communication bandwidth.

Besides, verifying the analytical study, the experiments with PV panels paved the design pathway for extracting the maximum possible communication bandwidth out of an off-the-shelf solar panel. The following design considerations must be included in a PV-based FSO system to achieve the best possible data rate: the transmitter wavelength should be considered around the peak responsivity of the material of the solar cell; the transmitted optical beam should cover the whole active area of the panel uniformly; the panel with the smallest size of solar cells should be considered.

In the fifth chapter, a receiver circuit was designed for the solar panel to extend its communication bandwidth, enable simultaneous energy harvesting and storage, and interface it with the DSP platform. Using analogue equalization, the -3 dB communication of the solar panel was stretched to 18 MHz from the inherent -3 dB bandwidth of 270 kHz. Additionally, different methods of interfacing the solar panel with the receiver circuits are proposed. The advantages and disadvantages of each method are also discussed. In the receiver circuit, the design of an MPPT circuit was included to achieve maximum solar power harvesting efficiency. The efficiency of the energy harvesting, and storage circuitry was measured to be 92.7%. The harvested power was stored in a 38 Wh Li-ion battery. Finally, some additional analogue signal conditioning was incorporated into the receiver circuit design to filter out the noise and prepare the signal for the DSP platform.

The world's first PV-based FSO system's design methodology and test results are discussed in the sixth chapter. The FSO system demonstrated a user throughput of 7.5 Mb/s over a distance of 80 m. With subsequent improvements, the maximum user throughput was increased to 28.3 Mb/s with simultaneous power harvesting of up to 4.5 W. Compared to the previous

state-of-the-art experiments, the maximum data rate that could be achieved using an off-the-shelf Si-solar panel was demonstrated in this chapter. The maximum data rate that was measured with this system under laboratory conditions was 74 Mb/s. The prototype was also used to provide internet connectivity to the residents of a remote island in the northern part of Scotland. Moreover, a link optimisation algorithm was developed and implemented which could maintain the communication link performance at its peak throughout its operation under varying weather conditions.

The idea of building a high-speed solar panel data receiver is proposed in the seventh chapter. The idea relies on the concept of WDM to increase the maximum data rate and the maximum power harvested. Also, the added notch filters on the PV sub-modules do not allow the sub-modules to be saturated by the solar irradiance. Therefore, they perform better as data communication receivers, while the energy harvesting performance is affected. Simulations show that the maximum data rate that can achieved with this panel is 109.1 Mb/s. Previously, it was shown that with a 5 W off-the-shelf solar panel the maximum data rate that can be achieved under-short circuit condition is 74 Mb/s. Using the new solar panel 74 Mb/s can be achieved while harvesting 2.1 W of solar power. Also, the architecture allows more solar panels to be attached to the MPPT circuit to increase the power harvesting capability up to 280 W. The estimations carried out in this chapter rely on experimental data sets and mathematical calculations. Furthermore, a fibre-coupled laser-based transmitter architecture is proposed to complement the receiver design. The proposed transmitter can transmit multiple wavelengths using a single collimation optics.

8.2 Limitations and future work

A major limitation in the design of a PV receiver based FSO system is that there will always be trade-off between energy harvesting and data

communication, when performed simultaneously. When the solar panel is harvesting electrical energy from optical energy, its operating in the photovoltaic mode (forward biased), as a result of this, the depletion region will be thinner. As the incident optical power increases, the voltage across the panel increases and the depletion region gets thinner, which increases the junction capacitance and negatively impacts the frequency response and responsivity of the solar panel. This limitation is also applicable to the recent generation of PV cells.

The second major limitation in this research was the maximum optical power that could be transmitted. In order to meet eye safety requirements, the maximum optical power from the transmitter was restricted. Increasing the transmitted optical power further will result in an increase in the received SNR, which will help in achieving higher data rates. However, if the solar panel is already saturated with very high solar irradiance, the additional transmitted optical will not be able to contribute to the additional SNR. As shown in Chapters 3 and 4, with an increase in solar power harvesting the number of free charge carriers are reduced.

In chapter 7, for the proposed design of a solar panel, the energy harvesting performance of the PV sub-modules covered were limited by the notch filters. As a future work, further investigation can be carried out into the optimal notch filter designs which will have flatter spectral response and sharp a notch only at the band of interest.

There has been significant research in the field of wireless optical power transfer (WOPT) using PVs [97]. In this thesis, the work was kept limited to solar energy harvesting and the main focus was to achieve the maximum data rate using an off-the-shelf Si solar panel with simultaneous energy harvesting from sunlight. Therefore, as future work, this research could be extended to explore the possibilities of the WOPT, as the system developed in this work

has the capability. Furthermore, the research could be extended to other generations of solar cell technologies such as GaAs, GaInP, InGaAs, *etc.* As the underlying principle of all the optical receiver when forward biased remains similar, the analytical work discussed in Chapter 3 could be parametrically modified and extended to other PV technologies. Using the future generations of solar cell technologies, the receiver technology could be highly miniaturised. The GaAs solar cell discussed in [24] has 0.8 mm^2 active area and could harvest 3.2 mW. Such solar cell technologies could be used in mobile applications to power smart devices such as smart watch, smart lenses, *etc*. Furthermore, these solar cells could be used as LiFi receivers enabling high-speed wireless communication to such devices while simultaneously charging them using WOPT.

Lastly, only one aspect of the application of this technology was exploited *i.e.*, as a backhaul link. The study can be extended to applications in space technology such as satellite-to-satellite communication. Satellites already possess the most advanced PV technologies and the ability of free-space optical communication. Hence, the advancements in PV technology can be majorly credited to space research. Furthermore, the application of solar cells for the dual purpose of communication and energy harvesting can undoubtedly be expanded to several other fields such as vehicle-to-vehicle communication or ship-to-ship communication where the requirement of optical alignment is very stringent and a receiver with a large active area can potentially solve a lot of first-hand issues.

Appendix A Transfer function of equalizer structure

The derivation of the transfer function of the filter structure, shown in Figure 5-2, is provided here. As it is a complex structure, star-delta transformation is used to simplify the structure in steps.

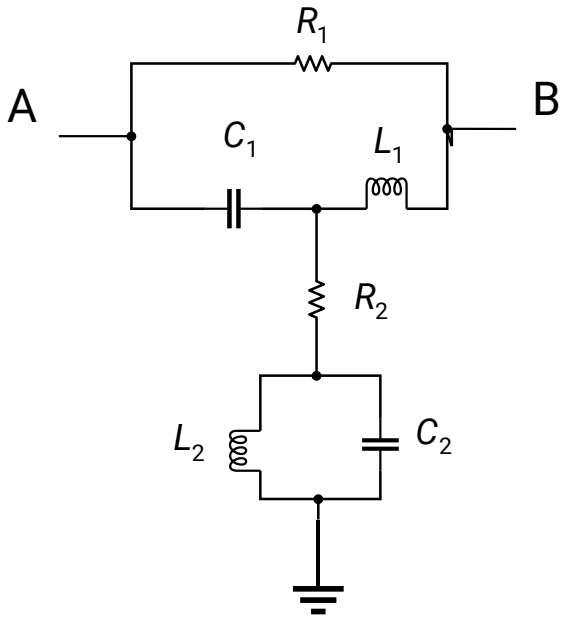

Figure A-1: Equalizer filter structure

The impedances offered by the reactive elements is denoted by X. The impedance offered by each reactive element is shown below:

$$X_{L1} = sL_1 \tag{37}$$

$$X_{L2} = sL_2 \tag{38}$$

$$X_{C1} = \frac{1}{sC_1} \tag{39}$$

$$X_{C2} = \frac{1}{sC_2} \tag{40}$$

Using Kirchhoff's circuit law, the circuit was simplified as shown in Figure A-2, where:

$$X_A = \frac{X_{L2}X_{C2}}{X_{L2}+X_{C2}} + R_2 \tag{41}$$

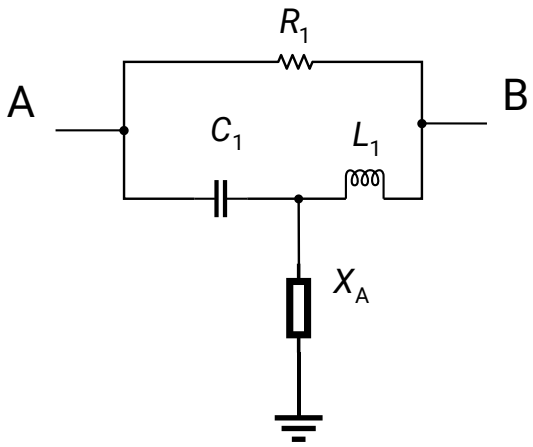

Figure A-2: Simplified equalizer structure

The structure can be further simplified using star-delta transformation as shown in Figure A-3.

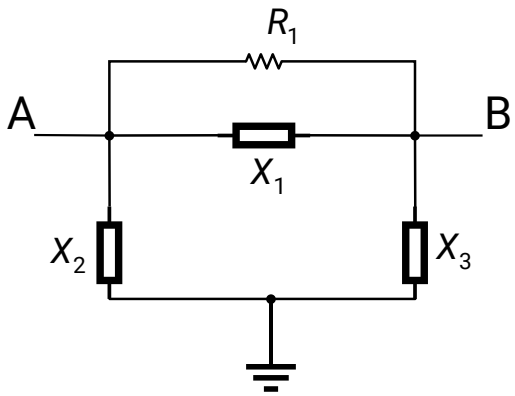

Figure A-3: Simplified equalizer structure after star-delta transformation

The resultant reactive elements are defined as shown in equations in (36), (37) and (38).

$$X_1 = \frac{X_{L1}X_{C1} + X_{L1}X_A + X_{C1}X_A}{X_{L1}} \tag{42}$$

$$X_2 = \frac{X_{L1}X_{C1} + X_{L1}X_A + X_{C1}X_A}{X_{C1}} \tag{43}$$

$$X_2 = \frac{X_{L1}X_{C1} + X_{L1}X_A + X_{C1}X_A}{X_A} \tag{44}$$

In Figure A-3, R_1 and X_1 are connected parallelly, therefore the resulting reactive element can be defined as $X_{11,}$ and

$$X_{11} = \frac{X_1 R_1}{X_1 + R_1} \tag{45}$$

The equalizer structure was simplified further using delta-star transformation on the network. The resulting network is shown in Figure A-4.

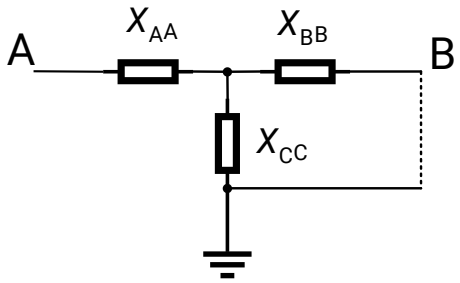

Figure A-4: Simplified equalizer structure after delta-star transformation

In Figure A-4, the dashed line depicts the virtual ground connection as the potential across B is measured with respect to the ground. Therefore, to obtain the transfer function short-circuit analysis method has been adopted. Moreover, the reactive elements X_{AA}, X_{BB}, and X_{CC} are defined in equations (40), (41), and (42).

$$X_{AA} = \frac{X_{11}X_2}{X_{11} + X_2 + X_3} \tag{46}$$

$$X_{BB} = \frac{X_{11}X_3}{X_{11}+X_2+X_3} \tag{47}$$

$$X_{AA} = \frac{X_2X_3}{X_{11}+X_2+X_3} \tag{48}$$

The transfer function of the equalizer structure can now be defined as a function of frequency as $H(s)$, where s is $j\omega$. In $j\omega$, j is $\sqrt{-1}$ and ω is $2\pi f$, where π is 3.142 and f is the frequency of the signal.

Therefore,

$$H(s) = X_{AA} + \frac{X_{BB}X_{CC}}{X_{BB}+X_{CC}} \tag{49}$$

Appendix B Design of the receiver circuit

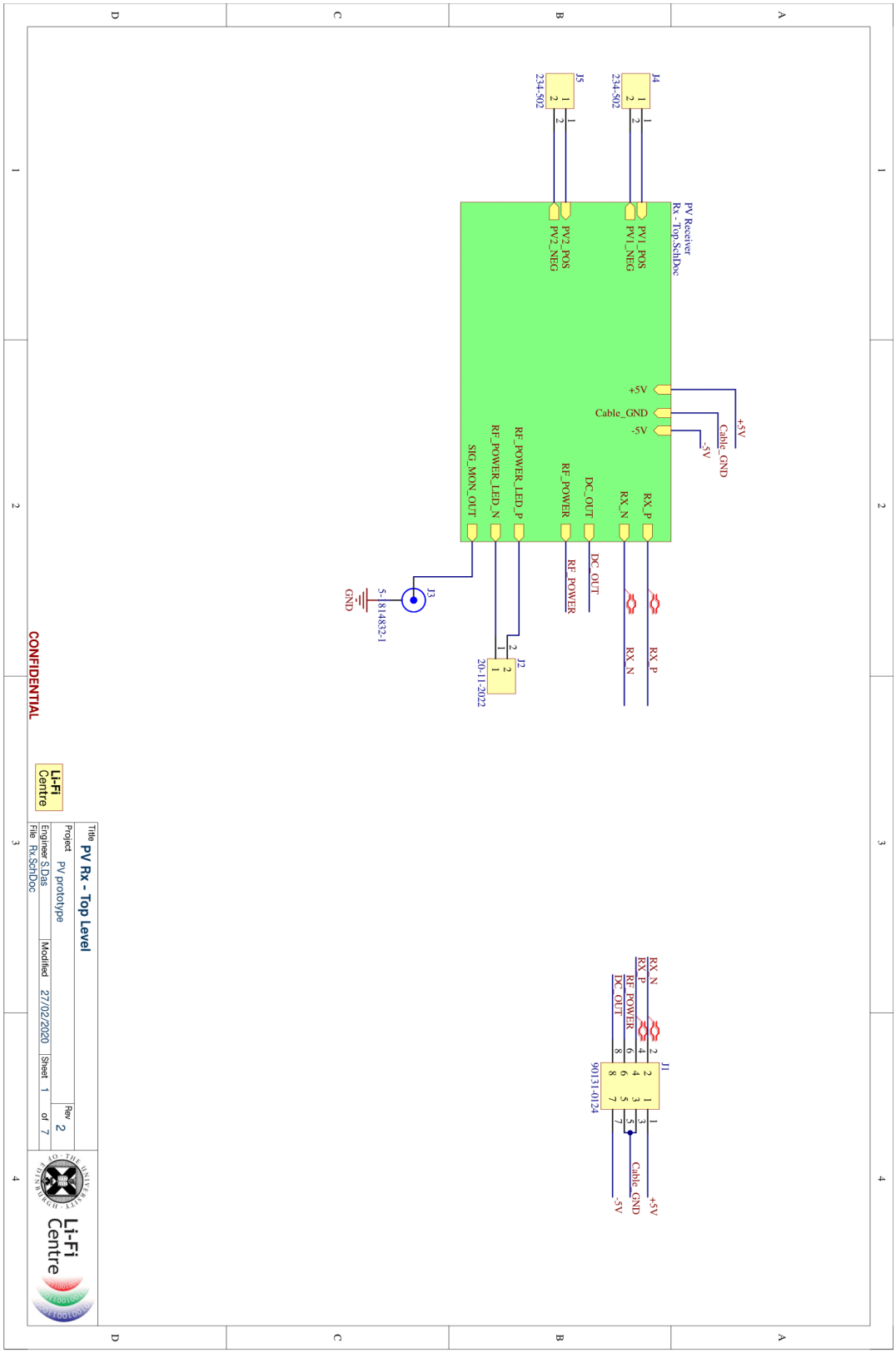

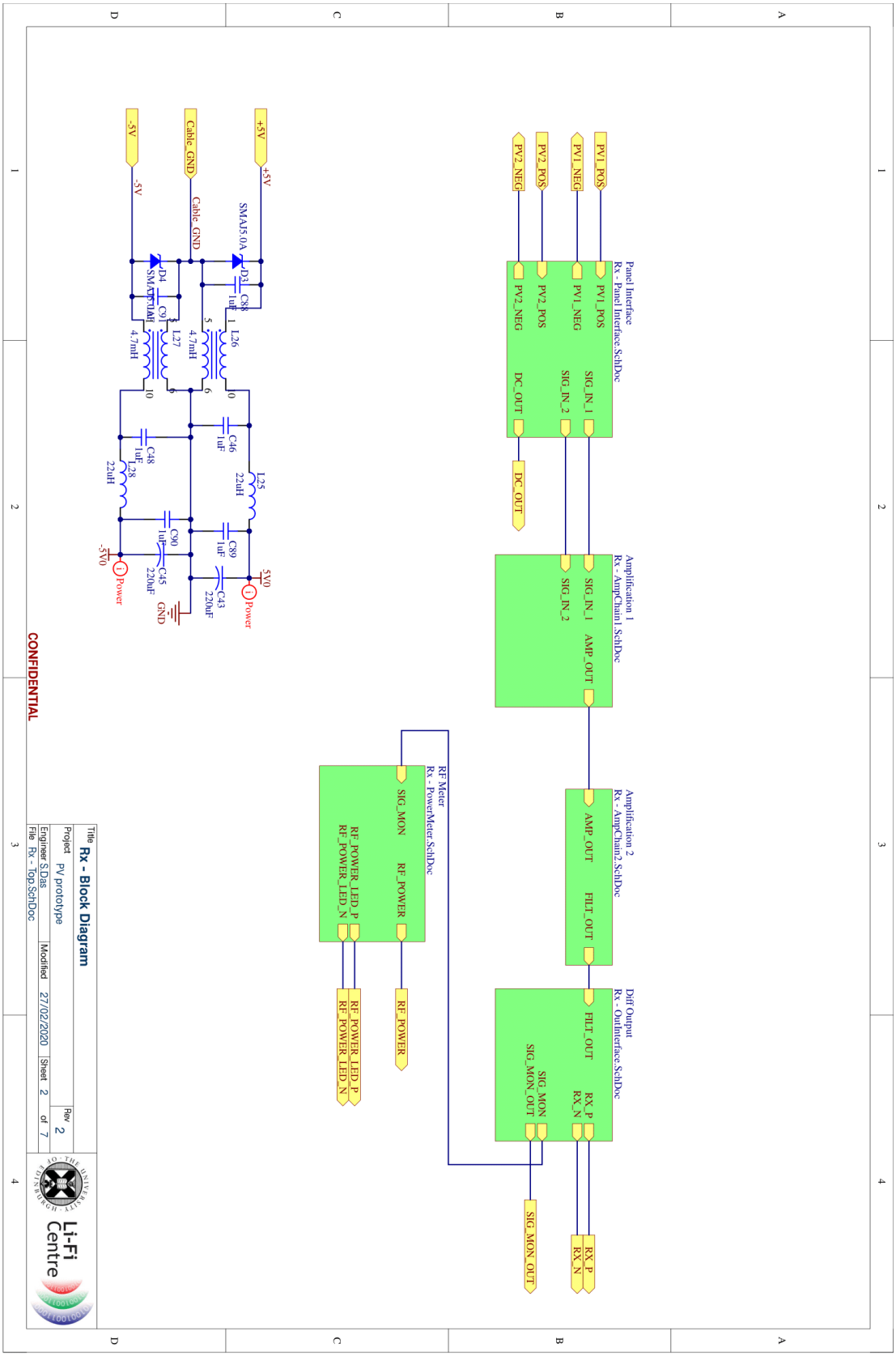
Panel Interface
Rx - Panel Interface.SchDoc
PV1_POS
PV1_NEG
PV2_POS
PV2_NEG
SIG_IN_1
SIG_IN_2
DC_OUT
Amplification 1
Rx - AmpChain1.SchDoc
AMP_OUT
Amplification 2
Rx - AmpChain2.SchDoc
FILT_OUT
Diff Output
Rx - OutInterface.SchDoc
RX_P
RX_N
SIG_MON
SIG_MON_OUT
RF Meter
Rx - PowerMeter.SchDoc
RF_POWER
RF_POWER_LED_P
RF_POWER_LED_N
+5V
-5V
Cable_GND
SMAJ5.0A
SMAJ5.0AH
4.7mH
1uF
22uH
220uF
GND
Power
CONFIDENTIAL
Title
Rx - Block Diagram
Project
PV prototype
Engineer S.Das
File Rx - Top.SchDoc
Modified 27/02/2020
Sheet 2 of 7
Rev 2
Li-Fi Centre

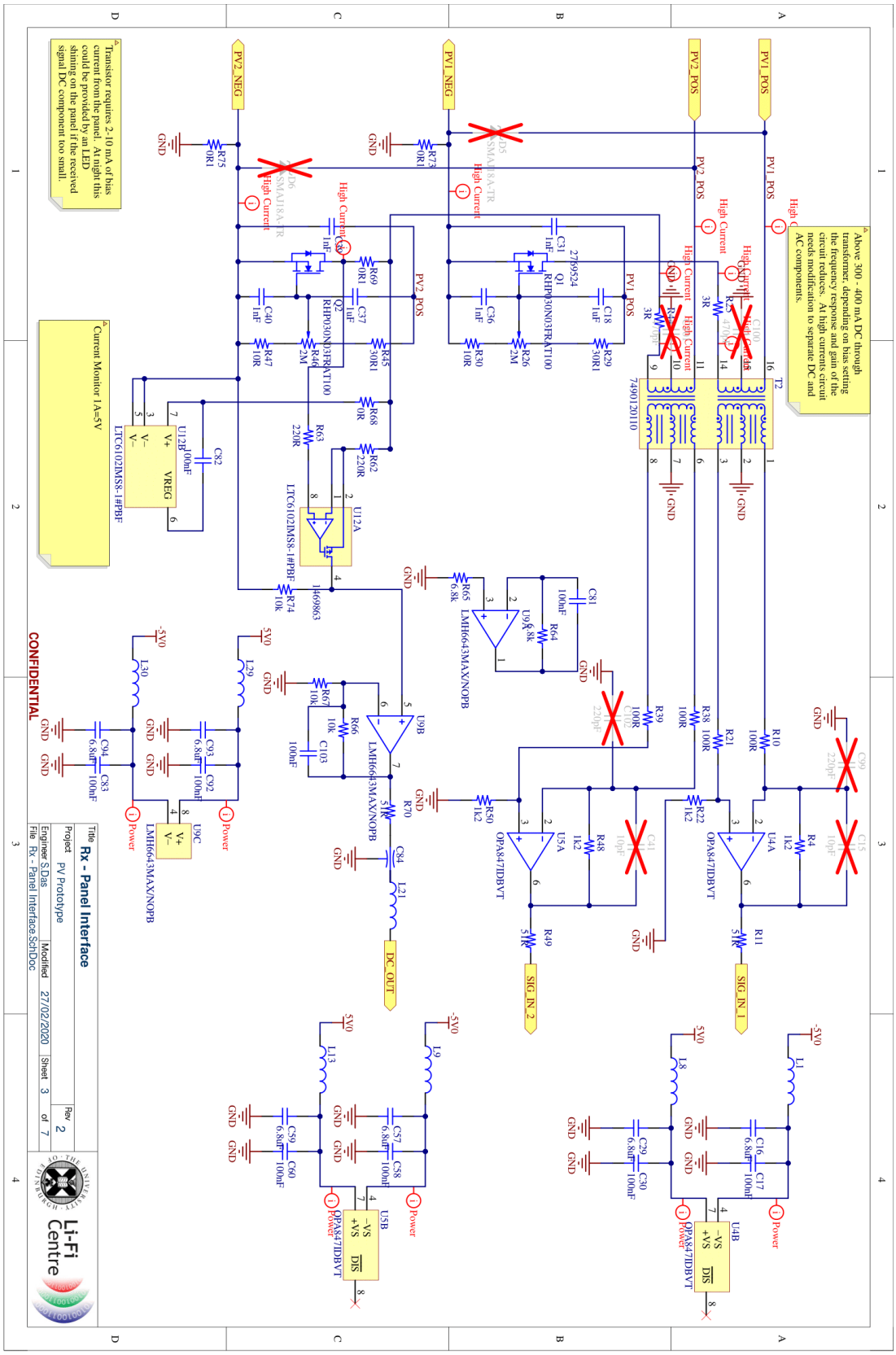
Above 300 - 400 mA DC through transformer, depending on bias setting the frequency response and gain of the circuit reduces. At high currents circuit needs modification to separate DC and AC components.
Transistor requires 2-10 mA of bias current from the panel. At night this could be provided by an LED shining on the panel if the received signal DC component too small.
Current Monitor 1A=5V
CONFIDENTIAL
Rx - Panel Interface
PV Prototype
Rx - Panel Interface.SchDoc
27/02/2020
Li-Fi Centre

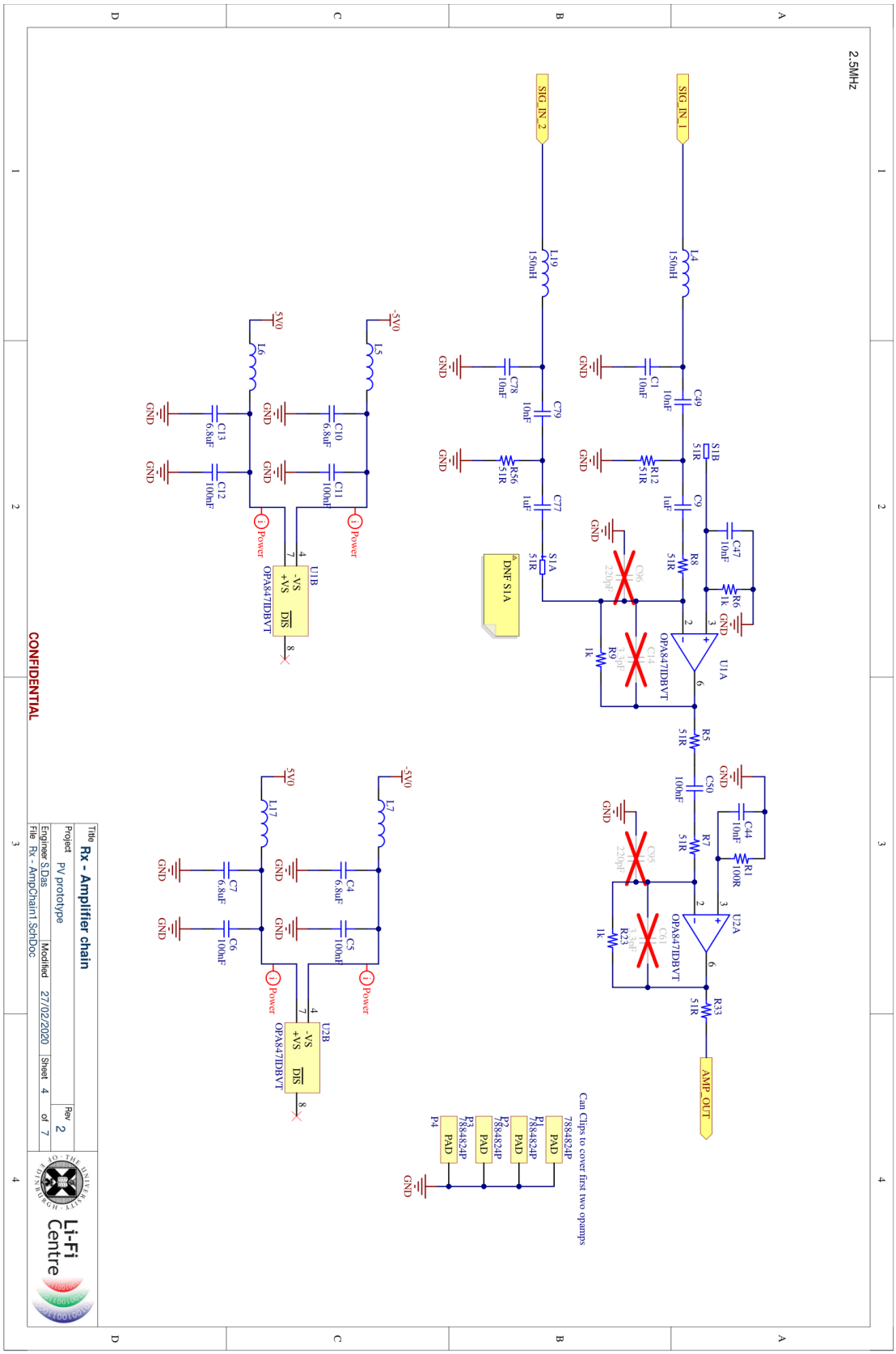
2.5MHz
SIG_IN_1
SIG_IN_2
AMP_OUT
L4
150nH
L19
150nH
C1
10nF
C49
10nF
C78
10nF
C79
10nF
C77
1uF
C9
1uF
R12
51R
R56
51R
R8
51R
S1A
51R
S1B
51R
C47
10nF
R6
1k
C96
220pF
C14
3.3pF
R9
1k
DNF S1A
U1A
OPA847IDBVT
R5
51R
C50
100nF
R7
51R
C95
220pF
C61
3.3pF
R23
1k
U2A
OPA847IDBVT
C44
10nF
R1
100R
R33
51R
L6
L5
L17
L7
C13
6.8uF
C12
100nF
C10
6.8uF
C11
100nF
C7
6.8uF
C6
100nF
C4
6.8uF
C5
100nF
U1B
U2B
OPA847IDBVT
-VS
+VS
DIS
Power
GND
-5V0
5V0
Can Clips to cover first two opamps
7884824P
PAD
P1
P2
P3
P4
CONFIDENTIAL
Title
Rx - Amplifier chain
Project
PV prototype
Engineer S.Das
File Rx - AmpChain1.SchDoc
Modified
27/02/2020
Sheet 4 of 7
Rev 2
Li-Fi Centre

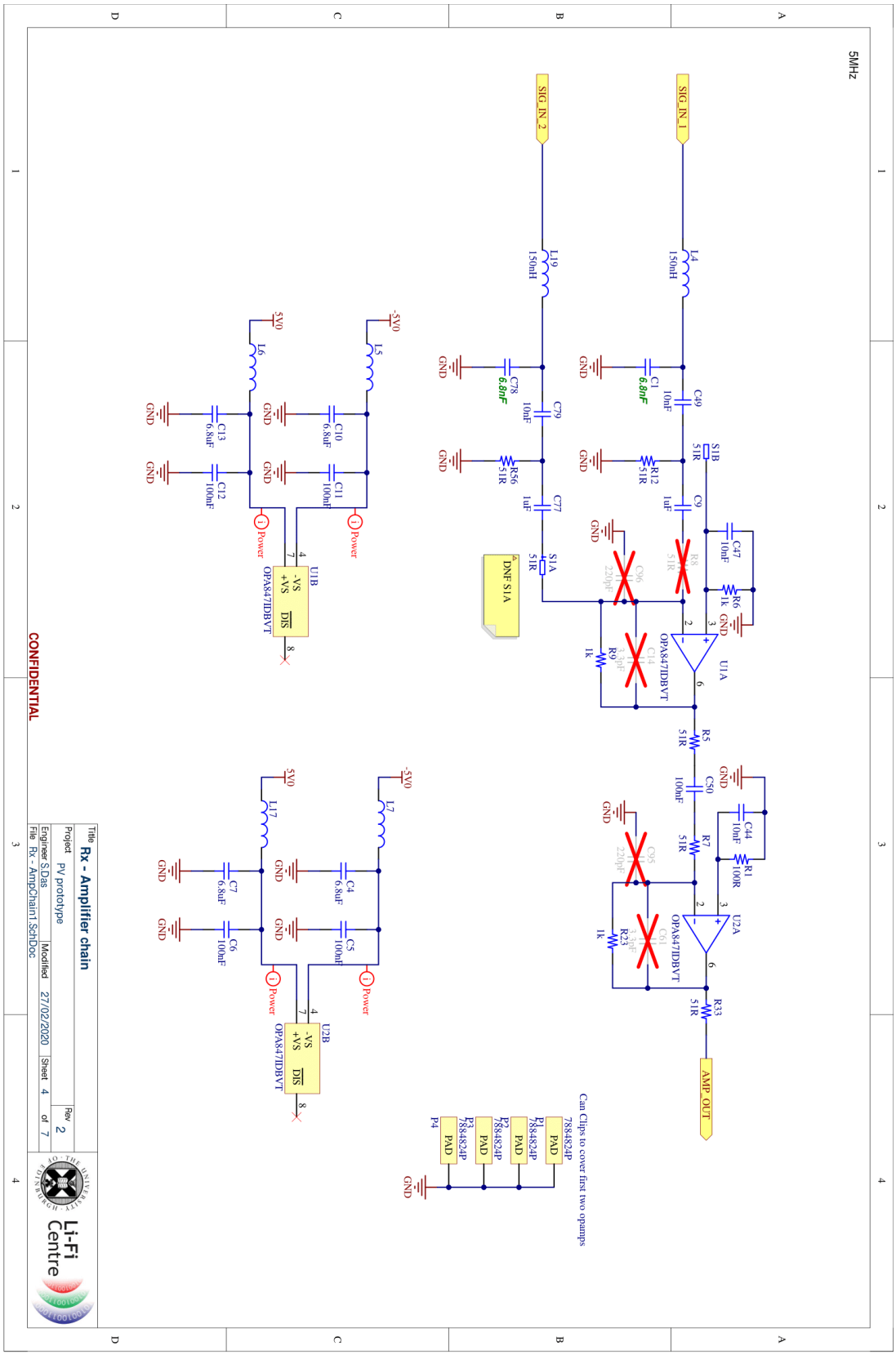
5MHz
SIG_IN_1
SIG_IN_2
L4
150nH
L19
150nH
C1
6.8nF
C78
6.8nF
C49
10nF
C79
10nF
C9
1uF
C77
1uF
S1B
51R
S1A
51R
R12
51R
R56
51R
R8
51R
C96
220pF
C14
220pF
R9
1k
DNF S1A
C47
10nF
R6
1k
U1A
OPA847IDBVT
R5
51R
C50
100nF
C44
10nF
R1
100R
R7
51R
C95
220pF
C61
220pF
R23
1k
U2A
OPA847IDBVT
R33
51R
AMP_OUT
Can Chips to cover first two opamps
P1
7884824P
PAD
P2
7884824P
PAD
P3
7884824P
PAD
P4
GND
L5
L6
C10
6.8nF
C11
100nF
C13
6.8nF
C12
100nF
U1B
OPA847IDBVT
-5V0
5V0
Power
L7
L17
C4
6.8nF
C5
100nF
C7
6.8nF
C6
100nF
U2B
OPA847IDBVT
GND
CONFIDENTIAL
Title
Rx - Amplifier chain
Project
PV prototype
Engineer S.Das
File Rx - AmpChain1.SchDoc
Modified 27/02/2020
Sheet 4 of 7
Rev 2
Li-Fi Centre

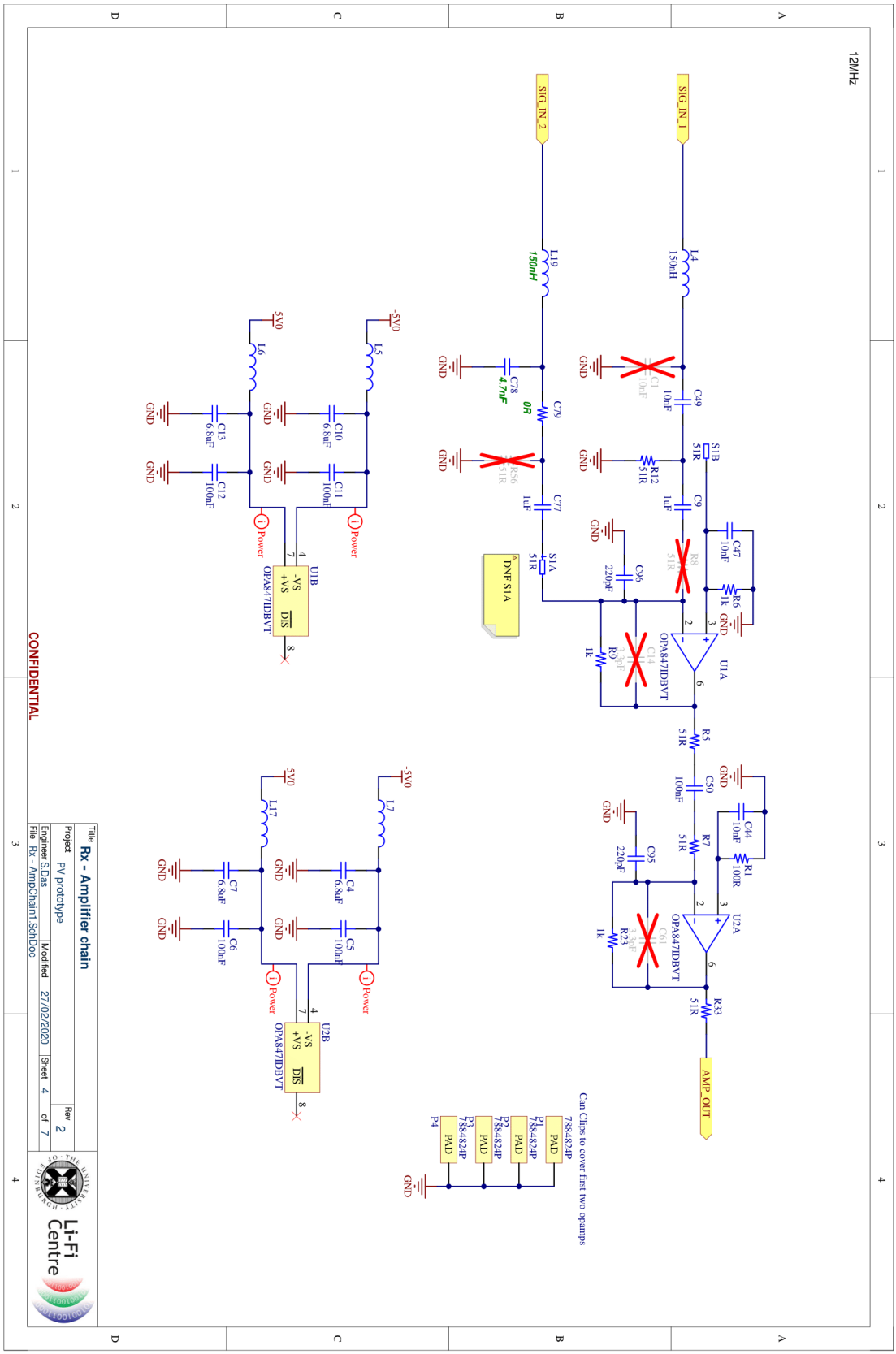
12MHz
SIG_IN_1
SIG_IN_2
L4
150nH
L19
150nH
C49
10nF
C1
10nF
S1B
51R
R12
51R
C9
1uF
R8
51R
C47
10nF
R6
1k
U1A
OPA847IDBVT
C96
220pF
C14
DNF
R9
1k
S1A
51R
C77
1uF
C78
4.7nF
C79
0R
R856
51R
DNF S1A
R5
51R
C50
100nF
C44
10nF
R1
100R
R7
51R
C95
220pF
C61
DNF
R23
1k
U2A
OPA847IDBVT
R33
51R
AMP_OUT
GND
-5V0
5V0
L5
L6
C10
6.8uF
C11
100nF
C13
6.8uF
C12
10nF
U1B
OPA847IDBVT
L7
L17
C4
6.8uF
C5
100nF
C7
6.8uF
C6
10nF
U2B
OPA847IDBVT
Power
Can Clips to cover first two opamps
788424P
PAD
P1
P2
P3
P4
CONFIDENTIAL
Title
Rx - Amplifier chain
Project
PV prototype
Rev
2
Engineer S.Das
Modified
27/02/2020
Sheet
4
of
7
File
Rx - AmpChain1.SchDoc
Li-Fi
Centre

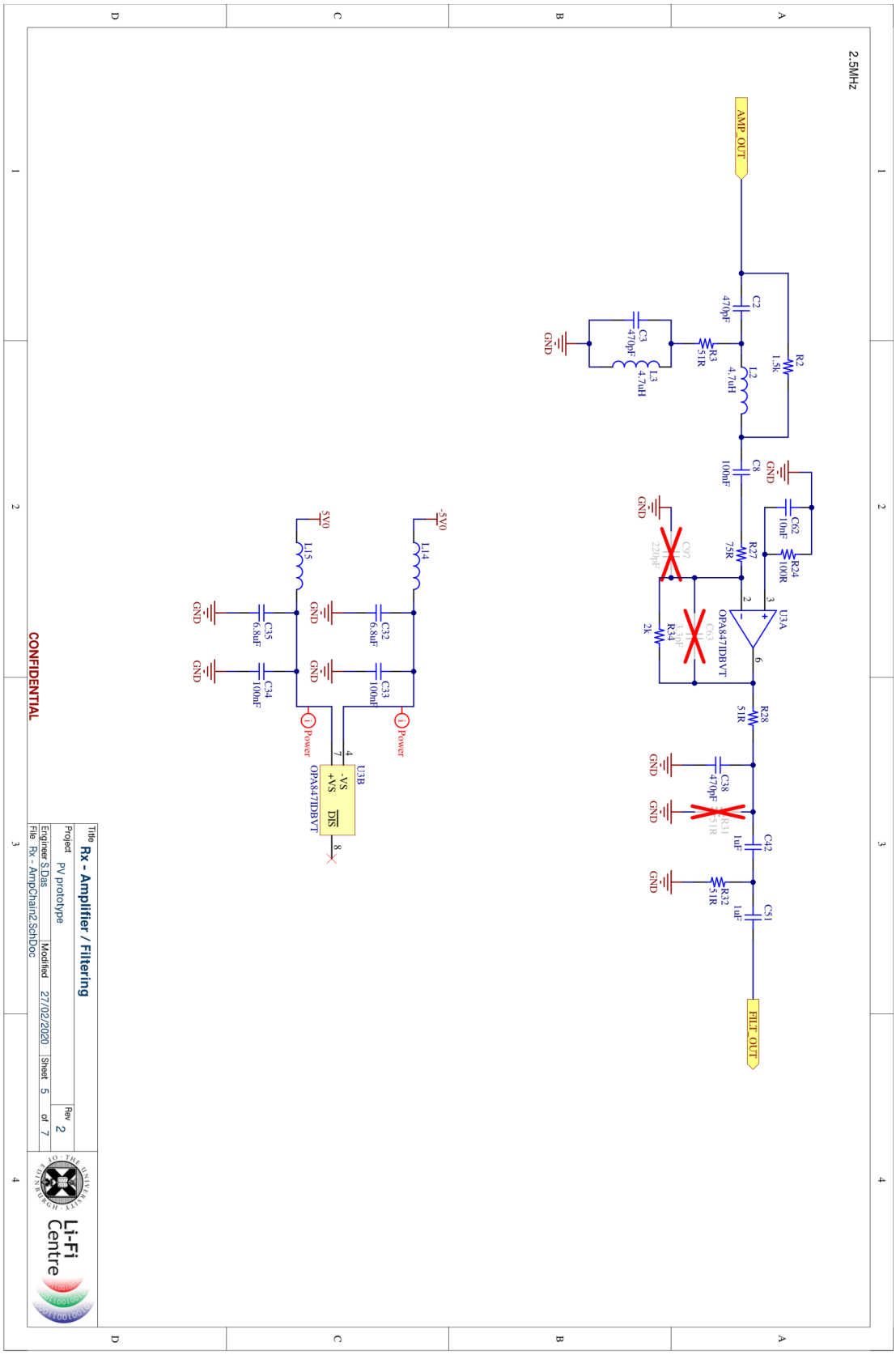
2.5MHz
AMP_OUT
C2
470pF
R3
51R
C3
470pF
L3
4.7uH
L2
4.7uH
R2
1.5k
GND
C8
100nF
C62
10nF
R24
100R
R27
75R
C37
220pF
R34
2k
C39
3.3pF
U3A
OPA847IDBVT
R28
51R
C38
470pF
R31
51R
C42
1uF
R32
51R
C51
1uF
FILT_OUT
-5V0
L14
L15
C32
6.8uF
C33
100nF
C35
6.8uF
C34
100nF
Power
U3B
OPA847IDBVT
-VS
+VS
DIS
CONFIDENTIAL
Title
Rx - Amplifier / Filtering
Project
PV prototype
Engineer S.Das
File
Rx - AmpChain2.SchDoc
Modified
27/02/2020
Sheet
5
of
7
Rev
2
Li-Fi Centre

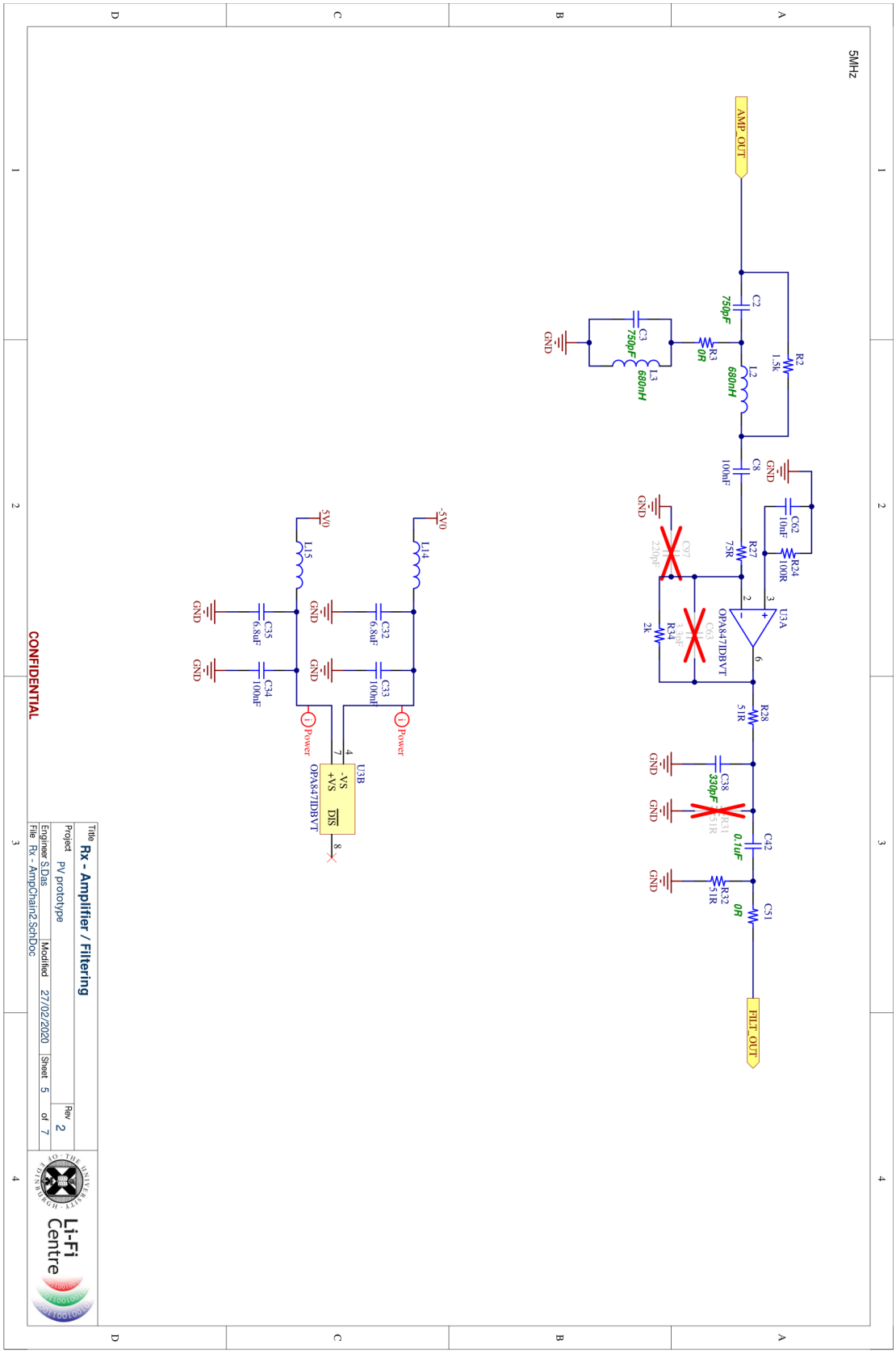
5MHz
AMP OUT
C2
750pF
C3
750pF
R3
0R
L3
680nH
L2
680nH
R2
1.5K
C8
100nF
C62
10nF
R24
100R
R27
75R
C97
220pF
R34
2k
C98
3.3pF
U3A
OPA847IDBVT
R28
51R
C38
330pF
R31
51R
C42
0.1uF
R32
51R
C51
0R
FILT_OUT
GND
-5V0
L14
L15
C32
6.8uF
C33
100nF
C35
6.8uF
C34
100nF
Power
U3B
OPA847IDBVT
-VS
+VS
DIS
CONFIDENTIAL
Title
Rx - Amplifier / Filtering
Project
PV prototype
Engineer S.Das
File Rx - AmpChain2.SchDoc
Modified 27/02/2020
Sheet 5 of 7
Rev 2
Li-Fi Centre

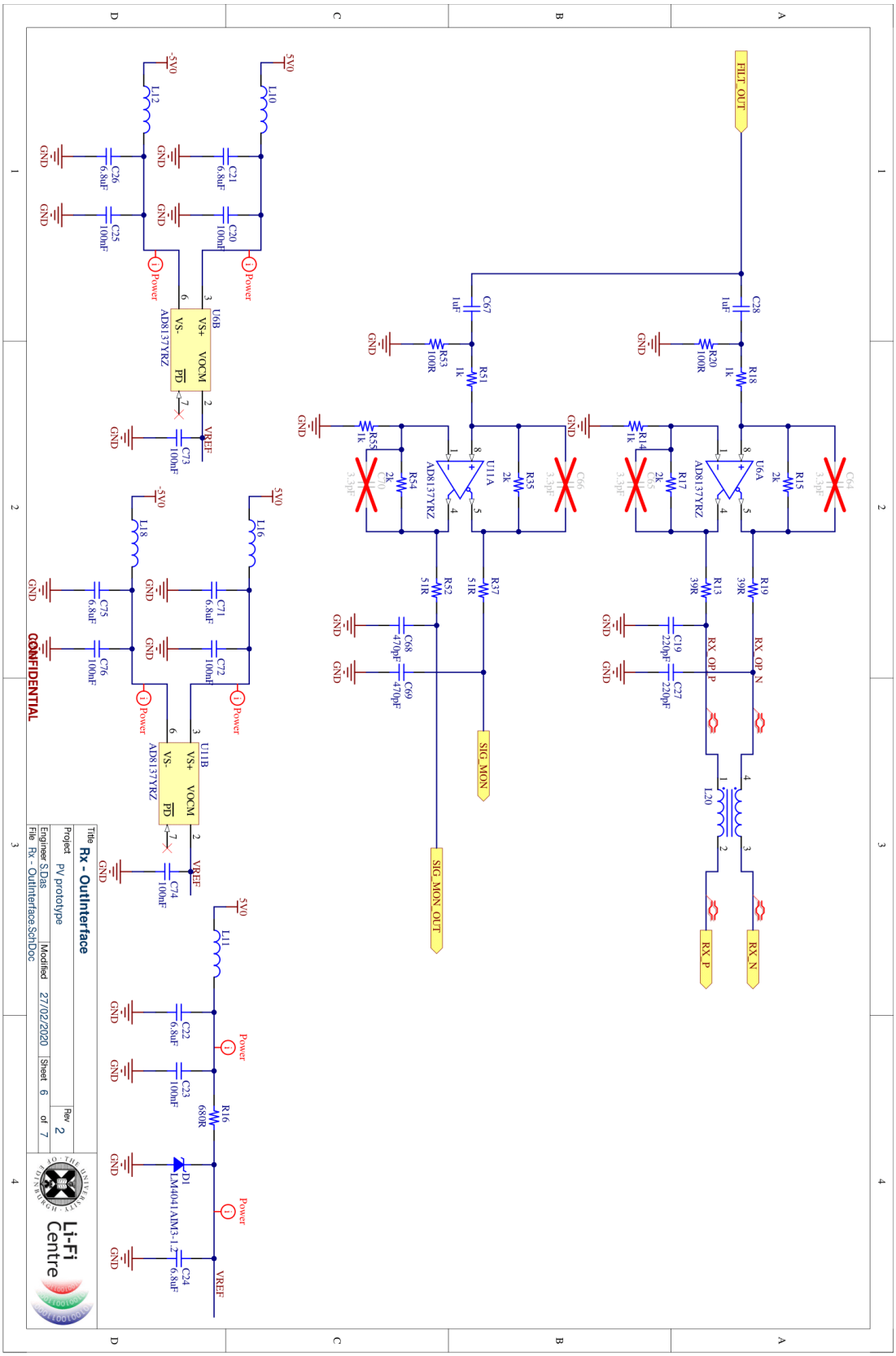
FILT_OUT
U6A
AD8137YRZ
U11A
AD8137YRZ
U6B
AD8137YRZ
U11B
AD8137YRZ
SIG_MON
SIG_MON_OUT
RX_OP_N
RX_OP_P
RX_N
RX_P
5V0
-5V0
GND
VREF
Power
CONFIDENTIAL
Rx - OutInterface
PV prototype
S.Das
Rx - OutInterface.SchDoc
27/02/2020
Li-Fi Centre

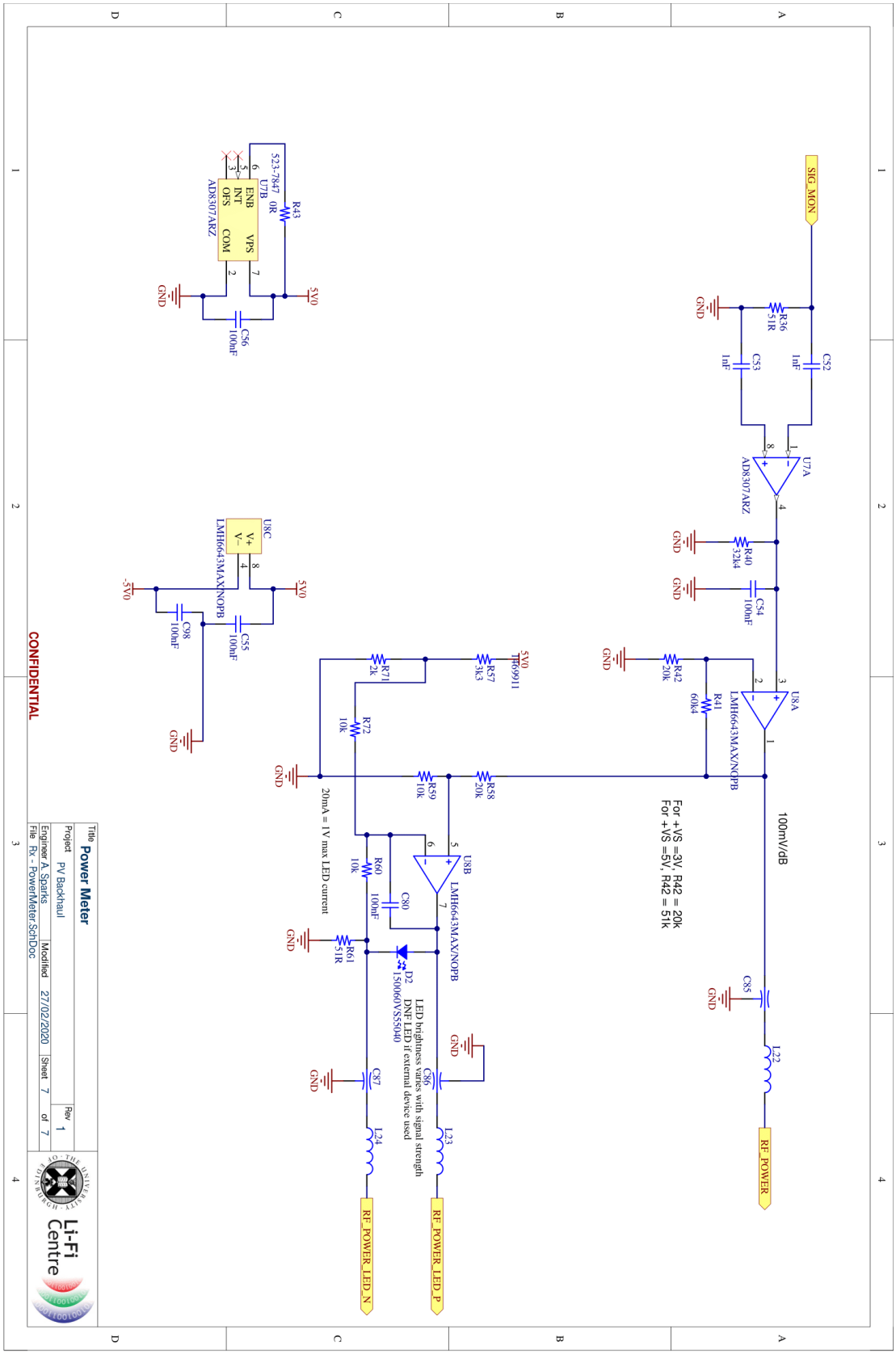
SIG_MON
R36 51R
C53 1nF
C52 1nF
U7A AD8307ARZ
R40 32k4
C54 100nF
R42 20k
R41 60k4
U8A LMH6643MAX/NOPB
100mV/dB
For +VS =3V, R42 = 20k
For +VS =5V, R42 = 51k
C85
L22
RF_POWER
U7B AD8307ARZ
523-7847
R43 0R
C56 100nF
5V0
GND
U8C LMH6643MAX/NOPB
C98 100nF
C55 100nF
-5V0
R71 2k
R57 3k3
TP6911
R72 10k
R59 10k
R58 20k
20mA = 1V max LED current
U8B LMH6643MAX/NOPB
R60 10k
C80 100nF
R61 51R
D2 150060VS55040
LED brightness varies with signal strength
DNF LED if external device used
C86
C87
L24
L23
RF_POWER_LED_N
RF_POWER_LED_P
CONFIDENTIAL
Title Power Meter
Project PV Backhaul
Engineer A. Sparks
File Rx - PowerMeter.SchDoc
Modified 27/02/2020
Sheet 7 of 7
Rev 1
Li-Fi Centre

Appendix C Selected publications

C.1. Conference Papers

S. Das, J. Fakidis, A. Sparks, E. Poves, S. Videv and H. Haas, “Towards 100 Mb/s Optical Wireless Communications Using a Silicon Photovoltaic Receiver,” in *IEEE Global Communications Conference*, Taipei, Taiwan, 2020

C.2. Journal Papers

S. Das, E. Poves, J. Fakidis, A. Sparks, S. Videv and H. Haas, “Towards Energy Neutral Wireless Communications: Photovoltaic Cells to Connect Remote Areas,” *Energies*, vol. 12, no. 19, pp. 3772-3791, 2019

S. Das, A. Sparks, E. Poves, S. Videv, J. Fakidis and H. Haas, “Effect of Sunlight on Photovoltaics as Optical Wireless Communication Receivers,” *Journal of Lightwave Technology*, vol. 39, no. 19, pp. 6182-6190, 2021

energies

MDPI

Article

Towards Energy Neutral Wireless Communications: Photovoltaic Cells to Connect Remote Areas

Sovan Das *, Enrique Poves, John Fakidis, Adrian Sparks, Stefan Videv and Harald Haas

LiFi Research & Development Centre, Institute of Digital Communications, The University of Edinburgh, JCMB, King's Building, Edinburgh EH9 3FD, UK; enrique.poves@ed.ac.uk (E.P.); j.fakidis@ed.ac.uk (J.F.); adrian.sparks@ed.ac.uk (A.S.); s.videv@ed.ac.uk (S.V.); h.haas@ed.ac.uk (H.H.)

* Correspondence: sovan.das@ed.ac.uk

Received: 30 August 2019; Accepted: 27 September 2019; Published: 3 October 2019

check for updates

Abstract: In this work, we have designed, developed and deployed the world's first optical wireless communication (OWC) system using off-the-shelf lasers and solar photovoltaics. Four bidirectional OWC prototypes have been installed on the Orkney Islands of Scotland at a 30 m link distance for the provision of high-speed internet access to two residential properties. The silicon-made solar panels can harvest power up to 5 W from sunlight and they offer data rates as high as 8 Mb/s. Using additional analogue processing, data rates higher than the existing landline broadband connection are achieved. This breakthrough opens the development path to low cost, self-powered and plug-and-play free-space optical (FSO) systems.

Keywords: solar energy; energy harvesting; communication systems; optical wireless communications; free-space optical communication; light communication

1. Introduction

Optical wireless communications (OWC) have been widely accepted as a technology with the potential to meet the ever-increasing demand in network capacity [1]. Light fidelity (LiFi) is an optical wireless networking technology that typically uses light-emitting diodes (LEDs) for data transmission and photodiodes (PDs) for data reception in indoor environments [2]. LiFi is considered as the dominant networking technology in OWC and a lot of work has been carried out towards its convergence into the next generation of wireless networking [3]. While LEDs and PDs have traditionally been considered as the main communication devices in LiFi, other types of light sources and detectors such as lasers and photovoltaic (PV) panels can also be used [4]. Currently, the most common type of receivers used are positive-intrinsic-negative (PIN) and avalanche PDs due to their high-bandwidth and linear photodetection. However, these photodetectors require an external power source in order to operate. As mankind is shifting from fossil fuel to other renewable resources of energy, such as solar power. A solar panel can directly convert the optical signal to an electrical signal without the application of any external power source.

Since their invention, solar panels have already undergone three generations of development for optimizing their power efficiency. The first generation consists of solar panels made of monocrystalline or polycrystalline silicon (Si) [5] which is still the most commonly used type in conventional applications. Monocrystalline panels have a higher power output, better temperature stability and last longer than polycrystalline panels [6]. The second generation of solar panels consists of different types of thin-film solar cells and are mainly integrated into buildings or used in power stations or smaller solar power systems. Third-generation solar panels include a variety of thin-film technologies but many of them are still in the phase of research and development. Some of them generate electricity by using organic materials, while others use inorganic substances [6]. There are solar cells that use hybrid

organic-inorganic substances such as the perovskite solar cell. Perovskite solar cells have perovskite structured compound of tin or lead halide-based material as the light-harvesting layer [7]. The main advantage of perovskite solar cells over silicon-based cells is that they are cheaper to manufacture [7]. This study focuses mainly on the first generation of solar panels, as they are inexpensive and readily available for deployment.

The idea of using a Si solar cell as a data detector was demonstrated for the first time in 1977 [8]. However, the concept of simultaneous wireless information and power transfer in the optical spectrum was only recently studied in [9] and [10] using white LEDs and ordinary Si solar cells. The data rate of 3 kb/s achieved in [9] is considered insufficient for high-speed data communication. A significant data speed of 7 Mb/s and harvested power of 2.1 mW are reported in [10] by using a polycrystalline Si PV panel and OFDM. Going forward from these initial demonstrations, a 12 Mb/s wireless data link with a distance of 1 m was created in [11] using a white LED and the same solar panel receiver with that in [10]. Alternative PV technologies used for data detection include organic [12] and GaAs PV cells [13]. Those devices offer lower capacitances than Si-made solar panels due to their reduced sizes and their electrical bandwidth is much higher, i.e., of the MHz order. In [12], a data rate of 34.2 Mb/s is reported for a 1 m OWC link using an organic solar cell. A record data rate of 522 Mb/s has been achieved using a GaAs PV cell as a data detector in [13] at a 2 m link distance. However, there are strict alignment requirements for organic and GaAs PV cells due to their reduced areas.

All the experimental prototypes in [8–13] have only been tested in an indoor laboratory environment. In this paper, a world's first FSO system with solar panels as data detectors is shown to be deployed and tested under real-world conditions. The prototype was used as a solution for backhaul communication over a 30 m distance to provide internet connectivity to two residential properties on a remote island as depicted in Figure 1.

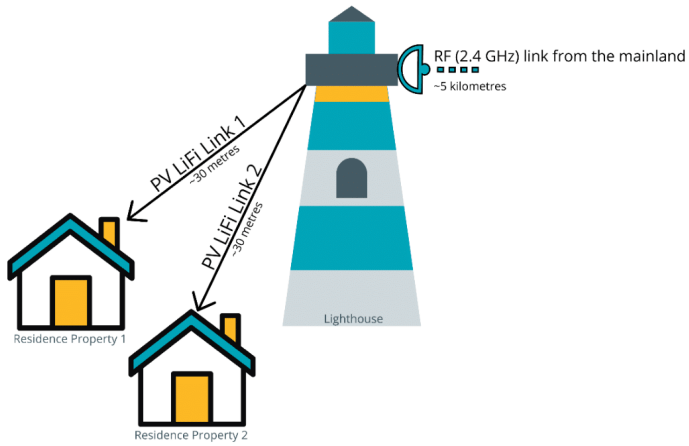

Figure 1. Deployment architecture.

A key advantage of using a solar panel as a data communication receiver over a conventual PD is the minimal requirement for beam tracking and alignment [11]. A conventional FSO system requires a highly complex system for beam tracking and alignment owing to the very small receiver dimensions. This leads to the need for highly precise alignment between the transmitter and receiver. As solar panels are significantly bigger than FSO receivers, the required mechanical control is much simpler. Although the large area of the detector reveals the potential for signal jamming and eavesdropping, the system

carries over all the physical and network layer security features which have already been deployed and tested for its robustness in 802.11 IEEE Wireless Local Area Network (WLAN) standards [14], making it similar to Radio Frequency (RF) based links.

The rest of this paper is organized as follows: Section 2 discusses how a solar panel can be used to harvest energy and receive data simultaneously; Section 3 presents an overview of the system and its main characteristics and in Section 4 results obtained after deployment are discussed. Finally, conclusions are presented in Section 5.

2. Background

Solar PV panels are not designed to function as OWC receivers. Therefore, the communication bandwidth of a solar panel was never considered during its manufacturing process. In order to use a solar panel as a data receiver, two aspects need to be considered: The electrical characteristics of the solar cells and the profile of the beam incident on the panel.

2.1. Electrical Characteristics

In order to design a suitable receiver with the silicon solar panel, it is necessary to determine important optical detector characteristics and choose the right type of solar panel. The performance of an optical detector may be defined by the following characteristics:

- Sensitivity to an incident optical signal
- Speed of response
- Linearity
- Temperature stability

2.1.1. Optical Sensitivity

The solar panel can be modelled as a PN diode structure as shown in Figure 2 where W_p and W_n are the widths of p-doped and n-doped regions respectively, V is voltage generated, I is the current flowing through the load resistance R_L.

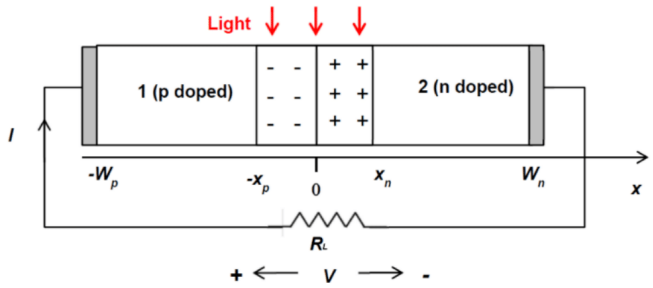

Figure 2. PN junction of a solar cell [15].

An important specification of a solar cell that needs to be considered is the quantum efficiency. The quantum efficiency of a solar panel η quantifies the capability of converting optical energy in different wavelengths to electrical energy, i.e., sensitivity to the incident light. It can be calculated using [15]:

$$\eta = (1 - R)\left[1 - e^{-\alpha(x_n + x_p)}\right], \quad (1)$$

where R is the responsivity, α is the absorption coefficient and $x_n + x_p$ denotes the thickness of the depletion zone, as shown in Figure 2.

2.1.2. Speed of Response

The bandwidth of a solar cell is critical to understand which affects the maximum data rate of the communication system. The bandwidth of a solar cell is dependent on the intrinsic bandwidth and extrinsic bandwidth. The intrinsic bandwidth is determined by the doping level which determines the thickness of the depletion region. When light is incident on the depletion region, an exciton (i.e., an electron-hole pair) is generated, resulting in potential difference across the terminals. As the electric field is directly proportional to the potential difference for a given distance, assuming the doping level across the substrate is homogenous the electric field through the semiconductor will be homogenous. The time taken by these charge carriers to traverse through the depletion region will determine the intrinsic bandwidth of this semiconductor device. Let the time taken by an electron be τ_e and for a hole be τ_h. The velocity at which these charges will be moving will be given by $\mu_e E$ and $\mu_h E$, where μ is the mobility factor and E is the electric field across the semiconductor. Hence, the time can be simply expressed by the distance divided by velocity, which is expressed using:

$$\tau_h = \frac{x_n + x_p}{\mu_h E} \tag{2}$$

and

$$\tau_e = \frac{x_n + x_p}{\mu_e E} \tag{3}$$

From Equations (2) and (3), it can be observed that the thinner the depletion region, the larger bandwidth of the solar cell will be.

As can be seen from Equations (1)–(3), the quantum efficiency and the speed of response are dependent on the thickness of the depletion region. The thicker the depletion region the higher the quantum efficiency, however, the solar cell will have a lower bandwidth. Therefore, during the manufacturing of a solar cell, there will always be a tradeoff between the energy harvesting capability and bandwidth.

The second factor which determines the bandwidth of a solar panel is the extrinsic bandwidth. The extrinsic bandwidth is dependent on the parasitic and junction capacitance between the interconnection of each solar cell in a PV module. In a semiconductor device, the capacitance associated with the charge variation in the depletion layer is called the junction capacitance and the capacitance associated with the excess carriers in the quasi-neutral region is called the diffusion capacitance.

The solar cell can be represented as a current source. Figure 3 gives an equivalent electrical circuit to a solar cell used as a data receiver [15]. Parameter $h(f)$ is the parameter which is dependent on the intrinsic bandwidth, and $P(f)$ is the time-varying optical signal as a function of frequency which is expressed as f [15]. The responsivity of the panel depends on the wavelength of the incident light and the material used. In the case of Si, the responsivity peaks at the wavelength window between 900 and 1000 nm [15].

$$h(f) = -\left(\frac{\frac{1}{2}}{1 + j2\pi f_{\tau e}} + \frac{\frac{1}{2}}{1 + j2\pi f_{\tau h}}\right), \tag{4}$$

$$I(f) = Rh(f)P(f)\frac{R_d}{R_d + R_{ext} + j2\pi f\left(C_j + C_d\right)R_d R_{ext}} \tag{5}$$

where $f_{\tau e} = 1/\tau_e$, $f_{\tau h} = 1/\tau_h$, R_{ext} is the external load resistance, R_d the diode resistance, C_d and C_j the diffusion and junction capacitance of the solar cell.

It can be observed that if the solar cells are connected in series, the effective diffusion capacitance reduces. The junction capacitance will completely depend on the process of how each solar cell is connected.

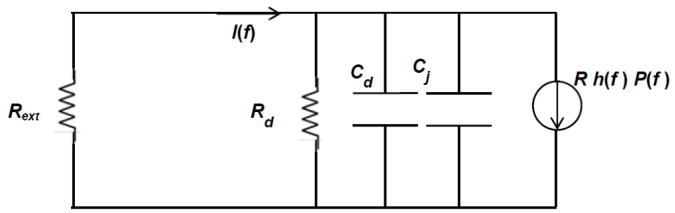

Figure 3. Circuit model of a solar cell as a data receiver [15].

2.1.3. Linearity

The linearity of the solar panel can be verified by considering its two different modes of operation commonly referred to as the PV mode and the short-circuit mode. In the PV mode, the load resistance R_L is very low compared to the effective cell shunt resistance R_{sh} as shown in Figure 4.

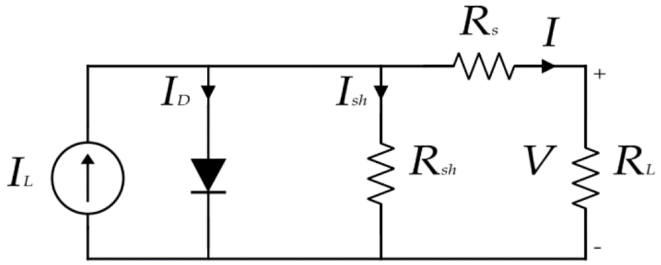

Figure 4. Single-diode model of a solar cell for energy harvesting.

For an open circuit, $I = 0$, hence the generated photocurrent I_L can be expressed as:

$$I_L = I_D + I_{sh}, \tag{6}$$

As the solar cell has been modelled as a PN diode we can use the diode equation:

$$I_D = I_0\left(e^{\frac{qV}{KT}} - 1\right), \tag{7}$$

where I_D is the current through the diode, I_0 is the saturation current, q is the charge of an electron, K is the Boltzmann's constant and T is temperature. For a constant temperature $\alpha = (q/KT)$ can be considered as a constant.

Substituting Equation (7) in Equation (6) and solving for V_D we have:

$$V_D = \frac{1}{\alpha}\ln\left(\frac{I_L - I_{sh}}{I_0} + 1\right) \tag{8}$$

Assuming $I_L >> I_{sh}$ and $I_L >> I_0$,

$$V_D = \frac{1}{\alpha}\ln\left(\frac{I_L}{I_0}\right) \tag{9}$$

Using the small-signal approach, it can be assumed that:

$$\frac{V_s}{I_{Ls}} \sim \frac{dV_D}{dI_L} = \frac{1}{\alpha I_L} \tag{10}$$

where V_S is the output voltage signal of the detector and I_{Ls} is the portion of I_L related to the incident optical signal. Here it is seen that the signal voltage gain is inversely related to the total radiant energy incident to the detector, which is composed of both the carrier and background illumination. In many applications, the detector will operate under conditions of widely varying signal strength and background illumination, which would make this mode of operation undesirable.

If we consider the short-circuit mode, in which $R_S + R_L$ is very small as compared to the diode effective shunt resistance, then

$$I_L = I, \tag{11}$$

and the small-signal gain is given by:

$$\frac{dI_s}{dI_L} = 1 \tag{12}$$

Equation (12) indicates a perfectly linear response with no dependence on the signal strength and background illumination which is highly desirable.

2.1.4. Temperature Stability

Temperature affects the characteristics of Si cells in two ways. Firstly, the diode saturation current depends strongly on temperature. Secondly, the photogenerated current varies because the spectral response of the cell shifts towards the infrared region as the temperature is increased.

Differentiating Equation (8) with respect to temperature T we get,

$$\frac{dV_D}{dT} = \frac{1}{\alpha}\left(\frac{1}{I_L}\frac{dI_L}{dT} - \frac{1}{I_0}\frac{dI_0}{dT}\right) + \frac{V_D}{T} \tag{13}$$

Since $I_L >> I_o$

$$\frac{dV_D}{dT} = \frac{V_D}{T} - \frac{1}{\alpha I_0}\frac{dI_0}{dT} \tag{14}$$

For Si, at T = 298 K, $\alpha = (q/KT)$ we have [8]

$$\frac{1}{\alpha I_0}\frac{dI_0}{dT} = 0.08\ /K \tag{15}$$

Typically, for Si V_D = 0.7 V. Hence, the voltage temperature coefficient we get is −0.078 V/K per solar cell.

Considering the theoretical voltage temperature coefficient from Equation (14), a 5 W polycrystalline solar panel was chosen with a voltage temperature coefficient of −0.13 V/K [16] for the whole panel. This was the solar panel with the closest voltage temperature coefficient available off-the-shelf.

All the above derivations assumed that the solar panel is a time-varying current source. Hence, a circuit that can hold the voltage across the solar panel constant would result in keeping the electric field (E) across the PN junction of the cells in Equations (2) and (3) constant thereby implying in Equation (6) that $h(f)$ is constant. Therefore, the bandwidth of the solar panel will depend only on the extrinsic bandwidth.

2.2. Beam Profile on the Solar Panel

In order to understand the effects of illumination of the laser beam on the frequency response of a solar panel, an experiment was carried out to measure its electrical output. In the experiment,

a 660 nm laser was used with a collimating lens, a plano-convex lens and a diffuser. The size of the beam was varied by changing the distance between the plano-convex lens and the collimating lens. Figure 5 shows the three different cases of illumination patterns: (a) Below 20% of the solar panel's area, (b) over 60% of the solar panel's area and (c) 100% of the panel's area.

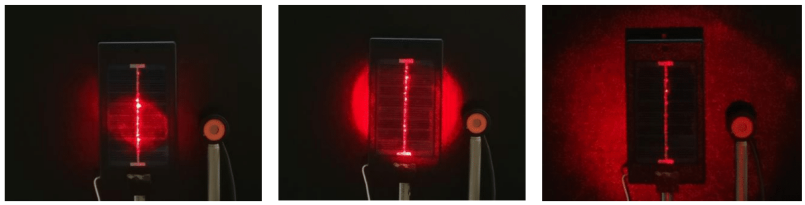

(**a**) (**b**) (**c**)

Figure 5. Illumination patterns on a solar panel (**a**) highly concentrated; (**b**) partially illuminated; (**c**) completely illuminated.

Figure 6 gives the normalized magnitude as a function of frequency. It is observed that when the solar panel is fully illuminated with the optical beam, it gives the best performance. This is in agreement with the energy harvesting results presented in [17]. This is because all the solar cells in the panel are connected in series and are illuminated with the most uniform pattern. Hence, the electrical performance of the panel is determined from the least illuminated cell. In this experiment, it was also found that a minimum of 6mW optical swing with a 660 nm laser source on the surface (306×218 mm^2) of the panel [16] is required to observe a corresponding electrical signal of ~1 mV_{pp}. Also, from Figure 6, it can be concluded that the solar panel has a low pass response.

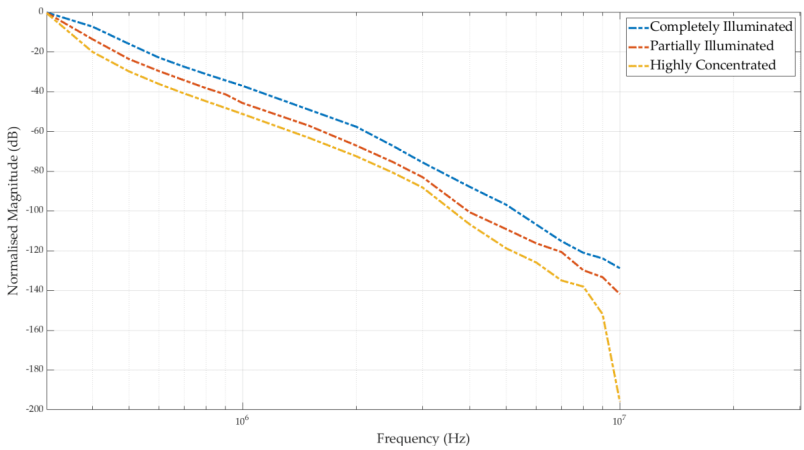

Figure 6. Frequency response of solar panel with different illumination levels.

3. System Design and Integration

3.1. Transmitter: Requirements and Limitations

One of the most important limitations in the design of an FSO communication system is eye safety [18]. The majority of FSO transmitters operate at a wavelength of 1550 nm due to their high

maximum permissible exposure (MPE), which is 100 mW/cm^2 [19]. However, the laser wavelength in this research is selected to be 940 nm because of the peak responsivity of Si cells in the region between 940 nm and 1000 nm. The MPE of 940 nm lasers is 3.1 mW/cm^2 and the laser system is certified to be classified as Class 1M. Another requirement in the optical domain is the transmission of a divergent laser beam that can overfill the solar panel. This is not only to project a uniform beam covering the entire solar panel, but also to tackle any misalignment due to unfavourable weather conditions such as strong winds. In addition, the transmitter should be able to dynamically control the signal's power based on the weather conditions. Hence, the control unit becomes crucial in order to maintain the link throughout varying weather conditions including cloud cover, rain and fog.

3.1.1. Laser Driver and Control Circuit

A voltage-controlled current-driven laser driver circuit was designed. A temperature sensor and digitally controlled attenuator were added to the design in order to control the signal input to the laser for maximising the link performance. The frequency response of the laser driver was measured using a 1 GHz AC-coupled optical receiver. From Figure 7 it can be inferred that the −3 dB bandwidth of the driver is 65 MHz, which was much higher than the bandwidth of the receiver.

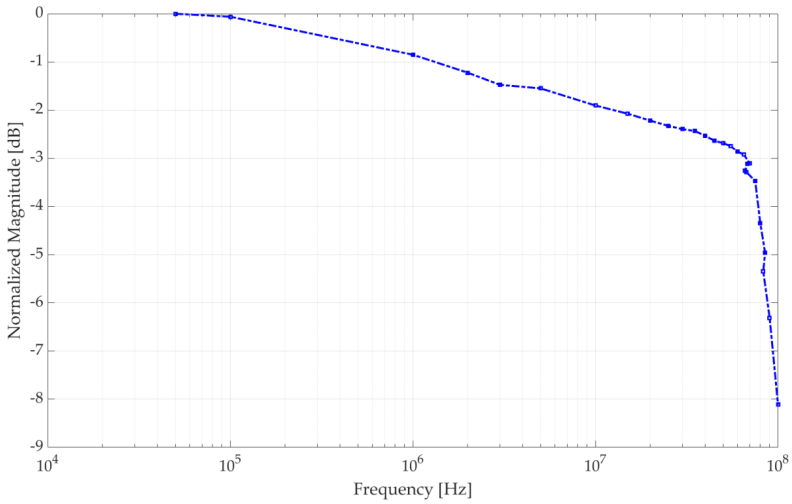

Figure 7. Frequency response of the laser driver.

3.1.2. Laser Beam and Optics

The optical design software Zemax was used for ray tracing and a calculation of the power budget of the link. A 2 × 2 vertical-cavity surface-emitting laser (VCSEL) array [20] is used with a diffuser on top of the package. The maximum DC optical power of the laser is 0.5 W. The VCSEL generates a rectangular beam pattern with four hot spots as shown in Figure 8. The laser beam has a wide horizontal and vertical divergence of 65° and 78°, respectively.

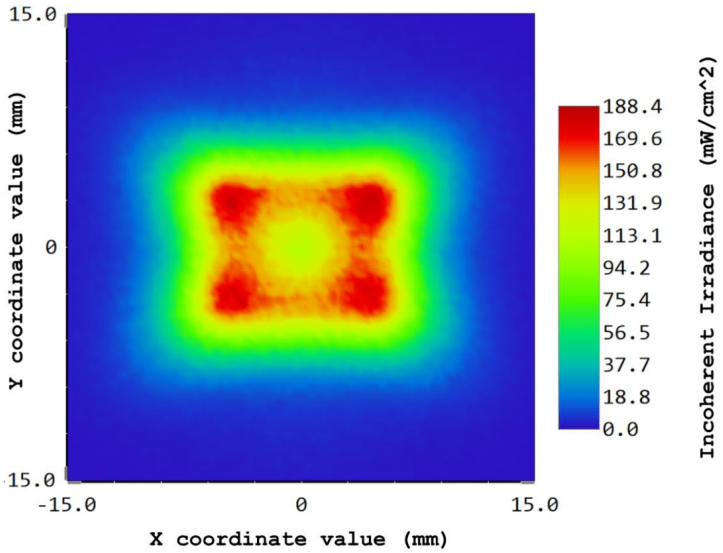

Figure 8. Incoherent irradiance of the vertical-cavity surface-emitting laser (VCSEL) array on a square detector at 1 cm.

In order to increase the directivity of the diffused laser beam and overfill the solar panel at a link distance of 30 m (designated for the installation in Orkney), an off-axis parabolic mirror Edmund Optics 35–533 with a diameter of 76.2 mm is used. Also, to ensure that no user can open the enclosure of the prototype and be exposed to any radiation above the MPE limit, the enclosure is locked with bolts as recommended by the laser safety agency. The transmitter's optical setup and the illumination pattern of the laser beam at the enclosure aperture are given in Figure 9. It was observed that only two of the four initial hotspots are transmitted in free space. This is because the rays of the bottom two hotspots of the rectangular VCSEL pattern travel a shorter distance than those of the top two hotspots towards the mirror; thus, they are getting reflected with higher power from the mirror.

In practice, to make sure that the laser source was placed at the focal point of the off-axis parabolic mirror; a pitch, yaw, x, y and z translation stage is used. The optical source is attached to the printed circuit board (PCB) of the laser driver and the PCB is mounted on the translation stage. Thus, the beam shape and size can be controlled by modifying any of the five degrees of freedom of the translation stage. In order to ensure that the beam covers the entire area of the solar panel at the 30 m link distance, the beam shape and size were optimized at 20 m distance. Figure 10 gives the simulated irradiance distribution of the beam and the beam observed through a camera and an infrared filter at 20 m. As the beam is not uniform, the beam is analysed along the vertical axes x and y and not along a single axis in Zemax. The Full Width at Half-Maximum (FWHM) intensity along the x-axis and y-axis is calculated to be 135 and 124 mm, respectively. Therefore, an average FWHM intensity of 129.5 mm is determined for the laser beam at 20 m from the transmitter. The beam diameter of the circle observed in practice was measured to be 325 mm, while the size of the solar panel is 306 × 218 mm^2 [16]. Hence, the laser beam was expected to cover the whole solar panel.

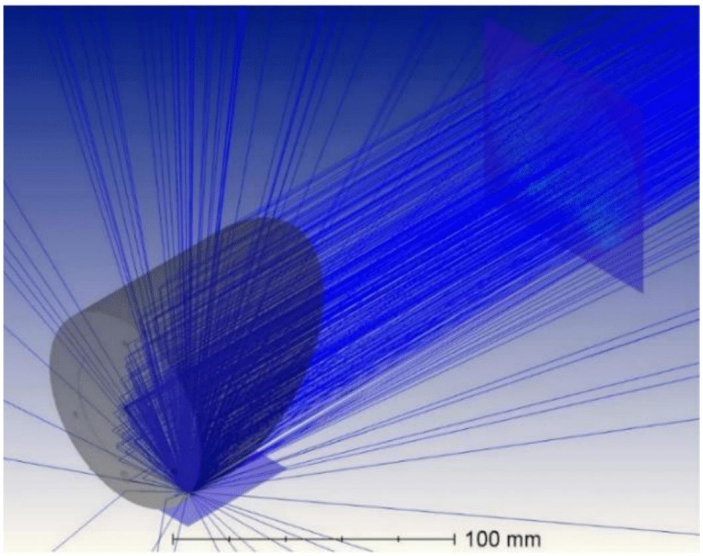

(**a**)

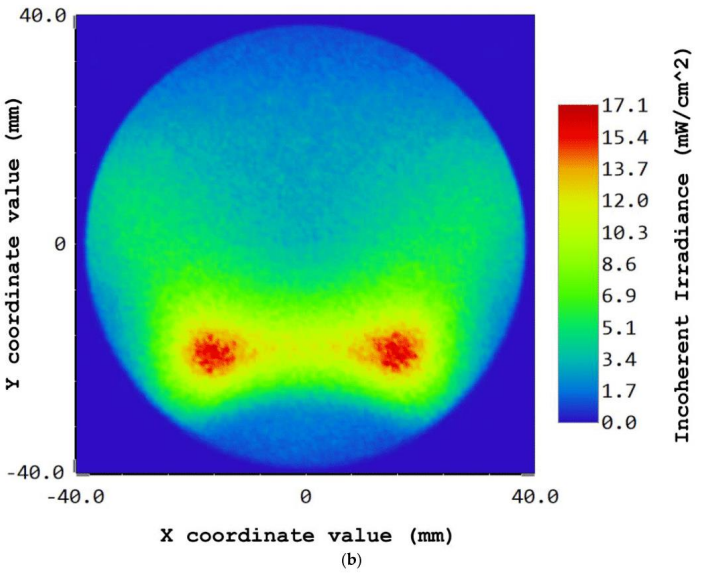

(**b**)

Figure 9. (**a**) Basic optical setup at the transmitter (**b**) laser beam at the enclosure's aperture.

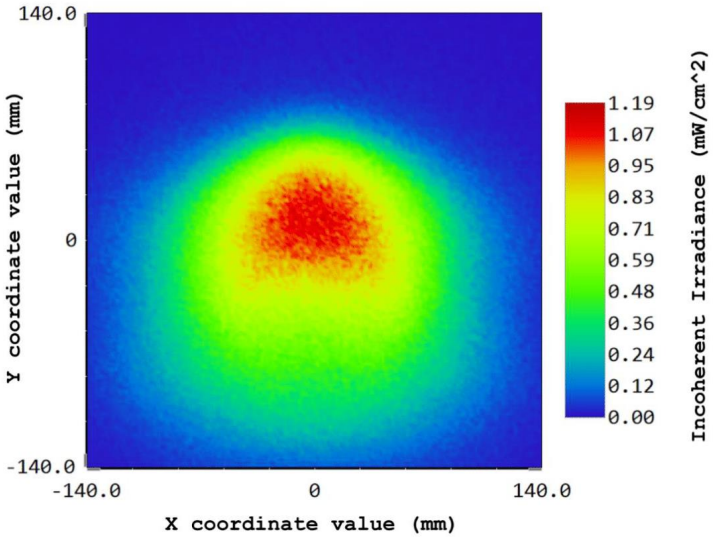

(**a**)

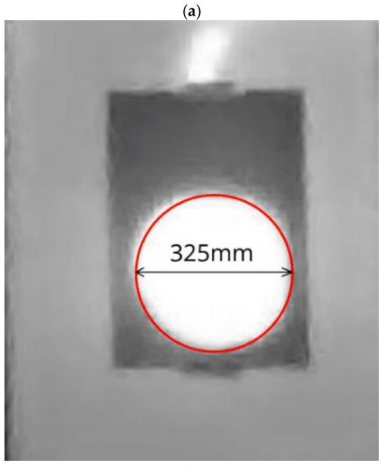

(**b**)

Figure 10. Beam profile at 20 m (**a**) simulated using Zemax; (**b**) captured using an infrared camera.

3.2. Receiver

As mentioned in Section 2, the solar panel has a low-pass frequency response. In order to achieve the optimum bandwidth, the signal needs to be drawn as a current source by holding the voltage constant across the cells. This function is performed by the solar-panel interfacing circuit; it holds the voltage constant across the panel and separates the DC power from the AC signal for further usage as shown in Figure 11.

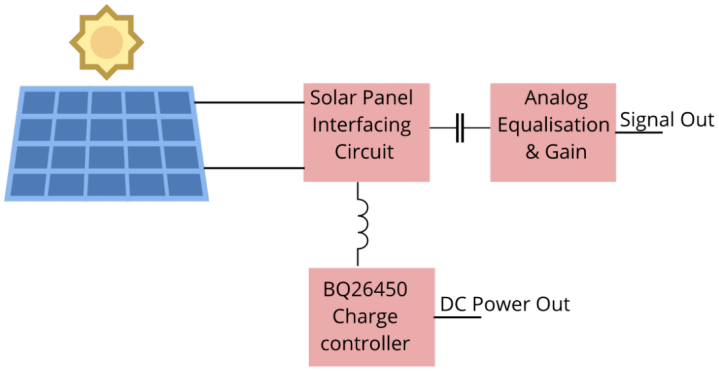

Figure 11. Receiver functional block diagram.

3.2.1. Energy Harvesting and Storage

To harvest energy from solar cells there are two widely used methods: Pulse Width Modulation (PWM) and Maximum Power Point Tracking (MPPT). MPPT has been proven to be the best, as it operates at the maximum point of the panel [21]. A solar panel has a unique point on the *I-V* curve, at which the entire photovoltaic system operates with maximum efficiency and produces its maximum output power; this is the point defined as the maximum power point.

In order to implement MPPT and charge a battery, a charge controller BQ24650 from Texas Instruments Inc. [21] was chosen. This device has the capability of MPPT by ± 0.6% input voltage regulation, the maximum power point can be set and can charge the battery with ± 0.5% charge voltage and ± 3% charge current regulation. The charge controller supports charging Li-Ion/Polymer, $LiFePO_4$ and lead-acid batteries [21]. It uses a constant voltage algorithm which is the simplest MPPT method, which is also desirable for the communication circuitry. The device can be set to a charging voltage threshold at which the voltage is held constant with only the charging current varying depending upon the power generated. Depending on the battery chosen, the charging current and voltage can be set.

A 300 W halogen lamp (OSRAM 64515) was used to illuminate the solar panel which was connected to the charge controller circuit and battery. Using a lux meter, the optical power incident on the panel was measured and at the same time voltmeters were used to measure the voltage across the panel and battery. Ammeters were used to measure the current flowing from the panel to the charge controller circuit and the current flowing from the circuit to the battery. Table 1 shows the data gathered from the measurement and it was calculated that using MPPT 92.7% of the power generated by the panel could be delivered to the battery. The efficiency of the panel was calculated to be 13.5% and the efficiency of the overall system was 12.5%.

Table 1. Power generated from the solar panel and power delivered to the battery.

Incident Light (W)	Power Generated (W)	Power Delivered (W)
30.45	4.11	3.81

From the sun graph [22] for Edinburgh, UK it can be noted that the longest duration of darkness in a year is 16 hours. Hence, a battery pack with a capacity to provide power back up for the unit through the longest darkness hours should be chosen. But on the contrary, the battery should be small enough such that it could be charged throughout the day. One of the two units face west directly, and the solar panels are positioned vertically as they are used as OWC receivers simultaneously. While the other

unit is facing eastwards, the average solar irradiance for vertical panel facing east is comparable to that facing west [23]. Reference [23] shows that the month of January has the least solar irradiance of 0.94 kWh/m^2 on the panel. Hence, the total energy that can be stored using the chosen 5 W Si-based panel with the MPPT charger circuit is calculated to be 7.05 Wh.

In June the solar irradiance is 2.55 kWh/m^2, therefore the total maximum energy that can be stored in a day is 19.13 Wh. As the system was being deployed in June, a battery of 38 Wh capacity was chosen which meant that it would take an average of two days to charge the battery unloaded.

3.2.2. Analogue Equalisation for Communication

In order to have real-time high-speed communication, low complexity in the digital processing chain is desired, which demands a flat channel response to avoid the need for digital filters. The measured 3 dB bandwidth of the chosen solar panel was measured to be 270 kHz. Using analogue equalisation, the bandwidth was increased to 5 MHz. Equalisation is the reversal of distortion incurred by a signal through a channel. Equalisers are used to render the frequency response flat from end to end. When a channel has been equalised, the frequency domain attributes of the signal at the input are reproduced at the output. Analogue equalisation can be achieved by selective attenuation or selective gain. In this system, both techniques were used with a higher weight given to selective gain. The orange curve in Figure 12 depicts the measured response of the solar panel post equalisation. The response was no longer a low pass within the 5 MHz bandwidth of interest. To ensure that the maximum data rate can be obtained, the quality of the signal post-processing can be quantified with Signal-to-Noise Ratio (SNR) i.e., the higher the better. Hence, the whole channel response was measured using the transmitter described in Section 3.1 and the receiver. From Figure 13 it can be inferred that the response is flat and the SNR peaks up to 30 dB, which enables 64-QAM, in other words, a higher data rate.

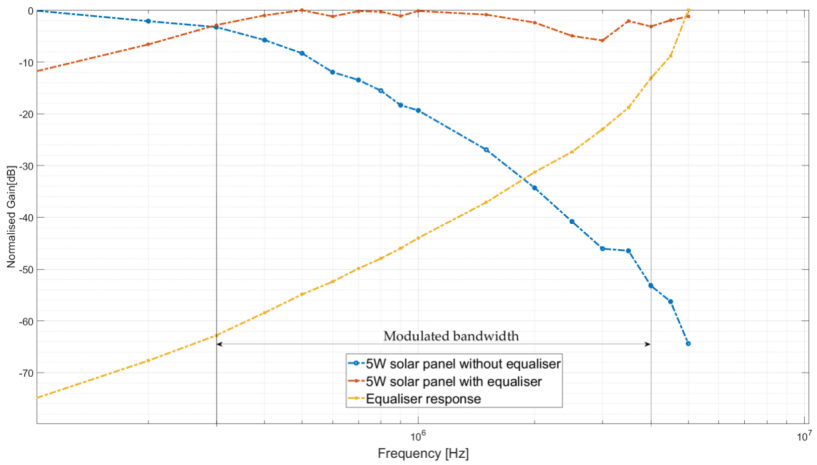

Figure 12. Frequency response of the solar panel with and without equalisation.

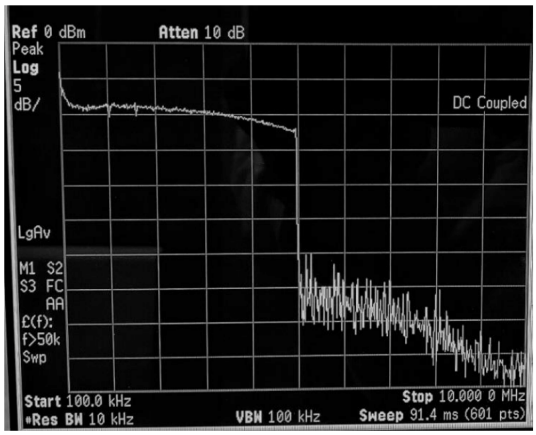

Figure 13. Channel response on a spectrum analyser.

3.3. Overall System Architecture

This section describes the flow of information from the transmitter to the receiver as well as the energy harvesting and storage capability of the system. Figure 14 depicts the working of the transmitter on one end and the receiver unit on the other end. The whole system is designed to be a fully functional bidirectional link with networking capability.

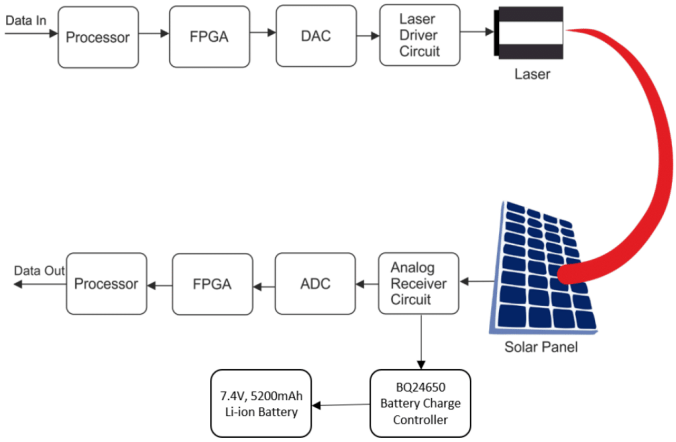

Figure 14. Overall system architecture.

As shown in Figure 14, the data is first fed to the processor to generate the packet with the information to be transmitted as the payload. Then this whole packet is passed on to the FPGA where this is converted to a time-based signal using an OFDM based modulation technique. The DAC then converts the time-based bit symbols to an analogue waveform. As the channel varies due to the change in ambient light, weather, wind and visibility, the laser driver circuit needs to precondition this

analogue waveform. This is based on the feedback of the channel conditions which is determined by the number of received packets dropped and ping time interval. When these two factors go above a given threshold, the optimum signal power search algorithm is triggered. The signal power is varied in a cyclic order of low-high-low on both the transmitters at each end. Meanwhile on both the receiver ends the received packets dropped and ping time interval is monitored. The combination of AC and DC signal power is chosen at each end at which the received packets dropped, and ping time interval is least. Then the signal is modulated onto the output intensity of the laser.

On the receiver side, the solar panel is simultaneously performing two tasks in one, harvesting energy from the sunlight and receiving the transmitted optical signal. As mentioned in Section 3.2, the receiver circuit separates the DC harvested energy from the AC signal. The equalised AC signal is then fed to the ADC which performs the inverse function of a DAC. Then the FPGA demodulates the time-based signal to back digital packets and passes it to the processor. Meanwhile, the DC harvested energy is fed to the charge controller circuit which charges a 3-cell 7.4 V Li-Ion battery with 5.2 Ah capacity. The peak power consumption of the processor, FPGA, DAC, ADC, the laser driver circuit and the receiver circuit is 6 W in total. The 38 Wh battery can, therefore, provide energy for the transceiver unit for about 6.33 hours in the absence of power, making it a self-sustained communication system.

4. Results

The developed OWC system was first deployed on the premises of the University of Edinburgh to test the communication performance under different daylight and weather conditions. The system was left unattended, running for two weeks to gather data.

Figure 15 shows the variation of the data rate of the link against varying wind conditions, visibility, daylight and weather conditions on a day. The weather data were collected from [24] for 7 May 2019 in Edinburgh. The throughput measurement was done using iPerf [25] and the traffic was forced to TCP/IP to emulate real-world bandwidth usage. The data rate peaks at 8 Mbps during nighttime and cloudy conditions. But during the sunnier parts of the day, the data rate dropped to 6.5 Mbps. This can be attributed to the additional thermal noise and shot noise generated in the solar panel when sunlight hits the panel directly. In this scenario, the generation of exciton would be at its peak which increases the thermal and shot noise. The added noise induces fall in signal-to-noise ratio leading to a noticeable drop in the data rate. The next noticeable drop is during periods of rain, where the data rate dropped to the lowest level of 4.5 Mbps. This fall in data rate can be attributed to the bad channel condition due to the presence of rain droplets that attenuate the signal power received [26].

After the testing phase, the system was deployed in Graemsay, Orkney Islands. Figure 16 shows the installation of the units on the properties. A comparison between the installed optical link and the existing broadband connection shows that the upload speed increased by 8 times and the download speed increased by 20% (see Figure 17). The two links were aggregated and provided to the residents thereby doubling the user download experience and enabling them to use higher bandwidth-demanding services such as streaming multiple high-definition videos, high-definition video calls, etc.

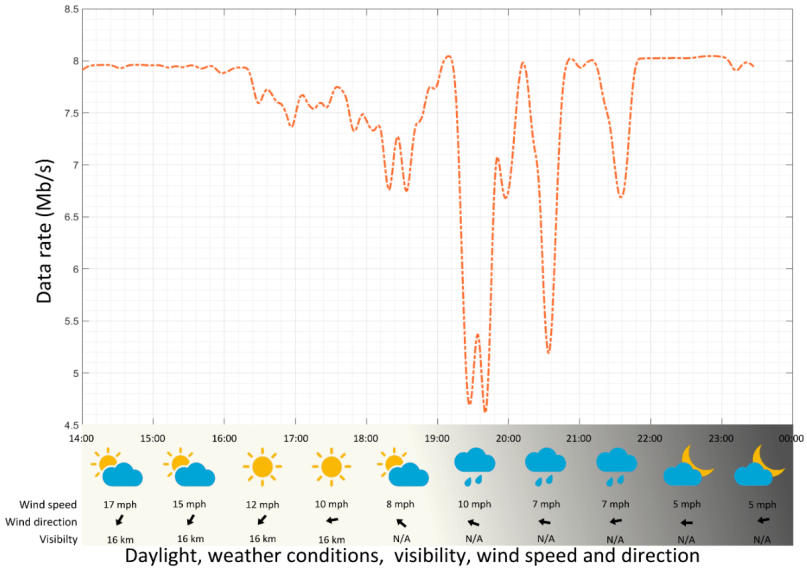

Figure 15. Data rate measurement plot against the daylight and different weather conditions.

(**a**) (**b**)

Figure 16. Installation at the location (**a**) residence property; (**b**) residence property to the lighthouse.

(**a**)

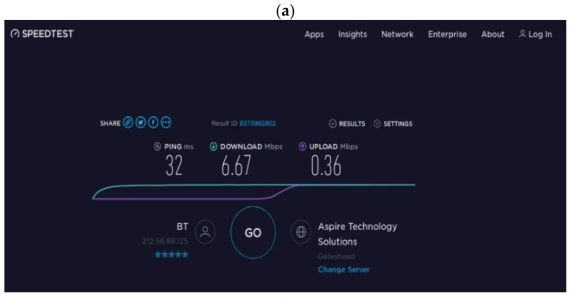

(**b**)

Figure 17. Internet speed test measurements (**a**) through the optical link and (**b**) through landline broadband.

5. Conclusions

This paper introduces an OWC system based on off-the-shelf lasers and solar cells. The solar panel simultaneously harvests 5 W of power and communicates at a data rate of 8 Mb/s. The system has been certified to be eye-safe (Class 1M) and has been installed on the Scottish island of Graemsay to demonstrate achievable performance in the field, under varying weather conditions. The data obtained shows no dropouts on the installed link, with data throughput in excess of existing landline-based broadband connections during 90% of the time.

The use of solar panels shows the possibility of self-powered optical data hubs providing long-distance communications at a much lower cost than exists presently. Cost reduction is achieved through equipment reuse, reducing the need for accurate optical alignment and removing the need for power delivery infrastructure without compromising on outcomes. This system is well suited to rural communities, where the cost of provisioning communication services can be prohibitive, despite strong demand from the scattered population.

The use of rooftop photovoltaic systems, consisting of large solar panel arrays, will enable the implementation of communication techniques designed to multiply the capacity of the link by using multiple independent receiver elements.

Author Contributions: S.D., J.F. and A.S. designed the system and performed the experiments; S.V. and E.P. performed the project administration and H.H. provided supervision and guidance.

Funding: This work was funded by the Department of Digital, Culture, Media and Sport of the United Kingdom as part of the 5G RuralFirst project.

Acknowledgments: The LiFi Research and Development Centre would like to express its gratitude to CloudNet IT Solutions and the Orkney Council for their advice on the design and deployment of the system and their work on the installation of the backhaul link. The LRDC would also like to thank the Northern Lighthouse Board for their support of the project.

Conflicts of Interest: The authors declare no conflict of interest.

Abbreviations

The following abbreviations are used in this manuscript:

ADC	Analog-to-Digital Converter
DAC	Digital-to-Analog Converter
FWHM	Full Width at Half-Maximum
FPGA	Field-Programmable Gate Array
LASER	Light Amplification by Stimulated Emission of Radiation
LED	Light-Emitting Diode
MPE	Maximum Permissible Exposure
MPPT	Maximum Power Point Tracking
OFDM	Orthogonal Frequency Division Multiplexing
OWC	Optical Wireless Communication
PD	Photodiode
RF	Radio Frequency
SNR	Signal-to-Noise Ratio
VCSEL	Vertical-Cavity Surface-Emitting Laser

References

1. Elgala, H.; Mesleh, R.; Haas, H. Indoor optical wireless communication: Potential and state-of-the-art. *IEEE Commun. Mag.* **2011**, *49*, 56–62. [CrossRef]
2. Haas, H.; Yin, L.; Wang, Y.; Chen, C. What is LiFi? *J. Lightwave Technol.* **2016**, *34*, 1533–1543. [CrossRef]
3. Light Communications Alliance. Light Communications Alliance. 2019. Available online: http://lightcommunications.org/ (accessed on 3 August 2019).
4. Tsonev, D.; Chun, H.; Rajbhandari, S.; McKendry, J.J.D.; Videv, S.; Gu, E.; Haji, M.; Watson, S.; Kelly, A.E.; Faulkner, G.; et al. A 3-Gb/s Single-LED OFDM-Based Wireless VLC Link Using a Gallium Nitride µLED. *IEEE Photonics Technol. Lett.* **2014**, *26*, 637–640. [CrossRef]
5. Charles, H.K., Jr.; Ariotedjo, A.P. Review of amorphous and polycrystalline thin film silicon solar cell performance parameters. *Sol. Energy* **1980**, *24*, 329–339. [CrossRef]
6. Hameiri, Z. Photovoltaics literature survey (No. 125). *Progress Photovoltaics Res. Appl.* **2016**, *24*, 405–407. [CrossRef]
7. Bhandari, K.P.; Ellingson, R.J. *A Comprehensive Guide to Solar Energy Systems*; Academic Press: Cambridge, MA, USA, 2018; pp. 233–254.
8. Saltsman, S.O. *The Silicon Solar Cell as an Optical Detector*; Florida Technological University: Orlando, FL, USA, 1976.
9. Kim, S.M.; Won, J.S. Simultaneous reception of visible light communication and optical energy using a solar cell receiver. In Proceedings of the 2013 International Conference on ICT Convergence (ICTC), Jeju, Korea, 14–16 October 2013; pp. 896–897. [CrossRef]
10. Wang, Z.; Tsonev, D.; Videv, S.; Haas, H. Towards Self-powered solar panel receiver for optical wireless communication. In Proceedings of the 2014 IEEE International Conference on Communications (ICC), Sydney, NSW, Australia, 10–14 June 2014.
11. Wang, Z.; Tsonev, D.; Videv, S.; Haas, H. On the design of a solar panel receiver for optical wireless communication with simultaneous energy harvesting. *IEEE J. Sel. Areas Commun.* **2015**, *33*, 1612–1623.
12. Zhang, S.; Tsonev, D.; Videv, S.; Ghosh, S.; Turnbull, G.A.; Samuel, I.D.W.; Haas, H. Organic solar cells as high-speed data detectors for visible light communication. *Optica* **2015**, *2*, 607–610. [CrossRef]
13. Fakidis, J.; Videv, S.; Helmers, H.; Haas, H. 0.5-Gb/s OFDM-Based Laser Data and Power Transfer Using a GaAs Photovoltaic cell. *IEEE Photonics Technol. Lett.* **2018**, *30*, 841–844. [CrossRef]
14. Lashkari, A.H.; Danesh, M.M.S.; Samadi, B. A survey on wireless security protocols (WEP, WPA and WPA2/802.11i). In Proceedings of the 2009 2nd IEEE International Conference on Computer Science and Information Technology, Beijing, China, 8–11 August 2009; pp. 48–52. [CrossRef]

15. Rana, F. Photodetectors and Solar Cells. In *Semiconductor Optoelectronics*; Rana, F., Ed.; Cornell University: Ithaca, NY, USA.
16. Solar Technology International Ltd. 5 Watt Solar Panel Kit. Available online: https://www.solartechnology.co.uk/pv-logic/5w-solar-panel-kit (accessed on 9 January 2019).
17. Fakidis, J.; Videv, S.; Kucera, S.; Claussen, H.; Haas, H. Indoor Optical Wireless Power Transfer to Small Cells at Nighttime. *J. Lightwave Technol.* **2016**, *34*, 3226–3258. [CrossRef]
18. Bloom, S.; Korevaar, E.; Schuster, J.; Williebrand, H. Understanding the performance of free-space optics. *J. Opt. Netw.* **2003**, *2*, 178. [CrossRef]
19. British Standards Institution. *Safety of Laser Products. Equipment Classification and Requirements*; BS EN 60825-1:2014; BSI: London, UK, 2014.
20. OSRAM Opto Semiconductors GmbH. BIDOS®, PLPVQ 940A. Available online: https://www.osram.com/ecat/BIDOS%C2%AE%20PLPVQ%20940A/com/en/class_pim_web_catalog_103489/global/prd_pim_device_5062066/ (accessed on 6 February 2019).
21. Texas Instruments Inc. BQ24650 High Efficiency Synchronous Switch-Mode Charger Controller—Solar battery charger. Available online: http://www.ti.com/product/BQ24650 (accessed on 25 March 2019).
22. Matti Tukiainen. Sun Graph Edinburgh. GAISMA. 2005. Available online: https://www.gaisma.com/en/location/edinburgh.html (accessed on 12 July 2019).
23. Greenstream Publishing Limited. Solar Irradiance. Solar Electricity Handbook. 2009. Available online: http://www.solarelectricityhandbook.com/solar-irradiance.html (accessed on 10 July 2019).
24. Time and Date. Time and Date. 1995. Available online: https://www.timeanddate.com (accessed on 7 May 2009).
25. Dugan, J.; Estabrook, J.; Ferbuson, J.; Gallatin, A.; Gates, M.; Gibbs, K.; Hemminger, S.; Jones, N.; Qin, F.; Renker, G.; et al. iPerf—The TCP, UDP and SCTP Network Bandwidth Measurement Tool. Available online: https://iperf.fr/ (accessed on 12 July 2019).
26. Khalighi, M.A.; Uysal, M. Survey on Free Space Optical Communication: A communication theory perspective. *IEEE Commun. Surv. Tutor.* **2014**, *16*, 2231–2258. [CrossRef]

© 2019 by the authors. Licensee MDPI, Basel, Switzerland. This article is an open access article distributed under the terms and conditions of the Creative Commons Attribution (CC BY) license (http://creativecommons.org/licenses/by/4.0/).

Towards 100 Mb/s Optical Wireless Communications Using a Silicon Photovoltaic Receiver

Sovan Das
Institute for Digital Communications, *School of Engineering*, *University of Edinburgh*
Edinburgh, United Kingdom
sovan.das@ed.ac.uk

John Fakidis, Adrian Sparks, Enrique Poves, Stefan Videv and Harald Haas
LiFi Research and Development Centre, *Department of Electronic & Electrical Engineering, University of Strathclyde*
Glasgow, United Kingdom
{john.fakidis, adrian.sparks, enrique.poves, stefan.videv, harald.haas}@strath.ac.uk

***Abstract*— In this paper, a low cost optical wireless communications link with a data rate of 74 Mb/s at a bit-error ratio of 3.3×10^{-3} is demonstrated. The components are all low cost, off-the-shelf parts, including the laser transmitter and silicon solar panel receiver. This performance is achieved by extending the usable bandwidth using analog equalization and digital techniques such as adaptive bit and power loading. Also, the performance of two spectrally efficient modulation schemes, namely direct-current biased optical orthogonal frequency division multiplexing (DCO-OFDM) and pulse amplitude modulation discrete multitone (PAM-DMT) is evaluated and compared. It is shown that DCO-OFDM outperforms PAM-DMT because of efficient bandwidth usage with adaptive bit loading and pre-distortion introduced by adaptive power loading. Furthermore, it is shown that PAM-DMT can avoid complex system designs and still achieve comparable data rates to that of OFDM with higher link reliability.**

Keywords—Free-space Optical Communication, Optical Wireless Communication, OFDM, PAM-DMT, Photovoltaics, LiFi

I. Introduction

With an ever-growing network of billions of interconnected smart devices in the era of the Internet of Things high-speed communication faces many challenges. One of these is the rapidly growing digital divide between urban and rural areas. In many rural parts of the world, the internet-based transformation of healthcare, education and commerce is slowed by poor network infrastructure. This coupled with an ever-rising demand for network capacity, effective solutions to improve the availability and capacity of rural connectivity are urgently needed.

Optical wireless communications (OWC) has been widely considered to be a potential technology to bridge the digital divide [1]. Light Fidelity (LiFi) [2] is a proven technology within OWC which utilizes light to offer an unprecedented amount of new communication spectrum – up to 2600 times the 300 GHz bandwidth of the current radio frequency (RF) spectrum. In OWC, light-emitting diodes (LEDs) or lasers are used for wireless data transmission in indoor or outdoor environments [3]. Typical p-type-intrinsic-n-type (PIN) or avalanche photodiodes (APD) are used as data receivers. These devices have two main disadvantages – they require an external power source to operate and their small active area makes alignment challenging. A promising solution to these problems is the use of solar panels as data receivers [4]. Solar panels are designed to convert solar energy to electrical energy. They can harvest electrical DC power, not only from sunlight but also from irradiation coming from lasers or LEDs. The active area of solar panels is typically much larger than that of conventional photodiodes. With the addition of electronic components, solar panels can also be repurposed into OWC receivers [5].

Photovoltaic (PV) panels have become one of the most inexpensive renewable sources of electrical energy. They are employed in many applications both on earth and in space. Choosing the appropriate panel technology can be difficult. Distinguishing between different types of solar panels often means differentiating between single-junction and multi-junction solar panels as well as first, second or third-generation devices [6]. Single-junction and multi-junctions solar cells differ in the number of layers on the solar panel that captures the sunlight, whereas the classification by generation focusses on the materials and efficiency of the different types of solar cells that make up a panel. The first generation of solar panels includes silicon (Si) solar panels that are widely installed due to their low manufacturing cost. They are divided into two categories: monocrystalline and polycrystalline. The former has higher efficiency and better temperature stability than the latter [6]. Second-generation solar panels refer to diverse types of thin-film solar cells and are mainly used in photovoltaic power stations. Thin-film solar cells are flexible and open up possibilities for alternative applications, such as windowpanes with solar panels, solar-powered car windshields and smartwatches. Third-generation solar panels include a variety of thin-film technologies, but most of these are still in the research and development phase. Some generate electricity by using organic materials, others use inorganic compound semiconductors such as cadmium telluride (CdTe), gallium arsenide (GaAs) and gallium indium phosphide (GaInP). These types of solar cells are also referred to as concentration PV (CPV) cells. They generate electricity in the same way as conventional PV systems, but they have a small active area which requires them to have an optical element such as a Fresnel lens to concentrate light on to the active area. The efficiency of a CPV panel can be high and results up to 47.1% has been reported under illumination density that corresponds to the equivalent of 143 suns concentration [7]. This efficiency gain comes with the disadvantages of a requirement for cooling, optical elements

to concentrate the light and complex systems to align the optical elements and track the sun.

There are several experiments reported in the literature that use solar panels or PV cells as data receivers in OWC systems [5]. In [8], a data rate of 522 Mb/s is reported to be achieved for a 2 m infrared wireless link by using a high-speed vertical-cavity surface-emitting laser (VCSEL) and a PV cell. The use of a single variable resistor in [8] has shown that simultaneous energy harvesting and data communication for the same value was not possible. Therefore, a follow-up study shown in [9] with an AC-DC decoupling receiver circuit achieved a record data rate of 1 Gb/s under short-circuit conditions. In [10], a data rate of 34.2 Mb/s is demonstrated by using a red laser diode and an organic solar cell with a wireless link distance of 1 m. The communication channel is optimally used in [8]- [10] by applying adaptive bit and power loaded OFDM.

In this paper, a 2 m wireless link consisting of an off-the-shelf VCSEL, off-axis parabolic mirror and a polycrystalline solar panel is developed. A data rate of 74 Mb/s is achieved with the use of OFDM adaptive bit and power loading, and analog equalization. To the best of our knowledge, this is the highest data rate reported in the literature for Si solar panels used as OWC receivers. Also, the spectrally efficient schemes of OFDM and PAM are compared. It is shown that OFDM outperforms PAM due to the optimal use of bandwidth and the pre-distortion induced by power loading.

The rest of the paper is structured as follows: In Section II, previous work is reviewed and background information is given. Section III gives the methodology used. Results are discussed in Section V and the concluding remarks are given in Section VI.

II. Photovoltaics as OWC receiver

Solar panels were never developed or designed as an optical communication receiver. Therefore, it is important to consider the electrical characteristics of a solar panel which are important to communications. These are linearity, speed of response, sensitivity to incident optical signal and temperature stability. As discussed in [11] the electrical AC signal output power of a solar panel changes proportionately with the incident optical power of the AC signal. The wavelength sensitivity of the solar panel depends on its material composition. For Si, the sensitivity peaks between 900 and 1000 nm [12]. Therefore, it is desirable to choose the optical transmitter wavelength within this range. This will result in improved signal output power from the receiver and thus improved electrical signal-to-noise ratio (SNR). In terms of temperature stability, it has been found that with an increase in temperature the efficiency of the solar panel decreases [6]. For the chosen solar panel, the temperature coefficient was found to be -0.13V/K [11], this is constant and the output deviation can be determined and compensated with thermal solutions if needed. The speed of response of the solar panel is one of the most important factors to be considered when using it as an optical communication receiver as this sets the link bandwidth. It is observed that the larger the active area, the larger the diffusion capacitance, and thus the intrinsic bandwidth of the solar cell is reduced [11]. The intrinsic bandwidth of a solar cell depends on the thickness of the depletion region, which is determined by the semiconductor doping levels. Other factors such as junction and parasitic capacitance affect the extrinsic bandwidth of a solar cell. Therefore we can observe significantly higher data rates in [10], [9] and [13] as the active area is comparatively small compared to [14], [11] and [5]. Another factor which plays a role in the achievable bandwidth of the solar panel is the illumination pattern of the optical signal on the active area. When all the cells in the panel are uniformly illuminated, the best performance of the panel can be expected [11]. With uneven illumination, darker cells act as a resistive load on the output from the more brightly illuminated cells, resulting in poor electrical output [11].

TABLE I. OWC links using Si PV cells as data receivers state of the art

Ref.	Active Area (cm^2)	Modulation Technique	Distance (m)	Data Rate (Mbps)
This work	667.08	QAM-OFDM	2	74.03
[15]	-	PAM-DMT	0.1	17.05
[14]	7.5	QAM-OFDM	2	15.03
[13]	432	QAM-OFDM	0.95	11.84
[11]	667.08	QAM-OFDM	30	8
[5]	432	QAM-OFDM	0.39	7.01
[16]	7.29	-	0.4	0.003

TABLE I. presents a comparison of the communication link performance between several publications, where Si-based solar panels are used. It can be seen that none of the experiments has achieved data rates beyond 17 Mb/s, far short of the 74 Mb/s reported here. Also, note that apart from [15] all the studies use either OFDM or PAM. Furthermore, in this work and in [11] a Si solar panel with a very large area compared with the panels in [5], [11]-[16] is used. This makes the proposed system more tolerant to vibrations, misalignment, and weather disturbances. Moreover, it also makes this particular system more suitable for simultaneous data transmission and energy harvesting. However, in [11] the longest communication distance has been achieved under real-world conditions.

III. Methodology

A. Transmitter

In this work, an off-the-shelf infrared (IR) 940 nm laser (OSRAM PLPVQ-940A) is selected because its wavelength of operation approaches the responsivity peak for Si solar cells. The device consists of a 2x2 array of VCSELs and an optical diffuser element on top of the package. An off-axis parabolic mirror (Edmund Optics 35-533) is used to decrease the divergence of the laser beam so that the solar cells – connected in series – of the panel are illuminated uniformly. The entire transmitter module is enclosed for safety [17]. Thus, the mirror placed at the aperture of the enclosure is seen as an extended optical source at a 2 m distance and this helps meet eye safety requirements. The laser-PV system is classified to be Class 1M and is considered to be safe, provided that the beam is not observed [17] through any magnifying optical aid such as binoculars or telescopes. The peak optical power of the laser is measured to be 420 mW.

The laser is driven using a voltage-controlled current driver and the -3 dB bandwidth of the laser driven by the driver is measured to be 65 MHz [11].

B. Receiver

A readily available 5 W polycrystalline solar panel (RS Pro 904-6128) is considered. This panel offers a large active area at a very low cost and avoids the issues faced with CPVs. It has previously been established that as the area of the panel increases, so does its capacitance. Due to the high capacitance, Si solar panels have very low -3 dB communication bandwidth compared to conventional photodiodes [11]. The frequency response of the solar panel has the shape of a low-pass filter (LPF), rolling off at 40 dB/decade between 100 kHz – 1 MHz and 80 dB/decade between 1 MHz – 10 MHz. This quick roll off makes digital equalization and pre-distortion challenging as the higher frequency subcarriers have very low signal power, which results in poor SNR. This is because the quantization noise of the digital-to-analog and analog-to-digital converters (DAC and ADC) is dominant over the low signal power. If the signal power is increased, the lower frequency subcarriers are clipped due to the limited dynamic range of the DAC and ADC. Therefore, equalization is the preferred approach. To equalize the frequency response of the solar panel, a combination of digital and analog equalization is required. The digital equalization is achieved by pre-distortion on the transmitted signal with adaptive power loading and is explained in Section III-C.

A passive filter within two amplifier stages has been designed, as shown in Fig. 1, to perform the analog equalization. The frequency response of such a structure has a 40 dB/decade gain and hence this will perform the reverse distortion of the signal, *i.e.* equalization. To perform the equalization a second-order filter was designed based on a modified version of a notch filter and a bandpass filter as shown in Fig. 2 and Fig. 3 respectively. The modified notch filter provides the reverse distortion to compensate the 40dB/octave roll-off and the bandpass filter is used to attenuate the undesired low and high frequencies. The resulting filter structure can be mathematically expressed as shown in (1). The values of L, C_1, C_2 and R determines the filter's stability and peak gain at the desired frequency. This is simulated in TINA-TI [18] and the AC transfer characteristic of the whole receiver circuit is shown in Fig. 4. It is important that the design results in low noise so that the signal quality does not deteriorate further; therefore, ultra-low-noise operational amplifiers are selected.

$$H(s)=\frac{x_a x_c+x_c R}{x_a R+x_a x_c+x_c R} \tag{1}$$

$$x_c=\frac{x_e LC_1 s^2+x_e C_1 s+Ls}{x_c C_1 s} \tag{2}$$

$$x_a=x_e LC_1 s^2+x_e C_1 s+Ls \tag{3}$$

$$x_e=\frac{L}{LC_2 s^2+1} \tag{4}$$

Furthermore, close attention needs to be paid on how the panel is interfaced to the receiver circuit as there should be

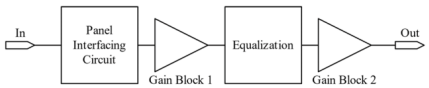

Fig. 1 Receiver Circuit

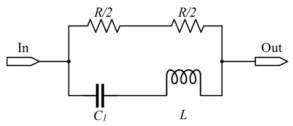

Fig. 2 Modified Notch Filter

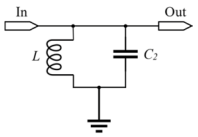

Fig. 3 Bandpass Filter

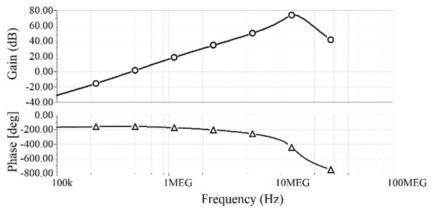

Fig. 4 Equalizer AC transfer characteristic

minimum reflection and attenuation at the solar panel and receiver circuit interface. As found in [11] and [5] the electrical load on the panel should be kept as low as possible to maximize the electrical bandwidth. Hence, the interfacing circuit ensures that the DC and AC from the solar panel are separated effectively and the receiver circuit and solar panel have no impedance mismatch.

C. Modulation Schemes

In OWC, intensity modulation and direct detection (IM/DD) is used, *i.e.* the intensity of the optical source is modulated with the desired signal to be transmitted, the change in the intensity is detected by a receiver and the signal is demodulated. The two most widely used, spectrally efficient, modulation schemes with IM/DD are DCO-OFDM and PAM [19].

OFDM is a digital modulation scheme where the digital data is encoded on multiple carrier frequencies that are orthogonal to each other. In conventional wireless and wired communication, OFDM is used because of its robustness against intersymbol interference (ISI) caused by a dispersive channel. Use of OFDM can be commonly seen in mobile communications. For optical communication, OFDM has an advantage over on-off-keying and pulse position modulation

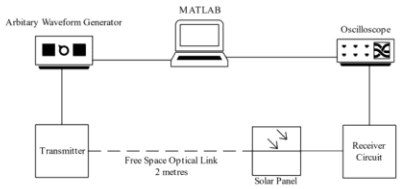

Fig. 5 Experimental Setup

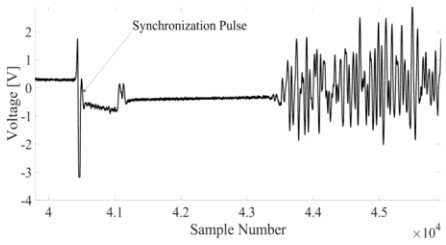

Fig. 6 Acquired OFDM Packet Capture with a synchronization pulse

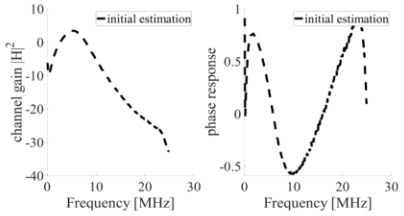

Fig. 7 Channel gain and phase response

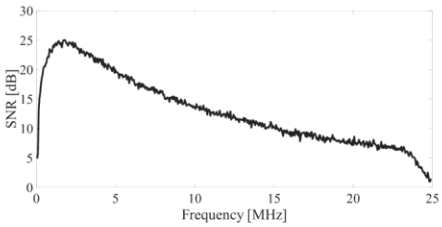

Fig. 8 SNR estimation

because of its spectral and power efficiency [19]. In conventional OFDM, the generated signal is bipolar and complex. Bipolar and complex signals cannot be used in optical communication as the intensity of light cannot be negative and phase modulation and detection in incoherent systems is not possible [19]. Real signals in OFDM are generated using Hermitian symmetry. This is achieved by mapping *N/2* complex symbols to subcarriers 0 to *N/2−1* and then assigning the respective complex conjugate value to the respective subcarrier with a negative index, where *N* is the total number of subcarriers. In this experiment 1024 subcarriers were used, *i.e.* inverse fast Fourier transform (IFFT) size was 1024. Hence, 511 subcarriers were loaded with data and the rest were loaded with the complex conjugate of the data. The discrete Fourier transform (DFT) of this symbol set results in a real-valued time-domain signal. This is normally performed after symbol mapping. When this signal is superimposed over the DC bias of the light source it becomes unipolar and is termed as DC-Optical OFDM. In DCO-OFDM after the channel estimation, if the channel response is not flat then additional power could be added to the attenuated sub-carriers. In practical systems pre-distortion and/or pre-emphasis is useful due to the LPF response. This process is known as adaptive power loading. Similarly, based on the SNR of each subcarrier, the appropriate modulation scheme is selected; this is known as adaptive bit-loading. The quadrature amplitude modulation (QAM) and demodulation are implemented using the communication toolbox of MATLAB [20]. The rest of the experimental OFDM stages are implemented using the communication and RF toolbox functions of MATLAB.

PAM is a signal modulation technique where the data is encoded on to the amplitude of a series of pulses. PAM is used in many systems, including Ethernet communication and digital television transmission. In optical systems, the channel can be accurately estimated since there is no fading and the channel varies slowly. Thus, pulse shapes are not distorted as easily as in RF communication. The generated digital PAM samples have real bipolar values. To avoid signal clipping the analog time-domain PAM signal needs to be scaled and biased to fit the dynamic range of the laser transmitter. Hence, this makes it an ideal choice for optical communication and the implementation is straight-forward. Also, to use the bandwidth efficiently multiple subcarriers are used similar to that in OFDM and this type of PAM is referred to as Pulse Amplitude Modulated Discrete Multitone (PAM-DMT) [19]. In this experiment, at the receiver, the signal is sampled at least twice the Nyquist rate, digitally matched filtered and down-sampled to the symbol rate. A minimum mean square error filter is applied to further reduce the ISI and noise. The PAM modulation and demodulation are implemented in the communication toolbox of MATLAB [21]. The subsequent stages were realized using RF toolbox of MATLAB, similar to the OFDM implementation.

IV. Experimental Setup

In this section, it is shown how the elements described in Secs III.A, III.B and III.C have been put together to build a complete communications link. The modulation techniques discussed in Sec. III.C are implemented in MATLAB. The OFDM and PAM packets are generated on a computer and then fed to a Keysight 33522A arbitrary waveform generator over Ethernet. The signal is then fed to the transmitter circuit over a coaxial cable, type RG-18. The transmitter and receiver circuits are powered using benchtop power supplies. Ferrite cores are used on the power supply cables to ensure external powerline and RF noise is not added to the transmitter and receiver circuits. Powerline noise can affect the SNR of the transmitted or received signals significantly. The signal output of the receiver circuit is connected to an Agilent MSO7000B oscilloscope using an RG-18 coaxial cable. The signal on the oscilloscope is then captured and

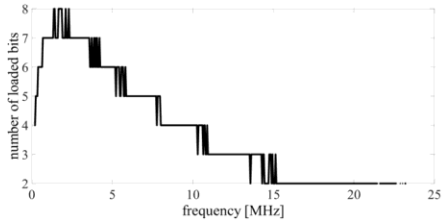

Fig. 9 Bit loading

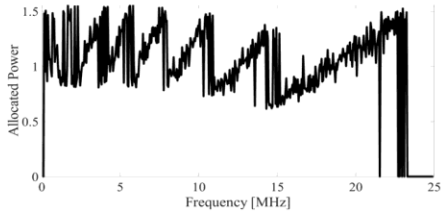

Fig. 10 Power Loading

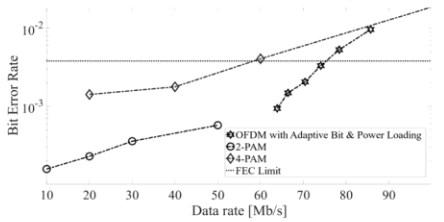

Fig. 11 BER vs. Data Rate for OFDM and PAM

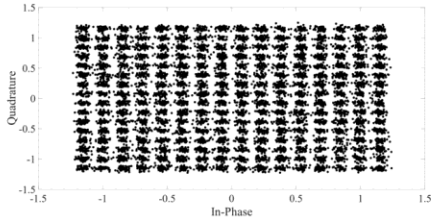

Fig. 12 Constellation Diagram (256-QAM)

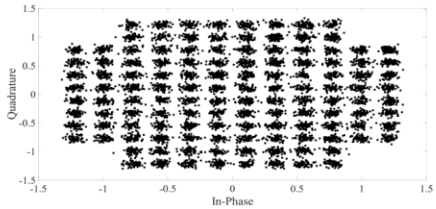

Fig. 13 Constellation Diagram (128-QAM)

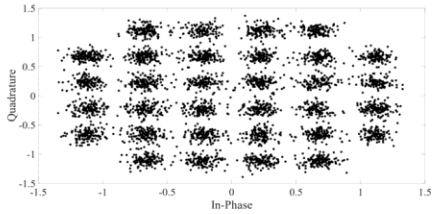

Fig. 14 Constellation Diagram (32-QAM)

transferred to the computer over USB for processing. The experiment is set up as shown in Fig. 5. For data rate and BER measurement with OFDM, the signal is generated with 250 Msample/s and 5 sample/symbol. Hence, the resulting symbol rate is 50 MBd and the bandwidth of the signal is 25 MHz. This generated signal was passed through the analog frontends and captured on the oscilloscope. A synchronization pulse as shown in Fig. 6 is used to trigger the oscilloscope. The captured signal was then processed in MATLAB and the experiment was repeated for different targeted BERs. The data rate is estimated and plotted against the respective BER and shown in Sec. V. Similarly, the experiment was repeated for PAM-DMT with 5 MHz, 10 MHz, 15 MHz and 25 MHz signal bandwidths for different modulation orders. The highest modulation order achieved is 4-PAM. 8-PAM or higher-order modulation could not be used due to the lack of sufficient SNR for the selected bandwidths. The measured data rate and BER for all the cases are tabulated in TABLE II. Also, the results are plotted in Fig. 11 for comparison with the OFDM results.

TABLE II. DATA RATE & BER MEASUREMENT FOR PAM-DMT

Bandwidth (MHz)	Modulation Order			
	2-PAM		4-PAM	
	Data rate (Mb/s)	BER	Data rate (Mb/s)	BER
5	10	1.5×10^{-4}	20	1.4×10^{-3}
10	20	2.2×10^{-4}	40	1.8×10^{-3}
15	30	3.5×10^{-4}	60	4×10^{-3}
25	50	5.7×10^{-4}	100	1.9×10^{-2}

V. EXPERIMENTAL RESULTS AND DISCUSSION

Upon successful completion of the experiment, the highest data rate achieved within the forward-error correction (FEC) limit is 74.03 Mb/s with a BER of 3.3×10^{-3}. The highest data rate that is achieved in the experiment is 100 Mb/s with 4-PAM, but the BER is 1.9×10^{-2}, which is over the FEC limit of 3.8×10^{-3} [22] and the erroneous data may not be recoverable. The additional results obtained from the experiment are the overall channel response and the estimated SNR as depicted in Fig. 7 and Fig. 8 respectively. Fig. 9 and Fig. 10 show that the adaptive bit and power loading has used the bandwidth efficiently. The subcarriers with an SNR below 10 dB are modulated with binary phase-shift keying (BPSK) while the subcarriers with SNR higher than 10 dB are modulated using constellations from 4-QAM to 256-QAM based on the SNR thresholds for the respective modulation orders. Fig. 12, Fig. 13 and Fig. 14 shows the received signal's constellation diagrams for 256-QAM, 128-QAM and 32-QAM. From the received signal's constellation

diagrams, it can be qualitatively inferred that most of the signal bits were decoded. Further investigating Fig. 8 and Fig. 10 it can be seen that the high-frequency subcarriers between 15 MHz – 22 MHz have a gradual increment in power which is comparable to the roll-off in channel gain. The intermittent peaks in power allocation could be attributed to compensation for signal harmonics. These harmonics could be generated by non-linearities in the signal chain amplifiers.

For PAM-DMT upon investigating Fig. 8 and TABLE II. it is noticeable that the BER is comparatively lower than OFDM. The performance of 2-PAM is highly robust over the whole bandwidth of 25 MHz achieving 50 Mb/s with a BER of 5.7×10^{-4} which is 6.6 times below the FEC limit [22]. On the other hand for 4-PAM the maximum usable bandwidth is 15 MHz as the BER of 4×10^{-3} is on the limits of FEC [22]. From this, it can be concluded that PAM-DMT is favourable over QAM-OFDM when the system design is desired to be uncomplicated and link reliability takes priority over a high data rate.

From Fig. 11 it is clear that OFDM achieves significantly higher data rates than PAM-DMT. The lowest data rate achieved with QAM-OFDM is 63.89 Mb/s with a BER of 9.39×10^{-4} while the highest usable data rate with PAM-DMT is 60 Mb/s with a BER of 4×10^{-3}. This difference in data rate can be attributed to the added benefit of adaptive bit and power loading in OFDM. The pre-distortion introduced by adaptive power loading and the efficient use of subcarriers with high SNR enhances the data rate achieved. In PAM-DMT, the modulation depth is fixed for the whole bandwidth, even if the subcarriers between 500 kHz – 5 MHz have an SNR above 20 dB. As the PAM levels are not adaptively loaded. Thus, the maximum modulation depth that could be used is 4-PAM which is dictated by the subcarriers beyond 10 MHz that have SNR below 13 dB.

Hence, it can be concluded that to achieve high data rates with a BER that is lower than the FEC limit using a solar panel receiver, OFDM with adaptive bit and power loading is desirable, at the cost of system complexity. However, the use of PAM-DMT can be helpful in cases where link reliability and simple system design are the major requirements and high data rates are not so important.

In this experiment, the optical frontends were not calibrated for long distance transmission. The signal processing techniques discussed in this paper can be combined with the optical front-ends used in [11] to increase the link distance to more than 2 m.

VI. Conclusions

In this paper, we have shown that analog equalization and adaptive bit and power loading in OFDM offer high-speed OWC links with solar panels as data detectors. Also, upon comparing two spectrally efficient modulation schemes *i.e.* PAM-DMT and DCO-OFDM for the same setup, it was evident that DCO-OFDM achieves higher data rates but at the cost of higher complexity. In addition, an analog equalizer for the PV receiver circuit was designed to compensate for the low pass response of the PV panel when used as an optical detector.

Acknowledgements

The work of H. Haas was supported by the Engineering and Physical Sciences Research Council under the Established Career Fellowship Grant EP/R007101/1, the Wolfson Foundation and the Royal Society.

References

[1] Mohammad Ali Khalighi and Murat Uysal, "Survey on Free Space Optical Communication: A communication theory perspective," IEEE Communications Surveys & Tutorials, vol. 16, no. 4, pp. 2231-2258, 2014.

[2] Harald Haas, Liang Yin, Yunlu Wang, and Cheng Chen, "What is LiFi?," *Journal of Lightwave Technology*, vol. 34, no. 6, pp. 1533-1543, 2016.

[3] Hany Elgala, Raed Mesleh, and Harald Haas, "Indoor optical wireless communication: potential and state-of-the-art," *IEEE Communications Magazine*, vol. 49, no. 9, pp. 56-62, 2011.

[4] Stephen O. Saltsman, "The Silicon Solar Cell as an Optical Detector," 1976.

[5] Zixiong Wang, Dobroslav Tsonev, Stefan Videv, and Harald Haas, "Towards Self-powered solar panel receiver for optical wireless communication," *IEEE ICC Optical Networks & Systems*, 2014.

[6] Ziv Hameiri, "Photovoltaics literature survey (No. 125)," *Progress in Photovoltaics: Research and Applications*, vol. 24, no. 3, pp. 405-407, 2016.

[7] John F. Geisz et al., "Six-junction III–V solar cells with 47.1% conversion efficiency under 143 Suns concentration," *Nature Energy*, vol. 5, pp. 326-335, April 2020.

[8] John Fakidis, Stefan Videv, Henning Helmers, and Harald Haas, "0.5-Gb/s OFDM-Based Laser Data and Power Transfer Using a GaAs Photovoltaic Cell," *IEEE Photonics Technology Letters*, vol. 30, no. 9, May 2018.

[9] John Fakidis, Henning Helmers, and Harald Haas, "Simultaneous Wireless Data and Power Transfer for a 1-Gb/s GaAs VCSEL and Photovoltaic Link," *IEEE Photonics Technology Letters*, vol. 32, no. 19, pp. 1277-1280, October 2020.

[10] Shuyu Zhang et al., "Organic solar cells as high-speed data detectors for visible light communication," *Optica*, vol. 2, no. 7, pp. 607-610, 2015.

[11] Sovan Das et al., "Towards Energy Neutral Wireless Communications: Photovoltaic Cells to Connect Remote Areas," *Energies*, vol. 12, no. 19, October 2019.

[12] Sudhakar K, Noopur Jain, and Shivani Bagga, "Effect of Color filter on the performance of solar photovoltaic module," in *International Conference on Power, Energy and Control*, 2013.

[13] Rohail Sarwar et al., "Visible Light Communication Using a Solar-Panel Receiver," in *International Conference on Optical Communications and Networks (ICOCN)*, Wuzhen, China, 2017.

[14] Zixiong Wang, Dobroslav Tsonev, Stefan Videv, and Harald Haas, "On the design of a solar panel receiver for optical wireless communication with simultaneous energy harvesting," *IEEE Journal on Selected Areas in communications*, 2015.

[15] Won-Ho Shin, Se-Hoon Yang, Do-Hoon Kwon, and Sang-Kook Han, "Self-reverse-biased solar panel optical receiver for simultaneous visible light communication and energy harvesting," *Optical Express A1300*, 2016.

[16] Sung-Man Kim and Ji-San Won, "Simultaneous reception of visible light communication and optical energy," in *International Conference on ICT Convergence (ICTC)*, Jeju, 2013.

[17] British Standards Institution, *Safety of laser products. Equipment classification and requirements [BS EN 60825-1:2014].*: BSI, 2014.

[18] Texas Instruments. (2020, May) TINA-TI SPICE-based analog simulation. [Online]. http://www.ti.com/tool/TINA-TI

[19] Mohamed Sufyan and Harald Haas, "Modulation Techniques for LiFi," *ZTE Communications*, vol. 14, pp. 29-40, 2016.

[20] Mathworks Inc. (2020, May) Quadrature Amplitude Modulation (QAM). [Online]. https://uk.mathworks.com/help/comm/ref/qammod.html

[21] Mathworks Inc. (2020, May) Pulse Amplitude Modulation. [Online]. https://uk.mathworks.com/help/comm/ref/pammod.html

[22] H. G. Weber and M. Nakazawa, *Ultrahigh-Speed Optical Transmission Technology.*: Springer-Verlag Berlin Heidelberg, 2007.

Effect of Sunlight on Photovoltaics as Optical Wireless Communication Receivers

Sovan Das, Adrian Sparks, Enrique Poves, Stefan Videv, John Fakidis, *Member, IEEE*, and Harald Haas, *Fellow, IEEE*

***Abstract*— This paper explores the effects of sunlight on using a low-cost off-the-shelf silicon solar panel as an optical wireless communication (OWC) receiver. A receiver circuit structure has been proposed to maximize simultaneous energy harvesting and data communication performance. An equivalent circuit model of the solar panel for simultaneous energy harvesting and wireless optical communication is discussed. By using the solar panel model, the effects of varying sunlight conditions on the performance of the model as an OWC receiver are estimated. Furthermore, an experimental setup is developed to study the effects and verify the simulated estimations. The experimental setup consists of a 3.5 m wireless optical link with a full Transmission Control Protocol and Internet Protocol (TCP/IP) network stack. The system uses DC-biased optical orthogonal frequency division multiplexing (DCO-OFDM) to use the available communication bandwidth efficiently. A 940 nm low-cost off-the-shelf laser device along with an off-the-shelf off-axis-parabolic mirror is used as the transmitter. The maximum user throughput achieved over the air is 28.3 Mb/s while simultaneously harvesting energy using the maximum power point tracking (MPPT) technique. The peak power harvested with simultaneous communication is 4.5 W. The harvested energy is stored in a 38 Wh lithium-ion (Li-ion) battery.**

***Index Terms*— Optical Wireless Communication (OWC), photovoltaics, LiFi, solar cell, energy harvesting, orthogonal frequency division multiplexing (OFDM)**

I. Introduction

THE first semiconductor-junction solar cell was made with copper and copper oxide by Wilhelm Hallwachs in 1904 [1]. Early silicon solar cells were used to power the Telstar communication satellite launched in 1962 and were developed further for use in terrestrial installations. Modern manufacturing techniques have made low-cost silicon solar cells readily available. This has prompted an investigation into their application in areas other than direct sunlight to electrical energy conversion. Solar cells can harvest electrical energy from electromagnetic radiation generated by lasers and light-emitting diodes (LEDs) as well as sunlight. More recently, there has been a growing interest in using solar cells that harvest indoor light to power electronic devices for the Internet-of-Things (IoT) [2]. Such photovoltaic (PV)-powered devices are attractive for use in smart homes, smart offices, and smart buildings. Also, with recent advancements in the lighting industry, indoor lighting is shifting to semiconductor based light sources such as LEDs and lasers. These are highly efficient, have a long lifetime, can produce any color of light, and can be used to simultaneously transmit data. LiFi is the bidirectional optical wireless communications (OWC) technology which includes all the networking mechanisms for transmitting data via LEDs and lasers in the visible or infrared (IR) part of the optical spectrum [3]. The encoded data is transmitted as a variation in the intensity of the light emitted by the source. The LED is envisioned to serve the dual purpose of illumination and communication. Long-distance optical communication using LEDs becomes challenging as the radiation is spatially and temporally non-coherent. On the contrary, the radiation from lasers is coherent and has a significantly higher coherence length than LEDs. Therefore, lasers are used in long-distance wireless optical communication systems. In telecommunication, there are two laser structures that are commonly used: edge-emitting lasers and vertical-cavity surface-emitting lasers (VCSEL). Two important aspects of VCSEL are the low beam divergence and the symmetric beam profile compared to that of edge-emitting lasers. This makes it easy to collimate the output beam with a simple optical element. Also, VCSELs have 3-dB communication bandwidth as large as 20 GHz [4]. These advantages make VCSEL an ideal choice as the optical signal source for long-distance transmission.

In the receiver photodiodes (PD) are typically used due to their high bandwidth and linear response. The most common types of PD used in LiFi technology are positive-intrinsic-negative (PIN) PDs and avalanche photodiodes (APDs). However, PDs can require additional power to generate the sometimes high bias voltage. Therefore, solar cells can be a good energy-neutral alternative to photodiodes (PDs) as they can convert variations in the intensity of the light to electrical signals without the application of reverse bias voltage. Furthermore, solar panels are by default manufactured with multiple solar cells connected in series and parallel configuration. This results in a large active area as a communication receiver and increases the energy harvesting capability. The optical energy harvested by a solar panel can be used to offset the energy consumed by the rest of the components of the communication system. Also, the large active area of the solar panel relaxes the process of alignment between transmitter and receiver (at long distances). Conventional PDs have a small area and can be very difficult to align when used for long-distance communication.

This paper discusses the effects and trade-offs when a solar panel is used simultaneously for energy harvesting and communication. The simultaneous energy harvesting and communication performance of a solar panel has been maximized using the proposed solar panel receiver circuit structure. The effect of sunlight on the communication performance of a solar panel as an OWC receiver is studied and estimated using an equivalent circuit model of a solar panel. The variation in frequency response and signal-to-noise ratio (SNR) is estimated for varying solar irradiance. An experimental setup was developed to verify the estimations

TABLE I. OWC LINKS USING PV CELLS WITH SIMULTANEOUS ENERGY HARVESTING

Ref.	Active Area (cm^2)	Modulation Technique	Communication Bandwidth used (MHz)	Distance (m)	Maximum Data Rate (Mb/s)	Maximum Power Harvesting (W)	Product of Simultaneous Power Harvested and Data Rate (WMb/s)
This work	667.08	DCO-OFDM	16	3.5	28.1**	4.5##	28.53
[7]	4	DCO-OFDM	2.77	0.4	363*	0.01##	3.63
[8]	432	DCO-OFDM	2	0.95	11.84*	0.11##	1.3024
[9]	0.008	DCO-OFDM	237.2	2	784*	0.001##	0.784
[10]	7.29	-	-	0.4	0.003*	1##	0.003
[11]	7.5	DCO-OFDM	4	2	15.03*	-	-
[12]	667.08	DCO-OFDM	5	30	8**	4.1#	-
[13]	432	DCO-OFDM	0.35	0.39	7.01*	-	-
[14]	26.05	QAM-OFDM	0.4	-	-	0.446##	-
[9]	0.008	DCO-OFDM	237.2	2	1041*	Short-circuit mode	-
[15]	667.08	DCO-OFDM	22	2	74.03*	Short-circuit mode	-
[16]	-	PAM-DMT	9	0.1	17.05*	Reverse-biased mode	-

*Offline processing without networking headers
**Real-time traffic with TCP/IP headers
Claimed based on the capability of the PV
With simultaneous data communication

from the equivalent circuit model. In the experiment, the maximum user available data rate with full networking capabilities achieved by the system is 28.3 Mb/s over a distance of 3.5 m, while it was able to simultaneously harvest energy using the maximum power point tracking (MPPT) [5] technique. The peak power that could be harvested from the solar irradiation is 4.5 W with a 5 W silicon (Si) solar panel, and the harvested energy is stored in a 38 Wh lithium-ion (Li-ion) battery. The variation in data rate and energy harvesting is shown for different solar irradiances. The experiment was conducted for a link of distance 3.5 m only because the main goal of this paper is to study the effects of the sunlight on the communication performance of the solar panel rather than the maximum link distance.

The rest of this paper is organized as follows: in section II all the experiments and models of solar panels as OWC receivers developed previously are discussed and reviewed. Section III describes the equivalent circuit model of the solar cell used in this paper and highlights the key parameters of the model that determines the energy harvesting and communication performance of a solar cell. In section IV the effects of varying sunlight conditions on the communication performance of the solar cell model are studied. Section V discusses the experimental setup and the system deployed in order to verify the estimations and simulations. In section VI the results are shown and discussed. And in section VII the concluding remarks of the paper are presented.

II. BACKGROUND

Solar cells have traditionally been developed to harvest energy directly from sunlight and relatively little investigation has been carried out into their use as an optical data receiver with simultaneous energy harvesting. There are several types of solar cells and choosing the appropriate technology can be difficult for simultaneous energy harvesting and communication applications. Solar panels can be differentiated based on the type of semiconductor junction and material used, but they are commonly classified by generation. Single-junction and multi-junction solar cells differ in the number of layers that capture the sunlight, whereas the classification by generation emphasizes the materials and efficiency of the different types of solar cells that make up a panel. The first generation of solar panels is based on Si solar cells. They are widely used for energy harvesting due to their low manufacturing cost. They are further divided into two categories: polycrystalline and monocrystalline [6]. The latter has higher efficiency and has better temperature stability than the former. Using a first-generation solar panel as an OWC receiver relaxes the strict alignment requirement and the need for complex optical elements on the receiver side as they have a large active area. These solar panels are also low-cost, easily available, and are commonly deployed for large-scale solar energy harvesting.

In this work, we have considered a first-generation solar panel as this knowledge can be used to upgrade the existing solar energy harvesting systems. These are most commonly based on first-generation solar panels, due to the easy availability of silicon and its low manufacturing cost. Furthermore, this study can be extended to later generations of solar panels as they operate on the same underlying principles. There have been several studies using solar panels as an OWC receiver. TABLE I. presents a comparison of the published figures for simultaneous data communication and energy

constant at a given wavelength and is defined as the responsivity of the material of which the solar cell is made. The relation $I = \mathcal{R}P_s$ is valid only if the I is interpreted as the average current generated. However, this is not the case for an ideal optical receiver. The four noise mechanisms (thermal noise, shot noise, dark current noise, and input noise) need to be considered to understand the effects of simultaneous energy harvesting and communication performance.

Thermal noise, also known as Johnson noise, follows a Gaussian distribution and can be characterized by its constant power spectral density given in (4), where Z_L is the load impedance, and T is the absolute temperature. The unit of σ_{th}^2 is W/Hz. For the solar panel as a receiver with communication bandwidth B, the mean-square noise current representing the total thermal noise power can be expressed as $\langle i_{th}^2 \rangle$ and is defined in (5).

$$\sigma_{th}^2 = \frac{4kT}{|Z_L|} \tag{4}$$

$$\langle i_{th}^2 \rangle = \sigma_{th}^2 B \tag{5}$$

Shot noise is white, therefore a Gaussian distribution can be used to define the shot noise statistics. The shot noise power spectral density σ_{sh}^2 can be expressed as in (6), where I is the photocurrent as shown in Fig. 1 and q is the electron charge. As $I = \mathcal{R}P_s$, σ_{sh}^2 can alternatively be defined by the responsivity and total optical power received as shown in (6). The mean-square noise current $\langle i_{sh}^2 \rangle$ for the interested bandwidth is shown in (7).

$$\sigma_{sh}^2 = 2qI = 2q\mathcal{R}P_s \tag{6}$$

$$\langle i_{sh}^2 \rangle = \sigma_{sh}^2 B \tag{7}$$

Dark current noise is the constant current that exists when no light is incident on the solar panel. The dark current noise can also be treated as white noise with Gaussian distribution, because the statistical nature of the charge carrier generation process is similar to that discussed for the shot noise. For I_D from (3), the noise power spectral density σ_D^2 is defined in (8). The dark current noise power $\langle i_D^2 \rangle$ for the selected bandwidth B can be expressed as shown in (9).

$$\sigma_D^2 = 2qI_D \tag{8}$$

$$\langle i_D^2 \rangle = \sigma_D^2 B \tag{9}$$

The optical signal is converted to current by a solar panel, but for further processing in the communication chain, the time-varying photocurrent signal needs to be converted to electrical voltage. An electrical trans-impedance amplifier is used to amplify the photocurrent signal and convert it to voltage. Noise generated by the first stage of the amplifier must also be considered in the receiver Signal-to-Noise Ratio (SNR) analysis because the amplifier noise power is comparable to the electrical signal power fed to the amplifier. The trans-impedance gain $Z_{amp} = v_{out}/i_{ac}$, where i_{ac} is the input signal current as depicted in Fig. 1 and v_{out} is the output signal voltage from the amplifier. The output voltage error v_{amp} is the output voltage from the amplifier when the input signal current is zero. This parameter is generally provided by the manufacturer of the operational amplifier in the corresponding datasheet. Henceforth, the output noise power from the amplifier is defined as $\langle v_{amp}^2 \rangle$ and the input noise power $\langle i_{amp}^2 \rangle$ can be calculated using (10).

$$\langle i_{amp}^2 \rangle = \frac{\langle v_{amp}^2 \rangle}{Z_{amp}^2} \tag{10}$$

Under real-world conditions, many communication devices are transmitting and receiving signals simultaneously and every wire connecting an optical receiver to the subsequent stages can be considered as an antenna. These radio frequency (RF) signals can be picked up unintentionally by the wires and terminals which create interference with the signal of interest. This problem is solved by creating a Faraday cage around the exposed terminals and wires. Therefore, for the noise estimation purpose, the interference and noise due to RF can be approximated to zero.

IV. Estimation of Communication Parameters

For an optical communication receiver, there are three main factors on which the communication performance will depend, namely spectral responsivity, frequency response, and noise performance. As a first-generation Si-based solar panel is used in this work, the optical to electrical energy conversion, *i.e.,* spectral responsivity, of Si peaks at around 1000 nm [6]. By choosing the appropriate optical signal transmitter's wavelength the optical to electrical signal conversion at the solar panel can be maximized. Next, the bandwidth and noise performance of the solar panel will depend on how the panel is interfaced with the subsequent stages of the communication system. As it can be seen in section III.B, the thermal noise power is inversely proportional to the load impedance Z_L, and a large load impedance magnitude helps reduce the thermal noise. However, as investigated in [9] and [12] an increase in load impedance would reduce the communication bandwidth. The best communication bandwidth is achieved under a short-circuit condition [9]. On the contrary, for energy harvesting purposes short-circuit conditions would generate no power as the voltage is zero. To overcome this issue the solar panel interfacing circuit is designed as shown in Fig. 1 so that the inductor L and capacitor C separate the DC and AC components of the signal. The DC Out terminal is then connected to an MPPT circuit which holds the voltage constant and non-zero across the panel ensuring that the communication bandwidth achieved is as large as possible. The MPPT circuit design is taken from the Texas Instruments reference design for the battery charge controller for solar power described in [18]. The impedance network Z in the interfacing circuit is a resistor-inductor-capacitor resonant circuit whose bandwidth is equal to the chosen communication bandwidth B. In this case, R_{DC} is 5.1 kΩ, C is 100 nF and L is 150 nH, as B is 16 MHz. This ensures the undesired low and high frequencies are filtered out and the effective impedance across the panel is only resistive with a low value.

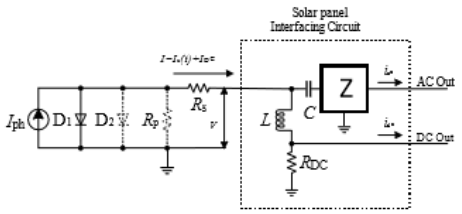

Fig. 1 PV cell model with an interfacing circuit

harvesting performance in PV OWC systems. In such systems, solar panels are meant for both power harvesting and data communication. Therefore, the product of the harvested power and the data communication rate has been used as a figure of merit. In this work, this product of the simultaneous power harvested and the data communication performance has been maximized for a first-generation Si-PV panel. These first-generation solar panels were never developed or designed to be used as OWC receivers. Therefore, the electrical characteristics of the panel relevant to communication such as linearity, speed of response, sensitivity to the incident optical signal, and temperature stability have been investigated in [12]. In [15] a data rate of 74 Mb/s has been demonstrated over a distance of 2 meters using a polycrystalline solar panel, and in [12] a communication distance of 30 meters has been achieved with a maximum data rate of 8 Mb/s with full networking capabilities. These publications have not modelled the effects of simultaneous energy harvesting and communication, and only consider the communications performance of the solar panel OWC receiver. The following sections show how important it is to understand the trade-off between data communication and energy harvesting when both are carried out simultaneously.

III. Principles of Operations and Modelling

To understand the effects of simultaneous energy harvesting on the data communication performance, an equivalent circuit model of a solar panel needs to be considered. We aim to create a circuit model that is electrically equivalent and is based on discrete ideal electrical components, whose behavior is well defined analytically.

A. Energy Harvesting & simultaneous communication model

Generally, a single diode model is used to represent a solar cell as used in [7] - [16]. The single diode model structure is identical to the structure shown in Fig. 1 without the dashed line components. Furthermore, a solar panel interfacing circuit is also shown in Fig. 1. In this paper, the single diode model is not considered because the single diode equation assumes a constant value for the ideality factor n, as studied previously in [7] - [16]. In [17], both the single diode model and double diode model of a PV was compared to study the energy harvesting parameters. In this work, the double diode model has been used to study the both the communication characteristics and simultaneously the energy harvesting performance of a solar panel. Using an accurate equivalent circuit model for the PV enables extending this work to other generations of PV cells such as organic PV cells, GaAs-based PV cells, multi-junction PV cells, *etc*. The electrical circuit parameters such as diode voltage, diode capacitance, internal resistance and current density will vary for each type of PV cell used in the system, based on the manufacturing technique and semi-conductor used in the PV cell. In reality, the ideality factor is a function of the voltage across the device [17]. At high voltages, when the recombination at the junction in the device is dominated by the surface and the bulk regions, the ideality factor is close to one, which is represented by the diode D_1. However, at lower voltages recombination in the junction dominates and the ideality factor approaches two. In this paper, the communication performance will be evaluated under varying solar irradiation and this will cause the voltage across the PN-junction to vary significantly. Therefore, the ideality factor needs to be considered for accurate modeling. The junction recombination is modeled by adding a second diode, which is depicted with a dashed line in Fig. 1. The ideality factor for this second diode is typically set to two [17]. Therefore, the total current generated by the solar cell is represented as I and defined by using Schottky's diode equation as shown in (1), where I_{ph} is the photogenerated current, I_{o1} is the diode saturation current for D_1, I_{o2} is the diode saturation current for D_2, V is the voltage across the solar panel, q is the charge of an electron, R_p is the shunt resistance, R_s is the series resistance, k is the Boltzmann's constant, and I is the sum of alternating current (AC) generated due to the received optical signal and the direct current (DC) generated due to the solar irradiation. Therefore $I = I_s(t) + I_{DC}$, where $I_s(t)$ is the AC signal component and I_{DC} is the DC signal component.

$$I = I_{ph} - I_{o1}\left[e^{\frac{q(V+IR_p)}{kT}} - 1\right] - I_{o2}\left[e^{\frac{q(V+IR_p)}{2kT}} - 1\right] - \frac{V+IR_s}{R_p} \quad (1)$$

In (1) the subtraction by 1 in the square bracket terms can be ignored for approximation, which makes the analysis easy. This is because the exponential terms give values typically much larger than 1 [17]. Therefore, (1) can be further simplified to (2).

$$= I_{ph} - I_{o1}\left[e^{\frac{q(V+IR_p)}{kT}}\right] - I_{o2}\left[e^{\frac{q(V+IR_p)}{2kT}}\right] - \frac{V+IR_s}{R_p} \quad (2)$$

I_{ph} in (2) represents the generated photocurrent. When there is no photocurrent generation $I_{ph} = 0$ and the solar panel will act as a passive load. Therefore, the dark current for the panel can be denoted as shown in (3) [17].

$$I_D = I_{o1}\left[e^{\frac{q(V-IR_p)}{kT}}\right] + I_{o2}\left[e^{\frac{q(V-IR_p)}{2kT}}\right] + \frac{V-IR_s}{R_p} \quad (3)$$

B. Noise Analysis

Solar panels convert an incident optical power P_s into an electric current I using the photovoltaic effect. In the photovoltaic effect, $P_s \propto I$ which implies $I = \mathcal{R}P_s$ where $\mathcal{R}$ is a

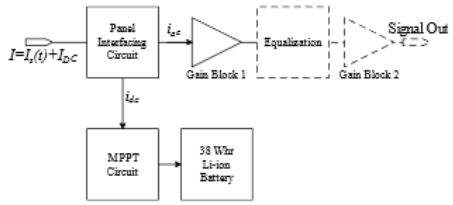

Fig. 2 Receiver circuit functional block diagram

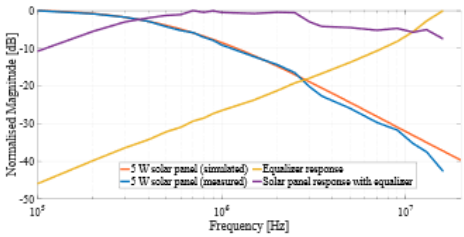

Fig. 3 Solar panel bandwidth

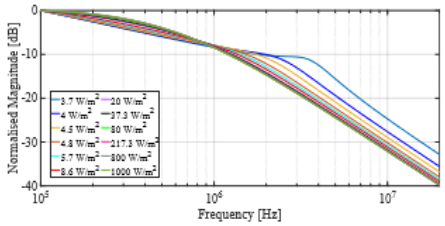

Fig. 4 Frequency response for varying solar irradiance

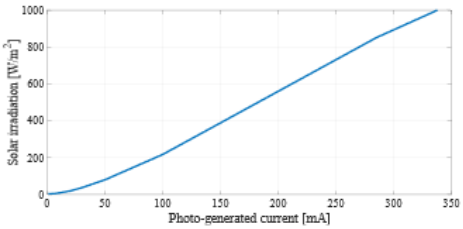

Fig. 5 Photo-generated current for varying solar irradiance

A. *Frequency Response of a solar panel*

Using the equations (2),(3), (11)-(14) and the equivalent circuit models discussed in section III, the frequency response of the panel was simulated using TINA-TI [19], which is a simulation program with integrated circuit emphasis (SPICE). The simulation was carried out with the receiver circuit structure as shown in Fig. 2 without the components depicted with dashed line. In the simulation, the temperature was kept constant at 298 K.

$$C_{\mathrm{d}} = \frac{k\tau_{\mathrm{n}} I_{\mathrm{d}}}{T} \tag{11}$$

$$R_{\mathrm{s}} = \left(\frac{P}{P_{\mathrm{MP}}} + 1\right)\frac{V_{\mathrm{oc}}}{I_{\mathrm{sc}}} \tag{12}$$

$$R_{\mathrm{p}} = \left(\frac{P_{\mathrm{MP}}}{P + P_{\mathrm{MP}}}\right)\frac{V_{\mathrm{oc}}}{I_{\mathrm{sc}}} \tag{13}$$

The diffusion capacitance, series and shunt resistances were defined by the equations as shown in (11)-(13). In equation (11) C_{d} is the diffusion capacitance [20], k is the Boltzmann's constant, I_{d} is the current through the diode, τ_{n} is the minority carrier lifetime which is defined in detail in [12] and T is the temperature. The diffusion capacitance for D_1 and D_2 is estimated separately for each diode using this equation. Furthermore, the series resistance is defined in equation (12) [21] where P is the power harvested for the incident optical power, P_{MP} is the maximum power that can be harvested by the panel, which is 5 W in this case, V_{oc} is the open-circuit voltage across the panel and I_{sc} is the short-circuit current. The open-circuit voltage and short-circuit current of the solar panel used in this case was 22 V and 330 mA, respectively [22]. Similarly, the shunt resistance R_{p} is defined in equation (13).

The receiver structure shown in Fig. 2 was implemented in practice and the frequency response simulation was verified experimentally. The simulated and measured frequency response of the solar panel is shown in Fig. 3. From Fig. 3 it can be inferred that the simulated double-diode model matches the response in terms of communication performance to the solar panel chosen in practice. Henceforth, the short-circuit current for the solar panel was measured by varying the incident optical power. A 1 kW PAR64 halogen lamp [23] with a 0.8 kW halogen bulb was used as a sunlight emulator. The color temperature of the halogen lamp was 3200 K, although the color temperature of sunlight on the surface of the earth on a bright sunny day is around 5700-6000 K [24]. Therefore, a color filter [25] was used in front of the halogen lamp set up to produce a light spectrum equivalent to the spectrum of sunlight. The halogen lamp was used with a parabolic reflector to concentrate the beam onto the 667 cm^2 active area of the solar panel and a dimmer was used to control the light output from the halogen lamp. The halogen lamp was placed at a distance of 60 cm from the solar panel such that the maximum intensity measured with a lux meter on the panel is approximately 130,000 lux. Using the solar irradiance to lux illuminance conversion factor of 0.0079 W/lux [26] the emulated solar irradiance on the solar panel was calculated, and the maximum value was 1000 W/m^2. Then the short-circuit solar panel current is measured while varying the emulated solar irradiance using the dimmer and this is plotted in Fig. 5. The short-circuit current measured is approximately equal to I_{ph}, as R_{s} is less than 1 Ω. Furthermore, using this short-circuit current as I_{ph} the frequency response for different solar irradiance was simulated and verified experimentally. Fig. 4 shows the variation in frequency response due to the variation in solar irradiance with the receiver circuit as depicted in Fig. 2. This variation in frequency response occurs due to the constant voltage held across the panel by the MPPT circuit. As the voltage across the panel is

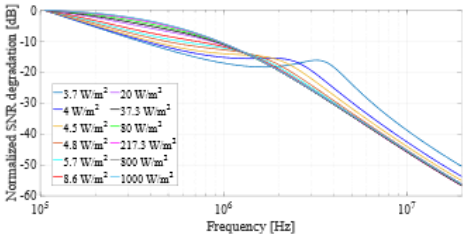

Fig. 6 Estimated SNR degradation for varying solar irradiance

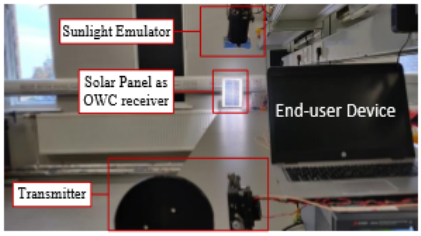

Fig. 7 Experimental setup

constant, the generated photocurrent is varying due to variations in the incident optical intensity. The internal effective resistance of the panel is varying due to changes in the photocurrent, which results in the variation of the time-constants of D_1 and D_2. The time-constants of D_1 and D_2 are directly related to the communications bandwidth of the solar panel.

B. *Estimation of SNR*

The next important parameter which determines the performance of the solar panel as a communication receiver is SNR. When OFDM is used, the magnitude of the SNR of the frequency subcarriers determines the modulation order that could be used over the selected communication bandwidth for a given bit error rate. The SNR for the received signal was calculated using the simulation results and equation (14) obtained from TI-TINA in MATLAB for the solar panel model discussed in section III. In Fig. 6 the normalized SNR for the received signal is plotted for different values of emulated solar irradiance incident on the panel. The SNR estimated in Fig. 6 depicts the degradation introduced by the solar panel during the optical to electrical signal conversion.

$$\mathrm{SNR} = \frac{\langle I_s^2(t)\rangle}{\langle i_{th}^2\rangle + \langle i_{sh}^2\rangle + \langle i_D^2\rangle + \langle i_{amp}^2\rangle} \qquad (14)$$

In Fig. 6 the SNR increases at the lower frequencies with the increase in emulated solar irradiance on the solar panel. This can be explained by the reduction of the diode resistances of D_1 and D_2 due to an increase in the photogenerated current. At higher frequencies, the reduction of SNR with an increase in optical intensity can be explained by the increase in shot and thermal noise. As seen in equations (6) and (7) the shot noise increases with the increase in total optical incident power P_s. In the case of thermal noise, the solar spectrum consists of both long and short IR radiation. This IR radiation will generate heat in most of the materials as the molecules resonate with the IR wavelength. Therefore, an increase in temperature T in equation (4) results in an increase in the thermal noise. Furthermore, the SNR plots for each solar irradiance follows the same trend as the frequency response, shown in Fig. 4. On the contrary, the dark current noise and the amplifier input noise are constant for the varying optical intensity as they are independent of the optical power incident and the temperature of the solar panel. Therefore, the estimations in this section show that there is a trade-off in communication performance when the solar panel is used simultaneously for harvesting solar energy.

TABLE II. PHYSICAL LAYER SPECIFICATION

Channel bandwidth	16 MHz
Subcarrier Spacing (Δf)	250 KHz (16 MHz/64 Pt FFT)
Modulation	BPSK, QPSK, 16QAM, 64QAM
Coding Rate	½, ⅔, ¾
FFT Period ($T_{FFT}=1/\Delta f$)	4 µs
Cyclic Prefix duration ($T_{GI2}=T_{FFT}/2$)	2 µs

V. EXPERIMENTAL SETUP

In order to verify the estimations obtained in section IV, it is necessary to evaluate the trade-off between energy harvesting and simultaneous communication. A real-time optical link with full networking capability is developed as shown in Fig. 7. To establish a real-time link with full networking capability a full-duplex link is required. In this setup, the downlink is the optical link, and the uplink is realized using a coaxial cable. The transmitter is based on the design developed in [12]. The transmitter uses an off-the-shelf 940 nm VCSEL as the optical source and the beam is collimated using a commercially available off-axis parabolic mirror. The transmitter is classified as class 1M and the VCSEL is driven by a current driver with a 3 dB communication bandwidth of 65 MHz [12]. The receiver circuit consists of an analog equalizer which flattens the frequency response of the solar panel up to 16 MHz, shown in Fig. 3. The proposed solar panel interfacing circuit, as discussed in sections III and IV, and the equalizer circuit are integrated into the receiver circuit design in order to enable the energy harvesting capability of the solar panel. The overall receiver circuit structure is shown in Fig. 2. As the receiver design includes an analog equalizer stage this helped in increasing the usable communication bandwidth of the solar panel to 16 MHz. In the MPPT circuit, the solar panel voltage needs to be adjusted. In this work, the voltage was set to 7.22 V, which is the nominal voltage *i.e.,* maximum power point as recommended by the manufacturer [22]. The harvested energy is stored in a Lithium (Li)-ion battery with a capacity of 38 Wh. For digital signal processing (DSP) an application-specific integrated circuit (ASIC) from pureLiFi [27] is used, which is based on the IEEE 802.11 wireless local area network (WLAN) standard [28]. The specification of physical (PHY) layer used in the experiment is shown in TABLE II. In IEEE 802.11 WLAN standard, OFDM is used primarily to utilize the channrl bandwidth efficiently. There are several variants in OFDM

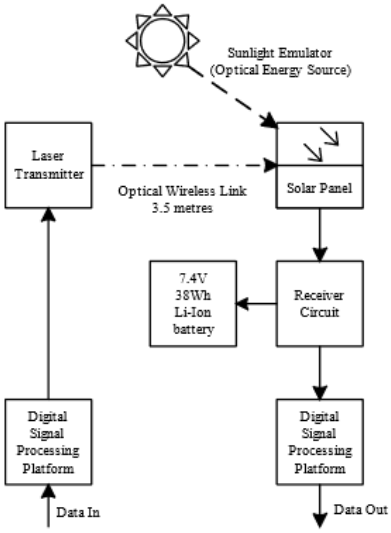

Fig. 8 System functional setup

employed in optical communication such as Asymmetrically Clipped Optical OFDM (ACO-OFDM) [29], Enhanced unipolar OFDM (eU-OFDM) [30], DC-biased optical OFDM (DCO-OFDM) [31], *etc*. In this experiment, the system uses DCO-OFDM, as with lower system complexity higher spectrally efficiency could be achieved compared to the other mentioned OFDM variants. The functional block diagram and the interconnection of each sub-system is shown in Fig. 8. As the DSP platform, *i.e.,* the pureLiFi ASIC, provides only the functionality of the PHY layer and lower medium access control (MAC) layer, a host processor is needed to implement the remaining three layers, *i.e.,* network, transport, and application layer of the transport control protocol and internet protocol (TCP/IP) network stack. Laptops on either end of the communication nodes were used as the host processor as well as the end-user device. To simulate real-time network traffic and measure the network bandwidth, iPerf [32] is used on the end-user devices. Using iPerf, the network bandwidth was measured at a constant optical intensity incident on the panel for 50 s and the average data rate was recorded. This process was iterated with different emulated solar irradiance ranging from 0 W/m^2 to 1000 W/m^2 using the procedure as discussed in section III.B. The data rate was measured up to 1000 W/m^2 as that is the nominal solar irradiation measured on the surface of the earth during a bright sunny day. Simultaneously, the DC voltage and current generated by the solar panel and the signal power at the receiver circuit output is recorded for different optical intensity incident on the solar panel. The recorded data is plotted and discussed further in section VI. Furthermore, a transmitted data packet from the DSP platform was captured using an oscilloscope. The captured data packet was used to simulate the double-diode model along with the whole receiver

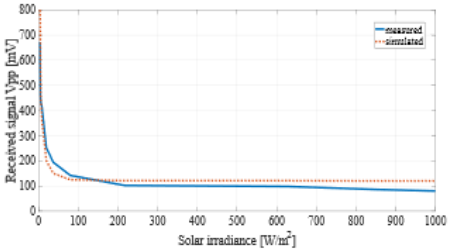

Fig. 9 Received signal power variation due to varying solar irradiation

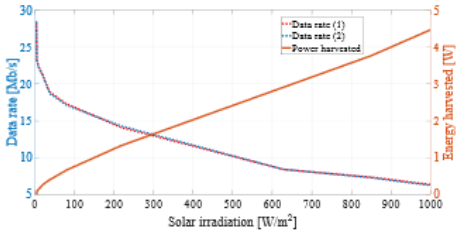

Fig. 10 Variation in data rate with simultaneous energy harvesting

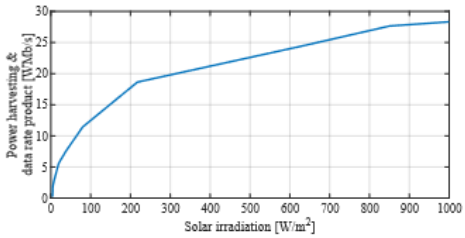

Fig. 11 Simultaneous power harvesting and data rate performance

circuit in TI-TINA to estimate the signal power at the receiver output against the varying optical power. These simulated results are compared with the experiment results and discussed further in the following section.

VI. Results & Discussions

The experiment was successfully conducted, and the obtained results are shown in Fig. 9 and Fig. 10. The highest data rate achieved between the two end-user devices is 28.3 Mb/s while harvesting no power. Alternatively, the peak power harvested with a 5 W solar panel at the equivalent illumination of the sun on a bright sunny day is 4.5 W simultaneously with a data rate of 6.34 Mb/s between the two end-user devices. Fig. 9 shows the received data signal power variation against the varying solar irradiation for both the simulated model and the experimental setup. The results from the simulated model align with the results from the experimental setup. Therefore, it can be inferred that the simulated model matches the experimental setup. The

exponential decrease in the received signal power with the increase in solar irradiance follows the trend shown by the reduction in frequency bandwidth when the emulated solar irradiance is increased in Fig. 4. In Fig. 10 the variation in data rate along with the power harvested from the solar panel is shown against the variation in solar irradiation. The decrement in data rate with the increase in solar irradiance follows the same trend as the frequency response and SNR as shown in Fig. 4 and Fig. 6. From this plot, it can be seen that there is a trade-off between communication and solar energy harvesting when a solar panel is used simultaneously for both. At 240 W/m^2 solar irradiance, there is an intersection of the data rate achieved and energy harvested simulation. At this point, the achieved data rate is 13.7 Mb/s and 1.6 W of power is simultaneously harvested. The achieved data rate is not as high as that in [15] as the highest order of modulation used by the ASIC in this experiment is 64-quadrature amplitude modulation (QAM) at ¾ code-rate under ideal conditions, while in [15] the maximum achieved modulation order was 512-QAM at ½ code rate and used offline processing on MATLAB. Also, the raw throughput measured in [15] is 74 Mb/s which neglects the bits occupied by the TCP/IP headers. The equivalent raw throughput for the setup in this paper is 37.63 Mb/s without the full networking stack overheads. The aim of this study was to investigate the effects of sunlight on a single Si-based PV when used as an OWC receiver and maximize power harvesting and data communication. Therefore, the product of two key parameters needs to be maximized. In Fig. 11, the product of power harvested, and the data rate achieved for a given solar irradiance is shown. It can be seen that with the increase in solar irradiance the product also increases. Furthermore, depending on the application, the data rate or energy harvesting capability can be maximized by choosing the appropriate voltage setting in the MPPT controller. Setting the voltage at a lower value will result in better communication performance as seen previously in [15] and a reduction in the energy harvested. Setting the voltage equal to the nominal voltage of the solar panel will achieve maximum energy harvesting, as shown in this paper, but resulting in reduced communications performance.

VII. Conclusion

In this paper, a trade-off between energy harvesting and communication performance when an off-the-shelf Si-based solar panel is used as an OWC receiver is shown. Moreover, a receiver circuit structure has been proposed which enables to maximize the simultaneous energy harvesting and data communication performance of a PV in an OWC system. The product of solar power harvested, and data rate achieved has been maximized up to 28.53 WMb/s. Using the receiver circuit, the performance of a solar panel for power harvesting and data communication in an OWC system has been enhanced 9 times than the previously published state of the art. Additionally, the proposed receiver structure could be used for other generation of PV cells to maximize the performance as the design and estimation is based on a more accurate PV circuit model. Additionally, the simulated estimations using the PV circuit model has been verified experimentally to show the accuracy. Furthermore, depending on the application's requirements, either communication or energy harvesting performance can be maximized with the appropriate settings. Moreover, this invites future work where smart software can be developed, which controls the settings continuously during the system operation while monitoring the daylight conditions, energy requirements, and user-throughput requirements to provide an optimal experience for the end-user.

Acknowledgments

The work of H. Haas was supported by the Engineering and Physical Sciences Research Council under the Established Career Fellowship Grant EP/R007101/1, the Wolfson Foundation and the Royal Society.

References

[1] L. M. Fraas, Low-Cost Solar Electric Power, Switzerland: Springer, 2014.
[2] J. Lin, W. Yu, N. Zhang, X. Yang, H. Zhang and W. Zhao, "A Survey on Internet of Things: Architecture, Enabling Technologies, Security and Privacy, and Applications," IEEE Internet of Things Journal, vol. 4, no. 5, pp. 1125-1142, 2017.
[3] H. Haas, L. Yin, Y. Wang and C. Chen, "What is LiFi?," Journal of Lightwave Technology, vol. 34, no. 6, pp. 1533-1543, 2016.
[4] K. Lear, V. Ochiai, H. Hou, B. Hammons, J. Banas and J. Nevers, "High-speed vertical cavity surface emitting lasers," in Digest of the IEEE/LEOS Summer Topical Meeting, Montreal, 1997.
[5] J. A. B. Vieira and A. M. Mota, "Maximum power point tracker applied in batteries charging with PV panels," in IEEE International Symposium on Industrial Electronics, Cambridge, 2008.
[6] Z. Hameiri, "Photovoltaics literature survey (No. 125)," Progress in Photovoltaics: Research and Applications, vol. 24, no. 3, pp. 405-407, 2016.
[7] I. Tavakkolnia, L. K. Jagadamma, R. Bian, P. P. Manousiadis, S. Videv, G. A. Turnbull, I. D. W. Samuel and H. Haas, "Organic photovoltaics for simultaneous energy harvesting and high-speed MIMO optical wireless communications," Light: Science & Applications, vol. 10, no. 41, 2021.
[8] Z. Wang, D. Tsonev, S. Videv and H. Haas, "On the Design of a solar panel receiver for optical wireless communication with simultaneous energy harvesting," IEEE Journal on Selected Areas in communications, 2015.
[9] J. Fakidis, H. Helmers and H. Haas, "Simultaneous Wireless Data and Power Transfer for a 1-Gb/s GaAs VCSEL and Photovoltaic Link," IEEE Photonics Technology Letters, vol. 32, no. 19, pp. 1277-1280, 2020.
[10] S.-M. Kim and J.-S. Won, "Simultaneous reception of visible light communication and optical energy," in International Conference on ICT Convergence (ICTC), Jeju, 2013.
[11] R. Sarwar, B. Sun, M. Kong, T. Ali, C. Yu, B. Cong and J. Xu, "Visible Light Communication Using a Solar-Panel Receiver," in International Conference on Optical Communications and Networks (ICOCN), Wuzhen, China, 2017.
[12] S. Das, E. Poves, J. Fakidis, A. Sparks, S. Videv and H. Haas, "Towards Energy Neutral Wireless Communications: Photovoltaic Cells to Connect Remote Areas," Energies, vol. 12, no. 19, October 2019.
[13] Z. Wang, D. Tsonev, S. Videv and H. Haas, "Towards Self-powered solar panel receiver for optical wireless communication," IEEE ICC Optical Networks & Systems, 2014.
[14] N. Lorriere, N. Betrancourt, M. Pasquinelli, G. Chabriel, J. Barrere, L. Escoubas, J.-L. Wu, V. Bermudez, C. M. Ruiz and J.-J. Simon, "Photovoltaic Solar Cells for Outdoor LiFi Communications," Journal of Lightwave Technology, vol. 38, no. 15, pp. 3822-3831, 2020.
[15] S. Das, J. Fakidis, A. Sparks, E. Poves, S. Videv and H. Haas, "Towards 100 Mb/s Optical Wireless Communications Using a Silicon Photovoltaic Receiver," in IEEE Global Communications Conference, Taipei, 2020.
[16] W.-H. Shin, S.-H. Yang, D.-H. Kwon and S.-K. Han, "Self-reverse-biased solar panel optical receiver for simulataneous visible light communication and energy harvesting," Optical Express A1300, 2016.
[17] V. Tamrakar, S. Gupta and Y. Sawle, "Study of characteristics of single and double diode electrical equivalent circuit models of solar PV

module," in International Conference on Energy Systems and Applications, Pune, 2015.
[18] Texas Instruments Inc., "High efficiency synchronous switch-mode charge controller - solar battery charger (BQ24650)," January 2020. [Online]. Available: https://www.ti.com/product/BQ24650.
[19] Texas Instruments Inc., "TINA-TI SPICE-based analog simulation program," Texas Instruments Inc., [Online]. Available: https://www.ti.com/tool/TINA-TI. [Accessed September 2020].
[20] S. K. Sharma, D. Pavithra, G. Sivakumar, N. Srinivasamurthy and B. L. Agrawal, "Determination of solar cell diffusion capacitance and its dependence on temperature and 1 MeV electron fluence level," Solar Energy Materials and Solar Cells, vol. 26, no. 3, pp. 169-179, 1992.
[21] M. Wolf and H. Rauschenbach, "Series Resistance Effects on Solar Cell Measurements," Advanced Energy Conversion, vol. 3, pp. 455-479, 1963.
[22] Solar Technology International Ltd., "5 Watt Solar Panel Kit," [Online]. Available: https://www.solartechnology.co.uk/pv-logic/5w-solar-panel-kit. [Accessed January 2019].
[23] Philips Lighting, "PAR64 1000W 240V NSP," Philips Lighting, [Online]. Available: https://www.lighting.philips.co.uk/prof/conventional-lamps-and-tubes/special-lamps/entertainment/dj-club/par56-and-par64/924783345504_EU/product. [Accessed October 2020].
[24] J. F. Collins, "The colour temperature of daylight," British Journal of Applied Physics, vol. 16, no. 6, 1965.
[25] LEE Filters, "Colour information and spectral charts for 201," [Online]. Available: https://www.leefilters.com/lighting/colour-details.html#201&filter=cf&sort=number. [Accessed October 2020].
[26] P. Michael, "A Conversion Guide: Solar Irradiance and Lux Illuminance," IEEE Dataport, 2019.
[27] Purelifi, "LiFi ASIC PL0300 Datasheet," 2019. [Online]. Available: https://purelifi.com/lifi-asic/.
[28] "IEEE Standard for Information technology—Telecommunications and information exchange between systems Local and metropolitan area networks—Specific requirements - Part 11: Wireless LAN Medium Access Control (MAC) and Physical Layer (PHY) Specifications," IEEE Std 802.11-2016 (Revision of IEEE Std 802.11-2012), pp. 1-3534, 2016.
[29] S. Hranilovic and R. Bai, "Absolute Value Layered ACO-OFDM for Intensity-Modulated Optical Wireless Channels," IEEE Transactions on Communications, vol. 68, no. 11, pp. 7098-7110, 2020.
[30] D. Tsonev, S. Videv and H. Haas, "Unlocking Spectral Efficiency in Intensity Modulation and Direct Detection Systems," IEEE Journal on Selected Areas in Communications, vol. 33, no. 9, pp. 1758-1770, 2015.
[31] S. D. Dissanayake and J. Armstrong, "Comparison of ACO-OFDM, DCO-OFDM and ADO-OFDM in IM/DD Systems," Journal of Lightwave Technology, vol. 31, no. 7, pp. 1063-1072, 2013.
[32] ESnet/Lawrence Berkeley National Laboratory, "iPerf," [Online]. Available: https://iperf.fr/. [Accessed September 2020].

Sovan Das received the Bachelors of Engineering degree in telecommunication engineering from PES Institute of Technology, Bangalore, India, in 2017. He is currently pursuing the Ph.D. degree in optical wireless communication at the University of Edinburgh. Simultaneously, he is also working as a development engineer at the LiFi Research and Development Centre, University of Strathclyde, UK. His primary research interest includes photovoltaics as FSO receivers, LiFi, optical wireless communications and autonomous aerial robotics.

Adrian Sparks is an Optoelectronics Engineer in the LiFi Research and Development Centre at The University of Strathclyde. He is an experienced industrial research and development professional with 15 patents granted. Previously he has led the development of RF over fibre and optical fibre sensing products, which are now sold all over the world. He started his career at Standard Telecommunications Laboratories (later Nortel Networks), Harlow, UK, working on liquid crystal displays and designing the world's first commercially available ferroelectric display system. He moved on to work on optical fibre telecommunications and designed analog integrated circuits for the first optically amplified transatlantic cable. He worked for 7 years on all optical network architecture for Nortel in Ottawa, Canada and in the UK, generating 7 patent applications. He has a BSc in solid state physics from the University of Bath, UK, and an MBA from the University of Essex, UK.

Enrique Poves received both M.Sc. and Ph.D. degrees in telecommunications engineering from Universidad Politécnica de Madrid, Madrid, Spain, in 2004 and 2010 respectively. After research in Universidad Politécnica de Madrid and University of Edinburgh, and 6 years working in industry, he is currently Applications Engineer with the LiFi Research and Development Centre of the University of Strathclyde. His main research is in optical wireless communications systems and modulation techniques, and the identification of use cases and applications for industry and consumer markets.

Stefan Videv is the Director of Engineering for the LiFi Research and Development Centre. Stefan received the B.Sc. degree in Electrical Engineering and Computer Science and the M.Sc degree in Communications, Systems and Electronics from Jacobs University, Bremen, Germany in 2007 and 2009 respectively. He received his PhD from the University of Edinburgh in 2013 for his thesis titled "Techniques for Green Radio Cellular Communications." As the Director of Engineering, Stefan leads industry engagement, all prototyping and development work, as well as driving the center's technology roadmap continued renewal and implementation. His research interests include high speed optical communications, resilient communication system design, and energy efficient communications.

John Fakidis was awarded the Diploma (MEng) in electrical and computer engineering from the Aristotle University of Thessaloniki, Greece in 2011. He was awarded the PhD for his thesis titled 'Optical wireless energy transfer for self-sufficient small cells' from the Institute for Digital Communications, University of Edinburgh, U.K. in 2017 in collaboration with Nokia, Bell Laboratories in Ireland. He has been a Postdoctoral Research Associate in Light Fidelity (LiFi) Systems at the LiFi Research and Development Center (LRDC) of the University of Edinburgh until 2020. John was an Optical Engineer with LRDC in the University of Strathclyde. He is the holder of world-record data rates in simultaneous optical wireless data and power transfer. John is currently working as an Optical Scientist at Microsoft Research Cambridge.

Harald Haas FREng FRSE FIEEE FIET received the Ph.D. degree from The University of Edinburgh in 2001. He is a Distinguished Professor of Mobile Communications at the University of Strathclyde and the Director of the LiFi Research and Development Centre. He also set-up and co-founded pureLiFi Ltd which it currently serves as Chief Scientific Officer. He has authored over 550 conference and journal papers. Haas' main research interests are in optical wireless communications, hybrid optical wireless and RF communications, spatial modulation, and interference coordination in wireless networks. His team invented spatial modulation. He introduced LiFi to the public at an invited TED Global talk in 2011. LiFi was listed among the 50 best inventions in TIME Magazine in 2011. He gave a second TED Global lecture in 2015 on the use of solar cells as LiFi data detectors and energy harvesters. In 2016, he received the Outstanding Achievement Award from the International Solid State Lighting Alliance. In 2019 he was recipient of IEEE Vehicular Society James Evans Avant Garde Award. Haas was elected a Fellow of the Royal Society of Edinburgh (RSE) in 2017. In the same year he received a Royal Society Wolfson Research Merit Award and was elevated to IEEE Fellow. In 2018 he received a three-year EPSRC Established Career Fellowship extension and was elected Fellow of the IET. Haas was elected Fellow of the Royal Academy of Engineering (FREng) in 2019.

Bibliography

[1] Y. Niu, Y. Li, D. Jin, L. Su and A. V. Vasilakos, “A survey of milimeter wave communications (mmWave) for 5G: opportunities and challenges,” *Wireless Networks,* vol. 21, pp. 2657-2676, 2015.

[2] M. Daily, S. Medasani, R. Behringer and M. Trivedi, “Self-Driving Cars,” *IEEE Journals & Magazines: Computer,* vol. 50, no. 12, pp. 18-23, 2017.

[3] Y. Wu, “Cloud-Edge Orchestration for the Internet of Things: Architecture and AI-Powered Data Processing,” *IEEE Internet of Things Journal,* vol. 8, no. 16, pp. 12792-12805, 2020.

[4] H. Elgala, R. Mesleh and H. Haas, “Indoor optical wireless communication: Potential and state-of-the-art,” *IEEE Communications Magazine,* vol. 49, no. 9, pp. 56-62, 2011.

[5] H. Haas, “Multi-Gigabit/s LiFi Networking for 6G,” in *IEEE CPMT Symposium Japan*, Kyoto, Japan, 2021.

[6] T. Ismail, E. Leitgeb and T. Plank, “Free Space Optic and mmWave Communications: Technologies, Challenges and Applications,” *IEICE Transactions on Communications,* Vols. 99-B, no. 6, pp. 1243-1254, 2016.

[7] J. Lin, W. Yu, N. Zhang, X. Yang, H. Zhang and W. Zhao, “A Survey on Internet of Things: Architecture, Enabling Technologies, Security and Privacy, and Applications,” *IEEE Internet of Things Journal,* vol. 4, no. 5, pp. 1125-1142, 2017.

[8] British Standards Institution, Safety of laser products. Equipment classification and requirements [BS EN 60825-1:2014], BSI, 2014.

[9] S. S. Haykin, Digital Communications, Wiley, 2006.

[10] L. M. Fraas, Low-Cost Solar Electric Power, Switzerland: Springer, 2014.

[11] Z. Hameiri, “Photovoltaics literature survey (No. 125),” *Progress in Photovoltaics: Research and Applications,* vol. 24, no. 3, pp. 405-407, 2016.

[12] J. F. Geisz, R. M. France, K. L. Schulte, M. A. Steiner, A. G. Norman, H. L. Guthrey, M. R. Young, T. Song and T. Moriarty, “Six-junction III–V solar cells with 47.1% conversion efficiency under 143 Suns concentration,” *Nature Energy,* vol. 5, pp. 326-335, 2020.

[13] K. P. Bhandari and R. J. Ellingson, “A comprehensive guide to solar energy systems,” T. M. Letcher and V. M. Fthenakis, Eds., Academic Press, 2018, pp. 233-254.

[14] S. A. Al-Gailani, A. A. Salem, M. F. Mohd Salleh, R. Q. Shaddad, U. U. Sheikh, N. A. Algeelani and T. A. Almohamad, “A survey of Free Space Optics (FSO) Communication Systems, Links, and Networks,” *IEEE Access,* vol. 9, pp. 7353-7373, 2020.

[15] V. W. S. Chan, “Free-Space Optical Communications,” *Journal of Lightwave Technologies,* vol. 24, no. 12, pp. 4750-4762, 2006.

[16] A. K. Majumdar, “Basics of Worldwide Broadband Wireless Access Independent of Terrestrial Limitations,” in *Optical Wireless Communications for Broadband Global Internet Connectivity*, Elsevier, 2019, pp. 5-38.

[17] S. O. Saltsman, “The Silicon Solar Cell as an Optical Detector,” Florida Technological University, 1976.

[18] Z. Wang, D. Tsonev, S. Videv and H. Haas, “On the Design of a solar panel receiver for optical wireless communication with simultaneous energy harvesting,” *IEEE Journal on Selected Areas in communications,* vol. 33, no. 8, pp. 1612-1623, 2015.

[19] Z. Wang, D. Tsonev, S. Videv and H. Haas, “Towards Self-powered solar panel receiver for optical wireless communication,” in *IEEE International Conference on Communications (ICC)*, Sydney, Australia, 2014.

[20] S.-M. Kim and J.-S. Won, “Simultaneous reception of visible light communication and optical energy using a solar cell receiver,” in *International Conference on ICT Convergence*, Jeju, South Korea, 2013.

[21] S. Zhang, D. Tsonev, S. Videv, S. Ghosh, G. A. Turnbull, I. D. Samuel and H. Haas, “Organic solar cells as high-speed data detectors for visible light communication,” *Optica,* vol. 2, no. 7, pp. 607-610, 2015.

[22] J. Fakidis, S. Videv, H. Helmers and H. Haas, “0.5-Gb/s OFDM-Based Laser Data and Power Transfer Using a GaAs Photovoltaic Cell,” *IEEE Photonics Technology Letters,* vol. 30, no. 9, pp. 841-844, 2018.

[23] I. Tavakkolnia, L. K. Jagadamma, R. Bian, P. P. Manousiadis, S. Videv, G. A. Turnbull, I. D. W. Samuel and H. Haas, “Organic photovoltaics for simultaneous energy harvesting and high-speed MIMO optical wireless communications,” *Light: Science & Applications,* vol. 10, no. 41, 2021.

[24] J. Fakidis, H. Helmers and H. Haas, “Simultaneous Wireless Data and Power Transfer for a 1-Gb/s GaAs VCSEL and Photovoltaic Link,” *IEEE Photonics Technology Letters,* vol. 32, no. 19, pp. 1277-1280, 2020.

[25] G. A. Cap, H. H. Refai and J. J. Sluss Jr, “FSO tracking and auto-alignment transceiver system,” in *SPIE Security + Defense*, Cardiff, United Kingdom, 2008.

[26] H. Haas, L. Yin, Y. Wang and C. Chen, “What is LiFi?,” *Journal of Lightwave Technology,* vol. 34, no. 6, pp. 1533-1543, 2016.

[27] Y. Deng and D. Chu, “Coherence properties of different light sources and their effect on the image sharpness and speckle of holographic displays,” *Scientific Reports,* vol. 5893, no. 7, 2017.

[28] K. Shimoda, Introduction to Laser Physics, Springer Berlin Heidelberg, 2013.

[29] O. Svelto, Principles of Lasers, Springer, 2010.

[30] K. Lear, V. Ochiai, H. Hou, B. Hammons, J. Banas and J. Nevers, “High-speed vertical cavity surface emitting lasers,” in *Digest of the IEEE/LEOS Summer Topical Meeting*, Montreal, 1997.

[31] B. Naimullah, M. Othman, A. Rahman, S. Sulaiman, S. Ishak, S. Hitam and S. Aljunid, “Comparison of wavelength propagation for Free Space Optical Communications,” in *Internation Conference on Electronic Design (ICED)*, Penang, Malaysia, 2008.

[32] S. B. Alexander, Optical Communication Receiver Design, SPIE Optical Engineering Press, 1997.

[33] G. E. Stillman and C. M. Wolfe, “Avalanche Photodiodes,” in *Semiconductors and Semimetals*, Academic Press, 1977, pp. 291-393.

[34] F. Xu, M.-A. Khalighi and S. Bourennane, “Impact of different noise sources on the performance of PIN- and APD-based FSO receivers,” in *International Conference on Telecommunications*, Graz, Austria, 2011.

[35] S. Chaudhary, A. Amphawan and K. Nisar, “Realization of free space optics with OFDM under atmospheric turbulence,” *Optik,* vol. 125, no. 18, pp. 5196-5198, 2014.

[36] M. Sufyan and H. Haas, “Modulation Techniques for LiFi,” *ZTE Communications,* vol. 14, pp. 29-40, 2016.

[37] Y. Wu and W. Y. Zou, “Orthogonal Frequency Division Multiplexing: a multi-carrier modulation scheme,” *IEEE Transactions on Consumer Electronics,* vol. 41, no. 3, pp. 392-399, 1995.

[38] W. Shieh and I. Djordjevic, OFDM for Optical Communications, Academic Press, 2009.

[39] K. S. Al-Mawali, F. S. Al-Qahtani and Z. M. Hussain, “Adaptive power loading for OFDM-based power line communications impaired by impulsive noise,” in *ISPLC2010*, Rio de Janeiro, Brazil, 2010.

[40] A. N. Barreto and S. Furrer, “Adaptive bit loading for wireless OFDM systems,” in *12th IEEE International Symposium on Personal, Indoor and Mobile Radio Communications*, San Diego, USA, 2001.

[41] Critical Link LLC, “MityDSP-L138-Spec,” [Online]. Available: https://www.criticallink.com/wp-content/uploads/2014/01/MityDSP-L138-Spec.pdf. [Accessed November 2020].

[42] “IEEE 802.3-2012- IEEE Standard for Ethernet,” 2012.

[43] Purelifi, “LiFi ASIC PL0300 Datasheet,” [Online]. Available: https://purelifi.com/lifi-asic/. [Accessed May 2019].

[44] “IEEE Standard for Information technology—Telecommunications and information exchange between systems Local and metropolitan area networks—Specific requirements - Part 11: Wireless LAN Medium Access Control (MAC) and Physical Layer (PHY) Specifications,” *IEEE Std 802.11-2016 (Revision of IEEE Std 802.11-2012),* pp. 1-3534, 2016.

[45] D. S. H. Chan and J. C. H. Phang, “Analytical methods for the extraction of solar-cell single-and double-diode model parameters from I-V Characteristics,” *IEEE Transactions on Electron Devices,* vol. 34, no. 2, pp. 286-293, 1987.

[46] F. Rana, “Photodetectors and Solar Cells,” in *Semiconductor Optoelectronics*.

[47] J. Zmuidzinas, “Thermal noise and correlations in photon detection,” *Applied Optics,* vol. 42, no. 25, pp. 4989-5008, 2003.

[48] W. Schottky, “Über spontane Stromschwankungen in verschiedenen Elektrizitätsleitern,” *Annalen der Physik,* vol. 362, no. 23, pp. 541-567, 1918.

[49] H. Kanbe, G. Grosskopf, O. Mikami and S. Machida, “Dark Current Noise Characteristics and Their Temperature Dependence in Germanium Avalanche Photodiodes,” *IEEE Journal of Quantum Electronics,* vol. 17, no. 8, pp. 1534-1539, 1981.

[50] M. Faraday, Experimental Researches in Electricity, Volume 1, Project Gutenberg, 2005.

[51] S. A. Kalogirou, McEvoy's Handbook of Photovoltaics, Academic Press, 2017.

[52] V. Tamrakar, S. Gupta and Y. Sawle, “Study of characteristics of single and double diode electrical equivalent circuit models of solar PV module,” in *International Conference on Energy Systems and Applications*, Pune, 2015.

[53] Texas Instruments Inc., “TINA-TI SPICE-based analog simulation program,” Texas Instruments Inc., [Online]. Available: https://www.ti.com/tool/TINA-TI. [Accessed September 2020].

[54] S. K. Sharma, D. Pavithra, G. Sivakumar, N. Srinivasamurthy and B. L. Agrawal, “Determination of solar cell diffusion capacitance and its dependence on temperature and 1 MeV electron fluence level,” *Solar Energy Materials and Solar Cells,* vol. 26, no. 3, pp. 169-179, 1992.

[55] M. Wolf and H. Rauschenbach, “Series Resistance Effects on Solar Cell Measurements,” *Advanced Energy Conversion,* vol. 3, pp. 455-479, 1963.

[56] Solar Technology International Ltd., “5 Watt Solar Panel Kit,” [Online]. Available: https://www.solartechnology.co.uk/pv-logic/5w-solar-panel-kit. [Accessed January 2019].

[57] M. A. Khalighi and M. Uysal, “Survey on Free Space Optical Communication: A communication theory perspective,” *IEEE Communications Surveys & Tutorials,* vol. 16, no. 4, pp. 2231-2258, 2014.

[58] S. Chander, A. Purohit, A. Nehra, S. P. Nehra and M. S. Dhaka, “A Study on Spectral Response and External Quantum Efficinecy of Mono-Crystalline Silicon Solar Cell,” *International Journal of Renewable Energy Research* , vol. 6, no. 1, 2005.

[59] S. H. Lim, W. Mar, P. Matheu, D. Derkacs and E. T. Yu, “Photocurrent spectroscopy of optical absoption enhancement in silicon photodiodes via scattering from surface plasmon polaritons in gold nanoparticles,” *Journal of Applied Physics,* vol. 101, no. 10, 2007.

[60] H. K. Charles Jr. and A. P. Ariotedjo, “Review of amorphous and polycrystalline thin film silicon solar cell performance parameters,” *Solar Energy,* vol. 24, no. 4, pp. 329-339, 1980.

[61] J. Flynn, J. M. Epstein, D. R. Palmer and J. V. Egan, “Total active area silicon photodiode array,” *IEEE Transactions on Electron Devices,* vol. 16, no. 10, pp. 877-879, 1969.

[62] W.-H. Shin, S.-H. Yang, D.-H. Kwon and S.-K. Han, “Self-reverse-biased solar panel optical receiver for simultaneous visible light communication and energy harvesting,” *Optics Express,* vol. 24, no. 22, pp. A1300-A1305, 2016.

[63] H. Sharma, A. Haque and A. Z. Jaffery, “Modeling and Optimisation of a Solar Energy Harvesting System for Wireless Sensor Network Nodes,” *Journal of Sensor and Actuator Networks,* vol. 7, no. 3, 2018.

[64] Texas Instruments Inc., “BQ24650 High efficiency synchronous switch-mode charger controller – solar battery charger,” Texas Instruments,

April 2016. [Online]. Available: http://www.ti.com/product/BQ24650. [Accessed March 2019].

[65] J. A. B. Vieira and A. M. Mota, “Maximum power point tracker applied in batteries charging with PV panels,” in *IEEE International Symposium on Industrial Electronics*, Cambridge, 2008.

[66] S. Anuphappharadorn, S. Sukchai, C. Sirisamphanwong and N. Ketjoy, “Comparision the Economic Analysis of the Battery between Lithium-ion and Lead-acid in PV Stand-alone Application,” *Energy Procedia,* vol. 56, pp. 352-358, 2014.

[67] J. F. Collins, “The colour temperature of daylight,” *British Journal of Applied Physics,* vol. 16, no. 6, 1965.

[68] LEE Filters, “Colour information and spectral charts for 201,” [Online]. Available: https://www.leefilters.com/lighting/colour-details.html#201&filter=cf&sort=number. [Accessed October 2020].

[69] P. Michael, “A Conversion Guide: Solar Irradiance and Lux Illuminance,” IEEE Dataport, 2019.

[70] LiFi Research & Development Centre, University of Edinburgh, “Short Range LiFi Solar Panel Links & High Speed RF Backhaul,” 5G RuralFirst Use Case Report, 2019.

[71] O. Ndili and T. Ogunfunmi, “Achieving maximum Possible Download Speed on ADSL Systems,” in *IEEE Workshop on Signal Processing Systems*, Shanghai, China, 2007.

[72] OSRAM Opto Semiconductors GmbH, “BIDOS®, PLPVQ 940A,” OSRAM Opto Semiconductors GmbH, [Online]. Available: https://www.osram.com/ecat/BIDOS%C2%AE%20PLPVQ%20940A/com/en/class_pim_web_catalog_103489/global/prd_pim_device_5062066/. [Accessed February 2019].

[73] S. Bloom, E. Korevaar, J. Schuster and H. Williebrand, “Understanding the performance of free-space optics,” *Journal of Optical Networking,* vol. 2, no. 6, 2003.

[74] Edmund Optics, “76.2 x 50.8mm EFL 90° Protected Gold 100Å Off-Axis Parabolic Mirror,” Edmund Optics, [Online]. Available: https://www.edmundoptics.com/p/762-x-254mm-pfl-90-off-axis-parabolic-gold-mirror/33592/. [Accessed May 2019].

[75] Newport Corporation, “Precision Lens Positioner, 2.0 in., 100 TPI XYθXθY, 80 TPI Z,” Newport Corporation , [Online]. Available: https://www.newport.com/p/LP-2A. [Accessed May 2019].

[76] L. F. Chaparro, Signals and Systems Using MATLAB, Academic Press, 2019.

[77] H. G. Weber and M. Nakazawa, Ultrahigh-Speed Optical Transmission Technology, Springer-Verlag Berlin Heidelberg, 2007.

[78] Y. Tang, M. Brandt-Pearce and S. G. Wilson, "Link Adaptation for Throughput Optimization of Parallel Channels with Application to Hybrid FSO/RF Systems," *IEEE Transactions on Communications,* vol. 60, no. 9, pp. 2723-2732, 2012.

[79] Time and Date, "Time and Date," [Online]. Available: https://www.timeanddate.com. [Accessed 7 May 2019].

[80] J. Dugan, J. Estabrook, J. Ferbuson, A. Gallatin, M. Gates, K. Gibbs, S. Hemminger, N. Jones, F. Qin, G. Renker, A. Tirumala and A. Warshavsky, "iPerf - The TCP, UDP and SCTP network bandwidth measurement tool," [Online]. Available: https://iperf.fr/. [Accessed July 2019].

[81] Raspberry Pi, "Raspberry Pi 4 Datasheet," January 2020. [Online]. Available: https://datasheets.raspberrypi.org/rpi4/raspberry-pi-4-product-brief.pdf. [Accessed October 2020].

[82] P. P. Vaidyanathan, "Design and Implementation of Digital FIR Filters," in *Handbook of Digital Signal Processing*, Academic Press, 1987, pp. 55-172.

[83] H. Ishio, J. Minowa and K. Nosu, "Review and Status of Wavelength-Division-Multiplexing Technology and its Application," *Journal of Lightwave Technology,* vol. 2, no. 4, pp. 448-463, 1984.

[84] S. I. Videv, H. Haas and S. Das, "Optical Wireless Communications System". USA Patent Appl.No. :16/616,708, 19 March 2020.

[85] F. Flory, Optical Thin Films and Coatings, Elsevier Science, 2018.

[86] N. Kaiser, Optical Interference Coatings, Springer Berlin Heidelberg, 2013.

[87] Thorlabs Inc., "Notch Filters," [Online]. Available: https://www.thorlabs.com/newgrouppage9.cfm?objectgroup_id=3880. [Accessed April 2021].

[88] National Renewable Energy Laboratory, "Solar Resource Data & Tools," [Online]. Available: https://www.nrel.gov/grid/solar-resource/spectra-am1.5.html. [Accessed April 2021].

[89] A. L. Wijesinha, Y.-t. Song, M. Krishnan, V. Mathur, J. Ahn and V. Shyamasundar, "Throughput measurement for UDP traffic in an IEEE 802.11g WLAN," in *Sixth International Conference on Software Engineering, Artificial Intelligence, Networking and Parallel/Distributed*

Computing and First ACIS International Workshop on Self-Assembling Wireless Network, Towson, MD, USA, 2005.

[90] Thorlabs Inc., "Wideband multimode circulator datasheet," [Online]. Available: https://www.thorlabs.com/drawings/d8d376e96136594b-392AE46F-F9FE-46BD-3F06E5C3274A9D58/WMC1H1S-SpecSheet.pdf. [Accessed April 2021].

[91] Z. Zhang, Y. Liu, J. Bai, H. Yuan, Z. Zhao, J. Liu and N. Zhu, "Ultra-wideband Butterfly Directly Modulated Semiconductor Lasers," *IEEE Photonics Journal,* vol. 9, no. 3, pp. 1-9, 2017.

[92] Thorlabs Inc, "Multimode Fibre Beam Lab Fact," [Online]. Available: https://www.thorlabs.com/images/TabImages/Multimode_Fiber_Beam_Lab_Fact.pdf. [Accessed April 2021].

[93] A. Snyder and J. Love, Optical Waveguide Theory, Springer Science, 1983.

[94] T. Geng and X. Zhang, "Propagation properties of the circular Airy beam with a Gaussian envelope in Fourier space," *Optics Express,* vol. 28, no. 2, pp. 2447-2455, 2020.

[95] R. Paschotta, Field Guide to Lasers, SPIE Press Book, 2008.

[96] Edmund Optics, "4.25" Diameter x 17.5" FL Protected Aluminum, Parabolic Mirror," [Online]. Available: https://www.edmundoptics.eu/p/425-diameter-x-175-fl-protected-aluminum-parabolic-mirror/2110/. [Accessed May 2021].

[97] J. Fakidis, S. Videv, S. Kucera, H. Claussen and H. Haas, "Indoor Optical Wireless Power Transfer to Small Cells at Nighttime," *Journal of Lightwave Technology,* vol. 34, no. 13, pp. 3226-3258, 2016.